University of Strathclyde Science

TOWARDS PLASMA-BASED ATTOSECOND-ÅNGSTROM CLASS FREE-ELECTRON LASER

by

Ahmad Fahim Habib

A thesis presented for the degree of

Doctor of Philosophy in Physics

University of Strathclyde

Department of Physics

2024

DECLARATION

This thesis is the result of the author's original research. It has been composed by the author and has not been previously submitted for examination which has led to the award of a degree. The copyright of this thesis belongs to the author under the terms of the United Kingdom Copyright Acts as qualified by University of Strathclyde Regulation 3.50. Due acknowledgement must always be made of the use of any material contained in, or derived from, this thesis.

Glasgow, United Kindom, March 2024

Ahmad Fahim Habib

ABSTRACT

Investigating electronic motions in matter at their natural time and length scale requires radiation pulses simultaneously providing attoseconds temporal and Ångstrom spatial resolution. This could reveal a previously unexplored realm of nature. While hard *X-ray Free-Electron Lasers* (XFELs) based on radiofrequency technology can routinely produce coherent radiation pulses with femtosecond durations and Ångstrom wavelengths, they require optimized kilometre-scale machines with limited beam time. This thesis shows that plasma-based accelerators can produce multi-GeV electron beams with superior beam quality on the sub-meter scale, paving the way for ultra-compact hard XFELs at meter-scale distances. Three innovations constitute the blueprint for the ultra-compact, plasma-based attosecond-Ångstrom class free-electron laser with unprecedented electron and photon beam quality. First, the experimental demonstration of the plasma photocathode injection in *Plasma Wakefield Acceleration* (PWFA) at *Stanford Linear Accelerator* (SLAC) *Facility for Advanced Accelerator Experimental Tests* (FACET) shows the feasibility of the plasma photocathode concept. In-depth simulations revealed the full reach of the plasma photocathode in PWFA. This study also highlighted that the impact of injector laser jitter on electron beam stability in the various building blocks is compatible with the requirements of XFELs, thanks to the fundamental physics of the mechanisms. Second, the development of a novel energy chirp compensation method allows for the minimization of the projected relative energy spread of ultra-high 5D brightness electron beams in the same plasma stage without compromising the nm-rad normalized emittances of the beams, enabling the preservation of emittances at the nm-rad level during the extraction from the plasma-stage. Third, an ultra-compact, plasma-based hard XFEL concept is developed and backed by a high-fidelity start-to-end simulations framework. A PWFA stage equipped with plasma photocathode injectors produces electron beams of unprecedented 6D brightness. The electron beam quality is preserved along the acceleration, dechirping, and extraction from the plasma stage. Then, an optimized beam transport line captures, isolates, and refocuses these ultra-high 6D brightness electron beams into an undulator without quality loss. A 10 m long

undulator section leverages these electron beams to power a hard XFEL near the cold beam limit. These electron beams straightforwardly generate nearly transform-limited photon pulses at attosecond duration down to sub-Ångstrom wavelength, with prospects towards higher photon energies and fully coherent radiation pulses. An experimental feasibility analysis concludes with prospects and opportunities for realizing the concept at linac-based PWFA facilities and/or at *Laser Wakefield Acceleration* (LWFA) facilities through the Hybrid LWFA→PWFA approach, which may enable truly ultra-compact plasma-based hard XFELs. The individual findings of this thesis may significantly advance their respective subjects, though a transformative impact emerges from the combined ramifications of the findings. For example, the realization of the concept with an all-optical Hybrid LWFA→PWFA system or in combination with a linac-based PWFA facility in collider geometry could enable collocated ultra-high brightness electron beams, TW- to PW-class laser pulses, hard XFEL photon pulses, or γ-ray pulses generated by these electron beams at the interaction point, all intrinsically synchronized. Such a configuration may allow the ubiquitous use of photon and electron beams in various permutations for completely novel photon science, nuclear and particle physics, fundamental science and quantum electrodynamics exploration.

PUBLICATIONS

The author has produced or contributed to the following publications during this study. The *-symbol indicates equal first authorship:

1. **Habib A. F.**, Heinemann, T., Manahan, G. G., Ullmann, D., Scherkl, P., Knetsch, A., Sutherland, A., Beaton, A., Campbell, D., Rutherford, L., *et al.* Plasma photocathodes. *Annalen der Physik* **535,** 2200655 (2023).
2. **A. F. Habib** *et al.* Attosecond-Angstrom free-electron-laser towards the cold beam limit. *Nature communications* **14,** 1054 (2023).
3. **Habib, A. F.**, Scherkl, P., Manahan, G. G., Heinemann, T., Ullmann, D., Sutherland, A., Knetsch, A., Litos, M., Hogan, M., Rosenzweig, J., *et al. Plasma accelerator-based ultrabright x-ray beams from ultrabright electron beams* in *Advances in Laboratory-based X-Ray Sources, Optics, and Applications VII* **11110** (2019), 111100A.
4. G. G. Manahan* and **A. F. Habib*** *et al.* Single-stage plasma-based correlated energy spread compensation for ultrahigh 6D brightness electron beams. *Nature Communications* **8,** 15705 (2017).
5. Delinikolas, P., Hidding, B. & **Habib, A.F.** *System for radiation therapy* US patent app. 17/762304 and EP patent app. 20780998.9. 2022.
6. Hidding, B., Manahan, G. & **Habib, A. F.** *Plasma accelerator* US patent app. 11013100 and EP patent app. 3510843. 2021.
7. Manahan, G. G. and **Habib, AF**, Scherkl, P, Ullmann, D, Beaton, A, Sutherland, A, Kirwan, G, Delinikolas, P, Heinemann, T, Altuijri, R, *et al.* Advanced schemes for underdense plasma photocathode wakefield accelerators: pathways towards ultrahigh brightness electron beams. *Philosophical Transactions of the Royal Society A* **377,** 20180182 (2019).

8. Deng, A., Karger, O., Heinemann, T., Knetsch, A., Scherkl, P., Manahan, G. G., Beaton, A., Ullmann, D., Wittig, G., **Habib, A. F.**, *et al.* Generation and acceleration of electron bunches from a plasma photocathode. *Nature Physics* **15,** 1156–1160 (2019).

9. Hidding, B., Manahan, G., Heinemann, T, Scherkl, P, **Habib, F**, Ullmann, D, Beaton, A, Sutherland, A, Knetsch, A, Karger, O, *et al. First measurements of Trojan Horse injection in a plasma wakefield accelerator* in *8th International Particle Accelerator Conference, Copenhagen, pp.TUYB1* (JACoW, 2017).

10. Scherkl, P., Knetsch, A., Heinemann, T., Sutherland, A., **Habib, A. F.**, *et al.* Plasma photonic spatiotemporal synchronization of relativistic electron and laser beams. *Phys. Rev. Accel. Beams* **25,** 052803 (2022).

11. Ullmann, D, Scherkl, P, Knetsch, A, Heinemann, T, Sutherland, A, **Habib, AF**, Karger, O., Beaton, A, Manahan, G., Deng, A, *et al.* All-optical density downramp injection in electron-driven plasma wakefield accelerators. *Physical Review Research* **3,** 043163 (2021).

12. Alotaibi, B. M., Altuijri, R., **Habib, AF**, Hala, A., Hidding, B., Khalil, S. M., McNeil, B. & Traczykowski, P. Plasma wakefield accelerator driven coherent spontaneous emission from an energy chirped electron pulse. *New Journal of Physics* **22,** 013037 (2020).

13. Emma, C., Van Tilborg, J., Assmann, R., Barber, S., Cianchi, A., Corde, S., Couprie, M. E., D'Arcy, R., Ferrario, M., **Habib, A. F.**, *et al.* Free electron lasers driven by plasma accelerators: status and near-term prospects. *High Power Laser Science and Engineering* **9,** e57 (2021).

14. Foerster, F. M. *et al.* Stable and High-Quality Electron Beams from Staged Laser and Plasma Wakefield Accelerators. *Phys. Rev. X* **12,** 041016 (2022).

15. Hidding, B., Beaton, A., Boulton, L., Corde, S., Doepp, A., **Habib**, t., *et al.* Fundamentals and applications of hybrid LWFA-PWFA. *Applied Sciences* **9,** 2626 (2019).

16. Hidding, B. *et al.* Progress in Hybrid Plasma Wakefield Acceleration. *Photonics* **10,** 99 (2023).

17. Assmann, R., Weikum, M., Akhter, T, Alesini, D, Alexandrova, A., Anania, M., Andreev, N., Andriyash, I, Artioli, M, Aschikhin, A, *et al.* EuPRAXIA conceptual design report. *The European Physical Journal Special Topics* **229,** 3675–4284 (2020).

18. Marangos, J. *et al.* UK-XFEL Science Case (2020).

19. Geddes, C., Assmann, R, Hogan, M. & Musumeci, P. Report of the Accelerator Frontier Topical Group 6 on Advanced Accelerator Concepts for Snowmass 2021. *arXiv:2208.13279* (2022).

ACKNOWLEDGEMENTS

I want to give a huge thanks to Bernhard Hidding for allowing me to work on cutting-edge projects. He has always encouraged me to develop new ideas and provided me with the right mentoring and support throughout the past few years. This significantly contributed to my development as an independent scientist and supported my professional development.

Many thanks to Brian McNeil for his co-supervision and for sharing his expert FEL knowledge. In particular, Brian ensured my employment during the writing-up phase and I would like to express my gratitude.

Thanks to the Engineering and Physical Sciences Research Council (EPSRC) for funding my PhD project under the Grant number: 1823175.

Particular thanks to Grace Manahan, with whom I shared my office and many scientific publications. Many of the achievements of this thesis were only possible thanks to many fruitful discussions.

Particular thanks to Paul Scherkl for many fruitful discussions at work and during leisure time. We always benefited from each other's know-how in various ways. Your Python skills are just next-level.

I would like to thank Oliver S. Karger and Alexander Knetsch for designing and performing large parts of the E-210 programme and post-processing the experimental data.

Thanks to Thomas Heinemann for many PIC simulation-related discussions and beyond. I enjoy our heated scientific discussions, which often result in progress.

Thanks to my flatmates and friends Michael C. and Maria W. Many thanks for the emotional support during the downtimes.

Finally, I would like to thank my family for their relentless support over the years. Much of this work would not have been possible without the encouraging words.

CONTENTS

LIST OF FIGURES

LIST OF TABLES

1

INTRODUCTION

This chapter provides motivation and an introduction to the thesis subject and concludes with the thesis outline and the author's contributions.

1.1 MOTIVATION

In the 21st century, humanity will face significant challenges that can be solved by utilizing science, technology, and innovation. These challenges include developing sustainable and abundant energy sources, developing functional materials, and understanding and precisely controlling chemical and biochemical reactions [1]. For example, by making scientific breakthroughs, we can create more efficient ways to harness energy from the sun, progress fusion energy research, create functional materials for carbon dioxide recycling, engineer sustainable fertilisers for food production, and manufacture eco-friendly goods and medications [1, 2]. Functional materials are integral to quantum and information technology and may enable the next generation of computing capabilities. Additionally, accurately controlling chemistry and biochemistry may allow us to create novel medications to treat diseases once thought to be incurable, for example, cancer, Alzheimer's disease, and more and develop custom medications with bioengineering for precision treatment [3] tailored to individual patients [4]. The foundation of bioengineering is built upon the breakthrough results and *Research and Development* (R&D) in molecular crystallography and material science from the past century.

Over the past century, molecular crystallography and material science have been transformed by *Synchrotron Radiation* (SR) sources (known as 3rd generation light sources). These novel radiation sources allowed investigation of atoms and molecules at their natural length scale of Ångstrom ($1\,\text{Å} = 10^{-10}\,\text{m}$). However, due to the comparably

long radiation pulses lasting *picoseconds* ($1\,\text{ps} = 10^{-12}\,\text{s}$), these sources have been limited to providing insights into the static structure of specific molecules and materials [5–7]. This changed with the advent of *Free-Electron Lasers* (FELs) (4^{th} generation light sources) in the soft and hard X-ray wavelengths [8, 9], offering *femtoseconds* ($1\,\text{fs} = 10^{-15}\,\text{s}$) temporal and nanometre-scale ($1\,\text{nm} = 10^{-9}\,\text{m}$) spatial resolution with radiation intensities many order of magnitude larger than SR sources [10, 11]. However, FELs require high-quality electron beams at multi-*Gigaelectronvolt* (GeV) electron beam energies, necessitating using kilometre-scale machines for generation, manipulation, acceleration, transport of high-quality electron beams, and radiation production. This high level of technology makes the cost of building hard XFELs facilities typically around 1 billion pounds sterling. Additionally, only a handful of XFEL facilities are available worldwide and are notoriously oversubscribed. More details on conventional accelerators are provided in section (2.1.1).

Novel technologies can unfold their impact across science and industry if access to technology is widespread. This is evident from femtosecond radiation sources enabled by high-power laser systems. Thanks to the breakthrough innovations of femtosecond pulse generation via *Chirped Pulse Amplification* (CPA) [12] at the *infrared* (IR) wavelength. Then, these femtosecond high-power laser pulses unleashed through threshold-tunnel ionization processes in gaseous media the production of attosecond duration pulses ($1\,\text{as} = 10^{-18}\,\text{s}$) at the extreme ultraviolet wavelength via the *High-Harmonic Generation* (HHG) [13–15], however, at comparably low intensities. Both achievements have been recognised by the recent Nobel Prizes in Physics [16, 17] and profoundly impacted science and society.

Using light from FELs and ultra-short laser pulses has significantly advanced science by allowing us to observe natural processes with femtosecond to attosecond temporal resolution. With these tools, researchers can now observe atomic motion, electronic excitation, and decay processes, which are essential for extracting crucial information regarding fundamental interactions inside atoms, molecules, and solids [1, 2, 18, 19]. This development has also nourished the femto- and atto-chemistry fields [20, 21] and significantly transformed our understanding of chemistry and biochemistry and many other areas in science [22, 23].

The next scientific breakthrough is expected to come from the combination of attosecond pulses and Ångstrom spatial resolution. This may allow us to reveal how

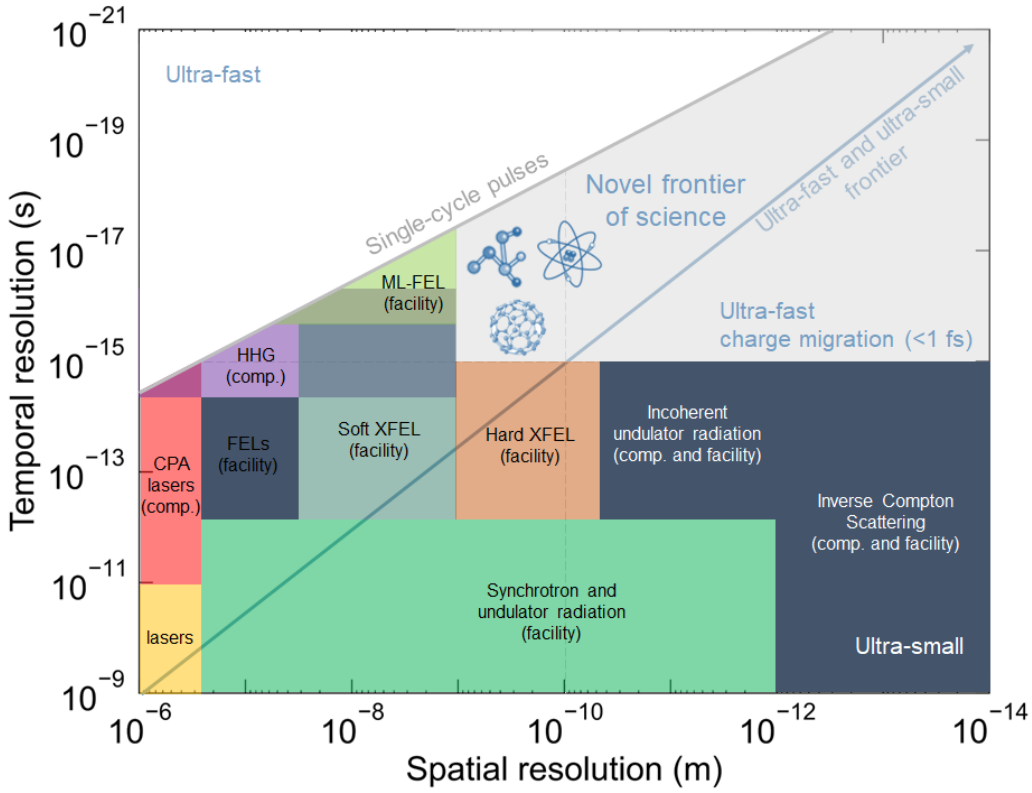

Figure 1.1: **Overview plot of temporal and spatial resolution of relevant radiation sources and a path to new science frontier.** Temporal and spatial resolution capabilities enabled by selected radiation sources with a spatial footprint from compact (few meters) to large-scale (km-scale) facility. Exploration of the novel frontier of science requires novel radiation and particle sources. The ranges for the different state-of-the-art radiation sources are estimated from [2, 22, 24]. Produced by the author for the thesis.

electrons move between electronic states in atoms, inside molecules and solids at the attosecond time and Ångstrom length scale and may enhance our understanding of ultra-fast charge transfer, electron-nuclear coupling, enable time-resolved observation of chemical reactions and more [25, 26]. Observing electronic motion at their natural time and length scale will ultimately allow the simultaneous manipulation and control of electrons and electronic states in matter with *attosecond pump and probe* experiments and, further, enable true *diffraction before distraction* type of single-molecule structural determination experiments [27, 28]. This motivates the development of new research tools to explore a previously hidden realm of nature. The breakthroughs anticipated from this research direction will not only improve our understanding of basic science but also have the potential to transform lives significantly. The ultimate goal is simultaneously having attosecond duration and Ångstrom wavelength capabilities from FELs. It is suspected that the future of attosecond science might be at FEL facilities [29].

Indeed, at the modern kilometre-size XFEL facilities, ingenious beam manipulation techniques with spoiler foils, the interaction of the electron beam with radiation produced by the electron beam itself, or manipulation of the electron beam with a fs duration laser pulse, are utilized to modulate or de-emphasise or promote parts of the electron beam for the generation of attosecond pulses [24, 30–34]. Many of these techniques are either limited to the soft X-ray wavelength or require an exact spatiotemporal overlap of the laser pulse with the electron beam and/or intricate arrangements of undulator modules for a *mode-locked FEL* (ML-FEL) configuration [24, 35]. Figure (1.1) provides an overview of the radiation sources discussed and the potential direction towards the ultra-fast and ultra-small frontier of science by delivering single-cycle radiation pulses at increasingly shorter wavelengths. The grey region indicates the temporal and spatial resolution capabilities, which may yield new scientific breakthroughs.

The attosecond metrology in soft and hard X-ray FEL regimes can only unleash its full potential across natural science if the XFEL technology is widely accessible. This requires a pathway to miniaturise XFELs, bring the capabilities to small university-scale laboratories, and increase the capacity to perform photon science experiments across the natural science sector. However, fundamentally state-of-the-art XFELs are highly optimised machines and are approaching their limit in terms of the accelerating gradient of 100 MV/m [36]. Further, the means of electron beam generation also limits the electron beam characteristics, which limits obtainable photon pulse properties (see

section (2.1)). Fortunately, emerging ultra-compact plasma-based particle accelerators may provide a way forward to increase capacity and enable potential novel capabilities and modalities in photon science and particle physics.

Plasma wakefield accelerators harness plasma waves excited in an ionized gaseous medium that can sustain accelerating gradients and focusing fields three or four orders of magnitude larger than conventional accelerators [37]. These plasma waves enable multi-GeV electron beam energy gains on sub-m-scale distances and nourish the hope for ultra-compact FELs on meter-scale distances. However, the electron beams from plasma-based accelerators fail to overcome the electron beam quality requirements for hard X-ray FELs. Hence, to close this electron beam quality gap, a great deal of effort has been devoted to beam quality improvement in recent years with partial success (see section (3.2.1)). One auspicious approach is the *plasma photocathode injection* (informally known as *Trojan Horse* (TH) injection) (see section (3.2.5)). The plasma photocathode injection can potentially improve electron beam quality by many orders of magnitude and even surpass the best state-of-the-art accelerators. Beyond generating sufficient-quality electron beams, subsequent preservation during acceleration and extraction from the plasma stage and transport towards the application is challenging.

The present thesis identifies key obstacles of plasma-based accelerators that prevent the realisation of ultra-compact hard XFELs and systematically develop innovative solutions which when aggregated pave the way for an ultra-compact attosecond-Ångstrom free-electron laser with encouraging first experimental results of the plasma photocathode injection method. Section (1.2) outlines the thesis alongside the author's role.

1.2 THESIS OUTLINE AND ROLE OF THE AUTHOR

The first half of chapter (2) reviews the fundamentals of high-brightness electron beams, the limitations of conventional electron beam production and acceleration methods and introduces the formalism governing the transformation of charged particle beams through beam transport lines. The second half of the chapter discusses the fundamentals of free-electron lasers with relevant theoretical concepts. Based on the findings of this chapter, electron beam quality requirements for the ultra-compact hard X-ray free-electron laser are established, which serve as reference values in the following chapters.

In chapter (3), plasma characteristics and generation are briefly introduced. This chapter continues with a comprehensive review of plasma-based acceleration, injection methods and limitations. The author identifies critical obstacles preventing the realisation of plasma-based free-electron lasers and outlines potential pathways to overcome electron beam quality limitations.

In chapter (4), the author presents the results of a novel plasma-based spatiotemporal alignment method based on plasma afterglow and the first experimental evidence for the plasma photocathode injection method, which is highly encouraging for ultra-compact hard XFELs. In the second half of the chapter, the author presents strategies and results for improving the quality and stability of the electron beams produced by plasma photocathode, addressing one of the obstacles towards ultra-compact hard XFELs. The author has contributed conceptually to the plasma afterglow publication [38] and significantly contributed to data and simulation interpretation and the publishing of the work. O. Karger and A. Knetsch led the data acquisition of the plasma photocathode injection experiment (E-210). The author contributed significantly to the post-processing, evaluation, and interpretation of experimental and simulation data. Further, the author contributed significantly to the writing and publishing of the manuscript [39]. This chapter's second half concerning stability and prospects is the author's original work and is published in [40, 41] as a first author.

In chapter (5), the author develops a versatile energy chirp/spread compensation method capable of dealing with electron beams of unprecedented brightness in the same plasma stage where the electron beam is generated and accelerated. The author expands the investigations by studying the stability and extraction of electron beams from the plasma stage while considering the newly developed energy chirp compensation approach. This chapter's innovation and findings are crucial components that solve one of the significant obstacles in plasma-based acceleration and enable the production of 6D phase space compact electron beams. The results of this chapter are the author's original work and are in parts published in [42] as an equivalent first author and contributing author in [43]. The author conceived the innovation, performed the simulation, and, jointly with co-authors, wrote the manuscript.

In chapter (6), a plasma-based attosecond-Ångstrom class free-electron laser concept is developed and is backed by a high-fidelity start-to-end simulations framework. Here, the innovations, results, and findings of previous chapters inform the design of a

dedicated plasma-based acceleration stage to produce electron beams with unprecedented brightness. Then, a beam transport line is designed and optimized to capture, transport, isolate and match the ultra-high quality electron beam into an undulator section without quality degradation. The undulator section harnesses the ultra-high quality electron beam for hard X-ray coherent photon production. This chapter concludes with a discussion of the experimental feasibility and stability of the plasma-based hard XFEL concept. The results of this chapter are the author's original work and are in parts published in [44] as the first author. The author conceived the concept, performed the start-to-end simulations, and led the manuscript writing jointly with co-authors.

In chapter (7), the results and conclusions of this thesis are summarised, and a brief outlook is provided.

2

FUNDAMENTALS OF FREE-ELECTRON LASERS

The first part of this chapter reviews conventional accelerator components and establishes basic concepts of charged particle optics and the characterisation of particle beams. The second part introduces the theory of free-electron lasers and defines electron beam target parameters for the PWFA-powered FELs.

2.1 HIGH-BRIGHTNESS BEAMS IN CONVENTIONAL ACCELERATORS

This section discusses *radio-frequency* (rf) based particle accelerators, their brief history and challenges. Further, the concepts of electron beam parameterisation and characterisation, beam focusing, and compression are introduced. This is an important background for the scope of this work. Further, state-of-the-art electron beam sources exploited in rf-accelerators for high-brightness beams are reviewed, and their limitations are described.

2.1.1 *Review of radiofrequency-based particle accelerators*

Particle beam experiments have played a significant role in studying the structure of matter and exploring fundamental science. One of the most notable experiments that contributed to this field was the 'gold foil experiment', conducted by undergraduate Ernest Marsden under the supervision of Ernest Rutherford and Hans Geiger [45]. During this experiment, Marsden directed α-particles at atoms from naturally occurring radioactive sources and observed unexpected scattering angles. This led to the discovery of a new theory of atomic structure [46]. Ernest Rutherford realized that higher energy

particles were necessary for advancing the field. To generate high-energy charged particle beams, interaction with electromagnetic fields is necessary. The interaction of charged particles with electromagnetic fields is governed by the Lorentz force equation, which reads

$$\mathbf{F} = q(\mathbf{E} + \mathbf{v} \times \mathbf{B}), \tag{2.1}$$

where q is the charge of the particle, $\mathbf{E}$ and $\mathbf{B}$ are the electric and magnetic field vectors, respectively, and $\mathbf{v}$ is the particle's velocity vector. The magnetic field produces a force perpendicular to the particle velocity, caused by the cross product of velocity and magnetic field vectors $\mathbf{v} \times \mathbf{B}$. In laboratory settings, electric fields can be used to accelerate charged particles. For example, a charged particle between two conducting plates will be accelerated along the electric field lines. The total energy gain in an electric field can be expressed mathematically with

$$\Delta W = q \int_0^L E_\mathrm{z}(s) ds, \tag{2.2}$$

where $E_\mathrm{z}(s)$ is the longitudinal electric field along the particle's propagation direction s, and L is the total acceleration length. Equation (2.2) shows that higher energies W can be achieved by increasing either the strength of the electric field or the acceleration distance. However, due to limitations arising from discharges between the conductive plates, the available electrostatic machines could not produce the desired particle energies for research at the time.

Gustav Ising suggested alternating drift tubes for linear particle acceleration in 1924, which aimed to overcome the limitations of existing techniques. Later, in 1928, Rolf Widerøe introduced the concept of using radio-frequency voltage between successive drift tubes. It led to the development of standing and travelling wave cavities. Currently, a cavity-based accelerator that utilizes rf-waves, similar to the one shown in Fig.(2.1) (top), is used to achieve accelerating gradients up to 100 MV/m [36]. Building tens of kilometres of *linear accelerator* (linac) infrastructure is necessary to achieve electron and positron beam energies at the TeV-level [36]. For example, modern XFELs utilize km-long linacs to achieve multi-GeV electron beam energies. Fig.(2.1) (bottom) shows a bird's-eye view of the km-size linacs operated at SLAC with annotation of FACET-II amount of other facilities.

Alternatively, particles can pass through an accelerating structure multiple times in a circular configuration, increasing their energy W with each turn. In 1931, Milton

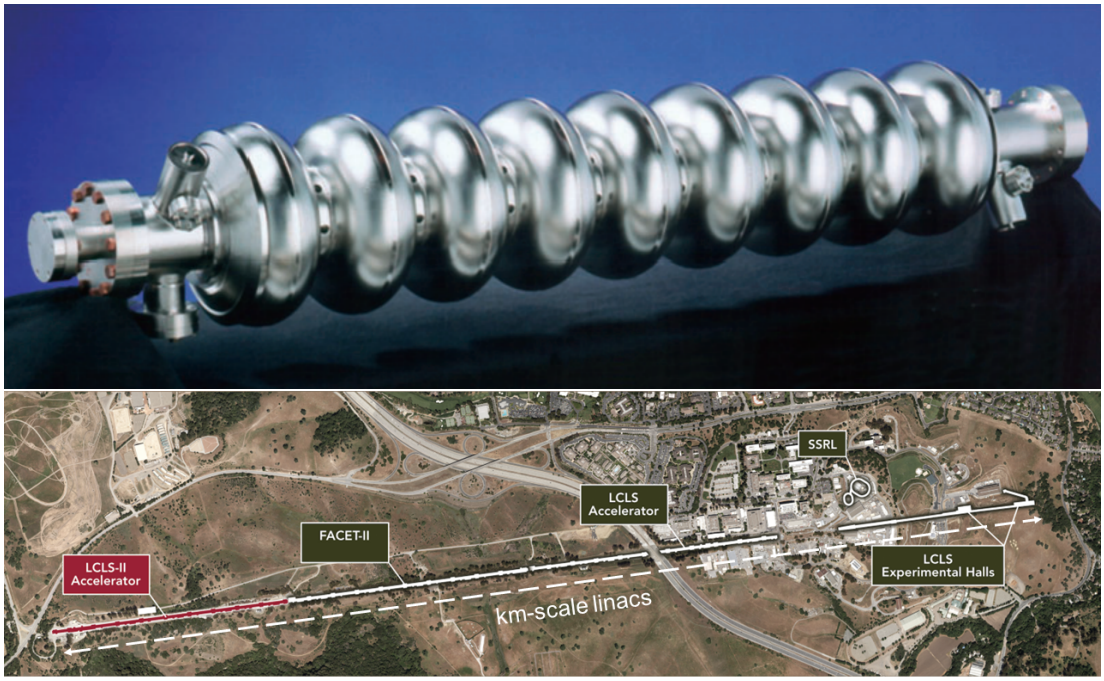

Figure 2.1: **A modern version of rf-cavity and modern linacs based on rf-technology.** A modern version of the rf-technology-based accelerator cavity (top) and modern linacs at SLAC (bottom) based on the rf-technology are depicted. Adapted from [36] (top) and SLAC homepage [47] (bottom). This work is openly licensed via CC BY 4.0.

Stanley Livingston and Ernest Lawrence began developing the cyclotron based on this concept [48]. A uniform magnetic field B is required to keep the particles in a circular motion with the particle bending radius r following the relation

$$r \propto \frac{B}{W}. \tag{2.3}$$

The revolution frequency of the particles in the non-relativistic limit is known as the cyclotron frequency

$$f = \frac{qB}{2\pi m_0}, \tag{2.4}$$

where m_0 is the mass of the particle species. When the rf-accelerating structure is tuned to the cyclotron frequency, particles gain energy with each turn and spiral outward with increasing energy, obeying Eq.(2.3). However, with increasingly relativistic energies, i.e., $\beta = v/c_0 \approx 1$, the relativistic mass increases

$$m^* = \frac{m_0}{\sqrt{1 - \left(\frac{v}{c_0}\right)^2}} = \frac{m_0}{\sqrt{1-\beta^2}} = \gamma_{\text{rel}} m_0, \tag{2.5}$$

where v is the velocity of particles, and c_0 is the speed of light in vacuum. This changes the cyclotron frequency to

$$f = \frac{qB}{2\pi \gamma_{\text{rel}} m_0}, \tag{2.6}$$

where $\gamma_{\text{rel}} = 1 + W/m_0 c_0^2$ is the relativistic Lorentz factor. This change in cyclotron frequency causes the particles to detune from the rf-signal, thereby preventing acceleration to ultra-relativistic energies ($\gamma_{\text{rel}} \gg 1$).

In Eq.(2.3), a solution is apparent that suggests keeping the radius constant instead of the magnetic field. This can be achieved by linearly increasing the particle beam energy through an rf acceleration section at each revolution. The bending magnetic field B should also be increased synchronously with the particle energy W to maintain a constant radius. However, this solution presents a challenge to the stability of the particle beams in the accelerator. The development of the strong focusing theory (see section (2.1.2)) provided a way out of this dilemma. It uses external multipole electromagnets to focus and keep the particle beam within the desired orbit. Nicholas Christofilos proposed the strong focusing approach in 1949 [49] and later independently developed by Ernest Courant, M. Stanley Livingston, Hartland Snyder, and J. Blewett at Brookhaven National Laboratory [50]. This conceptual breakthrough enabled circular particle accelerators to advance into sophisticated machines, such as the *Large Hadron*

Collider (LHC) at the *European Organization for Nuclear Research* (CERN). The LHC, with a circumference of 27 km, produces proton beams with an energy of 7 TeV for *High Energy Physics* (HEP) R&D.

It is ironic that Eq.(2.3) indicates a solution to the problem while also revealing the fundamental limitation of circular accelerators. As beam energies increase, the accelerator's bending magnetic field or radius must also be increased. However, since superconducting bending magnets based on current technology have hit their limits, the only variable left to increase is the size of the accelerator. The proposed *Future Circular Collider* (FCC) is an example of this, with a circumference of 100 km, compared to the existing LHC as shown in figure (2.2).

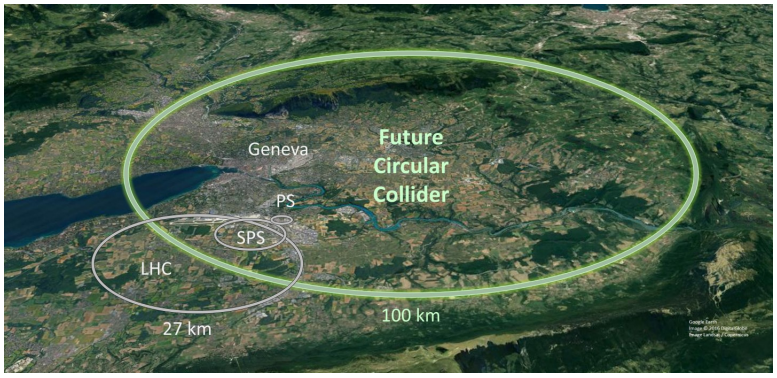

Figure 2.2: **Particle accelerator at CERN.** Bird's-eye view of the LHC and proposed FCC particle accelerator at CERN. Adapted from the CERN homepage [51]. This work is openly licensed via CC BY 4.0.

Thus, it is the primary motivation of R&D in *Advanced Accelerator Concepts* (AACs) to find ways to shrink the size and costs of future particle accelerators with potentially new particle beam capabilities and modalities beyond the reach of existing state-of-the-art technologies. Indeed, AACs has a vibrant R&D community with various proposals and concepts addressing particle acceleration, focusing and modifying particle beams, and novel diagnostic methods for extreme beams (see chapter (3)).

2.1.2 *Transverse dynamics of charged-particle beams*

When designing a beamline for a particle accelerator, many beamline elements are involved in accelerating, focusing and steering the particle beam. Solving and evaluating the equation of motion in the laboratory frame may become challenging. Therefore,

a right-handed coordinate system is introduced, mapping the laboratory frame into a co-moving *reference particle* frame. The *Frenet-Serret coordinate system* travels on the design orbit and simplifies the mathematical equations significantly. The reference particle is not necessarily an actual particle but rather a mathematical construct representing the centre of mass of a particle beam. Figure (2.3) illustrates the Frenet-Serret coordinate system spanned by three orthogonal basis vectors $\hat{x}$, $\hat{y}$, and $\hat{z}$, where $\hat{x}$, $\hat{y}$ are the horizontal and vertical directions, respectively, and $\hat{z}$ the longitudinal direction, and $\hat{s} = vt$ is the distance along the design orbit. In the figure, $\hat{z}$ points always tangentially to the design orbit because of the curved trajectory of $\hat{s}$; however, in linacs, z, s or t are often used interchangeably because the design orbit is usually a straight line for most of the linac. Now, a single particle can be uniquely described in this frame of reference by a six-dimensional state vector, three positions and corresponding momenta values

$$\mathbf{X} = \begin{bmatrix} x \\ x' \\ y \\ y' \\ \zeta \\ \delta \end{bmatrix}, \tag{2.7}$$

where $x' = \frac{dx}{dz} \approx \frac{p_\mathrm{x}}{p_0}$ and $y' = \frac{dy}{dz} \approx \frac{p_\mathrm{y}}{p_0}$ are the slopes/angles with $p_\mathrm{x,y}$ being the transverse momenta, $\zeta = z - z_0$ is the longitudinal beam coordinate and $\delta = \frac{\Delta p}{p_0}$ is the relative momentum deviation and p_0 is the central forward momentum. For particle beams consisting of millions of particles, tracking single particle trajectories becomes impractical for analytical expressions. For now, the single-particle picture is considered for simplicity. Later, concepts on the parameterization of particle beams are introduced.

Charged particles can be steered and focused very efficiently by magnetic fields, as discussed in section (2.1.1). Specialised magnets are installed along the design orbit with mid-plane symmetry $x = y = 0$ for guiding and deflecting the particle beams. Multi-pole expansion of the magnetic field $B_\mathrm{y}(x)$ at $x = 0$ reveals the higher order B-field components

$$B_\mathrm{y}(x) = \sum_{n=0}^{\infty} \frac{x^n}{n!} \frac{\partial^n B_\mathrm{y}}{\partial x^n} = \frac{p_0}{e} \left(k_0 + k_1 x + k_2 \frac{x^2}{2} + ... \right), \tag{2.8}$$

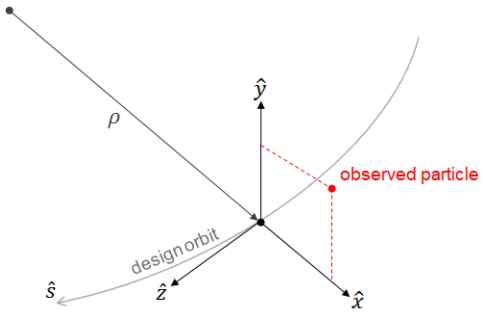

Figure 2.3: **The Frenet-Serret coordinate system is commonly utilized in accelerator physics.** $\hat{x}$, $\hat{y}$, and $\hat{z}$ form an orthogonal basis, $\hat{s}$ is the distance along the design orbit, and ρ is the local bending radius.

where e is the electron charge, and p_0 is the central momentum of the particle. The dipole k_0, quadrupole k_1 and sextupole k_2 terms read

$$k_0 = \frac{e}{p_0} B_0 = \frac{1}{\rho}\ [\mathrm{m}^{-1}], \qquad k_1 = \frac{e}{p_0}\frac{\partial B_\mathrm{y}}{\partial x}\ [\mathrm{m}^{-2}], \text{ and } \qquad k_2 = \frac{e}{p_0}\frac{\partial^2 B_\mathrm{y}}{\partial x^2}\ [\mathrm{m}^{-3}]. \tag{2.9}$$

The dipole and quadrupole components of the B-field are relevant to this work for beam steering and focusing. Still, higher-order components are utilized in particle accelerators for achromatic focusing or correction of the beam orbit and tilt. Considering the multi-pole fields Eq.(2.8) with the equation of motion Eq.(2.1) and using the paraxial approximation for $\delta \ll 1$, the *Hill's equations* is obtained for particle trajectories [52–54]

$$x'' + \Big(k_0(s)^2 - k_1(s)\Big)\, x = k_0(s)\delta \tag{2.10}$$

$$y'' + k_1(s) y = 0\ . \tag{2.11}$$

When δ equals zero, Eq.(2.10) becomes a classical harmonic oscillator, a homogeneous second-order differential equation with well-known solutions (see section (2.1.3)). If dipole fields are absent, then k_0 becomes zero, and the equation in the x-direction is further simplified to $x'' - k_1(s)x = 0$. The negative sign before the $k_1(s)x$ term indicates a fundamental property of quadrupole fields: the ability to focus particle beams only in one transverse plane while defocusing them in the other. To achieve net focusing in both transverse planes, a second quadrupole must be added that is rotated by 90° in the $x - y$ plane. A two quadrupole configuration is called a *doublet*.

A matrix formalism for particle beam optics can be formulated by solving Hill's equation. This formalism is similar to the ABCD-matrix formalism used in laser beam optics and allows for a convenient transformation of particle beams through a beamline.

The effect of a beamline component on an initial state vector $\mathbf{X}_\mathrm{i}$ of the particle can be evaluated by matrix multiplication

$$\mathbf{X}_\mathrm{f} = \mathbf{R}_i \mathbf{X}_\mathrm{i}, \tag{2.12}$$

where $\mathbf{R}_i$ is the transfer matrix of a beamline component, and $\mathbf{X}_\mathrm{f}$ is the final state of the particle. When a beamline consists of multiple elements, such as drifts, dipoles, and quadrupoles, then the transformation of $\mathbf{X}_\mathrm{i}$ through the entire beamline can be calculated by multiplying matrices of individual beamline elements sequentially

$$\mathbf{X}_\mathrm{f} = \mathbf{R}_\mathrm{n} ... \mathbf{R}_3 \mathbf{R}_2 \mathbf{R}_1 \mathbf{X}_\mathrm{i}. \tag{2.13}$$

The general form of the transfer matrix is

$$\mathbf{R} = \begin{bmatrix} R_{11} & R_{12} & R_{13} & R_{14} & R_{15} & R_{16} \\ R_{21} & R_{22} & R_{23} & R_{24} & R_{25} & R_{26} \\ R_{31} & R_{32} & R_{33} & R_{34} & R_{35} & R_{36} \\ R_{41} & R_{42} & R_{43} & R_{44} & R_{45} & R_{46} \\ R_{51} & R_{52} & R_{53} & R_{54} & R_{55} & R_{56} \\ R_{61} & R_{62} & R_{63} & R_{64} & R_{65} & R_{66} \end{bmatrix}. \tag{2.14}$$

Mathematically, matrix (2.14) is symplectic, and the elements are derived from the Hamiltonian description of motion, which can mediate particle beam transformation through beamline elements and allow beam dynamics computation to conserve, e.g., phase space volume [52]. In the case of a transport line that consists of linear elements such as drifts, dipoles, and quadrupoles, the transfer matrix can be simplified by removing coloured elements in the matrix (2.14). It is possible because the transverse planes are decoupled, and no acceleration is present.

The following arguments are provided to reduce the number of free parameters in the matrix (2.14). Well-aligned linear elements do not introduce coupling between the $x - y$ planes. Therefore, the off-diagonal elements in the blue region can be neglected. Without time-depended elements, such as rf-cavities, the purple region becomes zero except for the R_{55} element, an initial offset in z or s. The transport matrix $\mathbf{R}$ obeys the symplectic condition, $\mathbf{R^T U R} = \mathbf{U}$, where $\mathbf{R^T}$ is the transpose of $\mathbf{R}$ and $\mathbf{U}$ is a block matrix containing the identity matrices $\mathbf{I}_\mathrm{n}$. Further, the product of symplectic matrices is symplectic. Applying this to $\mathbf{R}$, the yellow elements in the fifth row can be expressed

in terms of $R_{26}, R_{16}, R_{46},$ and R_{36} [52]. Finally, the red row can be omitted because energy losses due to synchrotron radiation are minimal, and energy is conserved. The simplified transfer matrix reads

$$\mathbf{R} = \begin{bmatrix} R_{11} & R_{12} & 0 & 0 & 0 & R_{16} \\ R_{21} & R_{22} & 0 & 0 & 0 & R_{26} \\ 0 & 0 & R_{33} & R_{34} & 0 & R_{36} \\ 0 & 0 & R_{43} & R_{44} & 0 & R_{46} \\ R_{26} & R_{16} & R_{46} & R_{36} & 1 & R_{56} \\ 0 & 0 & 0 & 0 & 0 & 1 \end{bmatrix}. \tag{2.15}$$

Out of the initial 36 free parameters, only 16 describe beams' horizontal, vertical and longitudinal transformation. Each element of the beamline has a transfer matrix for drifts, dipoles, and quadrupoles. Matrices for the relevant beam optic elements are summaries in the appendix (8.1.1). These matrices can be combined to assemble, design, and optimize beamlines. Particle tracking codes are typically used to compute the trajectories of millions of particles through a complex beamline lattice. Particle tracking codes used in this work are discussed in section (2.3.1).

2.1.3 *Courant-Snyder parameters, emittance and brightness*

The following introduces important concepts of particle beam parametrisation and characterisation. Specifically, the Courant-Snyder, also called Twiss parameters, are discussed, allowing the design of beam transfer lines in particle accelerators. Electron beam emittance and brightness are introduced for beam quality characterisation.

The starting point is the Hills equation for a particle with nominal momentum p_0 in a focusing field

$$u'' + k_1(s)u = 0, \tag{2.16}$$

where $k_1(s)$ is a piecewise constant of the quadrupole focusing channel. The variable u represents an arbitrary transverse direction and assumes decoupled motion in the x and y planes. The *Ansatz* (trial function) [52, 55]

$$u(s) = A\sqrt{\beta(s)}\cos(\Psi(s) + \Psi_0) \tag{2.17}$$

and its first derivative, where $\Psi'(s) = \beta(s)^{-1}$ is used

$$u'(s) = \frac{A}{\sqrt{\beta(s)}} \left[\frac{\beta'(s)}{2} \cos(\Psi(s) + \Psi_0) - \sin(\Psi(s) + \Psi_0) \right], \tag{2.18}$$

is a solution of Eq.(2.16), where A and Ψ_0 are constants, $\beta(s)$ and $\Psi(s)$ is the *Twiss beta function* and *phase advance*, respectively. Note that $\beta(s)$ is the amplitude function of the betatron oscillation in the focusing channel and is not the relativistic beta term. Substituting the Ansatz into the Hills equation reveals the relation of Twiss beta and the phase advance as

$$\Psi(s) = \int_0^s \frac{ds'}{\beta(s')} \ . \tag{2.19}$$

The phase advance Eq.(2.19) describes the location of a particle on the trace space ellipse Eq.(2.21).

The trace space ellipse equation can be derived by combining $u(s)$ and $u'(s)$, and with the introduction of new Twiss parameters

$$\alpha(s) = -\frac{\beta'(s)}{2} \qquad \text{and} \qquad \gamma(s) = \frac{1 + \alpha^2(s)}{\beta(s)} \ . \tag{2.20}$$

This gives an ellipse equation in the trace-space $u - u'$

$$A^2 = \gamma(s) u'^2(s) + 2\alpha(s) u(s) u'(s) + \beta(s) u^2(s) \ . \tag{2.21}$$

Eq.(2.21) describes the evolution of the trace space along a beamline. The area of the ellipse defines the particle beam's *emittance* ϵ_{u}, a key measure of beam quality. Most importantly, the emittance of a particle beam under linear transformation is preserved. The slope and shape of the trace space ellipse are characterized by the Twiss parameters, where β is also a measure of the beam size, α represents the phase space ellipse slope (correlation of $u - u'$) and its orientation in the trace space, and γ denotes the angular envelope of the trajectory and is a measure for the divergence of the particle beam. Below, equation (2.31) shows the connection of measurable statistical beam quantities with Twiss parameters and the emittance. Figure (2.4) displaces a trace space with annotation of characteristic points and highlights that the trace space of a particle beam is fundamentally characterized by the emittance and Twiss parameters. As the particle beam travels through the beamline, the shape and slope of the ellipse may change; if emittance is preserved, the enclosed area of the ellipse πA^2 stays constant. Hence, this is known as the *Courant-Snyder invariant* A and represents the constant of motion of particles.

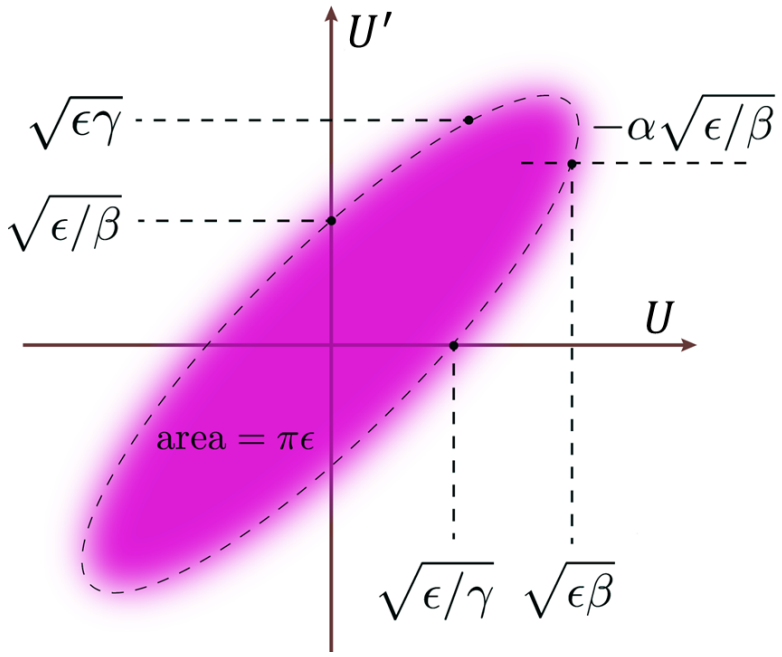

Figure 2.4: **The trace space ellipse of a particle beam.** The trace space ellipse envelopes the potential states of particles at a position along the beamline. The relation between Twiss parameters is highlighted.

The matrix formalism introduced in section (2.1.2) can be extended to transforming the Twiss parameters through a beamline. First, the trace-space ellipse equation is formulated as

$$A^2 = \mathbf{X}_u^T \cdot \mathcal{B}^{-1} \cdot \mathbf{X}_u = \begin{pmatrix} u & u' \end{pmatrix} \cdot \begin{pmatrix} \beta & \alpha \\ \alpha & \gamma \end{pmatrix} \cdot \begin{pmatrix} u \\ u' \end{pmatrix} \tag{2.22}$$

where $\mathcal{B}$ is the *beta matrix*

$$\mathcal{B} = \begin{pmatrix} \beta & -\alpha \\ -\alpha & \gamma \end{pmatrix}, \tag{2.23}$$

and defines the *sigma matrix*, also know as *beam matrix*

$$\Sigma = \epsilon_\mathrm{u}\mathcal{B} = \epsilon_\mathrm{u} \begin{pmatrix} \beta & -\alpha \\ -\alpha & \gamma \end{pmatrix}, \tag{2.24}$$

because $\det(\mathcal{B}) = \beta\gamma - \alpha^2 = 1$, the determinant of the Σ-matrix defines the emittance with

$$\epsilon_\mathrm{u}^2 = \det(\Sigma) \tag{2.25}$$

It is valid because, geometrically, the determinant of a $2n \times 2n$ matrix computes the stretching factor of an area or a volume. Hence, because of $\det(\mathcal{B}) = 1$, the determinant

$\det(\Sigma)$ measures the area enclosed by the phase space ellipse representing the *geometric emittance*. The geometric emittance is preserved under linear transformation in a beamline $\mathbf{R}$ with

$$\mathcal{B}(s_1) = \mathbf{R}_u \cdot \mathcal{B}(s_0) \cdot \mathbf{R}_u^T, \tag{2.26}$$

which recovers the Courant-Snyder invariant discussed before.

A particle beam consists of millions of individual trace space ellipses and corresponding single-particle emittances and Twiss parameters. It requires a statistical approach to beam characterisation to capture the dynamic of the entire beam. The covariance matrix encapsulates all relevant correlations of the six dynamic variables of a particle beam vector in a 6×6 matrix

$$\Sigma_{6\mathrm{D}} = \begin{pmatrix} \langle x^2 \rangle & \langle xx' \rangle & \langle xy \rangle & \langle xy' \rangle & \langle x\zeta \rangle & \langle x\delta \rangle \\ \langle x'x \rangle & \langle x'^2 \rangle & \langle x'y \rangle & \langle x'y' \rangle & \langle x'\zeta \rangle & \langle x'\delta \rangle \\ \langle yx \rangle & \langle yx' \rangle & \langle y^2 \rangle & \langle yy' \rangle & \langle y\zeta \rangle & \langle y\delta \rangle \\ \langle y'x \rangle & \langle y'x' \rangle & \langle y'y \rangle & \langle y'^2 \rangle & \langle y'\zeta \rangle & \langle y'\delta \rangle \\ \langle \zeta x \rangle & \langle \zeta x' \rangle & \langle \zeta y \rangle & \langle \zeta y' \rangle & \langle \zeta^2 \rangle & \langle \zeta\delta \rangle \\ \langle \delta x \rangle & \langle \delta x' \rangle & \langle \delta y \rangle & \langle \delta y' \rangle & \langle \delta\zeta \rangle & \langle \delta^2 \rangle \end{pmatrix}, \tag{2.27}$$

where $\langle ... \rangle$ denotes the first momentum of distribution (mean value). Note, matrix (2.27) is a 6D representation of the *sigma matrix*. For an ideal Gaussian beam without any cross-plane correlations, the green annotated regions can be neglected, and the sigma matrix simplifies to the block diagonal elements

$$\Sigma_{6\mathrm{D,r}} = \begin{pmatrix} \langle x^2 \rangle & \langle xx' \rangle & 0 & 0 & 0 & 0 \\ \langle x'x \rangle & \langle x'^2 \rangle & 0 & 0 & 0 & 0 \\ 0 & 0 & \langle y^2 \rangle & \langle yy' \rangle & 0 & 0 \\ 0 & 0 & \langle y'y \rangle & \langle y'^2 \rangle & 0 & 0 \\ 0 & 0 & 0 & 0 & \langle \zeta^2 \rangle & \langle \zeta\delta \rangle \\ 0 & 0 & 0 & 0 & \langle \delta\zeta \rangle & \langle \delta^2 \rangle \end{pmatrix}. \tag{2.28}$$

When the sigma matrix of a particle beam is block diagonal, the spatial directions are decoupled, and each plane can be independently treated. By evaluating the block of

x-direction (same analysis applies for y-direction), a statistical definition of the *root mean squared* (r.m.s or rms) geometric emittance is obtained with

$$\epsilon_{\mathrm{x,rms}}^2 = \det(\Sigma_{\mathrm{xx}}) = \det\begin{pmatrix} \langle x^2\rangle & \langle xx'\rangle \\ \langle x'x\rangle & \langle x'^2\rangle \end{pmatrix}$$
$$\epsilon_{\mathrm{x,rms}} = \sqrt{\langle x^2\rangle\langle x'^2\rangle - \langle xx'\rangle^2} \tag{2.29}$$

The r.m.s geometric emittance is preserved under linear transformation but will change with increasing particle beam energy. To be able to compare emittance values at different particle beam energies W, the *normalized emittance* is used, which reads

$$\epsilon_{\mathrm{x,n}} = \beta_\zeta \gamma_{\mathrm{rel}} \epsilon_{\mathrm{x,rms}}, \tag{2.30}$$

where β_ζ and γ_{rel} are relativistic factors and not Courant-Snyder Twiss parameters.

When the particle beam is at the waist, and no correlation is present ($\langle xx'\rangle = 0$), the r.m.s *projected beam size* and *divergence* read

$$\sigma_{\mathrm{x,rms}} = \sqrt{\langle x^2\rangle} = \sqrt{\epsilon_{\mathrm{x,rms}}\beta_{\mathrm{x}}} \qquad \text{and} \qquad \sigma_{\mathrm{x',rms}} = \sqrt{\langle x'^2\rangle} = \sqrt{\epsilon_{\mathrm{x,rms}}\gamma}. \tag{2.31}$$

Further, from bottom right block of the Σ-matrix (2.28) the definition for r.m.s *beam length* and projected r.m.s *relative energy spread* can be read out

$$\sigma_{\zeta,\mathrm{rms}} = \sqrt{\langle\zeta^2\rangle} \qquad\qquad \sigma_{\delta,\mathrm{rms}} = \sqrt{\langle\delta^2\rangle}\ . \tag{2.32}$$

This work also annotates beam length and relative energy spread with $\sigma_{\mathrm{z,rms}}$ and $\Delta W_{\mathrm{rms}}/W$. Eqs.(2.31) show the fundamental importance of particle beam emittance for the minimal achievable beam size and divergence.

Similarly to Eq.(2.29), the 6D emittance of a particle beam is

$$\epsilon_{\mathrm{6D,rms}}^2 = \det(\Sigma_{\mathrm{6D,r}}). \tag{2.33}$$

Matrix (2.28) is a block diagonal matrix; as such, the determinant of a block diagonal matrix A is equal to the product of the determinants of the diagonal blocks A_j, meaning

$$\det(A) = \prod \det(A_j), \tag{2.34}$$

with this and Eq.(2.29) and Eq.(2.30), the 6D normalized r.m.s emittance reads

$$\epsilon_{\mathrm{6D,n}} = \beta_\zeta^2\gamma_{\mathrm{rel}}^2\sqrt{\det(\Sigma_{\mathrm{6D,r}})} = \beta_\zeta^2\gamma_{\mathrm{rel}}^2\sqrt{\det(\Sigma_{\mathrm{xx}})\det(\Sigma_{\mathrm{yy}})\det(\Sigma_{\mathrm{z},\delta})} \tag{2.35}$$
$$\epsilon_{\mathrm{6D,n}} = \epsilon_{\mathrm{x,n}}\epsilon_{\mathrm{y,n}}\epsilon_{\mathrm{z,n}}\ . \tag{2.36}$$

Eq.(2.36) can be interpreted as the beam's 6D phase space volume. Combined with the particle beam charge Q, this provides a more generalized definition of the normalised 6D brightness of a particle beam

$$B_{\mathrm{6D,n}} = \frac{Q}{\beta_\zeta^2 \gamma_{\mathrm{rel}}^2 \sqrt{\det(\Sigma_{\mathrm{6D}})}} = \frac{Q}{\epsilon_{\mathrm{x,n}} \epsilon_{\mathrm{y,n}} \epsilon_{\mathrm{z,n}}} \tag{2.37}$$

The 6D brightness in Eq.(2.37) measures a particle beam's phase space charge density. Brightness is a crucial measure of beam quality and determines the performance of FEL and other applications. A more handy expression of 5D and 6D brightness is in terms of the peak current $I_{\mathrm{p}} \approx c\Delta Q/\Delta\zeta$ [56]

$$B_{\mathrm{5D}} = \frac{2I_{\mathrm{p}}}{\epsilon_{\mathrm{x,n}} \epsilon_{\mathrm{y,n}}} \qquad B_{\mathrm{6D}} = \frac{I_{\mathrm{p}}}{\epsilon_{\mathrm{x,n}} \epsilon_{\mathrm{y,n}} (\Delta W_{\mathrm{rms}}/W) 0.1\%\mathrm{bw}}. \tag{2.38}$$

The 5D brightness considers the transverse normalized emittance and the peak current I_{p}, and the 6D brightness additionally includes the relative energy spread in units of 0.1% bandwidth. The emittance and energy spread are crucial parameters for beam transport and dynamics and, in the context of FEL activity, determine thresholds for lasing. Generally speaking, emittance and energy spread should be minimized to achieve beams with dense real and phase space volumes. In this work, Eqs.(2.38) are used for brightness calculations, and a significant part of the study is concerned with improving the brightness of electron beams for the XFEL applications. Eq.(2.37) highlights that the most substantial contribution is expected from minimizing the electron beams' 6D phase space volume $\det(\Sigma_{\mathrm{6D}})$. Chapter (5) presents a novel approach for reducing an electron beam's 6D phase space volume in plasma-based accelerators.

2.1.4 *Electron beam generation and compression*

In a state-of-the-art accelerator, improving the brightness of electron beam sources opened the path towards FEL-based light sources [56] and high-energy colliders. The process of generating and subsequently accelerating electrons to high energies is the purpose of an electron injector in rf-accelerators. Typically, in the electron injectors, electrons are accelerated to non-relativistic or mildly relativistic energies, which are further accelerated to target energies in the high-energy section of the linac. Electron injectors can be divided into three different injector types.

In direct current injectors, an electric field is applied between a cathode and an anode, which can accelerate electrons to non-relativistic energies. A more sophisticated

electron injector design embeds a cathode material, typically metals (such as copper) or semiconductors (such as caesium telluride)[57], into an rf-cavity. The rf-cavity provides the extraction fields to accelerate electrons released from the cathode material and can be room-temperature or superconducting rf-cavities made of niobium (Nb). Superconducting rf-cavities electron injectors have the advantage of larger accelerating gradients up to 100 MV/m, which minimizes emittance degradation effects.

The materials' work function must be overcome to release electrons from the cathode material into the accelerating cavity. The energy source may be a strong electric field at the cathode material releasing thermionic electrons or, in a more controlled way, a laser pulse directly exciting electrons above the work function of the cathode material, well-known as Einstein's photoelectric effect [58]. Much of the effort is focused on producing electrons with reduced thermal emittance and preserving the emittance during acceleration to relativistic energies [57]. Projected normalized emittance from these cathodes is typically of the order of $\epsilon_{\mathrm{n}} \approx 1 - 100\,\mu$m-rad and in recent highly optimized photocathodes cathode injectors down to $\epsilon_{\mathrm{n}} \approx 0.2\,\mu$m-rad at few pC charge levels [59, 60]. Minimizing the emittance in both transverse directions and maximizing the peak current of the electron beam is vital for increasing the brightness of the electron beams according to Eq.(2.38).

However, electron beams from photocathodes typically have a few Ampere peak currents after the photocathode injector. In the subsequent accelerator structure, the off-crest acceleration of the electron beam introduces a time-energy correlation in the longitudinal phase space. This is known as the energy chirp and is displayed in the left panel of Fig.(2.5). The energy chirp is negative when the head of the electron beam has lower energy than the tail and positive when the head has higher energy than the tail. The sign of the energy chirp is important for the compression of the electron beam from initially picosecond to femtosecond beam duration and the corresponding increase of the current to a few kA. A magnetic chicane made of four dipoles in a C-shaped configuration (BC#) (see Fig.(2.5)) produces a dispersion section where an electron beam with negative energy chirp is compressed due to the path differences inside the chicane. Because the deflection of particles in dipole fields is energy-dependent, the low-energy head will travel a longer path than the high-energy tail of the electron beam, such that at the exit of the chicane, the electron beam has a shorter duration and higher peak current. The first-order longitudinal dispersion, the R_{56}-element of the transfer

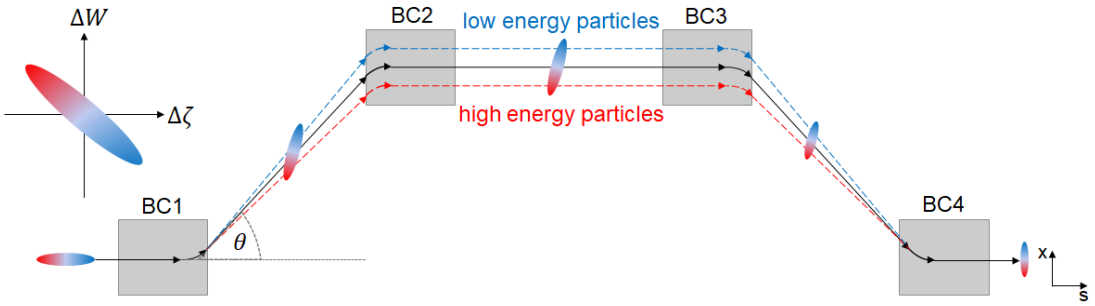

Figure 2.5: **Schematic representation of C-shaped chicane.** Schematic representation of C-shaped chicane based on four dipole magnets for electron beam compression or energy collimation. An electron beam with a negative energy chirp (see longitudinal phase space plot at the top left) enters the chicane from the left side and propagates on the design orbit (black solid line) to the right. The low-energy head of the electron beam has a longer path (blue dashed line) compared with the high-energy tail of the electron beam (red dashed line). Due to the energy chirp, the electron beam is compressed in the longitudinal direction after the chicane.

matrix (2.15) with the energy chirp h, dictates the compression of electron beams in magnetic chicanes. The R_{56}-element can be expressed as [61]

$$R_{56}(\theta) \approx -2\theta^2 \left(D + \frac{2L_\mathrm{d}}{3} \right), \tag{2.39}$$

where θ is the bending angle of the electron beam, L_d is the length of the dipoles, and D is the drift distance between the first two and last two dipoles in a C-shaped chicane.

The electron beam compression factor can be expressed as [61]

$$C = \frac{1}{1 + R_{56} h}. \tag{2.40}$$

The compression factor maximizes when $1 + R_{56}h = 0$. However, non-linearities in electron movement due to higher-order contributions through the chicane results in the caustics formation of the electron trajectories [62], which leads to double-horn current formation and limits the minimum achievable electron beam length. When an electron beam at nominal momentum exits the second dipole, its dispersion and transverse displacement are at their maximum. The maximum transverse displacement of the electron beam in a symmetric C-shaped chicane is [63, 64]

$$x_\mathrm{max}(\theta) = 2L \tan\left(\frac{\theta}{2}\right) + D \tan(\theta). \tag{2.41}$$

Remember θ is energy dependent, such that an electron beam with non-zero energy spread δ will lead to a spread of x-position after the second dipole.

The higher peak current after compression comes at a price. When strong compression is applied *Coherent synchrotron radiation* (CSR) generated by the electron beam interacts with the electron beam. It introduces density modulations, which can deteriorate the electron beam emittances in one or both transverse directions and reduce the overall brightness [62, 65, 66]. In section (2.2), the fundamentals of free-electron lasers are discussed and show that degradation of electron beam quality dramatically impacts the FEL performances. Therefore, maintaining high-beam quality during acceleration and transport to the entrance of the undulator section is paramount in FELs.

Plasma-based accelerators produce inherently fs duration particle beams with high peak currents and do not require additional compression via chicanes. Nevertheless, in this work, a C-shaped chicane is repurposed as an effective energy collimator by inserting slit collimators after the second dipole for isolating electron beams of different energies without degrading the beam quality thanks to the small R_{56}-element (see chapter (6)).

2.2 HIGH-GAIN FREE-ELECTRON LASER

This section starts with a brief review of free-electron laser developments. Further, the theoretical basis of high-gain FEL and performance estimates based on the Ming Xie formalism will be introduced.

2.2.1 *Review of free-electron lasers*

This section provides a concise overview of the development of free-electron lasers throughout history. The following paragraphs draw from the review conducted in [9, 67]. A free-electron laser exchanges energy between charged particles and an electromagnetic field. The electromagnetic field can be an external source or generated by the electron beam when forced on a sinusoidal path along the propagation direction. Typically, insertion devices called *undulators* are employed with alternating magnetic fields, resulting in the electron beam's oscillatory motion. The electron beam emits radiation which may coherently overlap along the undulator (see section (2.2.2) and (2.2.3)).

The idea of extracting energy in the form of radiation from electron beams was first proposed in a patent application by Gorn in 1947 [68] and later in peer-reviewed works by others [69, 70] in 1951. The initial experimental observations of bunching

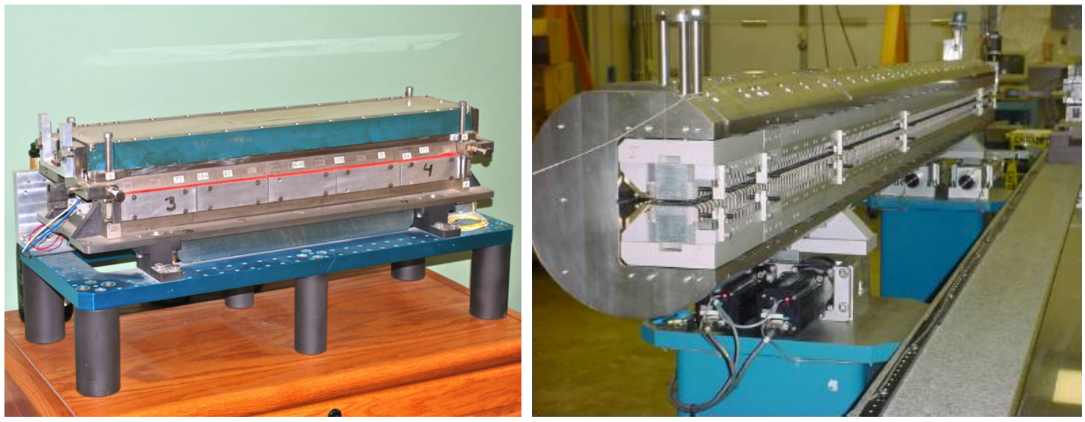

Figure 2.6: **Undulator used in the first experimental demonstration of SASE FEL and a modern undulator used at LCLS.** Undulator used in the first experimental demonstration of SASE FEL in the high-gain regime at 12 μm resonance wavelength [75] by Hogan *et al.* (left panel) and for comparison, a modern undulator segment employed at the LCLS (right panel). Adapted from [9] (left panel) and [76] (right panel). This work is openly licensed via CC BY 4.0.

and energy exchange were achieved by Phillips [71] in an undulator microwave device called "ubitron". This demonstrated the fundamental principles of energy exchange and marked a significant milestone. Later, Madey introduced the term *free-electron laser* in his seminal theoretical work on FELs [72], which was widely accepted following the experimental verification of the amplifier [73] and oscillator FEL [74].

Experimental work was accompanied by crucial theoretical progress that established the classical nature of the FEL process, as long as the electron recoil effects due to photon emission are negligible. It significantly simplified the theoretical framework for predictions [9, 67, 77, 78]. Much of the work focused on the so-called low-gain regime, where the equation of motion resembles the pendulum equations (see section (2.2.2)). However, a breakthrough was achieved by developing the high-gain FEL theory, a self-consistency model of electron and radiation evolution and interaction. The high-gain theory considers radiation coupling with the electron beam and back, treating radiation evolution in a self-consistent manner. It revealed a micro-bunching instability effect where the radiation modulates the electron beam current at the resonance wavelength, resulting in higher intensity radiation, enabling exponential radiation gain in a single pass. Developing high-gain FEL theory was a community-driven effort [9, 67].

Soon after, a proof-of-concept experiment demonstrated the high-gain regime at microwave wavelengths [79]. A critical scientific breakthrough was achieved at the Uni-

versity of California, Los Angeles (UCLA) by demonstrating *Self-Amplified Spontaneous Emission* (SASE) FEL at the infrared wavelength and verifying the properties of the output radiation against the high-gain theory [75] by Hogan *et al.*. Figure (2.6) (left) displays the undulator used during the UCLA experiment, and the right panel shows a modern undulator segment developed for *Linac Coherent Light Source* (LCLS). These results not only showed the verification of the high-gain theory but also demonstrated the scalability of the single-pass high-gain FEL towards harder photon energies, which was crucial for the realisation of the first X-ray laser at the Ångstrom wavelength [9].

Eventually, a convincing case for the LCLS at SLAC was proposed and approved [9, 80, 81]. Among other advancements, the key to the successful realization of LCLS was the development of advanced photocathode electron injectors to fulfil the stringent requirements on electron beam quality [9]. In 2010, LCLS produced its first light [82], and other facilities followed [83–85]. Since then, these machines made groundbreaking contributions in life and material science, chemistry and biology, and physics after a decade of operation [10, 11, 86–88]. Today, a handful of FEL facilities operate at the hard X-ray wavelength [82, 84, 85] with limited capacity.

It is important to note that developing highly efficient and specialised simulation tools incorporating the known theories was integral in developing FELs. Most notably, the wavelength-averaged FEL codes GINGER [89] and GENESIS [90] build the backbone of the simulation efforts for the LCLS and are widely used in FEL R&D today. However, the new class of electron beams from plasma-based accelerators push the boundaries of applicability; therefore, for the 5^{th} generation light source developed in this work, the *Parallel Unaveraged Fel INtegrator* (Puffin) FEL code [91] is utilized to model radiation production in high-fidelity simulations (see section (2.3.2) for more details on Puffin).

2.2.2 *Electron motion and undulator radiation*

A planar undulator is an insertion device made of electro- or permanent magnets with an alternating magnetic field in one transverse direction [92] of the form [93, 94]

$$B_y(z) = -B_0 \sin(k_{\text{u}} z), \tag{2.42}$$

where B_0 is the on-axis undulator peak field and $k_{\text{u}} = 2\pi/\lambda_{\text{u}}$ the undulator number corresponding to the undulator period λ_{u}. The force on a relativistic electron beam

can be obtained from the Lorentz force equation evaluating the $\mathbf{v} \times \mathbf{B}$ term, assuming that the longitudinal velocity is much greater than the transverse velocity $v_\mathrm{z} \gg v_\mathrm{x}$. The equation of motion yields the trajectory $x(z)$ and velocity $v_\mathrm{x}(z)$ of the electron beam in the undulating plane

$$x(z) = \frac{K}{\gamma_\mathrm{rel} k_\mathrm{u}} \sin(k_\mathrm{u} z) \qquad \text{and} \qquad v_\mathrm{x}(z) = \frac{cK}{\gamma_\mathrm{rel}} \cos(k_\mathrm{u} z), \tag{2.43}$$

where K is the *dimensionless undulator parameter* with

$$K = \frac{eB_0}{m_\mathrm{e} c_0 k_\mathrm{u}} \approx 0.9336 \cdot B_0[\mathrm{T}]\lambda_\mathrm{u}[\mathrm{cm}]. \tag{2.44}$$

The dimensionless undulator parameter measures the maximum deflection angle θ_max of an electron beam relative to the undulator axis, which reads

$$\theta_\mathrm{max} = \frac{eB_0}{\gamma_\mathrm{rel} m_\mathrm{e} c_0 k_\mathrm{u}} = \frac{K}{\gamma_\mathrm{rel}}. \tag{2.45}$$

Eq.(2.45) also dictates the opening angle of the radiation cone produced by an electron beam. These simplified considerations show that the opening angle of the radiation depends on the electron beam energy and the K parameter. The output radiation becomes forward-directed and highly collimated at increased beam energy and decreased K-parameter. At the same time, the undulator parameter depends on the undulator configuration defined by the peak magnetic field B_0 and the undulator period λ_u. The material, configuration and geometry of the pole tips used determine the accessible peak magnetic field in an undulator.

Generally, undulators are based on permanent magnets made of rare-earth materials, such as $SmCo_5$ or NdFeB, or are based on electromagnets. The magnets can be cryogenically cooled or superconducting, enhancing performance in peak magnetic fields and period length. Designing and engineering a new undulator can be challenging and requires dedicated effort; undulator design is an entire field of R&D in its own right and is an active field of research [92]. Nevertheless, a simplified fitting function for the peak magnetic field developed by Elleaume *et al.* in [95] provides an simple tool to estimate the magnetic field based on few accessible parameters such as material in use, λ_u and the undulator gap g between the pole tips. The corresponding fitting function is [95]

$$B_0 = a_1 \exp\left(a_2 \frac{g}{\lambda_\mathrm{u}} + a_3 \left(\frac{g}{\lambda_\mathrm{u}}\right)^2\right), \tag{2.46}$$

where the a_i's are the fitting coefficients. This fitting function is applicable for the gap range of $0.1 < g/\lambda_\mathrm{u} < 1$. Table (2.1) summarises the fitting parameters for a few common undulator configurations from Ref.[95].

Table 2.1: Fitting coefficients for three different planar undulator types.

Case	Undulator typ	a_1	a_2	a_3
I	Hybrid with iron poles	3.381	-4.730	1.198
II	Hybrid with vanadium permendur poles	3.694	-5.068	1.520
III	Superconducting undulator	12.4	$-\pi$	-2.2

As an example, a superconducting undulator at a gap-to-undulator period ratio of $\frac{g}{\lambda_\mathrm{u}} = 0.4$ and $\frac{g}{\lambda_\mathrm{u}} = 0.32$ can generate peak magnetic fields of $B_0 \approx 2.5\,\mathrm{T}$ and $B_0 \approx 3.5\,\mathrm{T}$ (note similar peak fields are desired for the PWFA FEL undulator configuration in chapter (6)), respectively. In state-of-the-art FELs, the undulator period is of the order of centimetres; however, advanced undulator designs suggest that mm-scale undulator periods with standard permanent magnet-based technology are possible [96] and novel directions based on *Micro electro-mechanical systems* (MEMS) and *Dielectric Laser Undulator* (DLU) promise further miniaturisation of undulators and beam optics [97–99]. Chapter (6) shows that short-period and advanced undulators go hand in hand with the ultra-high brightness beams driving an FEL.

Due to the sinusoidal motion of the electrons, described in Eq.(2.43), inside the undulator, the electrons emit radiation confined axially along the undulator with the opening angle scaling with the beam energy as $\theta \propto 1/\gamma_\mathrm{rel}$ (Eq.(2.45)). The radiation cone will spatially overlap in the forward direction for $\gamma_\mathrm{rel} \gg 1$ and $K \leq 1$. It may coherently overlap and become spectrally narrow due to coherence effects at the on-axis fundamental frequency ω and higher harmonics. The radiation is initially broadband, but the bandwidth decreases with increasing undulator period number N_u [92, 93]

$$\frac{\Delta\omega}{\omega} \approx \frac{1}{N_\mathrm{u}}. \tag{2.47}$$

Coherence effects can only take place for those wavelengths which meet the resonance condition, which reads [92, 93]

$$\lambda_\mathrm{n} = \frac{\lambda_\mathrm{u}}{2\mathrm{n}\gamma_\mathrm{r}^2}\left(1 + \frac{K^2}{2} + \gamma_\mathrm{r}^2\Theta^2\right), \tag{2.48}$$

where $\mathrm{n} = 1, 2, 3, \ldots$ represents the number of harmonic, γ_r is the relativistic factor at the resonance energy and Θ is the observer angle of the radiation. The odd harmonics are emitted on-axis, while even harmonics are radiated off-axis. Note the $\lambda_1 \propto \frac{\lambda_\mathrm{u}}{\gamma_\mathrm{r}^2}$

scaling of the radiation wavelength in Eq.(2.48); the γ_r^2-term results from the relativistic contraction of the undulator in the rest-frame of the electron beam and blue-shifting of the radiation from the observer point of view. In other words, the electron beam 'sees' an undulator with an effectively shorter period. This *undulator radiation* is monochromatic with well-defined spectral modes linearly polarised in the oscillation plane of the electron beam. When the undulator parameter $K \gg 1$, the deflection of the electron beams is much greater than the opening angle of the radiation cone such that the coherence effects are increasingly suppressed, and the radiation spectrum resembles the well-known broadband dipole radiation.

From a different point of view, the resonance condition (2.48) ensures the energy exchange between an electron beam and a radiation field. Consider now a plane *electromagnetic* (EM) wave of the form [92, 93]

$$E_\mathrm{x}(z,t) = E_{\mathrm{x},0}\cos(k_\mathrm{l} z - \omega_\mathrm{l} t + \phi_0), \tag{2.49}$$

where k_l is the radiation wavenumber, $\omega_\mathrm{l} = k_\mathrm{l} c_0$, the corresponding radiation frequency, and ϕ_0 is a phase. The energy exchange between an electron and an electromagnetic wave is

$$\begin{aligned}\frac{dW}{dt} &= -e v_\mathrm{x}(t) E_\mathrm{x}(t) \\ &= -\frac{e c_0 K E_{\mathrm{x},0}}{2\gamma_\mathrm{rel}}\cos(\psi),\end{aligned} \tag{2.50}$$

where ψ is called the *ponderomotive phase*

$$\psi = (k_\mathrm{u} + k_\mathrm{l})z - \omega_l t + \phi_0, \tag{2.51}$$

ψ measures the electron's longitudinal position relative to the radiation field phase. Eq.(2.51) shows that energy exchange is ensured when $\psi = \text{const}$, meaning $\frac{d\psi}{dt} \stackrel{!}{=} 0$ [92, 93]. After some algebra, evaluation of Eq.(2.51) under this condition leads directly to the resonance condition

$$\lambda_r = \frac{\lambda_\mathrm{u}}{2\gamma_\mathrm{r}^2}\left(1 + \frac{K^2}{2}\right). \tag{2.52}$$

Note the profound similarities between Eq.(2.52) and the previously presented resonance condition for undulator radiation in Eq.(2.48). Indeed, this confirmed that the resonance condition ensures a sustained energy exchange between an electron beam and a radiation field. The source of the radiation field can be external or produced by the electron beam itself.

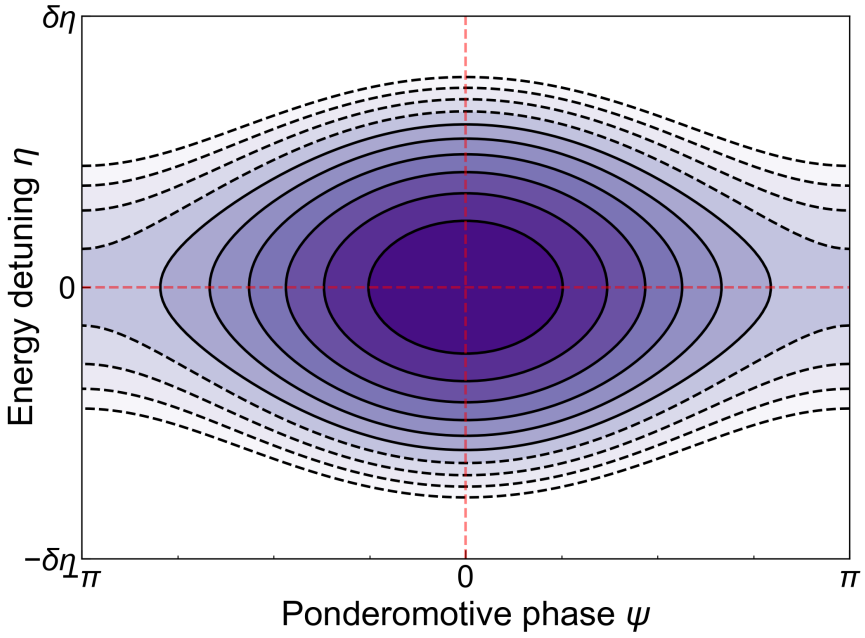

Figure 2.7: **FEL Separatrix.** FEL potential "bucket" with the electron motion trajectory (contour lines) is depicted in the ψ-η phase space. Closed contour lines are the bound electron motions (black solid lines) separated by the separatrix from the unbound motion (dashed black lines). The separatrix is the outermost contour line with a closed orbit. Electrons within the separatrix contribute to the energy exchange process. The red dashed lines separate the phase space into four areas of interaction, discussed in the main text.

In the low-gain regime, when the energy exchange is negligible compared to the electron beam energy, the evolution of the longitudinal phase space of the electron beam can be described by a simple pendulum equation. Redefining Eq.(2.50) in terms of normalized particle energy deviation or energy detuning $\eta = \frac{\gamma_{\mathrm{rel}} - \gamma_{\mathrm{r}}}{\gamma_{\mathrm{r}}}$ yields

$$\frac{d\eta}{dt} = -\frac{e\widehat{K}E_{\mathrm{x}}}{2m_{\mathrm{e}}c_0\gamma_{\mathrm{r}}^2}\cos(\psi). \tag{2.53}$$

Here, $\widehat{K}$ is the modified undulator parameter, taking the longitudinal oscillatory motion of the electron beam into account as $v_{\mathrm{z}} = \sqrt{v^2 - v_{\mathrm{x}}^2}$ with $v^2 = c_0^2(1 - 1/\gamma_{\mathrm{rel}}^2)$. The modified undulator parameter reads

$$\widehat{K} = K \cdot \left[J_0\left(\frac{K^2}{4+2K^2}\right) - J_1\left(\frac{K^2}{4+2K^2}\right)\right], \tag{2.54}$$

where J_0 and J_1 are Bessel functions of the zeroth and first kind, respectively. The time evolution of the ponderomotive phase is then

$$\frac{d\psi}{dt} = 2k_{\mathrm{u}}c_0\eta. \tag{2.55}$$

Eq.(2.53) and (2.55) is a system of differential equations describing the longitudinal phase space evolution of the electrons in the low gain regime. Figure (2.7) shows electron trajectories in the $\Psi - \eta$ phase space calculated from the pendulum equations (Eq.(2.53) and (2.55)). In analogy to the mathematical pendulum, two kinds of electron motions are present. The solid black lines indicate bound motion, and the dashed black lines are unbound electron motion within the ψ-η phase space. The rotation of electrons is clockwise on the solid black lines, and electrons within the separatrix contribute to the energy exchange. The length of each FEL bucket is $\Delta\psi = 2\pi$, corresponding to the resonance wavelength $\Delta\psi \equiv \lambda_{\mathrm{r}}$.

Fig.(2.7) highlights also that electrons in the left half of the FEL bucket with ponderomotive phase $\psi < 0$ move towards positive η, i.e. gain energy from the radiation field while electrons in the right half of the bucket $\psi > 0$ move towards negative η, i.e. lose energy to the radiation field, therefore, contributing to the radiation field amplification. At the same time, electrons change their relative position in ψ during propagation through the undulator. Electrons with lower energy than the resonance energy γ_{r} ($\eta < 0$) will slip back in phase, and electrons with higher energy will move ahead in the pondermotive phase. Fundamentally, this charge redistribution process describes the core mechanism behind the formation of micro-bunches at the scale of

the resonance wavelength. So far, the electric field change was considered 'small' in the low-gain regime. However, in the high-gain regime, the electric field of the radiation may grow exponentially in a single pass and evolve in its phase, which requires a self-consistent treatment of the interaction, which is discussed in the following section (2.2.3).

2.2.3 *High-gain free-electron laser theory*

In the high-gain FEL regime, spontaneous undulator radiation produced by the electron beam or an external seed field interacts with the electron beam and seeds the FEL process. An initially small amplitude radiation field modulates the energy of the electron beam. This energy modulation is translated into density modulation, leading to bunching at the resonance wavelength. This bunching then drives the radiation phase and promotes more energy modulation. At the FEL start-up, due to the randomly distributed electron phases, the emitted radiation is incoherent; hence, initially, the radiation amplification is small and the power scales linearly with the number of electrons N_e, as $P \propto N_\mathrm{e}$. However, bunching at the resonant wavelength results in increasingly coherent emission and increases the intensity of the radiation. The higher intensity radiation promotes stronger energy modulation, and this loop starts over again. As a result of this positive feedback loop, the radiation field grows exponentially along the undulator with power scaling of $P \propto N_\mathrm{e}^2$. Figure (2.8) displays this process schematically.

The FEL pendulum equations are extended to capture the positive feedback loop mathematically, such that radiation field evolution and bunching effects are self-consistently incorporated into the system of FEL equations. A few assumptions are required to simplify the mathematics. The *steady-state* approximation demands that the electron beam is infinitely long with uniform properties across the beam. The radiation field has only spatial dependency. Note, these approximations neglect that the electron beam propagates slower in the forward direction than the radiation field, leading to a relative slippage between the radiation field and electron beam over many undulator periods, $S_\mathrm{u} = N_\mathrm{u}\lambda_\mathrm{r}$. However, for now, this is a secondary consideration. A self-consistent complete set of coupled first-order 1D FEL equations can be derived [93, 100]

$$\frac{\mathrm{d}\psi}{\mathrm{d}z} = 2k_\mathrm{u}\eta \tag{2.56}$$

$$\frac{d\eta}{dz} = -\frac{e}{m_\mathrm{e}c_0^2\gamma_\mathrm{r}}\Re\left[\left(\frac{\widehat{K}\widetilde{E}_\mathrm{x}}{2\gamma_\mathrm{r}} + \widetilde{E}_\mathrm{z}\right)e^{i\psi}\right] \tag{2.57}$$

$$\frac{\mathrm{d}\widetilde{E}_x}{\mathrm{d}z} = -\frac{\mu_0 c_0 \hat{K}}{4\gamma_\mathrm{r}} \cdot \widetilde{j}_1 \tag{2.58}$$

$$\widetilde{j}_1 = 2j_0\langle e^{i\psi}\rangle = 2j_0 b, \tag{2.59}$$

where $\widetilde{E}_\mathrm{z}$ is the complex notation of the longitudinal space charge electric field, j_0 is the initial current density, and $b = \langle e^{i\psi}\rangle$ is the average modulation of the current

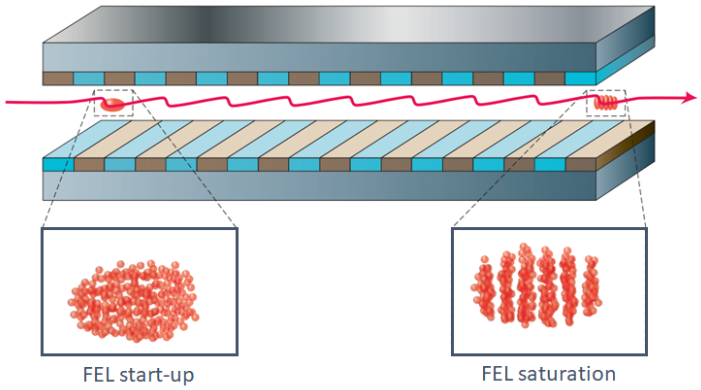

Figure 2.8: **Schematic representation of the FEL principle.** An initially unstructured electron beam radiates at the resonance wavelength inside the undulator (left). Interference effects of the randomly phased radiation fields produce a small amplitude coherent field. This initial field energy modulates the electron beam, resulting in density modulation at the resonance wavelength, and promotes coherent emission. This positive feedback loop progresses until the electron beam is bunched at the resonance wavelength, resulting in exponential radiation field growth along the undulator (right). Adapted from [67].

density at the scale of the resonance wavelength. The latter term is also known as the bunching factor b, and the modulus of the bunching factor can take values between $0 \leq |b| \leq 1$, whereby $|b| = 1$ corresponds to maximum modulation at the resonance wavelength. The bunching factor increases exponentially throughout the FEL interaction, leading to radiation power growth. It reaches its highest value when the FEL goes into saturation and decays afterwards [67, 93]. Like the FEL pendulum equations, the first two equations describe the dynamics in the $\psi - \eta$ phase space while taking into account self-consistently the electric field $\widetilde{E}_x$ of the radiation driven by the current density $\widetilde{j}_1$. The current density $\widetilde{j}_1$ depends on the ponderomotive phase ψ.

These FEL equations can be solved by the fourth-order Runge-Kutta method [101]. The uniform electron current density distribution in the longitudinal direction is produced with the Hammersley quasirandom sequence. It adds random *shot noise* to the electron beam distribution and is the initial source of the density modulation on the λ_r-scale. In the SASE FEL, this initial shot noise contains modes at the resonance wavelength, which are then amplified along the undulator. Additionally, the slippage effect leads to independent coherent spikes determined by the so-called cooperation length (see

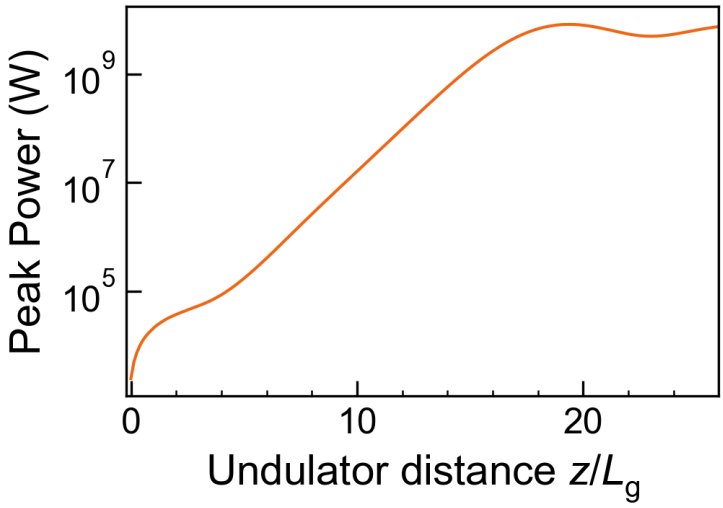

Figure 2.9: **Numerical solution of the 1D first-order coupled FEL equations.** The peak power gain curve is presented along the undulator distance. The undulator distance is normalised to the 1D gain length L_{g}. The undulator parameters are $\lambda_{\mathrm{u}} = 3\,\mathrm{cm}$ and $K = 2.4$. This 1D FEL simulation is performed for electron beam of $W \approx 10\,\mathrm{GeV}$ beam energy with uniform current profile of $I_{\mathrm{p}} \approx 4\,\mathrm{kA}$.

detailed discussion below and Eq.(2.66)). Hence, SASE FELs at saturation exhibit a spiky temporal profile from shot-to-shot.

Figure (2.9) presents a numerical solution to the one-dimensional first-order coupled differential FEL equations. The figure shows the peak power gain curve normalized to gain length. The gain curve is divided into three distinct sections. The FEL enters the start-up (**lethargy regime**) regime; The electron beam emits incoherent spontaneous undulator radiation at the resonance wavelength λ_{r}. It takes the FEL approximately $2-3$ power gain lengths [93] to build sufficient density modulation for increasingly coherent emission of radiation. An analytical description of the high-gain FEL in the limit of short-undulator [93] predicates a similar extent of the lethargy regime. When the density modulation of the electron beam is sufficiently developed at the scale of the resonance wavelength, an exponential increase in the radiation power is observed (**linear regime**). It reaches saturation when the bunching factor gets close to $|b| \approx 1$ approximately after $18-20$ power gain lengths, and the exact saturation distance depends on the initial noise level of the electron beam [67, 93]. The radiation becomes spatially coherent and has a narrow bandwidth. The final section is the **saturation regime**, where the exponential radiation power gain stops because the energy loss of the

electron beam becomes significant. Positive tapering of the undulator parameter $K(z)$ (decreasing K) post-saturation along the undulator allows for enhanced power extraction efficiency. These elevated peak power levels (up to TW) are typically produced at the expense of spectral coherence degradation due to spectral sideband peak amplification [102]. In contrast, when K increases, negative tapering can be exploited for energy chirp compensation in the electron beam or broadband radiation production [103, 104].

The following key parameters are introduced, allowing characterisation of the FEL performance, and much of the discussion is based on the works in [67, 93, 100]. The saturation length, peak power and the requirements on the electron beam quality are dictated by the Pierce parameter or FEL parameter [105]

$$\rho_{\mathrm{FEL}} = \left(\frac{1}{16} \frac{I_{\mathrm{p}}}{I_{\mathrm{A}}} \frac{\widehat{K}^2}{\gamma_{\mathrm{r}}^3 \sigma_{\mathrm{r}}^2 k_{\mathrm{u}}^2} \right)^{1/3} \tag{2.60}$$

where I_{p} is the peak current of the beam and $I_{\mathrm{A}} \approx 17\,\mathrm{kA}$ is the Alfvén current. For GeV scale energy and kA peak currents electron beams, the Pierce parameter is typically $\rho_{\mathrm{FEL}} \sim 10^{-4} - 10^{-3}$ for soft and hard X-ray wavelength, and the relative radiation bandwidth at saturation is of the same order. The Pierce parameter defines the 1D gain length in the limit of a **cold beam**; when energy spread, emittance and diffraction effects are omitted

$$L_{\mathrm{g,1d}} = \frac{\lambda_{\mathrm{u}}}{4\pi\sqrt{3}\rho_{\mathrm{FEL}}}. \tag{2.61}$$

In turn, the gain length dictates the saturation length and, hence, the overall length of the undulator section

$$L_{\mathrm{sat}} \approx 20 L_{\mathrm{g,1d}} \propto \frac{\lambda_{\mathrm{u}}}{\rho_{\mathrm{FEL}}}. \tag{2.62}$$

As such, the evolution of the power gain curve in the linear regime, in Fig.(2.9), can be approximated with

$$P_{\mathrm{rad}} \propto |\widetilde{E}_{\mathrm{x}}(z)|^2 \propto e^{z/L_{\mathrm{g,1d}}}. \tag{2.63}$$

The value of the final power values depends on the energy extraction efficiency from the electron beam, which is the FEL parameter ρ_{FEL}, hence, $\Delta\eta_{\mathrm{sat}} \propto \rho_{\mathrm{FEL}}$. Therefore, the more electrons from the electron beam contribute to the FEL process within a bucket, the larger the extraction efficiency. This connection can be utilized to estimate the radiation levels at the saturation with

$$P_{\mathrm{sat}} \approx \rho_{\mathrm{FEL}} P_{\mathrm{beam}} \qquad \text{, with} \qquad P_{\mathrm{beam}}[\mathrm{TW}] = W_0[\mathrm{GeV}] I_{\mathrm{p}}[\mathrm{kA}]. \tag{2.64}$$

Here, the electron beam power P_{beam} is written in terms of more practical units. Eq.(2.64) indicates that GeV energy and kA peak current electron beams allow the production of radiation pulses with GW-level power.

Because the Pierce parameter defines the FEL bandwidth, it also sets the acceptance level of relative energy spread of the electron beam [100, 106]

$$(\Delta W/W)_{\mathrm{s}} \leq \rho_{\mathrm{FEL}}, \tag{2.65}$$

where the subscript s denotes the slice property. Eq.(2.65) is known as the *energy spread criterion* and is challenging to meet due to the scale of the Pierce parameter $\rho_{\mathrm{FEL}} \sim 10^{-4} - 10^{-3}$. The energy spread condition has to be strictly satisfied by the slice relative energy spread of the electron beam. Hence, slice relative energy spread properties of the electron beam have a much stronger impact on the overall SASE FEL performance than projected values [100]. If no energy chirp is present in the longitudinal phase space of the electron beam, then slice and projected relative energy spreads converge, and the condition can be applied to the entire beam. However, when the electron beam has a significant energy chirp, the energy spread condition may be satisfied for individual slices but violated for the projected relative energy spread of the entire electron beam. In that case, it can harm the FEL performance or even completely suppress the high-gain regime because insufficient electrons in an FEL bucket are present to contribute to coherent amplification. However, in a SASE FEL, it may be sufficient to meet the energy spread condition over approximately one cooperation length L_{c}, which describes the total radiation slippage length over one gain length L_{g} [107]

$$L_{\mathrm{c}} = \frac{\lambda_{\mathrm{r}}}{\lambda_{\mathrm{u}}} L_{\mathrm{g}}. \tag{2.66}$$

This fact can be used to attempt formulating an energy spread condition for the projected energy spread $(\Delta W/W)_{\mathrm{p}}$ when dominated by energy chirp. This leads to the following expression

$$\frac{(\Delta W/W)_{\mathrm{p}}}{\sigma_\zeta} \leq \frac{\rho_{\mathrm{FEL}}}{L_{\mathrm{c}}} \tag{2.67}$$

$$(\Delta W/W)_{\mathrm{p}} \leq \rho_{\mathrm{FEL}} \frac{\sigma_\zeta}{L_{\mathrm{c}}} \tag{2.68}$$

where σ_ζ is the electron beam length. As long as $\sigma_\zeta \gg L_{\mathrm{c}}$ holds, the requirements on the projected energy spread will be less stringent compared to the slice relative energy spread condition in Eq.(2.65). However, the slice and projected energy spread conditions

converge when the electron beam length increasingly approaches the cooperation length. Note that slice parameter evaluation is typically performed with the slice widths of the order of $\Delta\zeta \approx L_\mathrm{c}$.

The coherence time, denoted as (τ_c), is the characteristic decay time of the auto-correlation function $\langle E(y,t)E(y,t+\tau)\rangle$ of the electric field. This function measures how the electric field at a specific position and time correlates with the field at the same position after a time delay (τ). In SASE FEL, the coherence time is estimated in Ref.[108] to be

$$\tau_\mathrm{c} \simeq \frac{1}{\rho_\mathrm{FEL}\omega_\mathrm{r}}\sqrt{\frac{\pi \ln N_\mathrm{c}}{18}}, \tag{2.69}$$

where $N_\mathrm{c} = I_\mathrm{p}/(e\rho_\mathrm{FEL}\omega_\mathrm{r})$ is the number of cooperating electrons and ω_r is the resonance frequency. The spectral bandwidth is then $\sigma_\omega \simeq \tau_\mathrm{c}^{-1} \propto \rho_\mathrm{FEL}\omega_\mathrm{r}$.

The number of coherent spikes with coherence time of τ_c in a SASE FEL pulse can be estimated with the M_SASE-number

$$M_\mathrm{SASE} = \frac{\sigma_{\zeta,\mathrm{rms}}}{2\pi L_\mathrm{c}}, \tag{2.70}$$

where $\sigma_{\zeta,\mathrm{rms}}$ is the r.m.s electron beam length. In state-of-the-art FELs, the electron bunch is typically much longer than the cooperation length. As a result, the radiation pulse at saturation contains many coherent spikes, usually ranging from $M_\mathrm{SASE} = 10 - 100$. These spikes have a duration of $\Delta\tau = L_\mathrm{c}/c_0$. Due to the spiked temporal profile, the radiation spectrum contains many modes, resulting in reduced temporal coherence. In case the FEL is seeded with an external coherent radiation source at the resonance wavelength, such as LCLS self-seeding [82], or it is operated at the single-spike regime, when $M_\mathrm{SASE} \approx 1$, the radiation pulse will exhibit both spatial and temporal coherence simultaneously [96, 109]. However, achieving the latter approach in the hard X-ray regime is quite challenging due to the elevated requirements on the electron beam in terms of duration and brightness. Further, when Eq.(2.70) is inserted into the right side of expression Eq.(2.68) the following relation becomes apparent

$$(\Delta W/W)_\mathrm{p} \leq 2\pi\rho_\mathrm{FEL}M_\mathrm{SASE}, \tag{2.71}$$

and suggest that when approaching the singe-spike regime, the projected energy spread requirements become more stringent when dominated by energy chirp. However, this connection has to be put to the test and will be evaluated in future works.

Similar stringent requirements apply to the transverse momentum spread of the electron beam, which is reflected by the emittance condition [100, 110]

$$\epsilon_{\mathrm{n}} \leq \frac{\gamma_{\mathrm{rel}}\lambda_{\mathrm{r}}}{4\pi}. \tag{2.72}$$

The emittance condition (2.72) defines the minimum achievable wavelength at a given electron beam energy. With the typically normalized emittance of 1-10 mm-mrad in rf-based accelerators, multi-GeV electron beams are required to fulfil the emittance condition at the hard X-ray wavelength. Most importantly, the emittance condition ensures spatial coherence of FEL radiation modes at saturation. How well the emittance condition is fulfilled defines the degree of transverse coherence [108]

$$\nu_{\mathrm{sat}} \simeq \left(\frac{\ln(N_{\mathrm{c}}/\widehat{\epsilon})}{4\widehat{\epsilon}}\right)^2 \tag{2.73}$$

where $\widehat{\epsilon} = 2\pi\epsilon/\lambda_{\mathrm{r}}$ is the normalized emittance condition, and ϵ is the geometric emittance of the electron beam. Effects such as optical and gain guiding [67] may allow marginal deviation from the ideal condition in Eq.(2.72), but in any case, the general concern is the better the emittance condition is fulfilled, the better the spatial coherence and gain.

2.2.4 *Ming Xie formalism*

The previous sections discuss the theoretical foundation crucial for the overall examination and numerical implementation of the FEL process. This foundation provides straightforward analytical expressions that help estimate the power gain length in the cold beam limit. However, when considering factors such as energy spread, emittance, and radiation diffraction, the effective gain length increases from the 1D case. As many of these factors are interrelated, finding a self-consistent analytical expression while simultaneously considering all the different contributions is challenging. To address this, M.Xie [111] developed a workaround by conducting a multi-parameter scan. It enabled the expression of the degradation effects in terms of a scaling parameter with coefficients obtained from the simulation campaign. The Ming Xie formalism merges these effects and enables optimization and exploration of the FEL performance [111]. The 3D gain length considering energy spread, emittance, and radiation diffraction contributions reads [100, 111]

$$L_{\mathrm{g}} = L_{1\mathrm{d}}(1 + \Lambda(\chi_{\gamma_{\mathrm{rel}}}, \chi_{\epsilon}, \chi_{\mathrm{d}})), \tag{2.74}$$

where Λ is the scaling parameter as a function of the energy spread $\chi_{\gamma_{\rm rel}}$, emittance χ_ϵ and diffraction $\chi_{\rm d}$ parameter. The fitting polynomial function is

$$\begin{aligned}\Lambda = a_1 \cdot \chi_{\rm d}^{a_2} + a_3 \cdot \chi_\epsilon^{a_4} + a_5 \cdot \chi_{\gamma_{\rm rel}}^{a_6} + a_7 \cdot \chi_\epsilon^{a_8} \cdot \chi_{\gamma_{\rm rel}}^{a_9} + a_{10} \cdot \chi_{\rm d}^{a_{11}} \cdot \chi_{\gamma_{\rm rel}}^{a_{12}} \\ + a_{13} \cdot \chi_d^{a_{14}} \cdot \chi_\epsilon^{a_{15}} + a_{16} \cdot \chi_{\rm d}^{a_{17}} \cdot \chi_\epsilon^{a_{18}} \cdot \chi_{\gamma_{\rm rel}}^{a_{19}},\end{aligned} \tag{2.75}$$

where the corresponding fitting coefficients a_i are collected in appendix table (8.1). Eq.(2.75) shows quantitatively that all three scaling parameters should be maintained small to minimize gain degradation. The accuracy of this model is approximately 10% compared to fully explicit numerical simulations. The scaling parameters $\chi_{\gamma_{\rm rel}}$, χ_ϵ and $\chi_{\rm d}$ are discussed below.

The energy spread parameter reads

$$\chi_{\gamma_{\rm rel}} = 4\pi \left(\frac{L_{\rm 1d}}{\lambda_{\rm u}}\right) \left(\frac{\Delta W}{W}\right)_{\rm s,rms} = \frac{1}{\sqrt{3}} \frac{(\Delta W/W)_{\rm s,rms}}{\rho_{\rm FEL}}, \tag{2.76}$$

and the contributions from $\chi_{\gamma_{\rm rel}}$ are minimised when $\chi_{\gamma_{\rm rel}} < 1/\sqrt{3}$. This is when the energy spread condition $(\Delta W/W)_{\rm s} \leq \rho_{\rm FEL}$ is satisfied. It ensures bound electron motion within the separatrix and increases the number of cooperating electrons.

A closer look shows that the emittance parameter

$$\chi_\epsilon = \left(\frac{L_{\rm 1d}}{\beta_{\rm av}}\right) \left(\frac{4\pi\epsilon_{\rm n}}{\lambda_{\rm r}\gamma_{\rm rel}}\right), \tag{2.77}$$

resembles the emittance conditions in Eq.(2.72) when $L_{\rm 1d}/\beta_{\rm av} = 1$, such that the average Twiss β-function inside the undulator equals the 1D gain length. Then the degradation effects from the emittance parameter are minimized when $\chi_\epsilon < 1$.

The diffraction parameter considers the radiation field diffraction. If the radiation diffracts much faster than the electron beam, the overlap between radiation and the electron beam is compromised, resulting in inefficient energy transfer. The diffraction of the SASE radiation pulse follows the Rayleigh length

$$Z_{\rm R,FEL} = \frac{4\pi\sigma_{\rm r}^2}{\lambda_{\rm r}}, \tag{2.78}$$

where $\sigma_{\rm r}$ is the radiation source size, which is dictated by the radius of the electron beam. The diffraction parameter reads then

$$\chi_{\rm d} = \frac{L_{\rm 1d}}{Z_{\rm R,FEL}} = \frac{L_{\rm 1d}\lambda_{\rm r}}{4\pi\sigma_r^2}. \tag{2.79}$$

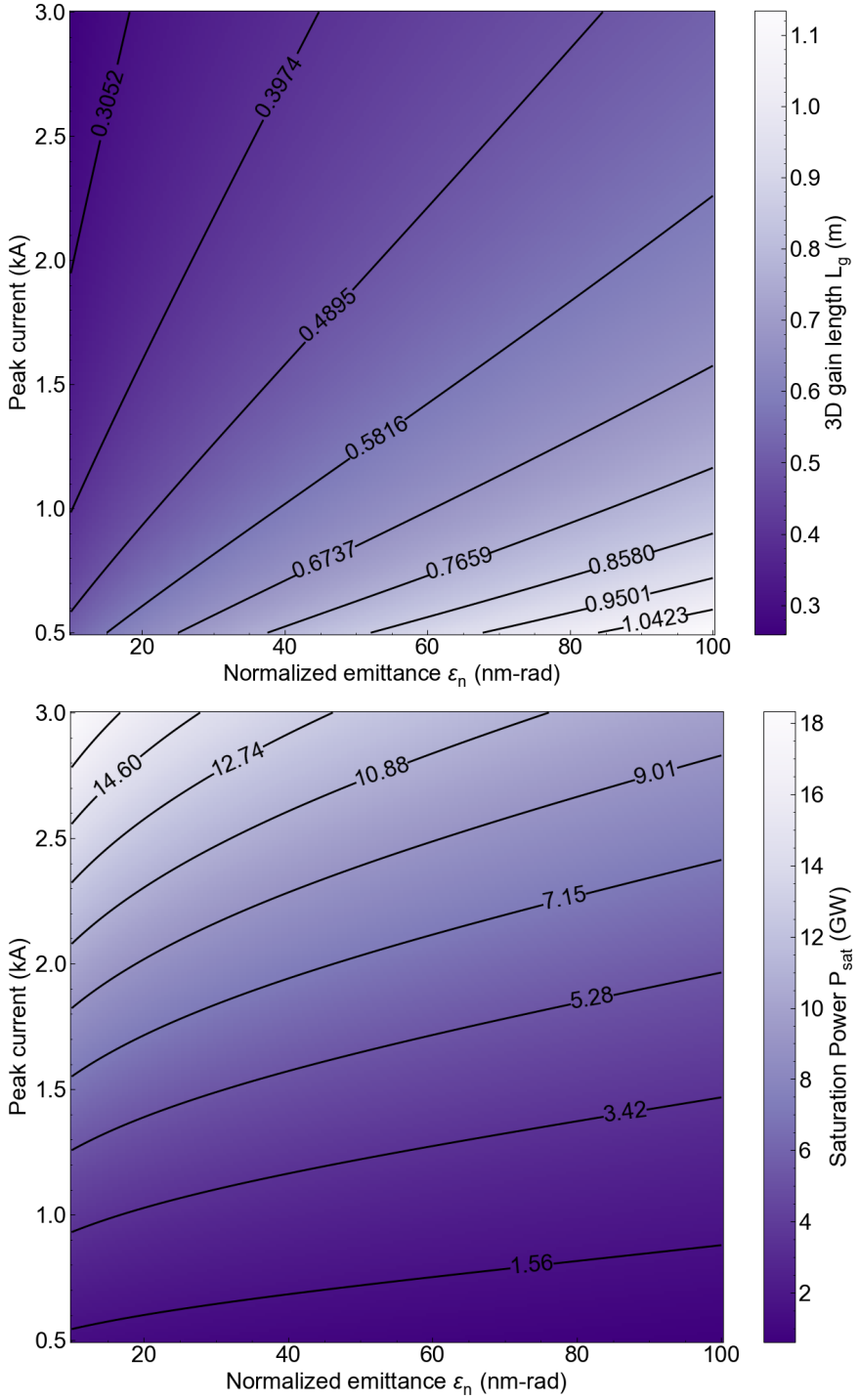

Figure 2.10: **Ming Xie formalism-based 3D gain length calculation.** Ming Xie formalism calculated 3D gain length (top) and saturation power (bottom) as a function of electron beam peak current and normalized emittance are presented. The undulator parameters $\lambda_u = 9\,\text{mm}$ and $K \approx 0.84$ are inspired by the study in Ref.[96]. The electron beam is focused down to the average beta function of $\beta_{\text{twiss}} \approx 5\,\text{m}$ at $W \approx 3\,\text{GeV}$ electron beam energy and $(\Delta W/W) \approx 0.016\,\%$ relative slice energy spread. These electron beam parameters are potentially realizable in future plasma-based accelerators, as suggested by the author in [42].

The contribution of radiation diffraction becomes negligible when $\chi_d \leq 1/2$ [93, 100]. This is ensured when $L_{g,1d} \leq 2Z_{R,FEL}$[93, 100].

Next, the Ming Xie formalism is utilized to explore requirements on the electron beam parameters for an ultra-compact FEL configuration at the hard X-ray wavelength (7 keV photons). This initial exploration considers electron beams of increased brightness for reduced gain length compared to what is possible today with rf-based technology. The electron beam energy is balanced such that it fully leverages the high quality of the electron beam and allows the use of existing or upcoming undulator technology. Figure (2.10) presents the results of this exploration, showing the accessibility of the 3D gain length and peak power as a function of electron beam peak current and normalized emittance. This calculation reveals that only a 3 GeV electron beam with emittances in the range of $10 - 100$ nm-rad, sub-0.1 %-level relative energy spread and peak currents of few kA suffices to enable ultra-compact hard X-ray FEL with gain length on the sub-meter scale at the GW-level peak power. Indeed, the assumed electron beam parameters sound very challenging to attain with state-of-the-art technology. This thesis will evaluate upcoming technologies based on plasma-based acceleration, not only shrinking the footprint of the acceleration section but also enabling electron beams with brightness values that are many orders of magnitude brighter than those accessible by state-of-the-art methods. This novel class of electron beams may enable exploration of the FEL regimes elaborated in figure (2.10).

2.3 NUMERICAL METHODS

This section briefly discusses numerical methods employed in this work for electron beam tracking from the plasma stage through an optimized beam line. Further, the FEL code Puffin is discussed, allowing high-fidelity modelling of the FEL interaction powered by the electron beams with unique properties anticipated from the plasma-based acceleration.

2.3.1 *Particle tracking code*

Electron beam transport post-plasma stage requires dedicated electron beam transport lines for the 6D phase space of the electron beam. Many different particle tracking

codes exist for various specialized scenarios such as for space charge and/or CSR-dominated regimes, for example, codes such as *A Space Charge Tracking Algorithm* (ASTRA) [112], and/or *General Particle Tracer* (GPT) [113]. These codes are exploited in this work mainly for sanity checks. However, the main part of the work is performed with the *ELEctron Generation ANd Tracking* (ELEGANT) code [114], which allows tracking of external 6D particle beam distributions with up to 3rd-order transfer matrices with simple space charge, wakefield and CSR models. Further, beamline optimization routines based on the *simplex* optimization algorithm enable the fast design of specialized beamlines and make them attractive for the design, optimization and particle tracking of electron beams from the plasma-based acceleration stage. A sophisticated simulation input deck is developed, automatically optimizing various beamline elements and configuration quantities with minimal user input. This input deck is embedded into a larger simulation framework with a streamlined procedure for high-fidelity *start-to-end* (S2E) simulations developed as part of this work.

2.3.2 *Free-electron laser modelling*

The simulations of free-electron lasers presented in this work, specifically in chapter (6), are based on the 3D Puffin code [91, 115, 116]. Puffin is a numerical solver that is massively parallel and handles an unaveraged 3D FEL system of equations. It is written in Fortran 90 and uses MPI and OpenMP [117]. Puffin is an 'unaveraged' FEL code, which does not rely on the *Slowly Varying Envelope Approximation* (SVEA) and undulator period averaging approximations. Instead, it employs an algorithm and macroparticle model similar to a *Particle-In-Cell* (PIC) code methodology that does not slice the beam phase space and radiation field. Therefore, *high-performance computing* (HPC) systems are required to perform the calculations, especially for problems with millions of microparticles in 3D. Additionally, Puffin includes standard beam transport components to model a 'realistic' undulator configuration. It can precisely model a 3D undulator with entries and exits tapering and natural focusing, radiation from large energy spread, and energy-chirped beams with a broad bandwidth frequency spectrum that is only limited by the Nyquist frequency of the mesh $f_{\mathrm{N}} = f_{\mathrm{s}}/2$, where f_{s} is the sampling rate of the electromagnetic field. Therefore, it can accurately resolve wavelengths down to $\lambda_{\mathrm{N}} = 2\lambda_{\mathrm{s}}$, where λ_{s} is the discretization cell length. A few more

capabilities are discussed in [115] but are irrelevant to this work. Puffin, when combined with a unified shot-noise model [118] and advanced particle upsampling methods [44, 119], allows for accurate modelling of spontaneous undulator and *Coherent Spontaneous Emission* (CSE) [120, 121]. Backwards wave emissions from the electron beam and space charge effects are not included due to their negligible contributions to the typical operation points of FELs. Puffin is extensively compared to other FEL codes and experimental results [122]. Therefore, the simulation results obtained are highly reliable.

2.4 DISCUSSION

This chapter provided the fundamental basics for developing electron beam transport lines for the post-plasma stage and electron beam characterisation and parametrisation. Many concepts discussed on electron beam optics also apply to electron beams in plasma-based accelerators. The FEL concepts are important for modelling radiation production in advanced codes such as Puffin and provide tools to estimate electron beam requirements for ultra-high gain FEL. The importance of electron beam emittance and brightness for elevated FEL performance becomes apparent, and subsequent chapters will investigate pathways to improve electron beam quality beyond the capabilities of stat-of-the-art rf-linacs. Finding ways to improve the overall slice and projected 6D brightness of electron beams will be the primary goal of the following chapters to unlock the path towards ultra-compact hard XFELs.

3

FUNDAMENTALS OF PLASMA AND WAKEFIELD ACCELERATION

This chapter introduces the essential characteristics of plasma and its role in PWFA, referring to beam-driver plasma-based acceleration and LWFA. The theory of plasma-based acceleration, including the formation of plasma waves and their inherent limitations, is explored. The injection of electron beams (*witness beams*) into these plasma waves is examined, and the concept of plasma photocathode injection in PWFA is introduced for ultra-high brightness beam generation. This chapter concludes by analyzing the preservation of witness beam quality and exploring potential future directions with the emerging Hybrid LWFA→PWFA platform. While reviewing the literature, the author identifies key challenges preventing the realization of ultra-compact hard XFELs.

3.1 BASIC PRINCIPLES OF PLASMA DESCRIPTION AND GENERATION

Plasma is an intriguing and distinct fourth state of matter that stands apart from solids, liquids, and gaseous media. The overview in this section offers a concise primer on the essentials of plasma physics based on [123–126] and relevant to plasma-based acceleration.

3.1.1 *Definition of plasma*

Plasma is partially or fully ionized matter that comprises an equal number of positively and negatively charged particles, making it electrically quasi-neutral, which can be expressed mathematically with

$$\sum Z_j n_j \approx 0, \tag{3.1}$$

where n_j is the number density of the jth species, Z_j is the charge state of the jth species, and the summation is taken over all plasma species.

The plasma density refers to the number of charged particles within a given volume. It is crucial in determining plasma systems' behaviour and collective effects. The plasma density can be calculated by adding up the number densities of all species of charged particles

$$n_\mathrm{p} = \sum n_j. \tag{3.2}$$

The temperature of the plasma is another essential factor that determines the distribution of kinetic energy among its charged particles. It greatly affects various plasma phenomena, such as particle collisions, energy transport, and wave propagation. The plasma temperature can be measured in several ways, including electron temperature, ion temperature, and electron-ion temperature ratio ($T_\mathrm{i}/T_\mathrm{e}$), where T_i and T_e is the ion and electron temperatures, respectively. Additionally, the thermal velocity of plasma electrons can be defined using the following equation

$$v_\mathrm{te} \equiv \sqrt{\frac{k_\mathrm{B} T_\mathrm{e}}{m_\mathrm{e}}}, \tag{3.3}$$

where m_e is the electron mass, k_B is the Boltzmann constant.

3.1.2 *Debye shielding, plasma frequency, and refraction index*

Debye shielding refers to the shielding of electric fields by surrounding plasma particles. It occurs due to the collective response of charged particles to the applied electric field and is essential for maintaining the quasi-neutrality of plasma. The characteristic length scale of Debye shielding is known as the Debye length λ_D and is defined as [127]

$$\lambda_\mathrm{D} = \left(\frac{\varepsilon_0 k_B T_e}{e^2 n_\mathrm{e}} \right)^{1/2}, \tag{3.4}$$

where ε_0 is the vacuum permittivity and n_e is the electron density. The Debye length in practical units can be expressed as

$$\lambda_\mathrm{D} \simeq 743 \times \left(\frac{T_\mathrm{e}}{\mathrm{eV}}\right)^{1/2} \left(\frac{n_\mathrm{e}}{\mathrm{cm}^{-3}}\right)^{-1/2} \mathrm{cm}. \tag{3.5}$$

The number of particles in a Debye sphere is

$$N_\mathrm{D} \equiv n_\mathrm{e} \frac{4\pi}{3} \lambda_\mathrm{D}^3. \tag{3.6}$$

This characterises plasma "collectiveness"; hence, when $N_\mathrm{D} \gg 1$, then the plasma is called "ideal plasma", and when $N_\mathrm{D} \ll 1$, it is categorised as non-ideal plasma.

Further, the plasma frequency is a characteristic frequency associated with plasma oscillations. It depends on the plasma density and represents the natural frequency at which charged particles collectively respond to external perturbations. The plasma frequency ω_p is given by

$$\omega_\mathrm{p} = \left(\frac{n_\mathrm{e} e^2}{m_e \varepsilon_0}\right)^{1/2}. \tag{3.7}$$

The corresponding plasma wavelength can be expressed in practical units as

$$\lambda_\mathrm{p} = \frac{2\pi c_0}{\omega_\mathrm{p}} \approx 3.34 \times 10^7 n_\mathrm{p}^{-1/2} \tag{3.8}$$

and the corresponding plasma wavenumber is then

$$k_\mathrm{p} = 2\pi/\lambda_\mathrm{p}. \tag{3.9}$$

The plasma frequency also defines the characteristic response time to recover quasi-neutrality. The ratio of Debye length Eq.(3.4) and thermal velocity Eq.(3.3) yields [127]

$$t_\mathrm{D} \simeq \frac{\lambda_\mathrm{D}}{v_\mathrm{te}} = \left(\frac{\varepsilon_0 k_B T_e}{e^2 n_\mathrm{e}} \times \frac{m_\mathrm{e}}{k_\mathrm{B} T_\mathrm{e}}\right)^{1/2} = \omega_\mathrm{p}^{-1}. \tag{3.10}$$

The plasma response time (Eq.(3.10)) dictates the interaction type of the plasma with time-varying external fields, such as lasers. Laser-plasma interaction can alter the plasma properties, but at the same time, the plasma can change the properties of the electromagnetic fields of a laser pulse. This coupling of EM-field with plasma gives rise to various phenomena relevant to the plasma-based acceleration concepts. Some of these aspects are discussed below and in the following paragraphs.

The following paragraphs introduce key elements of laser-plasma interaction, primarily focusing on laser pulse propagation through it. Consider an unmagnetized, cold plasma

with a monochromatic plane electromagnetic wave travelling through it. In this scenario, the dispersion relation can be expressed as follows [125]

$$\omega_l^2 = \omega_\mathrm{p}^2 + k_\mathrm{l}^2 c_0^2, \tag{3.11}$$

with ω_l being the laser angular frequency and k_l representing the wavenumber. Eq.(3.11) can be solved for the wave number k_l to obtain a deeper view

$$k_\mathrm{l} = \frac{\omega_l}{c_0}\sqrt{1 - \frac{\omega_\mathrm{p}^2}{\omega_l^2}}. \tag{3.12}$$

Upon closer inspection of Eq.(3.12), it becomes apparent that if $\omega_\mathrm{l} < \omega_\mathrm{p}$, the wave number k_l will be an imaginary number. This indicates that the electromagnetic wave is reflected on the plasma surface [128], commonly called an "overdense" plasma. On the other hand, if $\omega_l > \omega_\mathrm{p}$, the plasma is called "underdense", and the electromagnetic wave can propagate within it. This behaviour of EM waves inside plasma is a key ingredient for operating LWFA and the realisation of plasma photocathodes in PWFA (see section (3.2.2)) because it sets limitations on the accessible plasma densities which a laser pulse can penetrate at a specific laser wavelength. Furthermore, the phase velocity is calculated with $v_\phi = \omega_l/k_\mathrm{l} = c_0/\eta_\mathrm{ref.}$ and group velocity $v_\mathrm{g} = \partial\omega_l/\partial k_\mathrm{l} = c_0\eta_\mathrm{ref.}$ of the electromagnetic wave from Eq.(3.12), where $\eta_\mathrm{ref.}$ is the index of refraction

$$\eta_\mathrm{ref.} = \sqrt{1 - \frac{\omega_\mathrm{p}^2}{\omega_l^2}} = \sqrt{1 - \frac{n_\mathrm{e}}{n_\mathrm{cr}}}, \tag{3.13}$$

where $n_\mathrm{cr} = \omega_l^2 \epsilon_0 m_\mathrm{e}/e^2$ denotes the critical density. For a commonly used high-power laser system such as Ti:sapphire at $\lambda_l = 800\,\mathrm{nm}$ wavelength, the critical density is $n_\mathrm{cr} \approx 1.7 \times 10^{21}\,\mathrm{cm}^{-3}$. This means that when the plasma density n_e approaches n_cr, it will become overdense and reflect the laser pulse.

3.1.3 *Ionisation of gaseous media*

Thus far, the core principles of plasma physics are described. However, plasma formation via the ionization of gaseous media for plasma-based accelerators has yet to be introduced. Ionization ensues when an atom's bound electrons are released from the Coulomb electrostatic potential, for example, by electromagnetic radiation or particle collisions [129]. Electromagnetic radiation has various interaction routes with matter, but for ionization, two primary processes are important: *photoionization* and *field ionization*.

The Keldysh parameter γ_{K} determines the ionization regime between these two cases and reads [130]

$$\gamma_{\mathrm{K}} = \sqrt{\frac{I_{\mathrm{pot}}}{2U_{\mathrm{pot}}}}, \tag{3.14}$$

where I_{pot} is the atomic ionization potential and U_{pot} denotes the ponderomotive energy with

$$U_{\mathrm{pot}} = \frac{e^2 E_0^2}{4 m_{\mathrm{e}} \omega_l^2}, \tag{3.15}$$

where E_0 is the electric field amplitude and ω_l is the photon frequency. When the value of the Keldysh parameter is greater than one ($\gamma_{\mathrm{K}} \gg 1$), then the ionization process is mainly dominated by photoionization. On the other hand, if the value of the Keldysh parameter is less than one ($\gamma_{\mathrm{K}} \ll 1$), then field ionization [131] becomes the primary ionization process. This distinction becomes evident when the proportionalities of the Keldysh parameter are examined, which are $\gamma_{\mathrm{K}} \propto E_0^{-1} \lambda_l^{-1} I_{\mathrm{pot}}^{1/2}$. For high-power laser systems with a central wavelength of approximately 800 nm, the ionization process is strongly influenced by the electric field strength E_0.

When the strength of the electric field is moderate, single photon ionization occurs for $\gamma_{\mathrm{K}} \gg 1$ if the wavelength of the photons corresponds to the binding energy of the bound electron in the atomic potential. Valence electrons typically require visible light to soft X-rays, while inner shell electrons require hard X-ray photons to be released from the parent atom.

When the energy of the photons is insufficient for single photoionization, an electron can transition via the absorption of multiple photons N of longer wavelength λ_{l} from an initial state to a final state. The ionization rate $\Gamma_{i \to f} \propto I^N$ depends on the total number of photons involved.

For $\gamma_{\mathrm{K}} \ll 1$, the large-amplitude electric field deforms the atomic electrostatic Coulomb potential such that the bound electron experiences an effective lower potential barrier of the form

$$V_{\mathrm{eff}}(r) \propto -\frac{Z}{|r|} - \mathbf{E} \times \mathbf{r}, \tag{3.16}$$

where Z denotes the charge state of the atom or ion, and $\mathbf{r}$ is the vector displacement from the atomic core. Therefore, the bound electron has a finite probability of tunnelling through the distorted Coulomb potential into the free state [132]. Fig.(3.1) (a) visualizes the *Tunnel Ionisation* process in a simplified way. If the ionization happens "fast", for example, in a single cycle of an fs-laser pulse, and $I_{\mathrm{pot}} \gg \omega$ is valid, then

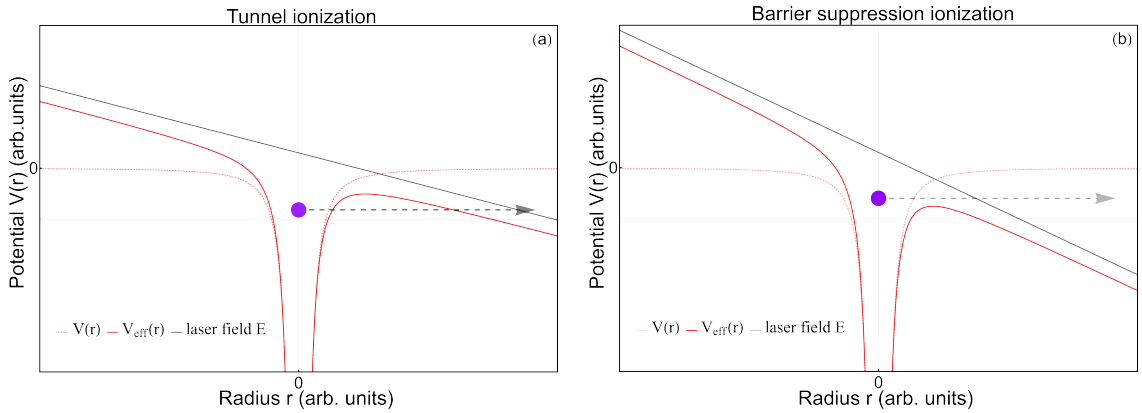

Figure 3.1: **Schematic field ionization mechanisms.** Schematic field ionization mechanisms are shown for the $\gamma_K \ll 1$ limit. The red solid line shows the effective electrostatic potential, while the grey line represents the external laser field. The purple circle indicates the bound electron and the grey arrows show the electron transition from being bound to a free state. The red dashed line represents the unperturbed potential for reference. (a) When an intense laser field is applied, it alters the initial potential, making it possible for a bound electron to tunnel quantum mechanically through the reduced potential barrier. (b) If the intensity of the laser field is increased, the potential barrier is suppressed below the ionisation energy of the bound electron. This means the electron can now classically escape the electrostatic potential, resulting in the atom's ionisation.

the ionization rates can be calculated in a semi-classical approximation [131]. The *Ammosov–Delone–Krainov* (ADK) ionization probability rate for this process is in a practical notation defined as [133]

$$\Gamma_{\mathrm{ADK}}[s^{-1}] \approx 1.52 \times 10^{15} \times \frac{4^{n^*} I_i[\mathrm{eV}]}{n^* \Gamma(2n^*)} \left(20.5 \frac{I_i^{3/2}[\mathrm{eV}]}{E[\mathrm{GV/m}]} \right)^{2n^*-1} \times \exp\left[-6.83 \frac{I_i^{3/2}[\mathrm{eV}]}{E[\mathrm{GV/m}]} \right], \qquad (3.17)$$

where $n^* \approx 3.69Z/I_i^{1/2}[eV]$ represents an effective principal quantum number, which describes the transition to an ionized state, and Γ is the gamma function. Figure (3.2) displays the ADK ionisation rates as a function of the electric field strength for the atomic species relevant to this work.

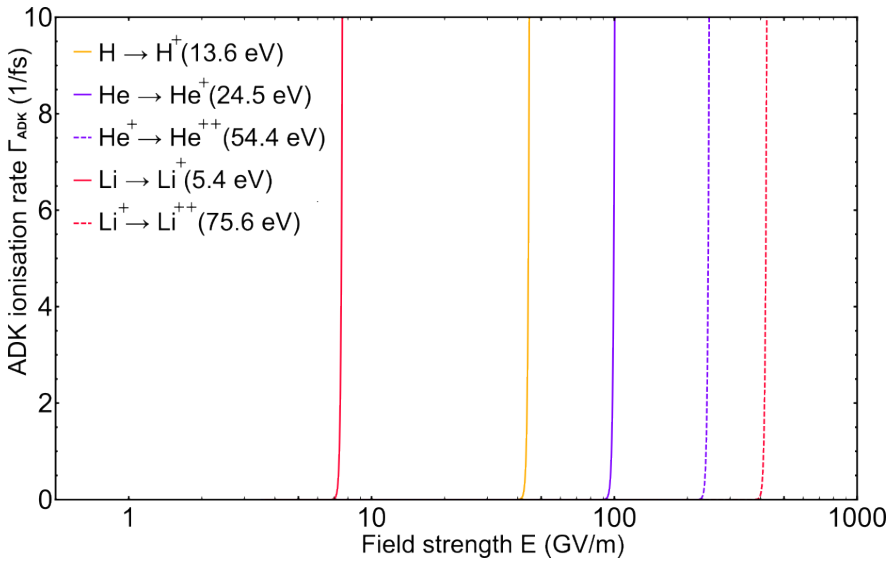

Figure 3.2: **ADK ionisation rates.** ADK ionisation rates as a function of incident laser field strength based on Eq.(3.17) for selected gas species relevant to this work. Annotation of the ionization potentials for the corresponding species is provided in eV.

When the electric field strength is increased to a critical value of $E_{\mathrm{crit}} \propto I_{\mathrm{pot}}^2/4Z$ [134] then barrier suppression ionisation dominates the ionisation rates. At this point, the Coulomb potential of the atom is suppressed below the bound state of an electron, which allows the electron to escape directly into the continuum in a classical way, as sketched in Fig.(3.1) (b).

3.1.4 *Laser-based ionisation and plasma source*

The previous section discussed the mechanisms for ionizing gaseous media in strong electromagnetic fields. Modern lasers based on the CPA [12] scheme deliver laser pulses

of few fs duration and electric field strength of the order of GV/m and higher, which is sufficient for ionising materials and gaseous media according to the ADK rates in Fig.(3.2). This section discusses the fundamentals of lasers and laser-based ionization of gaseous media.

The electric field propagation of a Gaussian laser pulse in a vacuum under the paraxial approximation (small divergence of the beam) reads [129, 135, 136]

$$\mathbf{E}(r,z,t) = E_0\hat{x}\underbrace{\frac{w_0}{w(z)}\exp\left(-\frac{r^2}{w(z)^2}\right)}_{\text{transverse term}}\underbrace{\exp\left[-\frac{(z-v_\mathrm{g}t)^2}{(c\tau)^2}\right]}_{\text{longitudinal term}}\underbrace{\exp\left[-i\left(kz-\omega_\mathrm{l}t+k\frac{r^2}{2R(z)}-\phi_\mathrm{G}(z)\right)\right]}_{\text{phase}}. \tag{3.18}$$

The first and second terms in Eq.(3.18) describe the transverse and longitudinal evolution of the laser pulse, and the last term represents the laser pulse phase.

The first term contains the *beam waist* $w(z)$ as a function of z

$$w(z) = w_0\sqrt{1+\left(\frac{z}{z_\mathrm{R}}\right)^2}, \tag{3.19}$$

where w_0 denotes the laser spot size at focus and z_R the *Rayleigh length*, which is defined as

$$z_\mathrm{R} = \frac{\pi w_0^2}{\lambda_\mathrm{l}}. \tag{3.20}$$

The Rayleigh length represents the distance the laser beam can effectively sustain a focused spot size. Figure (3.3) (left panel) shows schematically how a laser pulse undergoes the transition from focusing to defocusing phase with an indication of the $2\times z_\mathrm{R}$ range based on Eq.(3.19). Laser spot size at focus w_0 and Rayleigh length z_R can be expressed in terms of the f-number [129, 137]

$$N = \frac{f_\#}{D}, \tag{3.21}$$

which is the ratio of focal length f to beam diameter D of a collimated beam. The laser spot size at focus is $w_0 = 2\sqrt{2}/\pi\lambda_\mathrm{l} \approx 0.9\lambda_\mathrm{l}f_\#$ and $z_\mathrm{R} \approx 2.5\lambda_\mathrm{l}f_\#$. For example, focusing down a laser pulse from a commercially available Ti:sapphire lasers system at $\lambda_\mathrm{l} = 800\,\mathrm{nm}$ to $w_0 \approx 7\,\mu\mathrm{m}$ will require a $f/10$ focusing optic system. It is important to remember that these calculations are based on ideal beams. In reality, various imperfections, such as aberrations, non-uniform phase, and optics errors, will result in larger spot sizes at the interaction point. Nonetheless, the f-number is a useful parameter for designing optical systems for experiments.

The second term in Eq.(3.18) is the laser pulse group velocity, denoted by $v_\mathrm{g} = \partial\omega/\partial k$. It also includes the *full width at half the maximum* (FWHM) electric field's pulse

duration, represented by $\tau = 2\sqrt{2\log(2)}\sigma_t$. Here, σ_t refers to the r.m.s longitudinal pulse duration.

The third term in Eq.(3.18) represents the phase of the laser pulse. It includes the curvature of the wavefront, which is given by $R(z) = z(1 + (z_R/z)^2)$, and the Gouy phase term, which is denoted by $\phi_G(z) = \arctan(z/z_R)$.

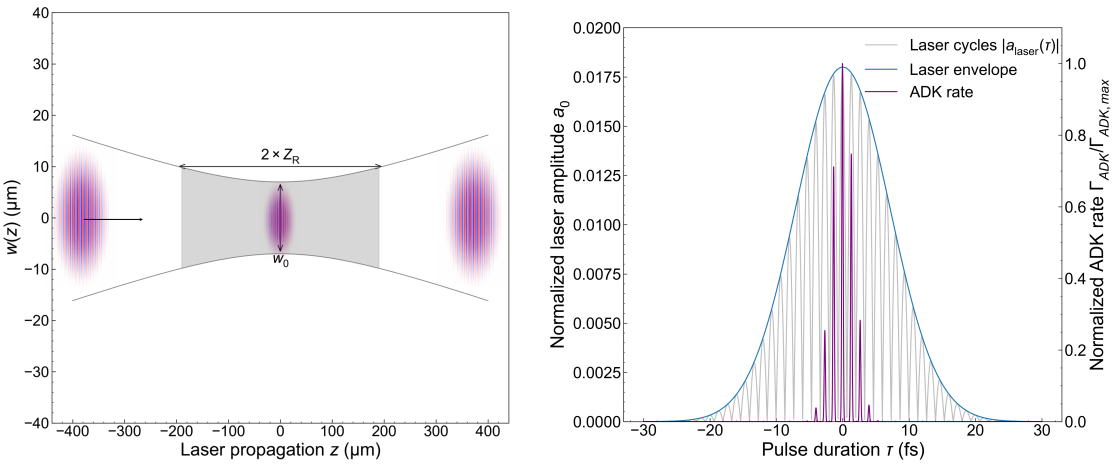

Figure 3.3: **Laser-based tunnel-ionization.** Schematic representation of Gaussian laser pulse focusing and ADK ionisation of the laser at focus. The laser pulse transitions from focusing to defocusing on the left panel with overlaid waist function Eq.(3.19) (solid grey line). The grey area indicates the range when the laser pulse waist is $w_0 \leq \sqrt{2}w_0$. On the right panel, single cycles of the laser beam (grey solid line) and the envelope of the temporal profile (blue solid line) are shown. The normalized ADK rate is presented for the above threshold ionization of helium when the laser beam is focused and reaches the maximum normalized vector potential of $a_0 \approx 0.018$.

The peak laser electric field E_0 of a linearly polarized Gaussian beam can be expressed as *normalized vector potential* [135]

$$a_0 = \frac{eE_0}{m_e c\omega_l} \cong 8.5 \times 10^{-10} I[\mathrm{Wcm}^{-2}]^{1/2} \lambda_l[\mu\mathrm{m}]. \tag{3.22}$$

Conveniently, the normalized vector potential a_0 defines the laser-matter interaction regimes. When $a_0 \geq 1$, the interaction is highly non-linear, so the laser pulse transfers significant energy to the plasma. In contrast, at moderate laser intensities $a_0 \leq 1$, the interaction regime is linear and increasingly resembles the classical interplay of laser light with the matter [131]. In particular, concerning this work is the regime of $a_0 \ll 1$ when laser intensity is sufficiently high (typically $I = 10^{15} - 10^{17}\,\mathrm{W/cm}^2$) to ionize gaseous media but low enough to minimize heating of the produced plasma such that the

laser-produced plasma remains "cold". Figure (3.3) (right panel) displays *above-threshold* laser ionization of helium, based on the ADK model discussed in section (3.1.3). Here, a linearly polarized Gaussian laser pulse of r.m.s pulse duration 30 fs, normalized vector potential of $a_0 \approx 0.018$ with a beam waist of $w_0 = 7\,\mu$m at focus reaches peak intensity just above the ionization threshold of helium. The highest ionization probability occurs at the laser pulse cycle peaks (purple) and spreads near the laser envelope maximum. These electrons first tunnel through the suppressed potential barrier of the atom and then gain energy through interaction with the passing laser pulse. This above-threshold ionization is the primary effect of heating the photoelectrons [138–140]. The photoelectrons' heating is negligible when the electrons are released at the laser pulse cycle peak and increase towards zero-crossing of the electric field [141]. Electrons resulting from above-threshold laser-ionized plasma can have temperatures within the range of a few $T_\mathrm{e} \approx 1\,$eV to a few $T_\mathrm{e} \approx 100\,$eV. These temperature effects are explored in figure (3.4), which presents PIC simulation results with the cylinder symmetric *Fourier-Bessel Particle-In-Cell* (FBPIC) code [142] on fully-resolved laser-produced plasma and corresponding plasma electron temperature for a few selected gas species. A 800 nm wavelength, $\sigma_\mathrm{t} = 50\,$fs long laser pulse with a spot size of $w_0 = 7\,\mu$m corresponding to $z_\mathrm{R} \approx 200\,\mu$m and $a_0 \approx 0.018$ at focus ionizes helium gas at a density $n_\mathrm{He} \approx 2.3 \times 10^{17}\,\mathrm{cm}^{-3}$. Figure (3.4) (left panel) shows that the plasma volume produced by the laser pulse extends approximately over $2z_\mathrm{R}$ in z and with a width of w_0 in x, y, and the plasma temperature is in the few eV-range. Hence, the ionization volume produced by the laser pulse can be approximated in the first order with

$$V_\mathrm{ion,approx} = \pi \int_{-z_\mathrm{R}}^{z_\mathrm{R}} w(z)^2 dz = \frac{8\pi^2 w_0^4}{3\lambda_\mathrm{l}}. \tag{3.23}$$

Equation (3.23) assumes that the gas within the $2z_\mathrm{R}$ volume is fully ionized; however, the ionization volume is an ellipsoid (see Fig.(3.4)). If the exact ionization volume $V_\mathrm{ion,ext}$ is known, then the total charge can be obtained with $Q_\mathrm{ion} \propto e n_\mathrm{He} V_\mathrm{ion,ext}$. Nevertheless, Eq.(3.23) reveals the strong dependency of the ionization volume on the laser beam waist w_0. Further, the right panel of the figure shows the plasma temperature dependency on the laser intensity for selected gas species. The electron temperature stays below the keV level even at the intensity levels of $I = 10^{17}\,\mathrm{W/cm}^2$, which resembles theoretical estimates (solid lines) based on thermal temperature calculations from [143, 144]. For laser peak intensities exceeding the ionization threshold, all atoms will be ionized by the

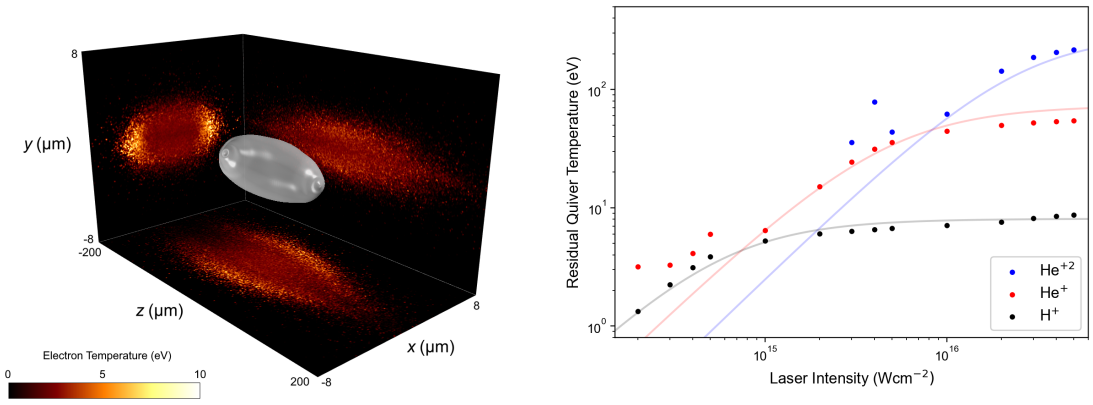

Figure 3.4: **Plasma temperature of laser-ionized gaseous media.** A laser pulse triggers the plasma volume and temperature that arise from ADK ionization. A Gaussian laser pulse forms the ellipsoid shape of the resulting volume. Projections of electron temperatures are displayed shortly after the laser pulse has passed (left panel). Simulation results (depicted as scatter points) illustrate the shift from partially ionized to saturation regimes. Furthermore, residual quiver temperatures for various species are showcased across a broad range of intensities with theoretical temperature prediction (solid lines) based on [143, 144] (right panel). Simulation performed by T. Wilson for [41] with input on laser and gas parameters from the author. This work is openly licensed via CC BY 4.0.

laser front before the pulse peak arrives. As a result, the electron temperature reaches a saturation state, plateauing at a constant value [41, 143, 144].

In section (3.2.5), these cold plasma electrons are utilized as a source for ultracold relativistic electron beam formation in PWFA via an underdense plasma photocathode [144]. Similar laser parameters are used for the jitter analysis of the plasma photocathode laser in section (4.2.2). Note that a fully-resolved laser pulse is utilised for the figure (3.4). However, envelope laser pulses are commonly used for computational efficiency at these laser intensities, producing comparable results regarding charge and final electron beam properties in the plasma photocathode PWFA configuration [145].

Plasma-based accelerators may require plasma sources extending over tens of cm to even meter scale. This can become challenging to produce with standard Gaussian beam focusing because the Rayleigh length of the laser pulse has to be on the cm to m scale. Manahan *et al.* highlighted the practical limitations by estimating a f-number of 1000 for a laser focusing optic producing $z_\mathrm{R} = 1\,\mathrm{m}$. The required laser diameter $D \approx 1\,\mathrm{mm}$ would produce intensities orders of magnitude higher on the optics than their damage

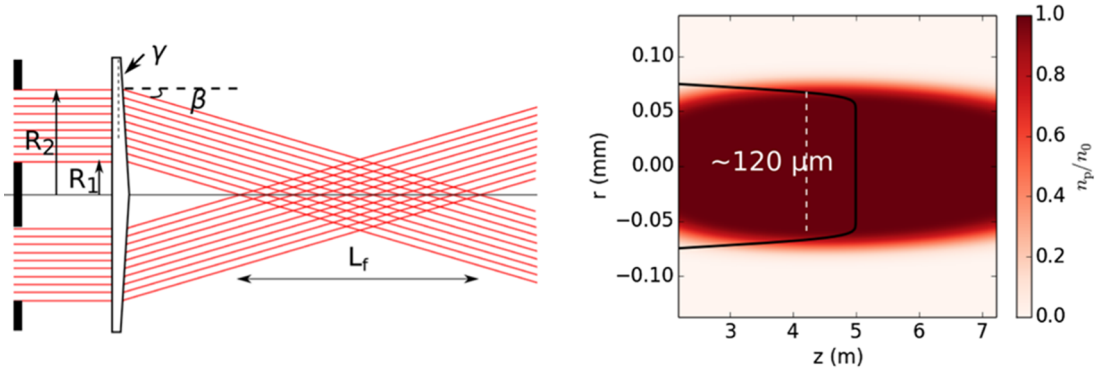

Figure 3.5: **A meter-scale plasma source produced by an Axicon optic.** Schematic representation of the axicon optical system (left panel) with annotation of inner R_1 and outer R_2 annular aperture radii, base angle $\gamma : \gamma_{\text{axi}}$, ray exit angle $\beta : \beta_{\text{axi}}$ and extent of the line focus L_{f} and resulting hydrogen plasma source (right panel) are presented. Adapted from [146]. This work is openly licensed via CC BY 3.0.

thresholds [146]. A possible solution is using an *axicon focusing lens* with an annular aperture, which enables a nearly uniform axial optical intensity profile of meter-scale [146–148]. It can ionize a background gas when the intensity of the laser is high enough for ADK ionization, producing multi-cm to meter-scale preformed plasma source for plasma-based acceleration [146]. For example, axicon type of optics have been employed in [149, 150] for generation of multi-cm scale *hydrodynamic optical-field-ionized* (HOFI) plasma channels for laser waveguiding.

Figure (3.5) displays simplified analytical calculations based on the ADK model of an axicon-produced hydrogen plasma source. The ADK calculations suggest that with approximately 500 mJ laser energy over a laser pulse duration of 70 fs and an axicon base angle of $\gamma_{\text{axi}} \approx 0.25°$ multi-meter long plasma source can be generated wide enough to support stable plasma-based acceleration. However, if the preformed plasma source is not wide enough or has a non-uniform density profile, various boundary effects arise during the acceleration. Section (4.1.4) elaborates on these effects within the context of the E-210 experimental results at SLAC FACET, where the metre-long plasma source had a non-ideal spatial and density topology.

3.2 THEORETICAL DESCRIPTION OF BEAM-DRIVEN PLASMA WAKEFIELD ACCELERATION

Plasma-based particle acceleration is a new method that uses the electric fields created in plasma by a high-energy intense particle beam or laser beam. This technique can be used in compact and high-energy particle accelerators, with potential applications in high-energy physics, X-ray free-electron lasers, and medical sciences. The following section will establish the fundamentals of novel particle accelerators, emphasising PWFA, stability and electron injection, and preservation of ultra-high brightness beams for X-ray free-electron laser applications.

3.2.1 *Review of plasma-based particle accelerators*

The quest for innovative particle accelerators can be traced back to as early as 1952 when "collective accelerators" were initially proposed by Alfvén & Wernholm [151]. In 1956, Budker [152], Veksler [153], and Fainberg [154] further investigated the possibility of high-gradient charged particle accelerators using the concept of collective accelerators. All three authors recognized the limitations of the existing technology and the potential prospects of novel accelerator technology. However, they also understood that the density of the electron beams required for collective accelerators was beyond the technological capabilities of that time. Nevertheless, there was rapid theoretical progress in the following years.

Ruth *et al.* [155] and Chen [156] proposed using charged particle beams to drive plasma wakefields. Katsouleas [157] described the *beam loading effect* to enhance acceleration efficiency and reduce the energy spread of accelerated beams. Shortly after discovering the nonlinear regime [158], Rosenzweig [158] reported the first experimental observation of Plasma Wakefield Acceleration in 1988 [159]. In 1991, Rosenzweig *et al.* [160] discovered the blowout regime, which provides strong and uniform focusing wakefields and large acceleration gradients (see section (3.2.2) for more details on blowout regime). Experimental verification of the blowout regime in PWFA was achieved at the *Argonne Wakefield Accelerator* (AWA) facility [161].

Since then, numerous theoretical and experimental advancements have been made. Some significant milestones in the field include the proposal of electron injection into

the blowout regime through a sharp plasma density downramps [162], the development of a nonlinear blowout theory [163], the successful demonstration of energy doubling of 42 GeV electron beam at SLAC to 84 GeV [164], the proposal of a plasma photocathode by Hidding *et al.* for ultra-high brightness electron beams in PWFA [144], the achievement of high energy efficiency two-bunch acceleration at the SLAC FACET facility [37], the proposal of an advanced plasma photocathode for ultra-high 6D brightness beams production [42] by Manahan, G. G. and Habib, A. F. *et al.*, and the successful demonstration of plasma photocathode [39, 165] and all-optical density-downramp injection [39, 166] in PWFA at SLAC FACET. Proton-driven PWFA was proposed by Katsouleas [157] and later evaluated in [167] and experimentally realized at CERN within the AWAKE collaboration [168]. Many more facilities are engaging or planning to contribute to PWFA (R&D), such as *Accelerator Test Facility* (ATF) (USA), CLARA FEBE (UK), DESY (Germany), INFN (Italy), and many more. Over the years, PWFA's R&D community has become increasingly organized and vibrant. The community has set strategic goals for the future, as evidenced by various publications such as [169–172]. Moreover, advanced accelerator concepts have found their way into multi-year R&D roadmaps in the USA, UK, and Europe [170, 173, 174].

Parallel to this, a different approach made advancements in novel accelerator technology. A groundbreaking research paper by Tajima and Dawson in 1979 [175] investigated the interaction between plasma and intense laser pulses using computer simulations. They found that short high-intensity laser pulses can create high amplitude plasma waves with accelerating gradients of up to GV/m. This discovery laid the foundation for LWFA. However, laser technology was not advanced enough to produce short, intense laser pulses capable of driving large-amplitude plasma waves. Out of necessity, a workaround was developed where two long laser pulses, typically with tens of picoseconds duration, resonantly drive a Plasma Beatwave Accelerator, when a matching condition $\omega_\mathrm{p} = \omega_1 - \omega_2$ is precisely satisfied. The frequencies of the two laser pulses are denoted by ω_1 and ω_2, respectively [176]. The experimental progress of this approach was manageable.

In 1985, Strickland & Mourou [12] achieved a breakthrough in CPA, which paved the way for generating sub-picosecond laser pulses necessary for driving high-amplitude plasma waves. This breakthrough significantly propelled the experimental work in the LWFA in the following years. Much of the research before 1990 concentrated on

accelerating electron beams injected externally into plasma waves. As the duration of those electron beams was much longer than the plasma period, only a small portion of the beams were accelerated by the plasma fields. As a result, the quality of the accelerated electron beams was inferior, with roughly 100 % energy spread. The Maxwellian-like spectral distribution at a maximum energy of a few MeV reflects this. With laser pulses becoming increasingly shorter on the 500 fs scale and their corresponding higher intensity, the combined effects of self-focusing and self-modulation of the laser pulse enable the production of a train of intense laser pulses that are spaced by the plasma wavelength. This leads to resonant excitation of *Self-Modulated Laser Wakefields Acceleration* (SM-LWFA) with accelerating gradients of 100 GV/m. The values of detected accelerating gradients started to approach the non-relativistic wave-breaking field, which reads [138, 177]

$$E_{0,\mathrm{w}} \equiv E_{\mathrm{wb}}[\mathrm{V/m}] = \frac{c_0 m_\mathrm{e} \omega_\mathrm{p}}{e} \cong 96 \times n_e^{1/2}[\mathrm{cm}^{-3}]. \tag{3.24}$$

For electron densities of $n_\mathrm{e} = 1.1 \times 10^{18}\,\mathrm{cm}^{-3}$, corresponding to a plasma wavelength of $\lambda_\mathrm{p} \approx 32\,\mu$m, Eq.(3.24) yields accelerating gradients of the order of 100 GV/m, similar to the SM-LWFA results.

A milestone was reached when wave-breaking injection was demonstrated in the SM-LWFA regime. Electrons were accelerated up to 44 MeV in a sub-mm distance at the Rutherford Appleton Laboratory [178]. The injection and acceleration of background plasma electrons marked a significant step forward. However, the quality of electrons in terms of energy spread and emittance was not competitive with conventional accelerators. Despite this limitation, the community achieved significant progress in generating and characterizing electron beams with Maxwellian spectral distributions at high repetition rates [179, 180]. There has been a recent revival in SM-LWFA schemes or similar due to significant theoretical and experimental advancements [181–183]. However, the LWFA research focus followed a different route.

Theoretical research conducted in 2002, based on three-dimensional PIC simulations, introduced a new acceleration regime in LWFA, known as the "bubble" regime (see section (3.2.2) for more details on the bubble regime), as described by Pukhov & Meyer-ter Vehn in [184]. This regime is highly nonlinear and is observed when the laser pulse duration is shorter than the plasma wavelength. The intensity of the laser pulse is high enough to break the plasma wave. When electrons are injected from the background plasma into the bubble (see section (3.2.4) on self-injection), they exhibit a

quasi-monoenergetic feature in the energy spectrum. This simulation-based observation showed a route towards better beam quality than the experimentally measured reality of typically Maxwellian spectral distributions. Following successful demonstrations of the production of monoenergetic beams from LWFA in the bubble regime by various groups in the UK, Europe, and the USA [185–187], and other groups in Germany reported quasi-monoenergetic electron beam features in the experiments [188, 189] as well. Since the seminal experimental results, numerous theoretical and experimental breakthroughs have been made in the field. These include novel plasma sources, new injection methods, and electron beam energy records [149, 150, 186, 190–196]. Significant advancements have been made in the field with nanocoulomb-class beam generation, controlled multi-colour electron beam injection, and long-term operation of LWFA [197–199]. Much of this progress in LWFA is contributing to a new approach called the Hybrid LWFA→PWFA [200], where electron beams produced in LWFA are used to power a subsequent PWFA stage. This innovative method opens up possibilities for new capabilities and increased capacity in PWFA R&D. Section (3.2.8) will discuss the Hybrid LWFA→PWFA concept.

Plasma-based acceleration has come a long way since its inception and has significantly progressed in technology reliability and maturity. Furthermore, the plasma-based community has a proven track record of turning simulation-based concepts into experimental reality. Several noteworthy examples demonstrate this trend. For instance, the initial proposals for PWFA and LWFA were based on simulation studies [155, 156, 175]. Shortly after, the blowout regime in PWFA was discovered [158] and experimentally observed [159]. Additionally, the bubble regime in LWFA was found [184], and it was experimentally verified at various laboratories worldwide [185–187]. The plasma photocathode in PWFA was invented [144], and it was experimentally realised at FACET [39]. Recently, the simulation-supported proposal of Hybrid LWFA→PWFA was made [201], and it was experimentally observed at various laboratories [202–206]. If this trend continues, novel simulation-based concepts may improve beam quality, stability, and reproducibility in plasma-based acceleration and transform this technology into state-of-the-art.

3.2.2 *Fundamentals of beam-driven plasma wakefield acceleration*

A high-charge density particle beam travelling at approximately the speed of light in an underdense plasma can excite plasma waves behind the particle beam. The unipolar space charge fields (Eq.(3.25)) of the particle beam displace plasma electrons from the propagation axis, leaving a stationary ion background behind. The immobile ions attract the plasma electrons to their initial position, and the plasma electrons oscillate at the plasma frequency ω_p. The plasma collective effects form then a wakefield behind the driver beam with electric field gradients of approximately 100 GV/m, which is much larger than typical rf-linacs with accelerating gradients of the order of $E_\mathrm{rf} \approx 100\,\mathrm{MV/m}$ [36]. This is known as PWFA. An intense ultra-short laser pulse can also excite large-amplitude plasma waves with 100 GV/m-scale wakefields, known as LWFA. However, the mechanism of plasma electron displacement in LWFA is mediated by the *Ponderomotive Force* of the laser pulse. A detailed description of LWFA is beyond the scope of this work, and the reader is directed to a few valuable references [126, 176, 207–209]. In both scenarios, the plasma waves become non-linear when the driver beam becomes increasingly intense. The plasma waves may exhibit favourable electron beam acceleration and focusing conditions, as discussed below.

In LWFA, the bubble regime is reached when the normalized vector potential becomes much larger than one $a_0 \gg 1$ [184], while in PWFA, the blowout regime is reached when the driver beam density is much larger than the ambient plasma density $n_\mathrm{d} \gg n_\mathrm{p}$ [158]. From the physics perspective, the terms bubble and blowout regimes are synonymous. They refer to the scenario when an electron-free cavity with an immobile ion background is produced behind the driver beam, be it a laser pulse or charged particle beam. In the bubble and blowout regime, the transverse focusing fields are linear. In principle, this allows the acceleration of electron beams within the accelerating cavity while preserving its quality in terms of transverse properties (see section (3.2.7) on beam quality preservation) [158].

In the case of an electron beam of Gaussian distribution, the peak electron beam density can be expressed as $n_{\mathrm{d},0} = Q_\mathrm{d}/(2\pi)^{3/2}\sigma_\mathrm{z}\sigma_\mathrm{r}^2$, where $Q_\mathrm{d} = Ne$ is the electron driver beam charge, σ_r and σ_z are the beam radius and length, respectively, the associated

transverse unipolar space charge field of a Gaussian-shaped electron beam in vacuum is given by [55]

$$E_{\mathrm{r,d}}(r) = \frac{n_{\mathrm{d},0}\sigma_{\mathrm{r}}^2}{\epsilon_0 r}\left[1 - \exp\left(\frac{-r^2}{2\sigma_r^2}\right)\right]. \tag{3.25}$$

To efficiently excite a plasma wave in PWFA, it is necessary to have an electron driver of a length equal to or even shorter than the plasma wavelength, with a characteristic length of $\sigma_{\mathrm{z,max}} \cong \lambda_{\mathrm{p}}/2$. The electron beam must be tightly focused so that $k_{\mathrm{p}}\sigma_{\mathrm{r}} \ll 1$ [210].

The excitation of wakefields in plasma-based acceleration can be described at various degrees of complexity. Hence, the following is a brief explanation of some important theoretical concepts. The Klimontovich equation is a microscopic approach that, when coupled with the Maxwell equations, provides a comprehensive description of plasma evolution [211]. However, solving the equations for every particle in the system is impractical due to the involved complexity. Therefore, a macroscopic approach is commonly used to describe plasma, governed by the *magnetohydrodynamic* (MHD) equations. The MHD approach is characterized by a field theory that loses the particle nature of plasma and is based on a limited number of evolution equations for local macroscopic quantities, such as density, velocity, temperature, etc. While this approach suits some problems, a more detailed description of plasma media dynamics is necessary for other cases. Kinetic models, such as the Vlasov-Maxwell equations, provide an intermediate description between the microscopic and macroscopic approaches [211, 212].

In plasma-based accelerators, it can be assumed that the plasma consists of two cold fluids, allowing for deriving a simple wave equation to study the fundamental physical properties of a plasma wave stimulated by a laser pulse or an electron beam. Several assumptions are made when utilizing the two-fluid plasma model in the context of the plasma wakefield accelerator. The primary gas species is assumed to be preionized, and the ion background is considered static during the interaction time between the plasma electrons and the laser pulse or electron driver. The plasma is assumed to be cold, meaning the thermal velocity spread (Eq.(3.3)) is minimal and can be treated as a negligible perturbation in the lowest order of fluid motion. The plasma should also be collisionless, which is achieved when the electron-ion collision frequency is negligible, i.e., much smaller than the electron plasma frequency.

First, only excitation of the wakefield by a driver beam (electron beam or laser pulse) in the 1D Poisson equation [176, 213, 214] is considered. This basis is utilised in chapter (5) to include contributions of trailing electron beams. It should be noted, however, that the Maxwell and Lorentz equations offer a more intricate derivation. The Poisson equation can be expressed in the following manner [176, 213, 214]

$$\frac{\partial^2 \phi}{\partial z^2} = -\frac{4\pi e}{m_\mathrm{e} c_0^2}\rho, \tag{3.26}$$

where $\phi = e\Phi/m_\mathrm{e}c_0^2$ is the scalar potential expressed in normalized units, and ρ is the charge density. The total charge density ρ_tot of the system comprises plasma electron density $-en_\mathrm{e}$, the positively charged background plasma-ions en_i and the electron driver density $-en_\mathrm{d}$ resulting into $\rho_\mathrm{tot} = -e(n_\mathrm{e} - n_\mathrm{i} + n_\mathrm{d})$. Inserting the total charge density into the Poisson equation (3.26) yields

$$\frac{\partial^2 \phi}{\partial z^2} = \frac{4\pi e^2}{m_\mathrm{e} c_0^2}\left(n_\mathrm{e} - n_\mathrm{i} + n_\mathrm{d}\right) \tag{3.27}$$

$$= k_\mathrm{p}^2 \left(\frac{n_\mathrm{e}}{n_\mathrm{i}} + \frac{n_\mathrm{d}}{n_\mathrm{i}} - 1\right). \tag{3.28}$$

It is reasonable to assume that an ultra-relativistic electron driver beam undergoes negligible evolution at the temporal scale of the plasma response $t_\mathrm{D} = \omega_\mathrm{p}^{-1}$ (Eq.(3.10)), allowing the use of the *quasi-static approximation* (QSA). The QSA facilitates a Galilean coordinate transformation, which effectively shifts the equation from its (z,t)-dependence to a co-moving frame of reference, using the co-moving coordinates (ξ,τ), where $\xi = z - v_\phi t$ and $\tau = t$. In this context, v_ϕ refers to the phase velocity of the wake. If a laser pulse driver is utilized, $v_\phi \cong v_\mathrm{g}$, signifying the laser pulse group velocity. When a highly relativistic $\beta_\mathrm{d} \to 1$ electron bunch is utilized as a driver, $v_\phi \cong v_\mathrm{d}$, where $v_\mathrm{d} \approx c_0$ is the driver velocity [214]. After the transformation, the Poisson equation reads

$$k_\mathrm{p}^{-2}\frac{\partial^2 \phi}{\partial \xi^2} = \left(\frac{n_\mathrm{e}}{n_\mathrm{i}} + \frac{n_\mathrm{d}}{n_\mathrm{i}} - 1\right). \tag{3.29}$$

The differential equation (3.29) contains an unknown $n_\mathrm{e}(\xi)/n_\mathrm{i}(\xi)$-term. According to [214, 215], the continuity equation of the system can be expressed in the QSA, then the $n_\mathrm{e}(\xi)/n_\mathrm{i}(\xi)$-term can be defined as a function of the normalized vector potential of the laser field $a_0 = eA/m_\mathrm{e}c^2$ (see Eq.(3.22)) and the scalar potential ϕ of the plasma

$$\frac{n_\mathrm{e}}{n_\mathrm{i}} = \frac{1 + a_0^2 + (1+\phi)^2}{2(1+\phi)^2}. \tag{3.30}$$

Inserting Eq.(3.30) into Eq.(3.29) yields the differential equation of the wake potential

$$k_\mathrm{p}^{-2}\frac{\partial^2 \phi}{\partial \xi^2} = \frac{n_\mathrm{d}(\xi)}{n_\mathrm{i}} + \frac{1 + a(\xi)^2}{2(1+\phi(\xi))^2} - \frac{1}{2}. \tag{3.31}$$

Equation (3.31) describes the electrostatic potential structure in a cold plasma fluid induced by either an intense laser pulse $a(\xi)$ or a high charge density electron beam $n_{\mathrm{d}}(\xi)$. This differential equation can be solved numerically for $\phi(\xi)$, which provides the axial electric field with $E_{\mathrm{z}} = -E_{\mathrm{wb}}\partial\phi/\partial\xi$. However, due to the assumption of cold fluid plasma, the accuracy of the model is limited to the linear regime when the wakefield has a sinusoidal-like structure [216] and the mildly non-linear regime when the axial electric field takes a "sawtooth"-like shape. Despite its simplicity, this model enables rapid study of various phenomena of plasma-based accelerators in 1D.

Figure (3.6) presents numerical solutions to the differential equation (3.31) in the mildly non-linear regime with a Gaussian-shaped driver beam for LWFA and PWFA. The strong wakefield has a "sawtooth"-like structure and a plasma density of $n_e \approx 10^{17}\,\mathrm{cm}^{-3}$ would yield an electric field gradient of the order of $E_0 \approx 32\,\mathrm{GV/m}$.

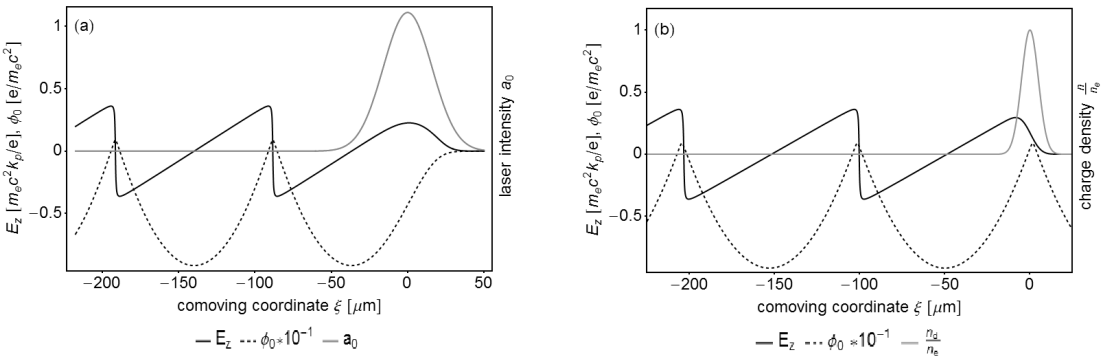

Figure 3.6: **Numerical solutions of the 1D Poisson equation.** Numerical solutions of the 1D Poisson equation for non-linear LWFA (a) and PWFA (b). In (a) and (b), the on-axis electrostatic potential of the wakefield ϕ (black dashed line) and corresponding electric field E_{z} (black solid line) is presented as a function of the co-moving coordinate ξ. The driver beam envelope profiles propagating to the right (laser and electron beam) are overlaid as a solid grey line. In both cases, the wakefield amplitude exhibits a "sawtooth"-like structure.

However, when highly non-linear plasma waves are formed in the bubble or blowout regime, the 1D cold fluid model breaks down due to the strong interaction of the drivers with plasma, which may lead to the violation of the cold fluid assumptions.

Advancements in theoretical work address limitations of early models' based on fluid theory, often for homogeneous plasma backgrounds in one spatial dimension. In the blowout regime, the driver beam creates a cavity depleted of electrons, leaving behind a uniform column of plasma ions. The plasma electrons create a thin electron

sheath surrounded by a slightly disturbed plasma at the boundaries of the blowout. These streams of sheath electrons form the boundaries of the blowout and the radius of the cavity $r = r_\mathrm{b}(\xi)$, which depends on the co-moving coordinate ξ. The plasma ions return these electrons onto the axis in about one plasma wavelength λ_p, closing the cavity behind the driver beam. The electrons cross each other's trajectories and overshoot at the rear of the wakefield. Several attempts have been made to describe this scenario [217–219]. However, the first complete theory was presented in [163], assuming a homogeneous plasma background and approximated form factor for the sheath electrons. A generalised model was recently proposed in [220, 221], and a self-consistent theory was published in [222]. In the generalised model, the plasma source density profile can take an arbitrary shape radially, and the generalised theory provides tools to compute the blowout border and resulting properties of the wakefield; however, it requires external input from PIC simulations on the plasma electron sheath profile.

The derivation of the differential equation starts by considering the current densities of the system in the QSA, which yields, after some algebra, the radial equation of motion of the sheath electrons. A detailed discussion is provided in [220, 221]. Here, the ordinary differential equation is presented, describing the blowout radius

$$A(r_\mathrm{b})r_\mathrm{b}'' + B(r_\mathrm{b})(r_\mathrm{b}')^2 + C(r_\mathrm{b}) = \frac{\lambda(r,\xi)}{r_b} \,, \tag{3.32}$$

where $A(r_\mathrm{b}), B(r_\mathrm{b}), C(r_\mathrm{b})$ are coefficient functions that depend on the integrated ion density and the electron sheath of the cavity [221]. The function $\lambda(r,\xi)$ considers the driver and witness beam integral current densities within the blowout structure. An exciting feature of this differential equation is that when assuming a radial uniform ion density, the ODE reduces to the results provided in [163], and further simplifications lead to phenomenological models such as [218, 219]. Under certain boundary conditions, equation (3.32) can be solved analytically. However, numerical solutions are accurate enough for quick estimates. Solving equation (3.32) produces the function $R_\mathrm{b}(\xi)$, which describes the blowout radius as a function of ξ. Comparison of a semi-analytical solution of the model to a multi-dimensional PIC simulation of PWFA shows good agreement (see Fig.(3.7)) and increases confidence in the model.

Once the radius of the blowout $R_\mathrm{b}(\xi)$ is determined, the longitudinal wakefield of the blowout can be expressed as $E_\mathrm{z} \propto -r_\mathrm{b}r_\mathrm{b}'/2$. In the case of a homogeneous plasma and a spherical blowout with a thin sheath, which is typical for an intense driver beam,

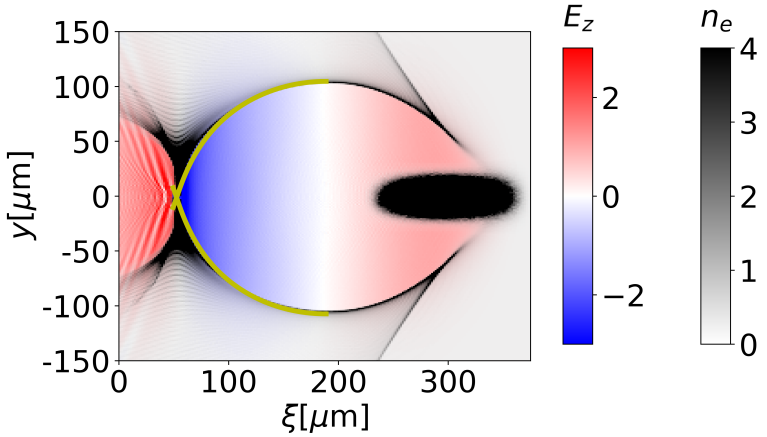

Figure 3.7: **Comparison of PIC simulation and 3D theory.** PIC simulation of a PWFA stage in the blowout regime is compared to the results obtained from the semi-analytical blowout theory. In the simulation, an electron beam moves towards the right (represented in black) into a uniform plasma source (represented in black and white colour scale), with the longitudinal component of the wakefield normalised to the cold wave-breaking field and colour-coded in red and blue. The solution of the system's differential equation (3.32) is a yellow solid line. The analytical solution agrees well with the trajectories of the sheath electrons from the advanced PIC simulation. Adapted from [41, 223]. This work is openly licensed via CC BY 4.0.

a simplified analytical experience can be obtained for the electromagnetic field of the wakefield [223], which reads

$$E_z = \frac{\xi}{2}, \qquad E_r = \frac{\xi}{4} - \lambda(r,\xi) \qquad B_\theta = -\frac{\xi}{4} - \lambda(r,\xi). \tag{3.33}$$

The linear slope of the longitudinal wakefield E and the radial linear focusing magnetic and electric fields are evident from Eq.(3.33), and these equations highlight essential electromagnetic field properties within the blowout structure. The wakefield has a steep axial accelerating gradient and linear focusing fields in the transverse direction in the blowout regime, which allows for the preservation of transverse beam quality.

The underlying assumptions of these theories limit their applicability to specific problems in PWFA. PIC simulations based on first principles can capture the full spectrum of physics involved in PWFA; however, for 2D and 3D simulations, PIC codes are executed on HPC systems and are too expensive for extensive parameter scans. Hence, efforts are made to develop tools to find a compromise between pure analytical expressions and expensive PIC codes. Baxevanis & Stupakov [224] developed a simulation framework in 2D cylindrical geometry employing QSA to model wakefields in the blowout regime. This allows the investigation of simple problems on a typical desktop computer and enables extensive parameter exploration. These reduced model simulations [224, 225] are powerful tools and are used as well in this work for initial exploration (see section (3.3.1) for more details on modelling).

3.2.3 *Limitations and challenges of PWFA*

This section briefly discusses the main limitations and challenges of a PWFA stage. It establishes a basis for designing a stable PWFA stage for ultra-high brightness electron beam generation and beam quality preservation for the PWFA-powered XFEL in chapter (6).

The kinetic energy W_d of an electron driver beam is an energy reservoir that can be transferred to a trailing witness beam. Therefore, electron driver beam energy fundamentally determines the maximum energy gain $W_{w,max}$ of a witness beam in PWFA. In PWFA, the front part of the sawtooth-like longitudinal electric field up to the zero-crossing is decelerating for electrons while the rear of the electric field is accelerating. An electron driver beam will then experience a decelerating electric field

and lose energy to the plasma when driving a wakefield. The total depletion length of the electron driver beam can be estimated with [226]

$$L_{\mathrm{dep,d}} = \frac{m_{\mathrm{e}} c_0^2 \gamma_d}{e|E_{\mathrm{z,\text{-}}}|}. \tag{3.34}$$

Here, $E_{\mathrm{z,\text{-}}}$ represents the peak decelerating field. However, a more interesting question from the accelerator point of view is the energy gain reach of a trailing electron beam. The so-called *Transformer Radio* (TR) describes the energy transfer efficiency from the driver to the witness beam. It considers the accelerating field at the witness beam position and divides it by the peak decelerating electric field [155, 157]

$$T = \left| \frac{E_{\mathrm{z,+}}}{E_{\mathrm{z,\text{-}}}} \right|, \tag{3.35}$$

where $E_{\mathrm{z,+}}$ is the accelerating field experienced by the witness beam.

In a PWFA stage, driver and witness beams are phase-locked due to the highly relativistic energies of beams, and the wakefield does not evolve significantly over the propagation distance. Hence, the maximum energy gain of a witness beam in PWFA reads [155, 157]

$$\Delta W_{\mathrm{w,max}} = W_{\mathrm{d}} \times T. \tag{3.36}$$

This feature is one of the fundamental advantages of PWFA, and it can be leveraged for stable and reproducible accelerator operation. In stark contrast, the driver laser pulse and corresponding wakefield in LWFA exhibit reduced phase velocity. A trapped relativistic witness beam may outrun the wakefield and enter the decelerating phase. This effect is known as the dephasing of the LWFA. For completeness, the effects of laser pulse diffraction and depletion also limit the total energy gain in LWFA. There are various strategies to overcome these fundamental limitations. However, a detailed LWFA discussion is beyond the scope of this work, and the reader is directed to a few selected LWFA review works [126, 176, 207–209] and Ref.[200] for similarities and differences of PWFA and LWFA.

Figure (3.8) demonstrates the depletion of a 1 GeV electron driver beam in a high-density PWFA stage. Fig.(3.8) (b) shows that at the up- and down-ramps, the energy loss is negligible compared to the energy depletion at the uniform part of the plasma stage when the target density is reached, and the blowout is fully formed. This substantial energy depletion is also evident from the increase in relative energy spread in Fig.(3.8) (c). Figure (3.8) (d) displays the longitudinal phase space of the driver beam at the

start of the plasma stage ($z = 0\,\mathrm{cm}$) and after the interaction ($z = 3\,\mathrm{cm}$) in Fig.(3.8) (d) and (e), respectively. It is important to note that the average energy of the electron driver beam after the plasma stage is approximately reduced by a factor of two (see Fig.(3.8) (b)); however, the minimum energy is significantly lower and is close to complete depletion (see Fig.(3.8) (e)). When the energies of those electrons become smaller than the rest-mass energy of the electron ($W \approx 0.511\,\mathrm{MeV}$), they will get non-relativistic and start slipping towards the blowout rear. They may be trapped in the wakefield and partially reaccelerated. Eventually, when electron driver beam energy is completely depleted, it will result in the catastrophic collapse of the blowout structure.

Fig.(3.9) shows a similar scenario as presented in Fig.(3.8); however, now the configuration comprises a driver-witness pair of the same initial energy, and the witness beam is placed at the accelerating phase of the wakefield. The witness beam gains energy at a constant rate in the uniform part of the plasma stage (see Fig.(3.9) (b)). The relative energy spread (Fig.(3.9) (c)) of the witness first decreases after the density upramp and increases linearly along the acceleration in the uniform part of the plasma density due to the development of time-energy correlation (energy chirp) in the longitudinal phase space.

This reduced model simulation shows that the initially 1 GeV witness beam (Fig.(3.9) (d)) can be accelerated to more than 2 GeV (Fig.(3.9) (e)) in a 3 cm plasma stage. This approximately corresponds to an energy increase by a factor of 2 and agrees with the estimation for longitudinally symmetric electron driver beams [37, 227]. Higher energy transfer efficiencies up to $T = 6$ can be obtained by tailoring the current profile of the electron driver beam into a triangular distribution or trains of electron driver beams [157, 210, 226, 228].

However, TR values beyond two do not guarantee high energy gains; the electron driver beam *Head Erosion* can limit energy gain in PWFA. It is less prominent in preionized PWFA and more severe when the electron driver beam ionizes the neutral gas with its unipolar space charge fields. In this self-ionized PWFA scenario, parts of the electron driver beam, which are ahead of the ionization front, will not experience the focusing forces of the plasma and, hence, will expand due to its divergence. It will reduce its density and the ability to field ionize the background gas. Over the propagation distance, the ionization front will gradually move towards the electron driver beam tail,

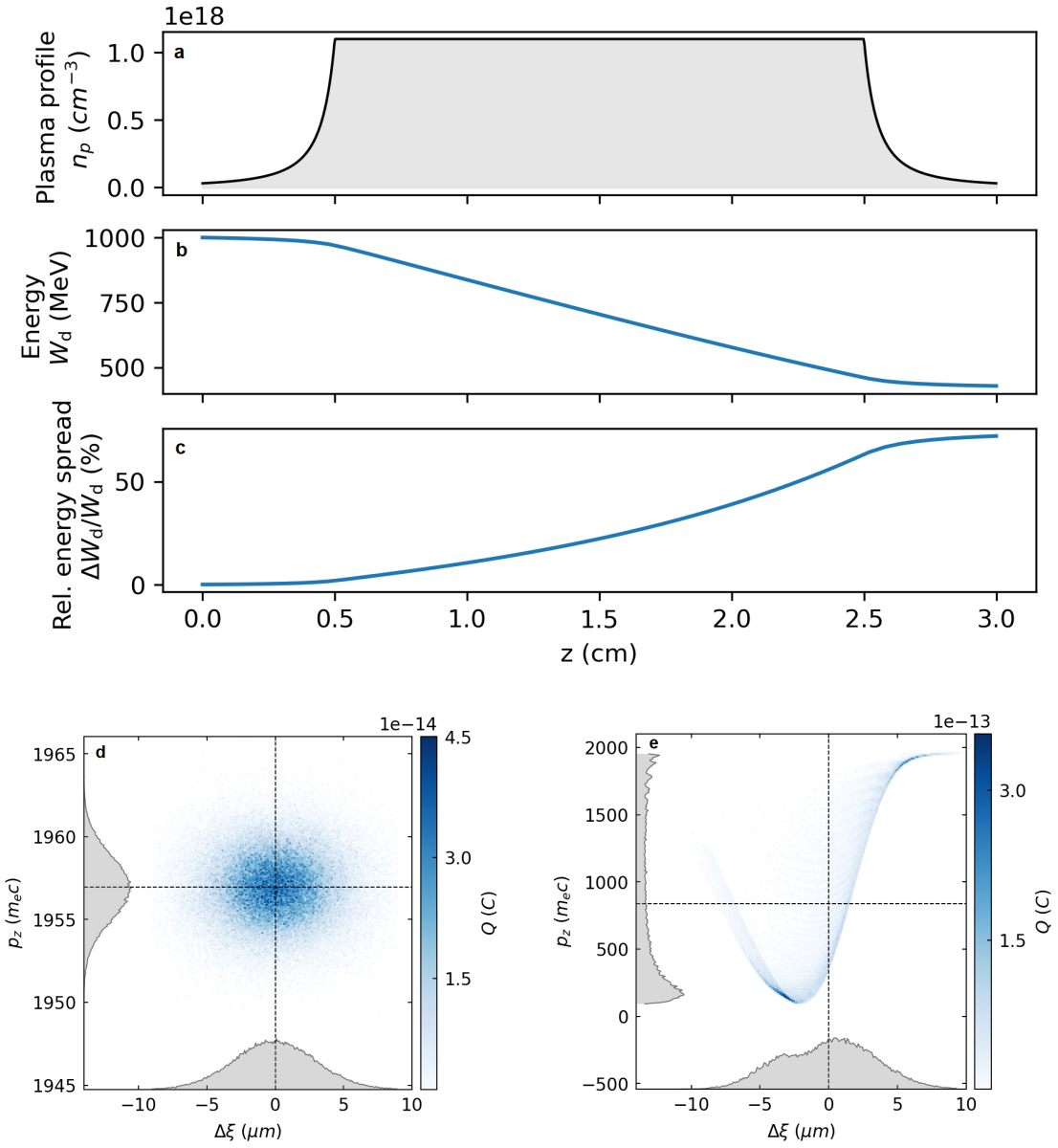

Figure 3.8: **Driver beam depletion in PWFA.** Reduced model simulation of a 3 cm long PWFA stage with the plasma profile in a) powered by a 1 GeV electron driver beam. Average electron driver beam energy (b) and relative energy spread (c) evolution are presented along the PWFA stage. The longitudinal phase space of the electron driver beam at the start and exit of the plasma stage are presented in (d) and (e) with projections of the profiles onto the axis, respectively.

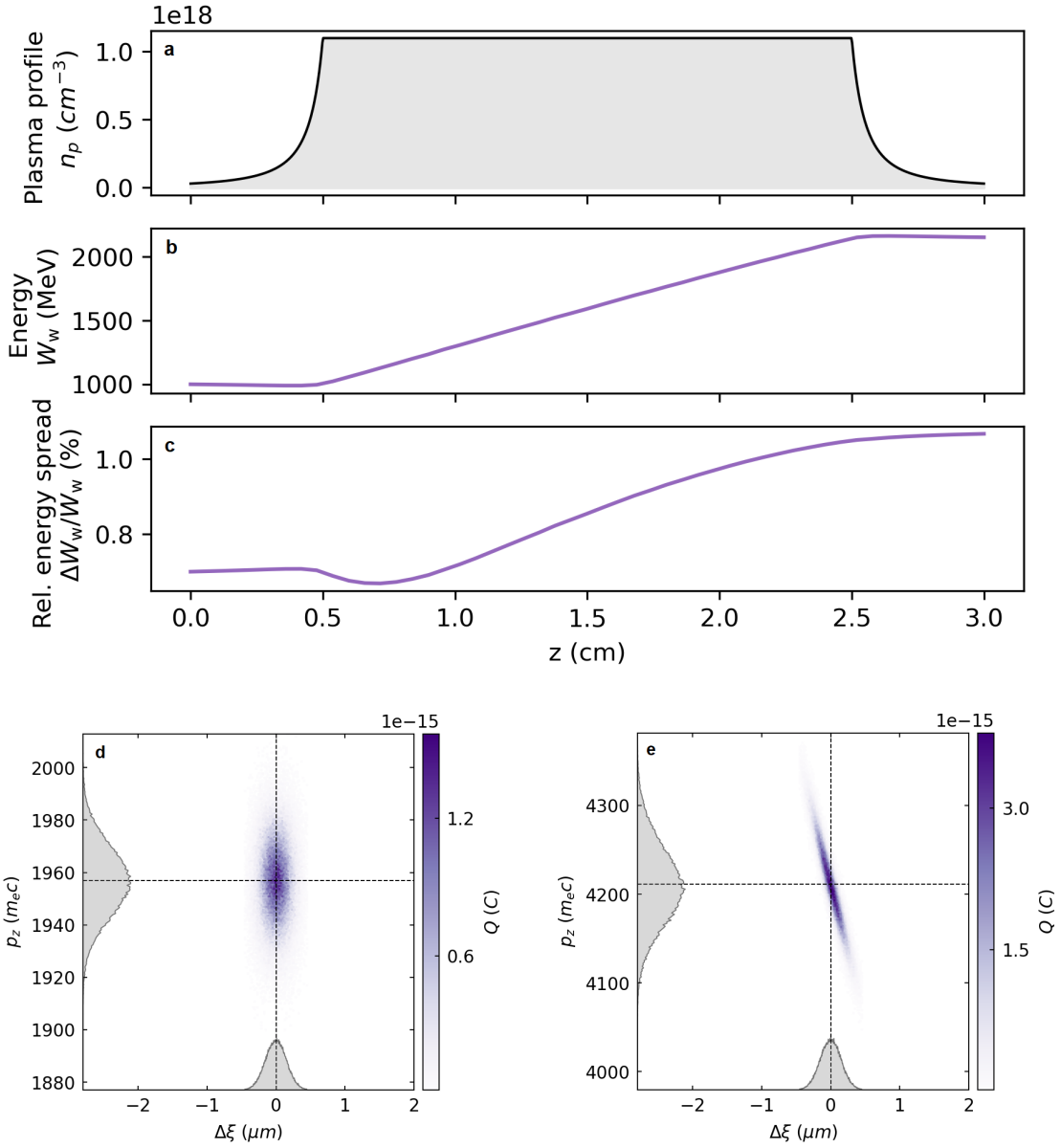

Figure 3.9: **Witness beam energy gain in PWFA.** Reduced model simulation of a 3 cm long PWFA stage with the plasma profile in a) powered by a 1 GeV electron driver beam with a 1 GeV trailing witness beam. Average witness beam energy (b) and relative energy spread (c) evolution are presented along the PWFA stage. The witness beam's longitudinal phase space at the plasma stage's start and exit are presented in (d) and (e) with projections of the profiles onto the axis, respectively.

and less charge from the electron driver beam will contribute to driving the wakefield [229, 230] up to the point when the wakefield collapses.

The *beam-breakup instability* (BBI) has been well-known in conventional rf-based accelerators since 1960 [231–233]. Electron beams in a beam pipe with a transverse offset can excite transverse wakefields, acting on the electron beam back and deflecting the electron beam further from the axis, leading to even stronger transverse wakefields. Such a feedback loop can cause dramatic electron beam instabilities, resulting in electron beam quality degradation or even electron beam loss in the accelerator structure [232, 234, 235]. BBI was regarded as a significant challenge of linear collider efforts [236]. Fortunately, the solution to the problem is comparably simple and was discussed in [237], known as *BNS-dumping*. The BNS-dumping works such that a longitudinal energy chirp is introduced to the electron beam, so the betatron frequencies from head to tail exhibit a betatron frequency chirp. This leads to incoherent oscillation along the electron beam and suppresses the resonance, which drives the instability.

A similar catastrophic effect was discussed by Whittum *et al.* in [238] for electron beams in ion channels, with exponentially growing centroid position of the electron beam concerning the plasma source axis. This so-called *Hose Instability* (HI) can prevent the stable acceleration of a trailing witness beam in plasma-based accelerators and even result in the complete collapse of the blowout structure. However, recent studies by Mehrling *et al.* [239] revealed that the intrinsic deceleration of the electron driver beam naturally mitigates HI in PWFA due to the decoherence of individual slices along the electron driver beam [239]. Follow-up works indicate that correlated energy spread, ion-motion and tailored electron driver beam radius can suppress the growth of HI [239–242]. Fundamentally, the solution to HI mitigation strategy in plasma-based acceleration is BNS-dumping [237], known in rf-based accelerators for decades. Section (3.2.7) highlights that witness beams may also develop HI, but fortunately, a similar mitigation strategy can be employed. This nourishes hope for future plasma-based colliders and stable production of multi-GeV electron beams for PWFA-based XFELs.

3.2.4 *Electron beam injection methods and trapping condition*

Previous sections address the generation and stability of PWFA itself. This section discusses the injection of electron beams into the PWFA for acceleration. Because the

injection process defines the final beam quality, much attention was devoted to novel, innovative injection methods. Numerous publications investigate and optimise various injection methods for the highest beam quality.

Fundamentally, electron beams are either injected externally or internally into the wakefield. The external injection method uses a driver-witness beam pair similar to the configuration in section (3.2.3). The two-bunch configuration in PWFA is either produced directly at the photocathode gun [243] or by inserting a mask into the electron beam path at a suitable position in a dispersion section (for example, at a chicane or a dog-leg section) in the rf-based accelerator [37, 159, 244, 245] and maybe directly produced in a LWFA stage to driver a Hybrid LWFA→PWFA stage [201]. There are a few more permutations [171]. However, it is beyond the scope of this work to discuss it in detail. In principle, this allows the production of witness and electron driver beams with a constant phase relationship at the entrance of the PWFA stage for witness beam acceleration and for probing the wakefield field structure [246, 247].

The external injection method is a versatile configuration as a PWFA R&D platform to study staging physics between PWFA stages towards a plasma-based linear collider or to boost the energy reach of an existing rf-accelerator. However, pointing and misalignment between the driver and witness beam are significant challenges and may result in hose instabilities with detrimental effects on the beam quality. Nevertheless, these challenges are incremental and can be solved long-term, with the first results being reported [243, 248]. Fundamentally, the trailing witness beam quality is limited to state-of-the-art electron beam production techniques. As an initial electron injection method, it requires a pre-existing rf-accelerator infrastructure. It negates the argument of an overall standalone compact particle accelerator.

Therefore, much effort is devoted to internal injection methods to improve the witness beam quality. These methods can be subdivided into electrons injected from the background plasma or directly released inside the blowout structure, for example, by localized ionization of a second gas component.

Background plasma electrons can be trapped through wave breaking when the accelerating gradient of the wakefield in a cold, non-relativistic plasma approaches the wave breaking limit in Eq.(3.24). The plasma wave amplitude in the rear of the plasma wave becomes large enough that plasma electrons enter the accelerating phase of the wakefield and become trapped. When a strong driver, be it a laser or particle beam,

drives a plasma wave, significant energy is transferred to the plasma electrons, which breaks the non-relativistic assumption in Eq.(3.24). A correction term is introduced to account for this effect, and the 1D relativistic wave-breaking limit becomes

$$E_{\mathrm{WB,rel}} \equiv E_{\mathrm{WB}}[\mathrm{V/m}]\sqrt{2(\gamma_\phi - 1)}, \tag{3.37}$$

where $\gamma_\phi = (1 - v_\phi^2/c_0^2)^{-1/2}$ is the Lorentz factor corresponding to the plasma wave phase velocity v_ϕ. In LWFA, wave-breaking can occur naturally when the laser pulse normalised amplitude approaches $a_0 \geq 1$ values, and the laser pulse excites a relativistic plasma wave. As discussed in section (3.2.2), the phase velocity of the wake in LWFA is defined by the group velocity of the driving laser pulse in plasma. Hence, in LWFA, the combination of reduced phase velocity of the wakefield and/or high-amplitude plasma wave [249] promote *self-injection* more easily as opposed to PWFA, where the phase velocity of the plasma wave is $v_\phi \approx c_0$ and self-injection is strongly suppressed due to $\gamma_\phi \gg 1$.

However, a naturally occurring self-injection is a chaotic process. It typically produces electron beams of poor quality and stability [178, 188, 189, 250]. Though, a sharp downward density transition $dn_\mathrm{e}/dz < 0$ (downramp) along the propagation path of the electron driver beam can trigger wave-breaking in a controlled and localized way [162, 251, 252]. A density downramp can be produced by inserting obstacles such as a blade or wire into the supersonic gas jets, generating hydrodynamic shocks with steep density gradients to induce injection in PWFA [205]. These mechanical parts are prone to vibrations, resulting in poor stability. Optically produced density spikes by ionizing a second gas component in plasma [39, 166, 253, 254] or by optically inducing an expanding plasma shock [206] similar to the HOFI plasma channels [149] promise a path towards higher stability. The quality of the electron beams from these approaches is relatively moderate, typically with %-level energy spreads and 1 mm-rad normalized emittances. Nevertheless, these electrons are somewhat "hot" and feature moderate electron beam quality because of the interaction of the electron driver beam with the plasma electrons before the injection event. Further, density downramp injection may be susceptible to electron driver beam asymmetries in the transverse directions. A non-cylindrical electron driver beam will excite asymmetric wakefields, which may impact the downramp injection process and degrade witness beam emittance [255].

The second category of internal injection methods involves the release of electrons at rest directly inside the wakefield. These electrons can be sourced from the ionization

of a plasma species or via the ionization of an additional background gas component. The *low-ionization threshold* (LIT) gas component is usually the blowout medium in many schemes. In contrast, a *high-ionization threshold* (HIT) component is the source of witness beam electrons. Since these particles are released within the blowout while at rest, they must be accelerated rapidly to reach relativistic energies to catch up with the plasma blowout, which moves nearly at the speed of light.

The condition for trapping is based on the constant of motion of particles, which move in a wake potential with a vector potential $\mathbf{A} = A(x, y, \xi)$ and a scalar potential $\Phi = \Phi(x, y, \xi)$. The quasi-electrostatic potential is formed by combining the two potentials with $\psi_{\mathrm{tot}} = \Phi - \frac{v_\phi}{c_0}\mathbf{A}$, resulting in an expression for the axial wakefield as $E_{\mathrm{z}} = -\partial_\xi \psi_{\mathrm{tot}}$ [192, 256] when considering the longitudinal component of $\psi = \Phi - \frac{v_\phi}{c_0}\mathbf{A}_{\mathrm{z}}$. According to [256, 257], the constant of motion can be derived from the Hamiltonian in the nonlinear blowout regime with $H_{\mathrm{f}} = \gamma_{\mathrm{w}} m_{\mathrm{e}} c^2 - v_\phi P_{\mathrm{z}} - e\psi = \text{const}$. The canonical momentum in the longitudinal direction is $P_{\mathrm{z}} = \gamma_{\mathrm{w}} m_{\mathrm{e}} v_{\mathrm{z}}$, where γ_{w} is the the Lorentz factor and v_{z} is the longitudinal velocity of the electrons. Consider an electron initially at rest, released into the wake potential by an arbitrary injection method, with $P_{\mathrm{z}} \approx 0$ and $\gamma_{\mathrm{w}} = 1$. In this case, the corresponding Hamiltonian is given by $H_{\mathrm{i}} = m_{\mathrm{e}} c^2 - e\psi_{\mathrm{i}}$, where ψ_{i} is the initial potential value experienced by the electron. The electrons will slip back towards the peak of the potential $\psi = \psi_{\mathrm{max}}$ at the blowout rear while subjected to the wakefield's accelerating gradient. If $H_{\mathrm{f}} = H_{\mathrm{i}}$ and the electron's velocity v_{z} reaches the phase velocity of the wake v_ϕ such that $P_{\mathrm{z}} = \gamma_{\mathrm{w}} m_{\mathrm{e}} v_\phi$, then these electrons are trapped in the wakefield. Hence, the trapping condition can be derived as follows

$$\begin{aligned} \gamma_{\mathrm{w}} m_{\mathrm{e}} c_0^2 - v_\phi P_{\mathrm{z}} - e\psi_{\mathrm{max}} &= m_{\mathrm{e}} c_0^2 - e\psi_{\mathrm{i}} \\ \gamma_{\mathrm{w}} \underbrace{\left(1 - \frac{v_\phi^2}{c_0^2}\right)}_{\gamma_\phi^{-2}} &= \frac{e}{m_{\mathrm{e}} c_0^2}(\psi_{\mathrm{max}} - \psi_{\mathrm{i}}) + 1 \\ \frac{\gamma_{\mathrm{w}}}{\gamma_\phi^2} &= \Delta\psi + 1 \end{aligned} \tag{3.38}$$

The trapping condition reads then [192, 256, 257]

$$\Delta\psi = \frac{\gamma_{\mathrm{w}}}{\gamma_\phi^2} - 1 = \frac{\sqrt{1 + (P_\perp / m_{\mathrm{e}} c_0)^2}}{\gamma_\phi} - 1, \tag{3.39}$$

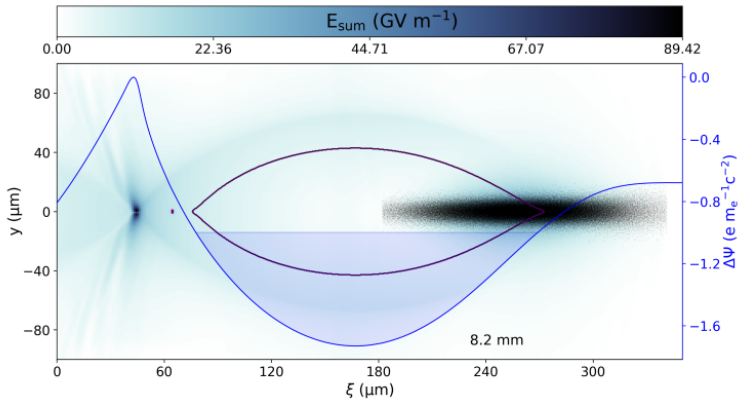

Figure 3.10: **Trapping potential in PWFA.** An electron driver beam (black dots) creates a strong blowout propagating to the right in a hydrogen plasma with a trapped witness beam (purple dots). The geometric sum of the wakefields is presented with colour coding. The blue solid line shows the scalar potential, and the shaded region indicates $\Delta\psi \leq -1$. The purple ellipse highlights the contour line $\Delta\psi = -1$. Electrons released within the purple ellipse can gain sufficient energy to catch up with the wake phase velocity $v_\phi \approx c_0$.

where $P_\perp$ denotes the perpendicular electron momentum. For particles released exactly on axis $P_\perp \ll m_e c_0$ and for ultra-relativistic electron driver beams $\gamma_\phi \gg 1$, then the trapping condition simplifies to

$$\Delta\psi \leq -1. \tag{3.40}$$

Figure (3.10) illustrates an electrostatic wake potential with a shaded region indicating the trapping potential based on Eq.(3.40). Electrons released outside this region will be lost to the background plasma.

The *plasma photocathode* is a versatile method of ionization injection in PWFA [39, 42, 144]. This method enables the release of ultra-cold electrons directly into the wakefield in a localized manner through laser-based tunnel-ionization of a HIT component. Unlike other ionization injection methods in PWFA, where the continuous injection is suppressed by spatially confining the HIT component for localized ionization injection by the wakefield itself or by the electron driver beams [192, 258–261]. In contrast, the injection process in plasma photocathodes is largely decoupled from the electron driver beam properties and the wakefield excitation. This allows for ultra-high-quality electron beam production, which is highly desired towards PWFA-driven hard XFEL. Section (3.2.5) introduces the fundamentals of plasma photocathode.

3.2.5 *Plasma photocathode injection in PWFA*

An unbiased perspective on the advantages and disadvantages of LWFA and PWFA inevitably leads to the emergence of two promising technologies: the Hybrid LWFA→PWFA platform discussed in section (3.2.8) and the innovative *plasma photocathode* injection method in PWFA. The Hybrid LWFA→PWFA scheme was initially proposed in [201], followed by introducing the plasma photocathode two years later in [144]. Today, both technologies have been experimentally demonstrated in the form of Hybrid LWFA→PWFA [262] and plasma photocathode [39] (see chapter (4)). Recent findings indicate that both trusts may be combined [263] (see section (3.2.8)), which is highly promising towards a standalone ultra-high brightness PWFA stage [40].

In PWFA, the plasma photocathode injection method utilizes a laser pulse spatially and temporally synced with a blowout structure for ionization injection. The process is depicted in figure (3.11). A blowout is created in a pre-ionized LIT medium (hydrogen) by an intense electron driver beam, satisfying the trapping condition in Eq.(3.40). However, the electron driver beam is not too intense to ionise a background HIT medium (helium), potentially causing dark current production in the wakefield [146] and hindering clean witness beam injection. To achieve controlled witness beam injection, a laser pulse of moderate intensity ($a_0 \ll 1$) with a few-fs pulse duration is tightly focused to a spot size of typically $w_0 < 10\,\mu$m. The intensity of the laser pulse at focus is just above the tunnel-ionization threshold of the HIT medium. The laser pulse then ionises the HIT medium and liberates helium electrons initially at rest directly inside the blowout structure within the total ionization duration of $\tau_{\mathrm{ion}} \approx 2Z_{\mathrm{R}}c_0^{-1}$. These liberated electrons are subject to the accelerating and focusing fields of the order of GV/m in the blowout. The electrons then slip backwards within the wakefield, become velocity compressed, gain relativistic energies at a rapid rate, and ultimately catch up with the wakefield phase velocity v_ϕ, which travels nearly at the speed of light $v_\phi \approx c_0$.

The trapping position of the witness beam within the blowout can be approximated by evaluating Eq.(3.39) following a similar derivation as in Refs.[192, 256, 257, 264–266], the final trapping position ξ_{f} can be expressed as a function of initial release position and plasma density as [41]

$$\xi_{\mathrm{f}} = -\left(\xi_{\mathrm{i}}^2 + \frac{4\alpha_{\mathrm{t}}}{n_{\mathrm{p}}}\right)^{1/2}, \tag{3.41}$$

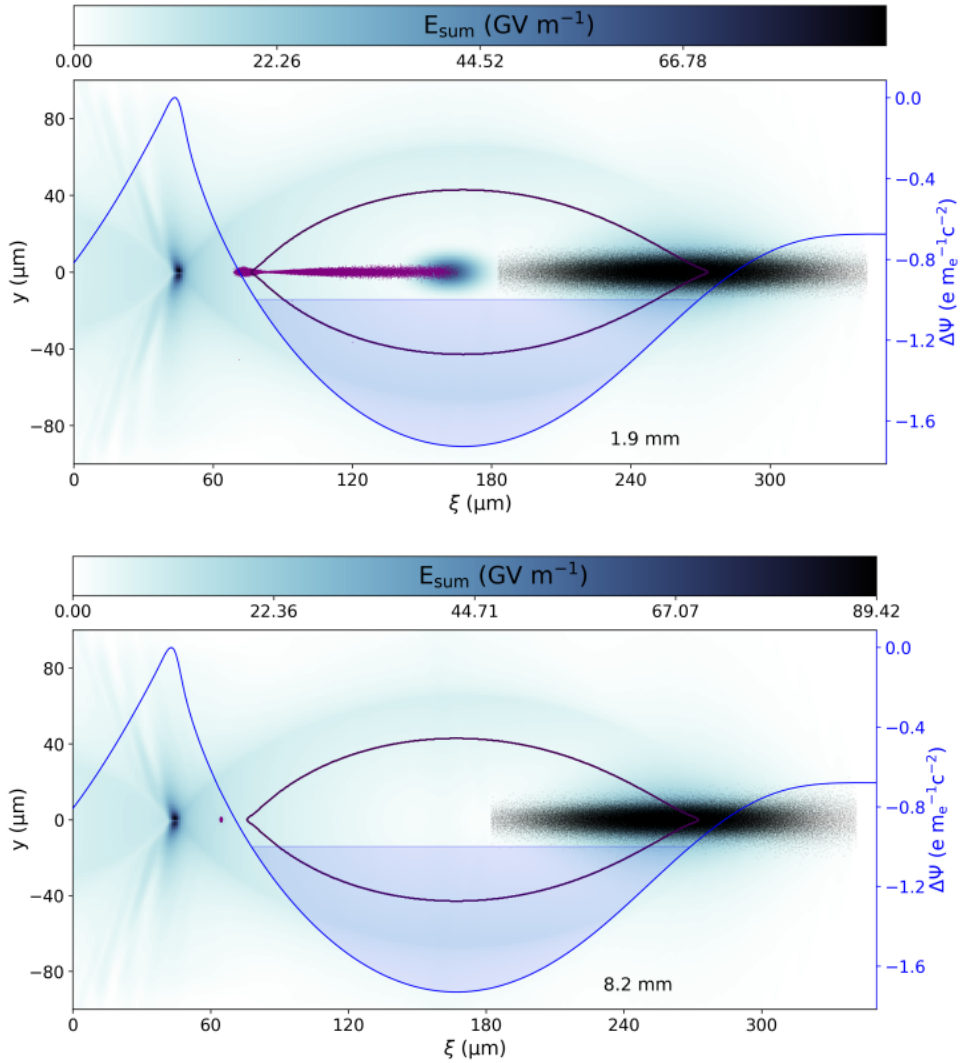

Figure 3.11: **Fully explicit 3D PIC simulation of plasma photocathode injection in PWFA.** An electron driver beam (black dots) creates a strong blowout propagating to the right in a pre-ionized hydrogen plasma of density $n_\mathrm{p} \approx 1.8 \times 10^{16}\,\mathrm{cm}^{-3}$ corresponding to a 250 μm plasma wavelength. A plasma photocathode laser pulse is ionising the background HIT medium (helium) and releasing ultracold electrons (purple dots) in the trapping potential $\Delta\psi$ of the wakefield at the release position ξ_i. These ultracold helium electrons are slipping backwards towards the blowout vertex and are pilling up at the trapping position ξ_f. The final witness beam is visible in the bottom panel. Produced by the author for [41]. This work is openly licensed via CC BY 4.0.

where $\alpha_t = \epsilon_0 m_e c_0^2 e^{-2}$ and ξ_i is the initial release position within the trapping potential. Note that in this representation $\Delta\psi(\xi_\mathrm{i} = 0) = \Delta\psi_\mathrm{min}$ yields the potential minimum. The following discusses witness beam properties in terms of accessible plasma, wakefield and laser parameters.

The study in section (3.1.4) revealed that the ionization of gaseous media happens near the peak of the laser envelope and has a spatial spread when operating just above the tunnel-ionization threshold. This region of ionization results in a spread of release positions $\delta\xi_\mathrm{i}$ within the trapping potential $\Delta\psi(\delta\xi_\mathrm{i})$. Consequently, there is a spread of trapping positions $\delta\xi_\mathrm{f}$ according to Eq.(3.41). The final witness beam duration is determined by the release position ξ_i within the wake potential and the spread of release positions $\delta\xi_\mathrm{i}$. It is important to note that within a given collinear plasma photocathode and PWFA configuration, the shortest witness beams are produced when the HIT electrons are released at the potential minimum [41] (see section (4.2.2)). However, this assumes that the release volume is within the trapping region and that all released electrons forming the trapped witness beam. Chapter (4) shows an opposite scenario where a plasma photocathode laser pulse with a long Z_R releases electrons in perpendicular geometry to the driver propagation direction. In this case, not all released electrons are captured by the passing blowout, which significantly changes the trapping dynamics and quality of the witness beam.

In the laboratory frame, the cigar-shaped ionization volume of the laser pulse, $V_\mathrm{ion,approx}$ (see Eq.(3.23)), is transformed into a pancake-shaped ionization front in the co-moving frame. The shape and duration of the ionization front determine the longitudinal properties of the final witness beam and the spatial volume occupied by the trapped witness beam in the transverse direction. The witness beam's ultra-compact transverse phase space results from the compact spatial volume and cold electrons with negligible transverse momenta, as discussed in section (3.1.4). Initially, these ultra-compact electron beams may not be immune to space charge effects, similar to the rf-based electron guns discussed in section (2.1.4). However, unlike the rf-based photocathode, the blowout's tens of GV/m accelerating gradient rapidly accelerates these electrons to relativistic energies, suppressing space charge degradation effects quickly [144, 145]. This rapid acceleration allows the production of electron beams with

normalized emittances of the order of a few nanometer-radians, with the normalized thermal emittances scaling as [143]

$$\epsilon_{\mathrm{n,th}} = k_{\mathrm{p}} w_0^2 a_0 \frac{3\pi r_{\mathrm{e}}}{4\sqrt{2}\alpha^4 \lambda_{\mathrm{l}}} \left(\frac{13.6\ (\mathrm{eV})}{I_{\mathrm{pot,HIT}}} \right)^{3/2} \tag{3.42}$$

Using the estimated ionisation volume from Eq.(3.23) with $w_0^2 \propto \sqrt{V_{\mathrm{ion,approx}} \lambda_{\mathrm{l}}}$ the thermal emittance can be expressed in terms of the ionisation volume as

$$\epsilon_{\mathrm{n,th}} \propto k_{\mathrm{p}} a_0 \frac{w_0^2}{\lambda_{\mathrm{l}}} \left(\frac{13.6\ (\mathrm{eV})}{I_{\mathrm{pot,HIT}}} \right)^{3/2} \tag{3.43}$$

$$\epsilon_{\mathrm{n,th}} \propto k_{\mathrm{p}} a_0 \left(\frac{V_{\mathrm{ion,approx}}}{\lambda_{\mathrm{l}}} \right)^{1/2} \left(\frac{13.6\ (\mathrm{eV})}{I_{\mathrm{pot,HIT}}} \right)^{3/2}. \tag{3.44}$$

The constants are set to unity in this representation to highlight proportionality clearly. Eq.(3.44) suggests that the choice of laser pulse parameters, ionization volume, plasma density and HIT medium fundamentally determine the reach of the electron beam emittance and, therefore, the transverse quality of the witness beam.

Similarly, the laser pulse and the plasma parameters also define the reach of the minimum energy spread. The *residual energy spread* of the beam is estimated in chapter (5) and Ref.[42], which reads

$$\Delta W_{\mathrm{res}} \approx \frac{2\pi}{5} E_{\xi,\mathrm{trap}} \frac{w_0^2}{\lambda_{\mathrm{l}}}, \tag{3.45}$$

$E_{\xi,\mathrm{trap}}$ is the accelerating field at the witness beam trapping position. Substituting w_0^2 with $w_0^2 \propto \sqrt{V_{\mathrm{ion,approx}} \lambda_{\mathrm{l}}}$ leads to

$$\Delta W_{\mathrm{res,vol}} \propto \frac{2\pi}{5} E_{\xi,\mathrm{trap}} \left(\frac{V_{\mathrm{ion,approx}}}{\lambda_{\mathrm{l}}} \right)^{1/2}. \tag{3.46}$$

Indeed, it is striking that the final witness beam's transverse and longitudinal thermal properties have the same dependency on the ionization volume and laser wavelength in both spatial directions. Equation (3.44) and (3.46) suggest that the overall electron beam quality may profit significantly from reduced ionization volumes.

The ionization volume can be reduced with innovative laser pulse configurations and modes with specialized optics, but keep in mind that reduced ionization volumes result in less charge in the final witness beam. However, it can be compensated by increasing the HIT density. For example, figure (3.12) presents two possible pathways for reducing the ionization volumes of plasma photocathodes in PWFA beyond a standard Gaussian injector laser pulse. The top panel depicts the principles of *Simultaneous Spatial and*

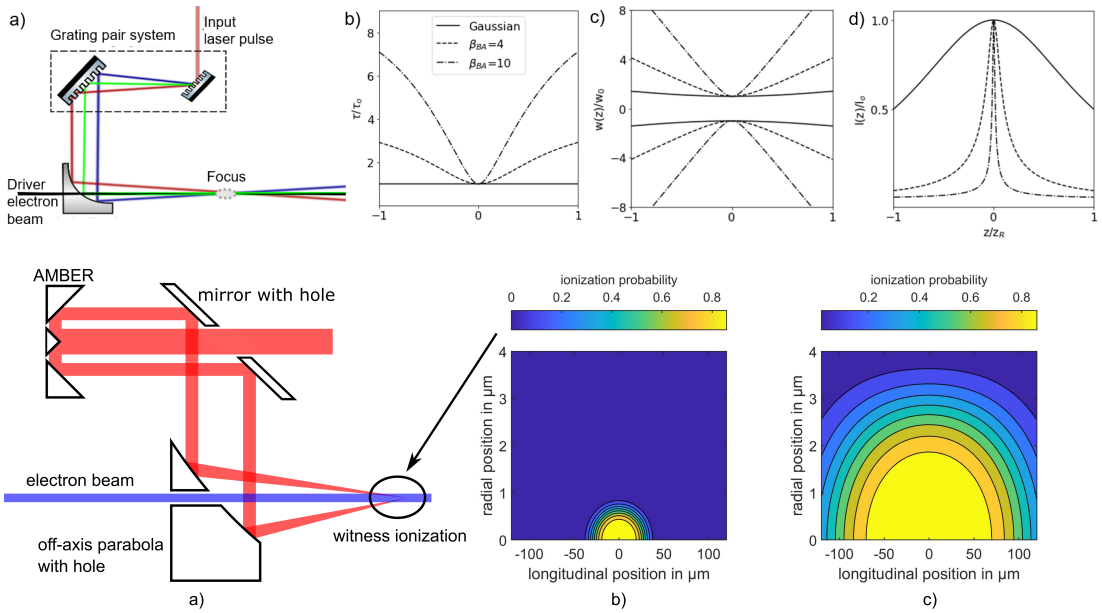

Figure 3.12: **Exotic plasma photocathodes in PWFA.** Simultaneous spatial and temporal focusing (SSTF) (top panels) and Axicon Mirror Beam ExpandeR (AMBER) optics (bottom panels) based plasma photocathode laser pulses towards reduced ionization volumes for ultra-compact phase space witness beams in PWFA. Adapted from [41, 43, 268]. This work is openly licensed via CC BY 4.0.

Temporal Focusing (SSTF) plasma photocathode laser pulse [43], inspired by [267]. The bottom panels display the proposal of reflective optics called *Axicon Mirror Beam ExpandeR* (AMBER), generating a focusing doughnut-shaped laser pulse [268]. Both approaches overcome the limitations of Gaussian laser pulses and enable dramatically reduced ionization volumes.

In section (2.1), 5D and 6D brightness are introduced as useful measures for beam quality characterisation. It takes into account the phase spaces in all three dimensions. For instance, electron beams from plasma photocathodes with multi-kA peak currents and nm-rad normalized emittances may have 5D brightness values of approximately $B_{5\mathrm{D}} \simeq 10^{21}\,\mathrm{A/m^2rad^2}$ [41, 144]. By minimizing the projected energy spread/energy chirp through the innovative energy chirp compensation approach developed in chapter (5), similarly high 6D brightness values can be expected [41, 42, 44].

Summarising, the plasma photocathode injection method in PWFA enables a path towards an electron beam injector, compressor, and accelerator in the same PWFA stage. The multi-kA peak currents and nm-rad normalized emittances of these electron beams may exhibit 5D brightness values many orders of magnitude higher than existing

electron beam sources, whether they are rf- or plasma-based electron sources. This ultra-high 5D brightness reach combined with the dechirper developed in chapter (5) may enable electron beams of ultra-high 6D brightness. The new class of electron beams may unleash the potential of ultra-compact hard XFELs. It may even provide a pathway towards high luminosity plasma-based linear colliders, high-field physics and beyond [41].

3.2.6 *Beam loading and energy spread*

Suppose a witness beam with a sufficient amount of charge is loaded into the accelerating phase of the blowout. Then, the self-wakefields of the witness beam in superposition with the plasma wakefields will change the local accelerating gradient and focusing fields of the blowout. This effect is known as *beam loading* [269, 270]. The accelerating slope may become more uniform along the witness beam, and the overall energy extraction efficiency may increase [37, 269, 270]. Because the electron beam experiences a more uniform accelerating gradient, the projected relative energy spread of the electron beam can be reduced. However, multi-kA peak current electron beams are typically required to load the wakefield in the blowout regime. Figure (3.13) shows the beam loading of a Gaussian-shaped witness beam (purple) in a 100 μm plasma wavelength blowout (grey colour coding) with the final longitudinal phase space (bottom panel) of the witness beam after acceleration to approximately 1 GeV. The projected energy spread of the witness beam is significantly higher than the slice energy spread. The higher projected energy spread is because the longitudinal phase space of the witness beam exhibits non-linear curvatures characterised by the wings at the head and tail of the beam. After all, the accelerating gradient is only uniform at the central part of the beam (see Fig.(3.13) top right). One could attempt to increase the charge of the witness beam further. However, this will overload the wakefield and imprint a positive energy chirp on the witness beam, increasing the projected relative energy spread.

A uniform current profile can result in a flatter accelerating gradient at the witness beam position. Figure (3.14) shows the beam loading of a witness beam with similar parameters as shown in Fig.(3.13), but with a uniform current profile. The accelerating gradient is more uniform, reflected by the longitudinal phase space and the reduced energy spread of the witness beam. The projected relative and the relative slice energy

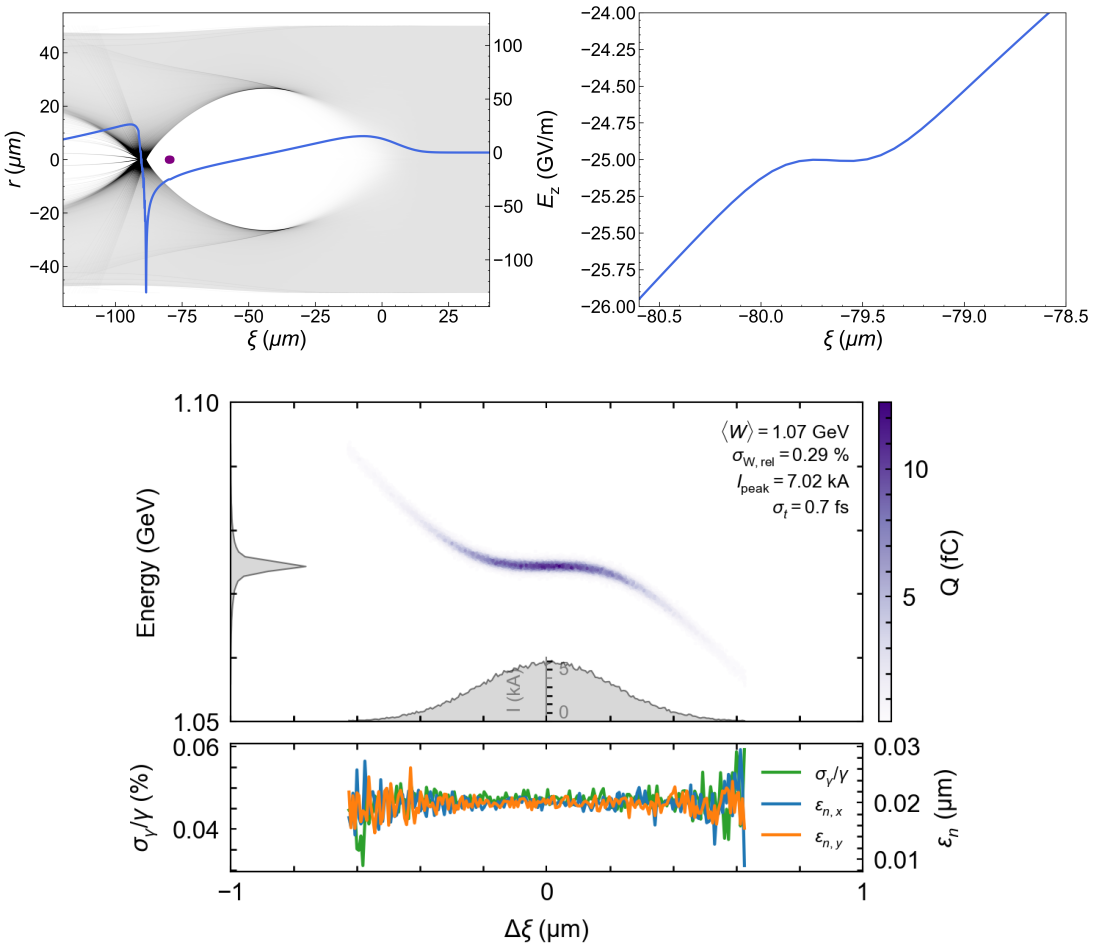

Figure 3.13: **Beam loading in PWFA with a Gaussian-shaped witness beam.** Reduced model quasi-static simulation of a PWFA stage with a Gaussian-shaped witness beam (purple) for optimum beam loading. The top left panel shows the blowout propagating to the right with the overlaid on-axis wakefield (blue solid line). The top right panel zooms in on the wakefield at the witness beam trapping position. The bottom panel presents the final longitudinal phase space of the witness beam with the project spectrum (y-axis) and current profile (x-axis). Further, slice properties such as relative energy spread (green solid line) and normalised emittance (blue and orange solid line) of the witness beam are shown.

spread nearly converge due to the decrease of non-linear components in the longitudinal phase space. A trapezoidal current profile optimized for the corresponding trapping position of the witness beam can lead to a perfectly loaded wakefield [269, 270].

Achieving the desired current profile, peak currents, and exact phase within the wakefield is challenging; however, precisely controlling the witness beam's final energy spread is crucial. Then, slight variations in peak current, current profile, and trapping phase may lead to variations in beam loading and, therefore, impact the final energy spread of the witness beam at the plasma-stage exit. The required witness beams with multi-kA peak currents may have lower quality in normalized emittance due to space charge forces during the initial formation phase when the electron beams are not yet relativistic. This is particularly concerning for internal injection methods where electrons are trapped from rest and are vulnerable to space charge degradation effects.

Additionally, the hose instability mentioned in section (3.2.3) is also a potential issue for the witness beam. A reliable strategy to combat this instability is increasing the witness beam's energy spread and chirp. This approach leads to the decoherence of individual slices along the witness beam and suppresses the catastrophic feedback loop through BNS-dumping [237]. It is worth noting that hose instability is a concern when aiming for ideal beam loading to minimize the energy spread of witness beams. While there are other types of beam-plasma instabilities, like two-stream instability and Weibel instability which can also occur when aiming for perfectly beam loading the wakefield [271]. However, a detailed discussion is outside the scope of this work, but potentially, for some of these instabilities, a BNS-dumping type of suppression may be a viable mitigation strategy as well.

In conclusion, taking advantage of beam loading is a potential pathway for minimizing the energy spread of electron beams. However, electron beam quality degradation may compromise witness beam emittances, which may become incompatible with producing ultra-high 6D brightness beams for hard XFEL applications. There are strict requirements for energy spread and emittances for hard XFEL systems, as discussed in sections (2.2.3) and (2.2.4). This work reevaluates strategies for minimising energy spreads of ultra-high 5D brightness electron beams in chapter (5), which results in the invention of a new energy chirp compensation approach specifically addressing ultra-high 5D brightness electron beams.

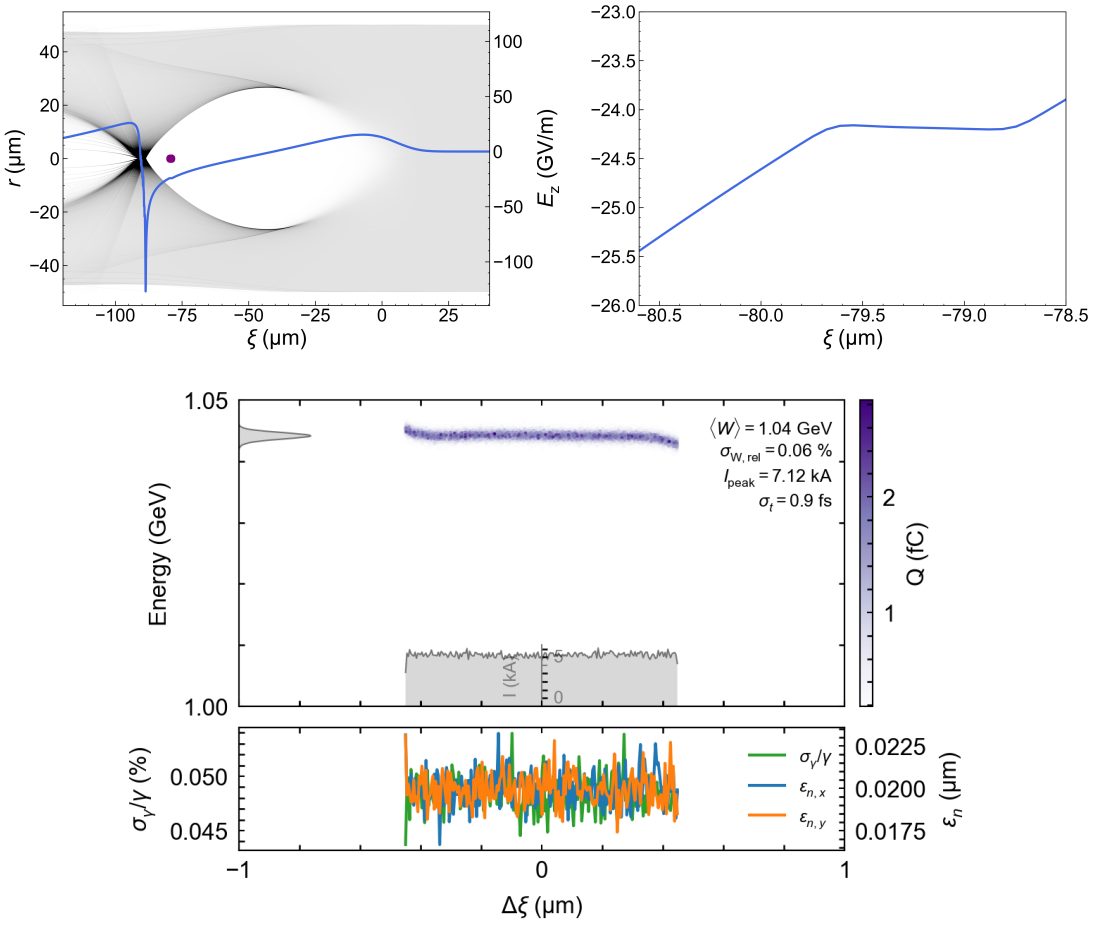

Figure 3.14: **Beam loading in PWFA with a uniform-shaped witness beam.** Quasi-static simulation of a PWFA stage with a uniform-shaped witness beam (purple) for optimum beam loading. The top left panel shows the blowout propagating to the right with the overlaid on-axis wakefield (blue solid line). The top right panel zooms in on the wakefield at the witness beam trapping position. The bottom panel presents the final longitudinal phase space of the witness beam with the project spectrum (y-axis) and current profile (x-axis). Further, slice properties such as relative energy spread (green solid line) and normalised emittance (blue and orange solid line) of the witness beam are shown.

3.2.7 *Electron beam quality preservation in PWFA*

The ability to generate and accelerate ultrahigh brightness beams with nm-rad normalized emittances in PWFA is crucial for advanced applications like XFELs or plasma-based linear colliders. However, maintaining the beam quality during the acceleration within the plasma stage and post-plasma transport lines towards the application is becoming increasingly important. For instance, an acceptable normalized emittance growth on the order of few 0.1 μm-rad for 1.0 μm-rad emittance beams does not cause significant issues. However, few 0.1 μm-rad emittance growths would be unacceptable for beams with few tens of nm-rad initial emittance as promised by plasma photocathode.

In multi-stage scenarios, which may consist of hundreds of plasma stages, even a few nm-rad emittance growths per stage can accumulate into unacceptable overall emittance growth. Lioville theorem states that the emittance of a particle beam remains invariant under linear transformation as long as linear focusing forces are present. In the blowout regime, PWFA provides the desired linear focusing forces, though remember that this is not ensured in the linear regime of PWFA. However, various effects may contribute to non-linearity, leading to emittance dilatation. The following discusses the effects of relevant emittance degradation in PWFA in the blowout regime. From this, conclusions are derived for designing a PWFA stage for the XFEL application in chapter (6). Note that in LWFA, the driving laser pulse transverse matching will have different dependencies, as discussed in [150].

Hill's equation (2.10) governs the transverse dynamics of a charged particle beam in a focusing plasma ion column with uniform density, and it is assumed that no plasma electrons are present [52]

$$\frac{1}{2}(s)\beta(s)\beta'' - \frac{1}{4}\beta'(s)^2 + k_\beta(s)^2\beta(s)^2 = 1, \tag{3.47}$$

where $k_\beta = k_\mathrm{p}/\sqrt{2\gamma_\mathrm{rel}}$ is the focusing constant in plasma. Note that γ_rel has no s dependency. However, γ_rel can generally increase or decrease during the propagation. For simplicity, γ_rel is assumed constant along the propagation. When the beam is matched to the immobile ion background of the plasma source. The emittance-driven divergence of the electron beam is precisely compensated by the linear focusing forces of the ion column acting on the electron beam. Therefore, the electron beam size is non-evolving in s. Mathematically, this means in Eq.(3.47) that the β function is non-evolving in s,

such that $\beta'(s) = \beta''(s) = 0$. Applying this consideration to Eq.(3.47) gives the matched Twiss parameters

$$\beta_{\mathrm{m}} = \frac{\sqrt{2\gamma_{\mathrm{rel}}}}{k_{\mathrm{p}}} \ , \ \alpha_{\mathrm{m}} = -\frac{\beta'(s)}{2} = 0 \ , \ \gamma_{\mathrm{m}} = \frac{1}{\beta_{\mathrm{m}}}. \tag{3.48}$$

The matched beam size is derived by rearranging $\sigma_{\mathrm{m}}^2 = \epsilon_{\mathrm{n}}\beta_{\mathrm{m}}/\gamma_{\mathrm{rel}}$ and substituting β_{m} in Eq.(3.48)

$$\begin{aligned} \frac{\sigma_{\mathrm{m}}^2\gamma_{\mathrm{rel}}}{\epsilon_{\mathrm{n}}} &= \frac{\sqrt{2\gamma_{\mathrm{rel}}}}{k_{\mathrm{p}}} \\ \sigma_{\mathrm{m}} &= \left(\frac{2}{\gamma_{\mathrm{rel}}}\right)^{1/4}\left(\frac{\epsilon_{\mathrm{n}}}{k_{\mathrm{p}}}\right)^{1/2}. \end{aligned} \tag{3.49}$$

An electron beam is regarded as *mismatched* when the Twiss parameters deviate from Eq.(3.48). The degree of mismatching can be quantified with the mismatch parameter [272]

$$\mathcal{M} = \frac{1}{2}\left(\tilde{\beta} + \tilde{\gamma} + \sqrt{(\tilde{\beta} + \tilde{\gamma})^2 - 4}\right), \tag{3.50}$$

where $\tilde{\beta} = \beta/\beta_{\mathrm{m}}$, $\tilde{\alpha} = \alpha - \alpha_{\mathrm{m}}\tilde{\beta}$, and $\tilde{\gamma} = (1 + \tilde{\alpha}^2)/\tilde{\beta}$ are the normalized errors of the Twiss parameters. Eq.(3.50) returns unity, $M = 1$, for a perfectly matched electron beam and gives $M > 1$ for a mismatched electron beam. Degradation of electron beam emittance caused by mismatched electron beam slices can be elegantly expressed in terms of the mismatching parameter as [273, 274]

$$\frac{\epsilon_{\mathrm{f}}}{\epsilon_{\mathrm{i}}} = \frac{1}{2}\left(\mathcal{M} + \frac{1}{\mathcal{M}}\right), \tag{3.51}$$

where ϵ_{i} and ϵ_{f} are the initial and final emittance, respectively. A matched electron beam to the immobile ion background with zero energy spread will remain matched, and no emittance growth will occur. However, if the electron beam exhibits a finite energy spread δ, even if the central energy is matched to the immobile ion background, different energy slices of the beam will rotate at different rates in the transverse phase space due to the energy-dependent focusing forces [275–277]. It will lead to projected emittance growth because of the increased phase space occupied by the electron beam. Figure (3.15) illustrates this *chromatic dephasing* scenario. The left panel shows the transverse phase space of the electron beam at the start with a finite energy spread. Different energy slices rotated at different rates after the electron beam propagated through the plasma source, increasing the transverse phase space area.

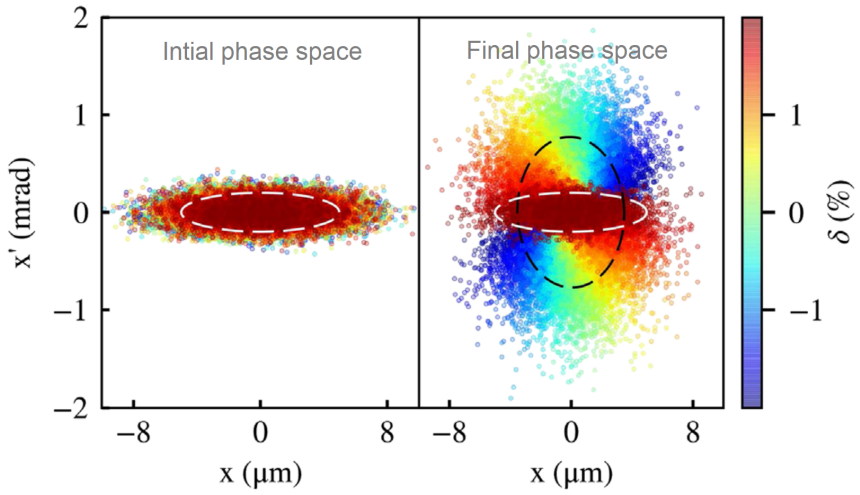

Figure 3.15: **Emittance growth due to chromatic dephasing.** The initial phase space of the electron beam (left panel) and after the electron beam is fully dephased (right panel). The white and black dashed-lined ellipses indicate the initial and final rms phase space ellipses. The area of the final emittance is four times larger compared with the initial phase space ellipse. Adapted from [277]. This work is openly licensed via CC BY 4.0.

The distance over which chromatic dephasing saturates leading to final emittance ϵ_{f} is estimated with [275]

$$L_{\mathrm{dc}} = \frac{2\pi\beta_{\mathrm{m}}}{\sigma_{\mathrm{W}}}, \tag{3.52}$$

where σ_{W} is the r.m.s relative energy spread. The expected emittance growth as a function of the chromatic amplitude and relative energy spread is [273, 274]

$$\frac{\Delta\epsilon^2}{\epsilon^2} = \mathcal{W}_{\mathrm{ca}}^2\sigma_{\mathbf{W}}^2, \tag{3.53}$$

and the chromatic amplitude $\mathcal{W}_{\mathrm{ca}}$ [278] is

$$\mathcal{W}_{\mathrm{ca}} = \sqrt{\left(\frac{\partial\alpha}{\partial\delta} - \frac{\alpha}{\beta}\frac{\partial\beta}{\partial\delta}\right)^2 + \left(\frac{1}{\beta}\frac{\partial\beta}{\partial\delta}\right)^2}. \tag{3.54}$$

Eq.(3.52), (3.53), and (3.54) highlight the significant impact large energy spreads can have on the emittance growth resulting from mismatching of the electron beam.

Additionally, if a relativistic electron beam is not aligned with the plasma source's principal axis, the restoring force of the ions will attract the electron beam towards the axis and cause it to perform betatron oscillation. During betatron oscillation, different parts of the electron beam will experience different focusing fields, which can lead to decoherence of the beam's phase space and enlarge the area of the phase space ellipse.

This can result in emittance growth, similar to decoherence due to large energy spreads. The impact of misalignment may be more severe on electron beams injected at relativistic energies into the blowout than on electrons injected at rest via the plasma photocathode method because the betatron amplitude of non-relativistic electrons rapidly dumps with increasing beam energy (see section (4) and (4.2.2)).

Indeed, preservation of transverse beam quality in plasma-based acceleration arising from large energy spreads and misalignment is a challenging task and an active field of research with various strategies [273–276]. The electron beam quality can degrade inside the plasma stage, during extraction from the plasma stage, and along the beam transport line. Beam-loading strategies discussed in section (3.2.6) can be employed to reduce the energy spread of the electron beams, which can mitigate emittance growth due to chromatic decoherence if adequately matched to the immobile ion background of the plasma stage. However, at low energy spread levels, hose instabilities discussed in sections (3.2.3) and (3.2.6) may become an issue for the witness beams.

On the one hand, energy spread and energy chirp minimization are required to preserve electron beam quality during the acceleration, extraction from the plasma stage and transport. On the other hand, small energy spread in an electron beam may promote catastrophic instabilities, resulting even in complete electron beam loss. The novel dechirping approach in chapter (5) attempts to resolve this dilemma by maintaining some level of energy chirp for stability and reducing it in a controlled manner directly inside the plasma stage for beam quality preservation downstream of the PWFA stage. Crucially, it also allows dealing with electron beams of ultralow emittance and ultrahigh brightness.

3.2.8 *Hybrid LWFA→PWFA*

This section aims to provide an in-depth review of the Hybrid LWFA→PWFA concept, which is highly relevant to PWFA-driven FELs. The figure (3.16) depicts a schematic representation of the Hybrid LWFA→PWFA concept, highlighting the plasma photocathode injection in the PWFA stage.

Experimental work on PWFA R&D was previously conducted exclusively at rf-based facilities like SLAC FACET,AWA, ATF, AWAKE CERN, DESY, INFN and others. As such, progress in PWFA advancement has been limited by the availability of beam time

at these large-scale facilities. On the other hand, LWFA facilities routinely produce high-charge relativistic electron beams [197, 199, 279], which have increased significantly over the years [200] with electron beams capable of driving a PWFA stage. This progress is arising from the wider availability of high-power laser system facilities capable of LWFA.

The Hybrid LWFA→PWFA approach, which employs electron beams from LWFA to drive a PWFA in a second plasma stage, has recently gained popularity. Computer simulations in [201] indicated that a two-electron beam configuration temporarily separated by sub-picoseconds from LWFA could be utilized to drive a double-bunch PWFA stage and increase the energy of the trailing bunch by a factor of two. This is similar to the early linac-based energy-doubling PWFA experiments at SLAC [164]. Some experimental results suggest that driving a PWFA with the electron beams from LWFA can occur naturally [279–282], even in a single plasma stage, due to dephasing and laser pulse diffraction [283]. The hybrid LWFA→PWFA approach uniquely offers new capabilities, such as operating the PWFA at higher densities and accelerating gradients, and opens avenues for increased PWFA R&D capacities.

In recent years, several experimental works underpinned the advantages of the Hybrid LWFA→PWFA approach [262]. The first collective deceleration of the electron driver beam in a well-separated LWFA and PWFA stage was reported [202], indicating that the LWFA beams can be sufficiently dense to drive a subsequent PWFA stage at high plasma densities. In [204], the authors demonstrated PWFA at plasma densities of the order of $n_\mathrm{p} \approx 10^{19}\,\mathrm{cm}^{-3}$ with 100's of GV/m accelerating gradients. The high plasma density also allowed the use of shadowgraphy diagnostics [204] to image the PWFA plasma wave. The probing of the PWFA stage with laser pulses was attempted before at FACET for understanding plasma evolution [284]; however, at comparably low plasma density and with tens of femtosecond laser pulses, which prohibited direct observation of the plasma waves. However, the results in [204] at *Ludwig-Maximilians-Universität München* (LMU) reported direct observation of ion motion in the PWFA stage [204]. This was theoretically predicted in PWFA [285] and eventually directly observed in the Hybrid LWFA→PWFA platform. The production of nC-class electron beams from LWFA [197] allowed the realization of Hybrid LWFA→PWFA at the *Helmholtz-Zentrum Dresden Rossendorf* (HZDR). The same laboratory demonstrated the acceleration of witness beams to ≈100 MeV energies in a preionized plasma source [203]. Shortly after,

density downramp injection was demonstrated via hydrodynamic shock injection in the PWFA [205].

The Hybrid LWFA→PWFA platform has the significant advantage of offering an intrinsically synchronized laser and electron beams due to the same laser system powering the LWFA and PWFA stages [144]. This simplifies the investigation of PWFA physics with laser-based diagnostics, such as shadowgraphy [204, 286] and optical injection methods with high stability due to the reduced timing jitter [206]. Recently, a signature of plasma photocathode injection in Hybrid LWFA→PWFA was observed [263] at the HZDR within the Hybrid Collaboration. It is noteworthy that if the Hybrid LWFA→PWFA platform powers an ultra-compact XFEL, the intrinsic synchronisation argument can be extended to X-ray pulses from XFELs, electron beams and laser pulses as well, which can be advantageous for the pump-probe type of experiments.

In conclusion, the Hybrid LWFA→PWFA approach is an exciting research area offering several advantages for PWFA R&D, and significant progress was made in recent years [262]. It also enables new capabilities and modalities for the investigation of PWFA physics. The next generation of Hybrid LWFA→PWFA may involve controlled in and out-coupling between the LWFA and PWFA stages with dedicated electron beam transport and manipulation capabilities, significantly advancing the reliability and applicability of the Hybrid LWFA→PWFA for demanding applications, such as XFELs. Overall, this novel direction of PWFA is promising and may open the path towards "truly" compact PWFA, XFELs and other light sources [40, 44].

3.3 NUMERICAL METHODS OF PLASMA-BASED ACCELERATION

A plasma-based accelerator comprises a plasma system containing approximately $N \approx 10^{10}$ particles that interact with each other in the co-moving frame. Obtaining an analytical solution in the 6D phase space is challenging without significant simplifications, as discussed in section (3.2.2). Solving Maxwell's equation for $N \approx 10^{10}$ particles would be difficult or even impossible with the present computing capabilities. Therefore, various numerical techniques are applied to represent the plasma system as accurately as possible while keeping the computational demand manageable. The following two sections will discuss the numerical methods used in this work, which are part of a sophisticated start-to-end simulation framework. The S2E framework includes handshakes between

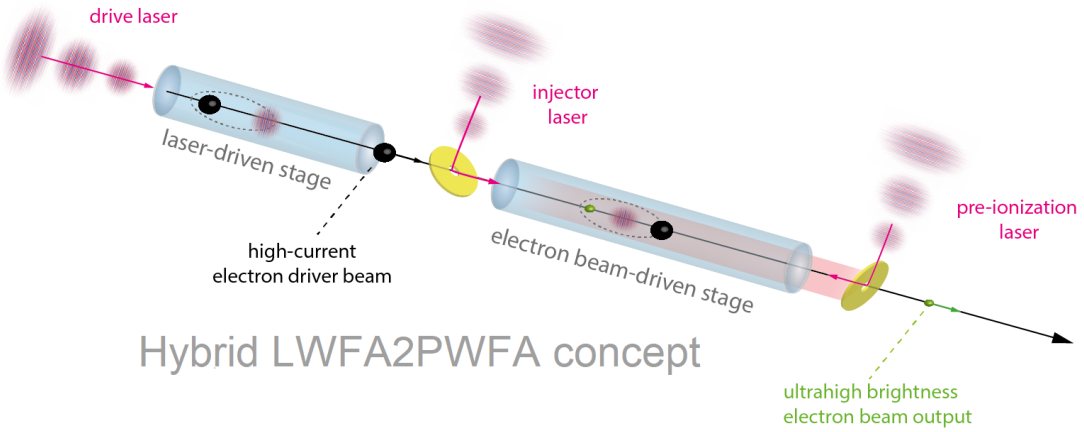

Figure 3.16: **Schematic representation of the Hybrid LWFA→PWFA concept.** The LWFA stage (top left) produces a high-charge electron driver beam, which drives a subsequent PWFA (bottom right) suitable for plasma photocathode injection. Produced by the author for [200] and adapted for the thesis. This work is openly licensed via CC BY 4.0.

plasma-stage simulations, electron beam transport lines and FEL modelling (see also section (2.3.1)).

3.3.1 *Particle-In-Cell code*

The basic approach behind Particle-In-Cell codes relies on decreasing the number of particles without altering the physical system. One efficient way to achieve this is to represent many real particles by *macroparticles* and represent the fields on a grid. The system's time evolution is computed by discrete time steps $\Delta\tau$. This results in a significant reduction in computing time. Nowadays, PIC codes are widely established and irreplaceable in the plasma-based accelerator community. This work performs most production runs with the fully explicit electrodynamic and relativistic PIC-code VSim [287] on a 3D Cartesian grid. Exploration studies are performed with the cylinder symmetric FBPIC code [142] and reduced models discussed in section (3.3.2). Fig.(3.17) outlines the basic principle of a PIC-code algorithm, which consists of four steps.

The standard *Yee finite-difference time-domain* (FDTD) solver is used in VSim on a Cartesian grid. The Courant-Friedrichs-Lewy condition dictates the time step size $\Delta\tau_{\mathrm{CFD}} = a\Delta r/c$ [289], where the spatial cell size in the three dimensions is

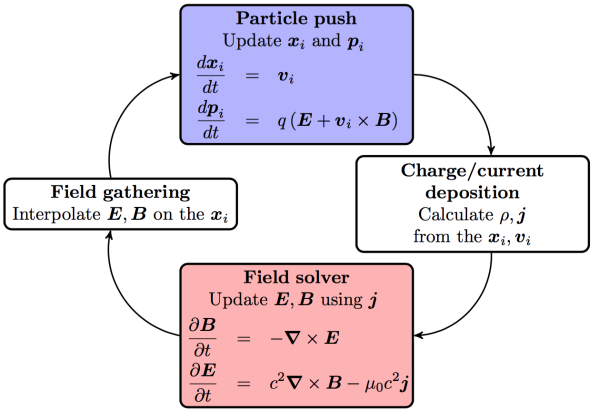

Figure 3.17: **PIC-code cycle.** The process of a PIC-code cycle can be broken down into four steps. First, the currents are deposited on the mesh points or grid. Second, the self-consistent fields are solved on the grid points using the complete set of Maxwell's equations. Third, the new fields are interpolated from the grids to the particles. Finally, using the Lorentz equation, a new particle position is computed. This loop represents a single-time step in the simulation, denoted by $\Delta\tau$. Adapted from documentation in [288]. This work is openly licensed via CC BY 4.0.

$\Delta r = (\Delta x^2 + \Delta y^2 + \Delta z^2)^{1/2}$ and $a < 1$ needs to be ensured for numerical stability. The optimized time step suggested in [290] is utilized for numerical stability in all simulations performed in this work. The Yee FDTD field solver discretizes the spatial and time derivatives in the Maxwell equations, which can result in spurious numerical dispersion, producing unphysical *Numerical Cerenkov* (NC) radiation [290]. When this NC radiation interacts with the relativistic electron beam, it may cause numerical emittance growth [291]. The emittance growth can be a few 100 nm-rad and more. Therefore, significant efforts are dedicated to minimizing numerical artefacts and NC radiation in VSim with its "perfect dispersion" module [292], and a split field approach is employed for general noise and stray field reduction. This allows high-fidelity modelling of the advanced PWFA stages for the PWFA-driven FEL in chapter (6).

In contrast, FBPIC solves the fields in the spectral space where Maxwell's equations can be integrated analytically in time. It makes the solver intrinsically dispersion-free in all directions and mitigates NC radiation. However, FBPIC is a cylinder-symmetric code suitable for problems with strict cylinder symmetry and is employed for specific problems. In summary, both PIC codes are used complementary in the context of this work jointly with reduced model simulations presented in section (3.3.2).

3.3.2 *Reduced models of plasma-based accelerators*

Much of this work's initial exploration of parameters is based on various configurations of reduced models. These reduced model simulations employ QSA or a variation in 1D, 3D, or quasi-3D configuration (cylinder symmetry) or treat the interaction between particle beams and wakefields semi-analytically, such as the model in chapter (5) developed by the author for [42]. The primary motivation for this method is to find a balanced approach between purely analytical expression and fully explicit PIC codes, which require significant computing resources. The reduced model presented in [224] is a simulation framework that utilizes QSA to model wakefields in the blowout regime in 2D cylindrical geometry. Even though the model does not solve the equations self-consistently, it shows good agreement in its implementation in *Wake-T* [225] with the cylindrical PIC code FBPIC [225]. However, reduced models are helpful for exploration and initial studies, but production runs are performed with fully explicit, highly-optimized 3D PIC codes for high-fidelity results.

3.4 DISCUSSION

This chapter discussed the fundamental principles of plasma-based accelerators and their applicability for designing a stable PWFA stage for ultra-compact XFELs. Various electron injection methods are also reviewed. The plasma photocathode injection method can produce high-quality electron beams that meet the stringent requirements of FELs, potentially down to hard XFELs. The method can deliver witness beams with nm-rad normalized emittances at kA peak currents and 5D brightness order of magnitude higher than state-of-the-art. However, witness beams accelerated in plasma-based accelerators inherently develop time-energy correlation (energy chirp) in their longitudinal phase space. Beam loading methods to suppress the accumulation of energy chirp may not be suitable for producing the highest 6D brightness witness beams due to non-negligible space charge forces. Therefore, energy chirps and resulting projected energy spread can significantly challenge beam quality preservation during the plasma stage and beam transport line and even suppress the FEL interaction. As a result, innovative solutions are required, particularly for dechirping ultra-high brightness witness beams expected

from plasma photocathodes in PWFA. The following chapters will present experimental and conceptual breakthroughs, opening the path towards PWFA-driven hard XFELs.

4

DEMONSTRATION OF PLASMA PHOTOCATHODE INJECTION AND PROSPECTS

This chapter discusses the prime results of the E-210 proof-of-concept experiment of the plasma photocathode injection scheme at the SLAC FACET facility. The primary goal of the E-210 experiment and collaboration was to demonstrate the feasibility of the plasma photocathode injection scheme. Therefore, the injection laser geometry of 90° compared to the collinear geometry discussed in section (3.2.5) was a strategic decision to simplify experimental conditions. The SLAC FACET facility is a testing ground for plasma photocathode injection, which is no coincidence. The facility provided the required combination of high-current, relativistic electron beams for driving strong wakefields in the blowout regime, a synchronized laser system for preionization and plasma photocathode laser capability and extensive PWFA R&D experience. The main goal of this chapter is to report on the key findings of the E-210 experimental programme relevant to PWFA-powered XFELs and to elaborate on future direction in the second half of the chapter.

4.1 A PATH TOWARDS HIGH-BRIGHTNESS ELECTRON BEAMS

This section focuses on the results of the E-210 experiment at SLAC FACET and reports on the key findings. Demonstrating plasma photocathode feasibility marks an essential milestone towards generating ultra-high brightness electron beams required for high-gain PWFA XFEL. First, an overview of the experiment is provided, and then a novel plasma-based diagnostic is introduced. In the second half of this section, experimental results are presented, and the limitations of the setup are discussed. For

more technical details, the reader is guided towards the leading publication [39] and other follow-up works [38, 40, 41].

4.1.1 *Overview of the E-210 experiment at SLAC FACET*

The E-210 experiment at SLAC FACET was groundbreaking, incorporating several innovations to implement the plasma photocathode approach discussed in section (3.2.5). The primary objective of the experiment was to demonstrate the feasibility of the plasma photocathode injection in PWFA. It demanded simultaneous management, coordination, and synchronization of varying length and time scales at the *interaction point* (IP) in sector 20 of the SLAC FACET linac. Figure (4.1) presents a schematic representation of the IP of the experiment. For instance, the SLAC FACET linac, spanning kilometres in length, generated a relativistic electron beam with a charge up to $Q \approx 3.2\,\mathrm{nC}$ from a thermionic electron gun, compressed by a magnetic chicane to a longitudinal length of $\sigma_{\mathrm{z,rms}} \approx 20 - 40\,\mu\mathrm{m}$ at a repetition rate of up to $10\,\mathrm{Hz}$ and beam energy of $W \approx 20.35\,\mathrm{GeV} \pm 2\,\%$ FWHM. Upstream of the IP, the FACET electron beam is focused by a final focusing quadruple doublet to a beta-function of $\beta_{(x,y)} \approx (100, 25)\,\mathrm{cm}$ corresponding to a beam size of $\sigma_{(x,y)} \approx (30, 25)\,\mu\mathrm{m}$, which is determined by the FACET electron beam normalized emittances of $\epsilon_{n,(x,y)} \approx (10, 100)\,\mu\mathrm{m} - \mathrm{rad}$. The IP section is isolated upstream by an $50\,\mu\mathrm{m}$ beryllium and downstream by a $100\,\mu\mathrm{m}$ thick diamond foil. It is flooded with a hydrogen/helium gas mixture at densities of $n_{\mathrm{H2}} \approx n_{\mathrm{He}} \approx 0.65 \times 10^{17}\,\mathrm{cm}^{-3}$, such that the molecular hydrogen gas serves as LIT and helium gas as HIT medium. The gas mixture is selectively preionized by a Ti:sapphire 55 fs (FWHM) duration laser pulse with the energy of 170 mJ and a Bessel beam intensity profile produced by a holographic axilens [294] with a focal length of 3 m and depth of focus of 1 m. The Bessel beam is directed with a holed mirror into the FACET electron beam path and aligned with *Optical transition radiation* (OTR) screens at the IP. The peak intensity of the Bessel beam $I_{\mathrm{pre}} \approx 3 \times 10^{14}\,\mathrm{W/cm^2}$ is sufficient for ADK-ionization of hydrogen but is below the ionization threshold of helium; hence, the background helium gas remains largely neutral. ADK calculations assisted by selective laser profile intensity measurements suggest that a $\Delta z \approx 70\,\mathrm{cm}$ long plasma source with a maximum transverse diameter of $D \approx 130\,\mu\mathrm{m}$ can be generated with a peak hydrogen plasma density $n_{\mathrm{e,H}} \approx 1.3 \times 10^{17}\,\mathrm{cm}^{-3}$, corresponding to a plasma

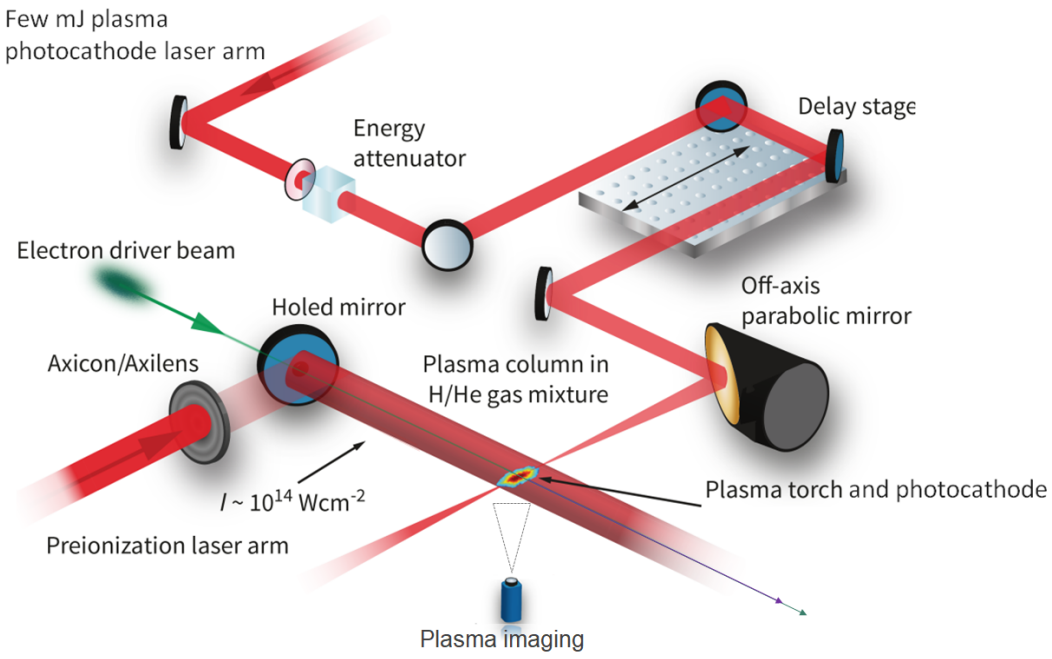

Figure 4.1: **The E-210 experimental configuration.** Schematic representation of key components of the E-210 experimental programme. Adapted from [39, 293]. This work is openly licensed via CC BY 4.0.

wavelength of $\lambda_p \approx 98\,\mu$m [39]. The plasma source likely had a complex topology along the propagation direction regarding transverse width variation and density profile. Figure (4.2) displays the 2D density profile of the plasma source likely encountered at E-210. This non-trivial topology profoundly impacts the performance of the PWFA stage and the injection stability of the plasma photocathode-injected witness beams in terms of the final energy reach [39] (see also section (4.1.4)). The choice of hydrogen plasma density is informed by various factors arising from the need to create a strong blowout for internal injection while avoiding unwanted dark current production [146]. It is also important to manage the alignment of the injector laser pulse and fit the dimensions of the blowout produced by the FACET electron driver beam into the plasma source. Due to these boundary conditions, the range of plasma densities and electron driver beams at the E-210 experiment was limited. These considerations are discussed in detail in section (4.1.4) and are extensively elaborated in Refs.[**Hidding2017first**, 39–41].

The plasma photocathode injector pulse, a 65 fs (FWHM) duration laser pulse from the main laser system, is split into two pulses independently tunable in energy and equipped with delay stages for temporal synchronization. One collimated laser arm is sent to an upstream *electro-optic sampling* (EOS) diagnostic for shot-to-shot *time-*

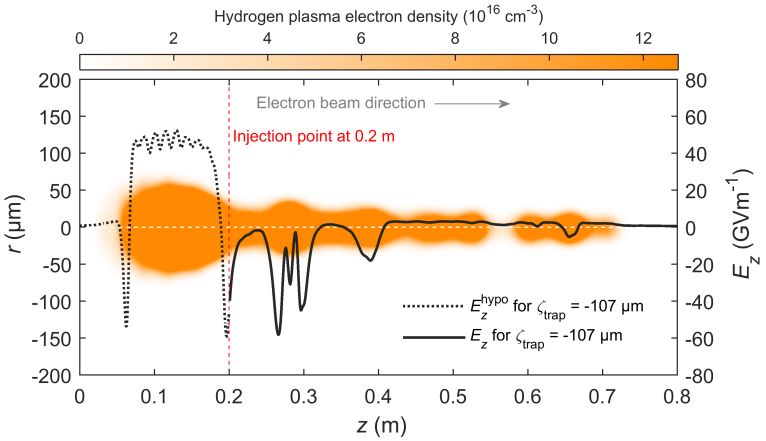

Figure 4.2: **ADK calculation of expected plasma source from the axilens and preionization laser pulse encountered at the E-210 experiment**. The orange structure represents the hydrogen plasma topology at full hydrogen ionization density of $n_{e,H} \approx 1.3 \times 10^{17} \mathrm{cm}^{-3}$. The maximum diameter of the plasma source is $D \approx 130\,\mu$m near $z \approx 10\,$cm and narrows down to $D \leq 50\,\mu$m further downstream. The black solid line shows the on-axis acceleration field E_z (obtained from 3D PIC simulation) experienced by a witness beam at the rear of a blowout. The witness beam is injected at the laboratory position $z \approx 20\,$cm (vertical red dashed line). Adapted from [39].

of-arrival (TOA) measurement of electron driver and injector laser beam. The EOS measured TOA jitter was $\approx 109\,$fs (see [39] and [265], for more details on EOS). The second laser arm is focused perpendicular to the FACET electron beam propagation axis in 90° geometry by an $f/22.9$ *off-axis parabolic mirror* (OAP) to a spot size of $w_{0,\mathrm{rms}} \approx 20\,\mu$m. The plasma photocathode laser pulse energies attenuation between 0.5-5 mJ allowed to access peak laser intensities of $I_{\mathrm{inj}} \approx 1.17 \times 10^{15} - 1.17 \times 10^{16}\,\mathrm{W/cm^2}$ at the IP. This is sufficient for the ionization of the helium gas on top of the hydrogen plasma in the propagation path of the electron driver beam. The injector-laser-generated plasma filament is imaged with a *charge-coupled device* (CCD) camera measuring the visible plasma afterglow light (see a brief discussion in section (4.1.2)).

Downstream of the diamond window, an imaging energy spectrometer beamline consisting of a quadrupole doublet and dipole magnet captures, focuses and disperses the electrons onto a CCD-monitored phosphor screen. Before and after the plasma stage, *Beam position monitors* (BPMs) measured the electron charge with an accuracy of 4-5 %, such that excess charge can be associated with a witness beam. Additionally, the

intensity of the phosphor screen is used to measure witness and driver beam charges calibrated with the BPM measurement with a combined accuracy of 10 %.

4.1.2 *Plasma-based spatiotemporal alignment*

The spatiotemporal coordination of the 90° geometry injector laser pulse and the FACET electron driver beam was a challenging task in the E-210 experiment. The traditional synchronization and alignment diagnostic methods fail when dealing with focused electron and laser beams at the IP because the intense electron and laser beams pose a risk to the integrity of solids due to ionization [38]. In contrast, plasma is a responsive medium to EM fields, and using plasma as a detector medium is the philosophy behind developing plasma-based diagnostics by utilizing the plasma afterglow single originating from the recombination and/or relaxation light of plasma as a measurable observable on a standard CCD camera integrated over a ms-time scale [38, 266].

A new method for enhanced plasma afterglow diagnostics has been developed by the E-210 collaboration to address the challenges involved in aligning intense electron and laser beams spatiotemporally. The E-210 experimental setup (see figure (4.1)) is leveraged to create a plasma filament perpendicular to the electron beam orbit by using a 90° laser pulse. The preionization laser pulse is turned off to observe only the confined plasma afterglow light from the laser-generated plasma filament. The CCD camera captures the plasma afterglow signal from the laser-only plasma filament when no electron beam is present to interact with it. This seed plasma can act as a detector medium when interacting with charged particle beams. When the plasma filament is produced picoseconds ahead of the electron driver beam's TOA (negative Δt_{delay} values), the plasma afterglow signal is significantly enhanced, as shown in figure (4.3) (top). In contrast, when the ionizing laser pulse arrives after the electron driver beam, the enhancement of the plasma afterglow signal disappears (positive Δt_{delay} values). The region between $-1 \leq \Delta t_{\text{delay}}(\text{ps}) \leq 1$ is when the electron and laser beams coincide in space and time. In figure (4.3) (bottom), a similar observation is made when the ionizing laser pulse is significantly misaligned in the transverse direction relative to the electron beam orbit; no plasma afterglow enhancement is measured. The signal is maximized when the electron and laser beams are spatially aligned, corresponding to $\Delta y = 0$. An

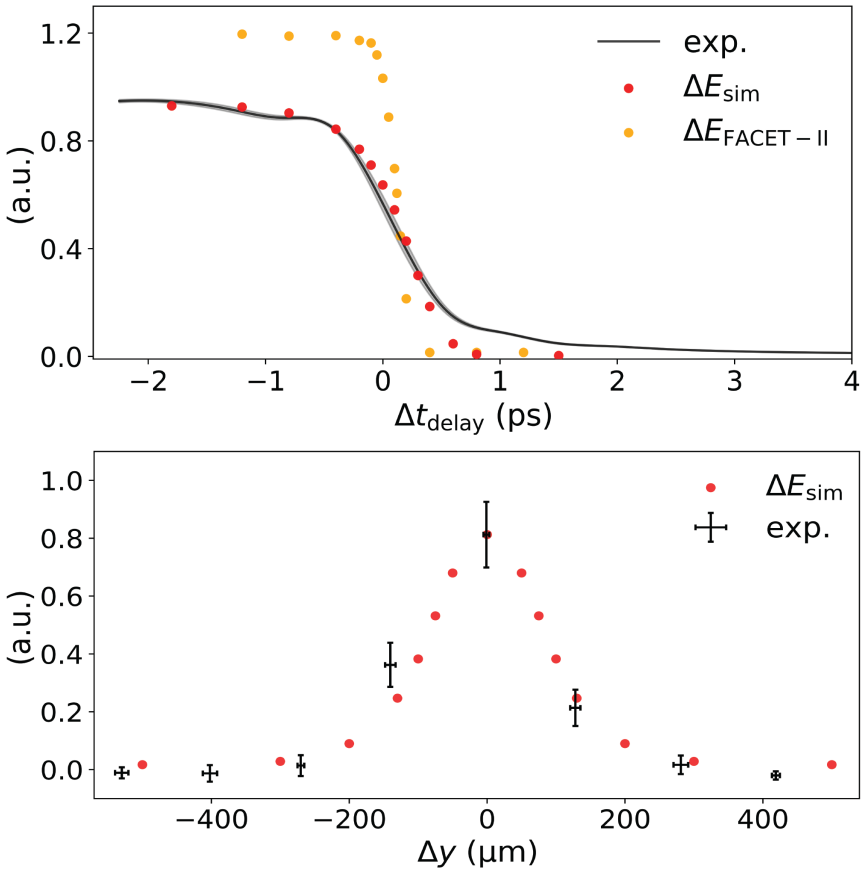

Figure 4.3: **Enhanced plasma afterglow measurements.** Enhanced plasma afterglow measurements of electron and laser beam temporal synchronization (top) and spatial alignment (bottom) curves. The 3D PIC simulations show the total energy deposition of the FACET electron beam into the plasma filament (red dots). The PIC simulation results agree with the measured afterglow signal and give an outlook to a potential FACET-II scenario (yellow dots). Adapted from [38] and produced by P. Scherkl with assistance from the author. This work is openly licensed via CC BY 4.0.

OAP roll scan produces a Gaussian-like integrated plasma afterglow alignment curve, as shown in figure (4.3) (bottom).

PIC simulation study of electron and laser-produced plasma filaments revealed [38, 266] that the underlying mechanism of the enhanced afterglow is energy deposition of the electron driver beam into the plasma filament. The space charge fields of the electron beam accelerate predominantly the plasma electrons in the initially cold plasma volume. This leads to plasma electron oscillation with increased plasma temperature. This heated plasma filament has an electron energy spectrum between eV and keV, which coincides with the impact ionization cross-section of hydrogen and helium [38].

The surrounding neutral gas is then ionized or excited to a higher state by the plasma electrons and potentially plasma ions on a longer time scale, producing more plasma to contribute to the plasma afterglow signal via recombination or relaxation of excited neutral atoms. This likely starts an avalanche effect and increases the plasma due to secondary ionization until the deposited energy from the electron beam dissipates to the surrounding gas. That is why the energy deposition by the electron beam is a function of delay, and alignment agrees very well in the figure (4.3). This highly complex interaction on fs time and μm length scale manifests as an enhanced plasma afterglow signal observable with a simple CCD camera integrated over the ms time scale.

Because of the simplicity of this approach of using plasma as a detector medium [38, 266], it found its way into other facilities [254] and is part of the experimental programme at SLAC FACET-II as a standalone experiments, named E-315 and E-316. Most importantly, the enhanced plasma afterglow diagnostic unlocked the synchronisation and alignment of intense electron and laser beams required to access the spatiotemporal sweet spot of the plasma photocathode injection regime in PWFA.

4.1.3 *Experimental results of plasma photocathode injection*

The coherent interplay of the individual components of the E-210 experiment (see Fig.(4.1)) is the key that enabled access to the plasma photocathode regime. The synchronization and alignment of the electron driver beam and the preionization laser are crucial initial steps to establish strong driver coupling to the hydrogen plasma source, ultimately generating a strong wakefield with a sufficiently deep trapping potential for internal injection. The hydrogen plasma source is produced approximately 20 ps ahead of the electron driver beam arrival in the IP, eliminating the need for fs timing synchronizations. An indication that the electron driver beam drives a wakefield is the observation of the deceleration signature of the driver beam on the imaging spectrometer (similar to the Fig.(3.8)) while mitigating trapped dark current and hot spots within the blowout [146]. Subsequently, the preionization laser is switched off, and spatiotemporal synchronization of the injector laser and electron driver beam is established on the sub-ps and μm time and length scale (as discussed in section (4.1.2)). Then, the plasma source is switched on, and the injector laser TOA is scanned.

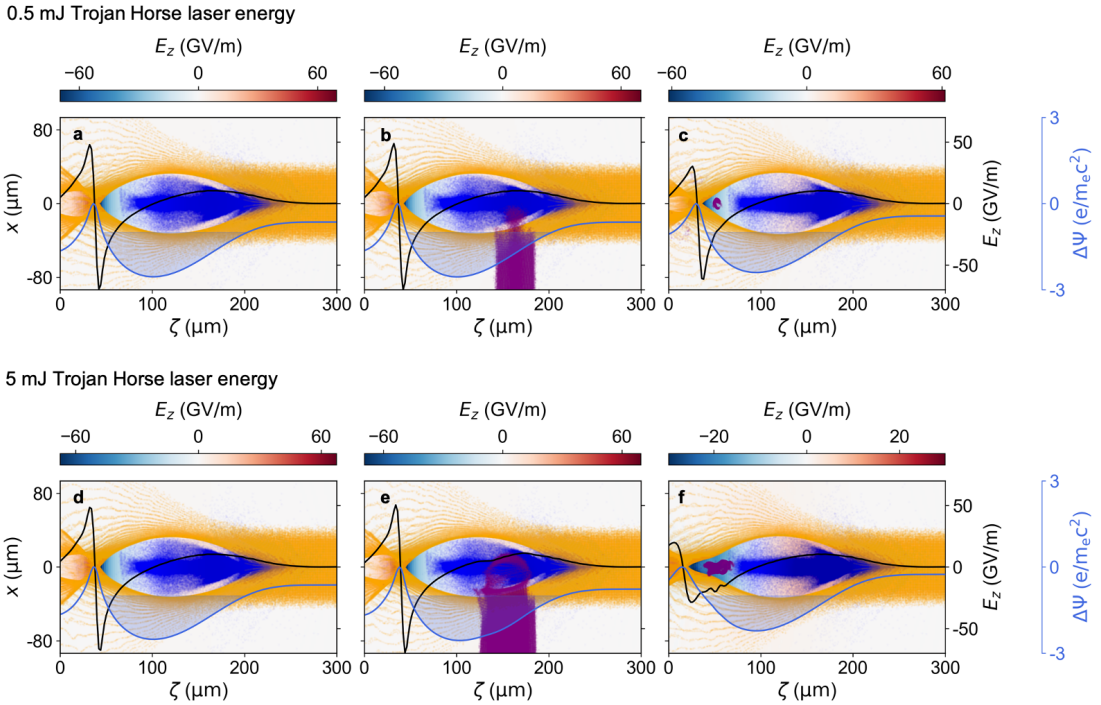

Figure 4.4: **3D PIC simulation of plasma photocathode injection at E-210.** Snapshots of a representative 3D PIC simulation of plasma photocathode injection in 90° geometry encountered at the E-210 experiment are presented for two different injector laser energies (top and bottom panels). The electron driver beam (blue) propagated through the plasma source (yellow dots) presented in Fig.(4.2) up to the injection position at $\Delta z \approx 20\,\mathrm{cm}$. The electron driver beam drives a strong blowout with a peak on-axis accelerating gradient (solid black line) of the order of $\approx 60\,\mathrm{GV/m}$ sufficient to facilitate internal injection, evident from the deep trapping potential (blue solid line). The top panel displays the situation before (a) $t = 0$, during (b) $t \approx 667\,\mathrm{fs}$ and after (c) $t \approx 9.3\,\mathrm{ps}$ witness beam injection with an injector laser pulse at 0.5 mJ energy; the bottom panel represents the corresponding situations when the injector laser energy is increased to 5 mJ. The higher laser energy in the bottom case produced a high charge witness beam, significantly loading the wakefield. Produced from the data in [39] for [41] jointly with D.Ullmann. This work is openly licensed via CC BY 4.0.

As a stepping stone towards plasma photocathode injection, the plasma torch injection was demonstrated in the same setup; an optically triggered downramp injection in PWFA [253]. For this, the injector laser timing is set such that the injector laser arrives picoseconds ahead of the electron driver beam. Then, the injector laser pulse generates a fully formed helium plasma filament when operated at the maximum laser energy of 5 mJ. This additional helium plasma produces a plasma density hump on top of the hydrogen plasma with a density gradient for downramp injection [39, 166]. This density downramp injection was shown for the first time in PWFA and is an important novel injection method in its own right [39, 166]. A detailed discussion on the realization of plasma torch injection at SLAC FACET and prospects are presented in [166, 265, 293, 295].

The plasma torch injection method facilitated a smooth transition into the plasma photocathode injection regime by adjusting the timing delay of the injector laser pulse towards the TOA of the electron driver beam and by reducing the injection laser energy. When the injector laser arrives after the electron driver beam, helium electrons are released directly inside the blowout, as shown in figure (4.4) for two different injector laser energies.

The corresponding results of the experimentally measured witness beam charge as a function of the relative TOA of the electron driver beam and injector laser pulse for three different laser energies are presented in figure (4.5). The values of TOA < 0 correspond to when the laser pulse arrives ahead of the electron driver beam, TOA > 0 when the laser pulse arrives after the electron driver beam, and TOA $= 0$ is when the electron driver and laser beams arrive simultaneously. In Fig.(4.5) (a) for TOA < 0, the 5 mJ injector laser pulse is intense enough to ionise sufficient amount of helium gas to trigger plasma torch injection in PWFA. For TOA $\gg 0$, the amount of injected charge decays rapidly; however, the transition region TOA > 0 corresponds to when the helium electrons are released inside the blowout. Reducing the injector laser energy in (b) and (c) shows that the plasma torch injection regime gradually disappears and only injected charge, for $0 <$ TOA (ps) < 1, is observed on the imaging spectrometer. In (c) at the injector laser energy of 0.5 mJ, corresponding PIC simulation Fig.(4.4) (a-c), the timing window where the injection is observed, is approximately ΔTOA ≈ 300 fs, which corresponds to approximately the plasma wavelength employed at the experiment. This 2D transition of injector laser energy and timing is reflected by the bin average (black

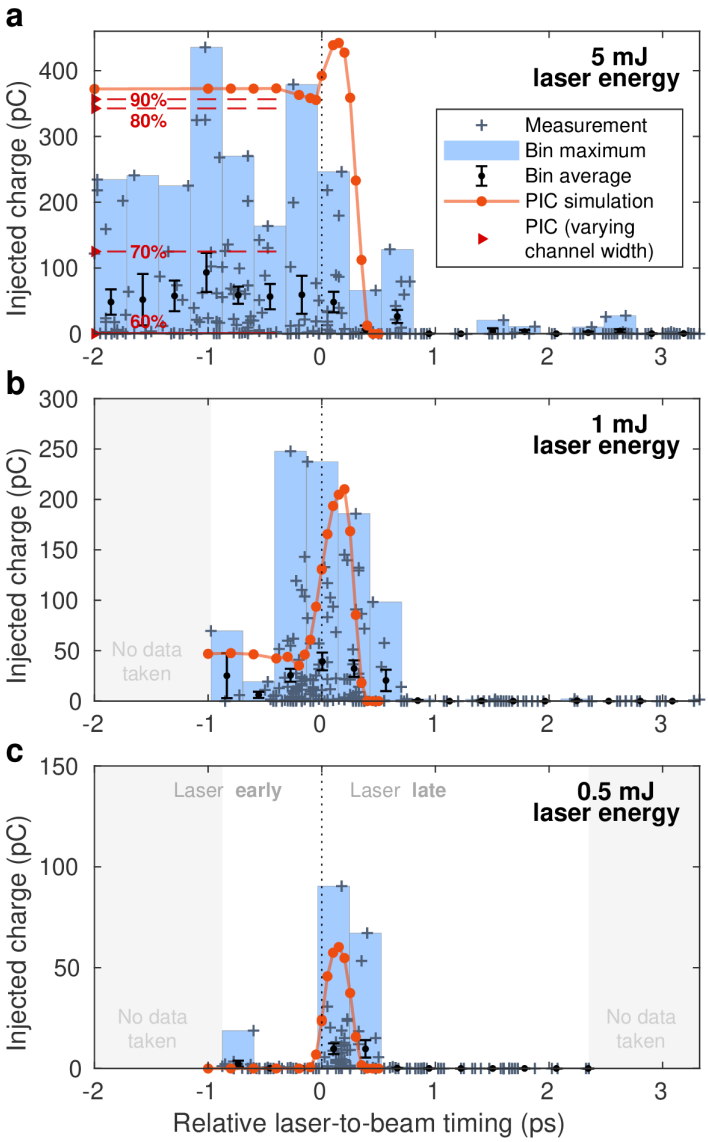

Figure 4.5: **Experimentally measured injected charge on the downstream spectrometer at the E-210.** Experimentally measured injected charge on the downstream spectrometer as a function of relative laser-to-electron beam timing (TOA) at three different laser energies. Grey crosses are individual shots; the blue bars show the bin maximum, and the black dots represent the bin average with a standard error of mean. The witness beam charge from PIC simulations is present (orange dots). The horizontal red dashed lines in (a) show the charge levels for different channel widths at the injection position. *Laser early* timing corresponds to when the injector laser pulse arrives ahead, and *laser late* timing corresponds to when the injector laser arrives after the electron driver beam. The vertical dotted line indicates the timing when laser and electron beams arrive simultaneously. Produced by O. Karger with support from the author for [39].

dots) with the standard error of the mean. The 3D PIC simulation for the optimistic experimentally accessible plasma source also agrees with the experimentally observed charge (orange dots) and variation in plasma source diameter (dashed red horizontal line) reproduces the injected charge variation range.

Figure (4.6) displays witness beam spectra observed on the downstream imaging spectrometer for the 0.5 mJ injector laser case from Fig.(4.5) (c). The imaging energy of the spectrometer is at 0.5 GeV. The shots are presented in consecutive order with an average energy range from 0.3 GeV to 0.7 GeV. The energy reach and spread agree well with the 3D PIC simulation of the configuration (supplementary material in [39]), and the details of the acceleration and injection dynamics are addressed in section (4.1.4). In (b), the energy of the witness beam is at the imaging energy. It yields a minimum relative energy spread measurement of $(\Delta W/W)_{\mathrm{rms}} \approx 2.1 \pm 0.3\,\%$ and the shot in (c) is away from the spectrometer imaging energy with a horizontal divergence (non-dispersion plane) of $\sigma_{\theta,\mathrm{rms}} \approx 0.38 \pm 0.03$ mrad and estimated normalized emittance of $\epsilon_{\mathrm{n}} \approx 1.5$ mm mrad, considering a calculated Twiss beta-function of $\beta_{\mathrm{y}} \approx 1.5$ cm at the exit of the plasma stage. These initial estimates already suggest that the witness beam likely had better quality than the initial driver beam in terms of normalized emittance. Further, it is very likely the witness beam duration was much shorter than the electron driver beam duration according to the simulations (see Fig.(4.4)). The relatively long Rayleigh length $Z_{\mathrm{R}} \approx 1.57$ mm of the injector laser pulse filled a significant fraction of the blowout (blowout radius of $R_{\mathrm{b}} \approx 60\,\mu$m) with helium electrons. Consequently, the release volume inside the blowout covered a significant fraction of the wakefield phases, including the space charge fields of the electron driver beam. Fundamentally, this prevented the production of normalized emittances at the nm-rad level. For example, operation at a longer plasma wavelength with a short Rayleigh length injector laser pulse can produce normalized emittances on the order of 100's of nm-rad in 90° geometry (supplementary material in [39]).

In conclusion, the results presented in this section confirm that the plasma photocathode works as intended in the PWFA. Advanced 3D PIC simulations reproduce the experimental data accurately and provide insights into areas of potential improvement. These findings increase confidence in plasma photocathodes' ability to produce ultra-high brightness electron beams in the future and enhance trust in the 3D PIC simulations and their predictions. The following section (4.1.4) discusses the limitations of the E-210

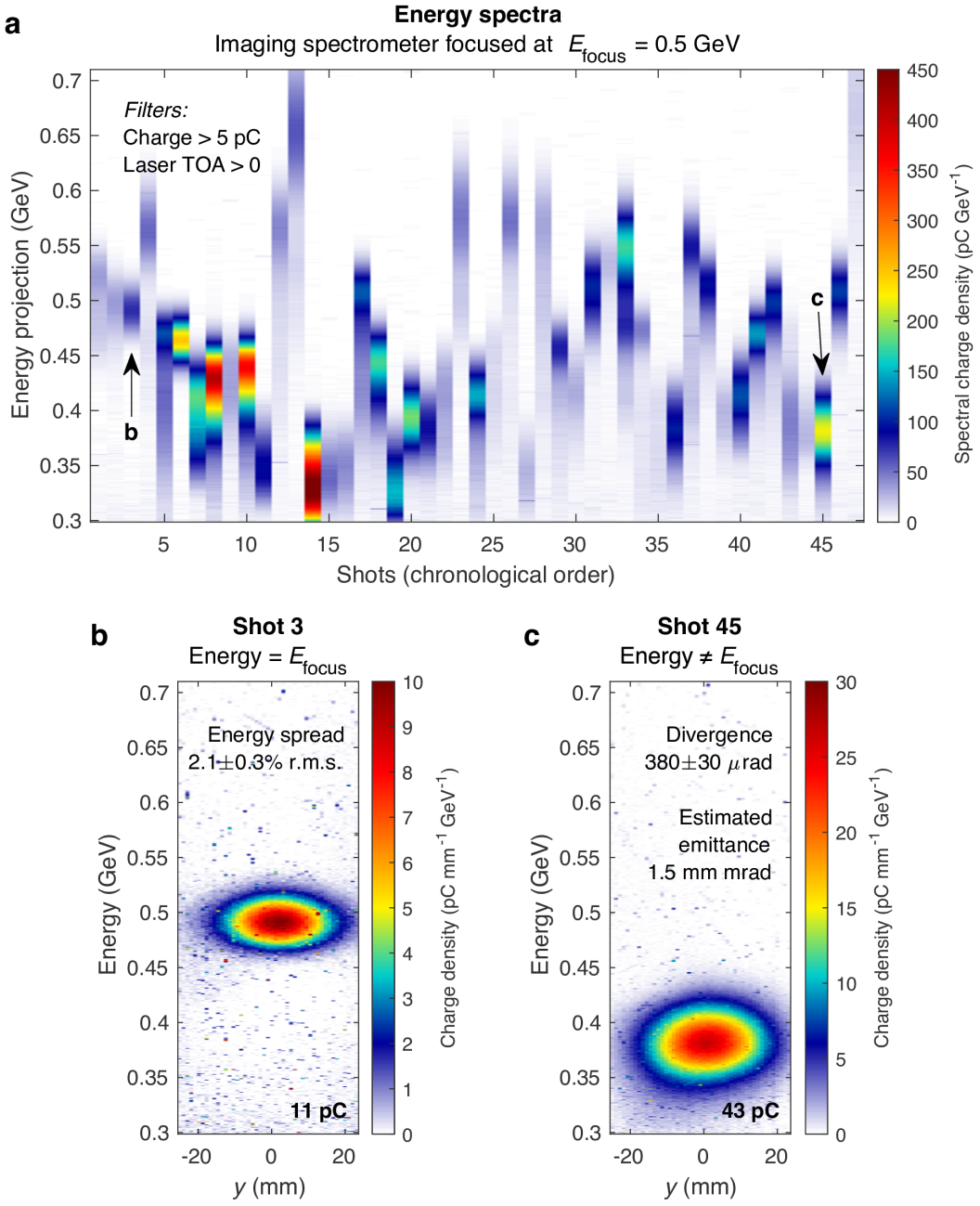

Figure 4.6: **Experimentally measured injected charge on the downstream spectrometer.** Waterfall plot of the imaging spectrometer data of consecutive shots of plasma photocathode injected witness beams (a) and selected spectra at the imaging energy of $E_f = 0.5\,\text{GeV}$ (b-c) are presented. Injected electron beam energy spectra corresponding to the shots presented in Fig.(4.5) with charge higher than 5 pC and TOA > 0 with colour-coded charge density. Selected witness spectrum (b) at the imaging energy of $E_f = 0.5\,\text{GeV}$, shows a minimum relative energy spread of $(\Delta W/W)_{\text{rms}} \approx 2.1 \pm 0.3\,\%$ and shot (c) with energy far from the imaging energy, indicating a horizontal divergence of $\sigma_{\theta,\text{rms}} \approx 0.38 \pm 0.03\,\text{mrad}$ and estimated normalized emittance of $\epsilon_n \approx 1.5\,\text{mm mrad}$. Reproduced from the data in [39].

experiments and elaborates on potential pathways to improve electron beam quality and stability.

4.1.4 *Limitations of witness beam acceleration and injection*

This section provides a detailed discussion of the limitation and boundary conditions encountered at E-210, which limited the energy reach, quality and stability of the witness beams.

Simulations presented in Fig.(4.4) and Fig.(4.5) are informed by various boundary conditions and measured parameters of the electron driver beam, preionization and injector laser and extensive theoretical and simulation work by the E-210 collaboration aiming at approaching the experimental conditions as close as possible [39, 41]. As such, the simulations can be seen as a representative best-case scenario within the constraints of the experiment and can serve as a reference point for interpretation beyond the initial conclusions and findings of the experimental data. A closer look into the simulation and experimental data is provided below.

The figure (4.7) (top) depicts the evolution of simulated on-axis longitudinal wakefield $E_z(\zeta)$ as a function of the co-moving coordinate ζ and the propagation distance z, considering the plasma source in Fig.(4.2). The electron driver beam peak current position is at the co-moving coordinate $\zeta = 0$. In the first part of the plasma source, up to the injection position $z \approx 0.2\,\mathrm{m}$, the wakefield in the first and second buckets of the blowout is relatively stable. However, downstream of $z \approx 0.2\,\mathrm{m}$, the blowout starts to contract and expand in the longitudinal direction in a quasi-periodic fashion and towards the end of the plasma source, the longitudinal accelerating wakefield vanishes, and the so-called *wakeless regime* is briefly observed. This phenomenon is due to the narrowing and expanding width of the plasma source and the interaction of the blowout sheath electrons with the plasma source boundaries [39, 41]. This wakefield dynamic can significantly impact the acceleration rate and stability of the injected witness beam. A trapped witness beam in this varying wakefield would experience changing accelerating gradients and even end up in the wakefield's decelerating phase or the blowout vertex's defocusing region. The relatively low energy gain and stability of the witness beam observed at the imaging spectrometer (see Fig.(4.6)) can be attributed to this wakefield

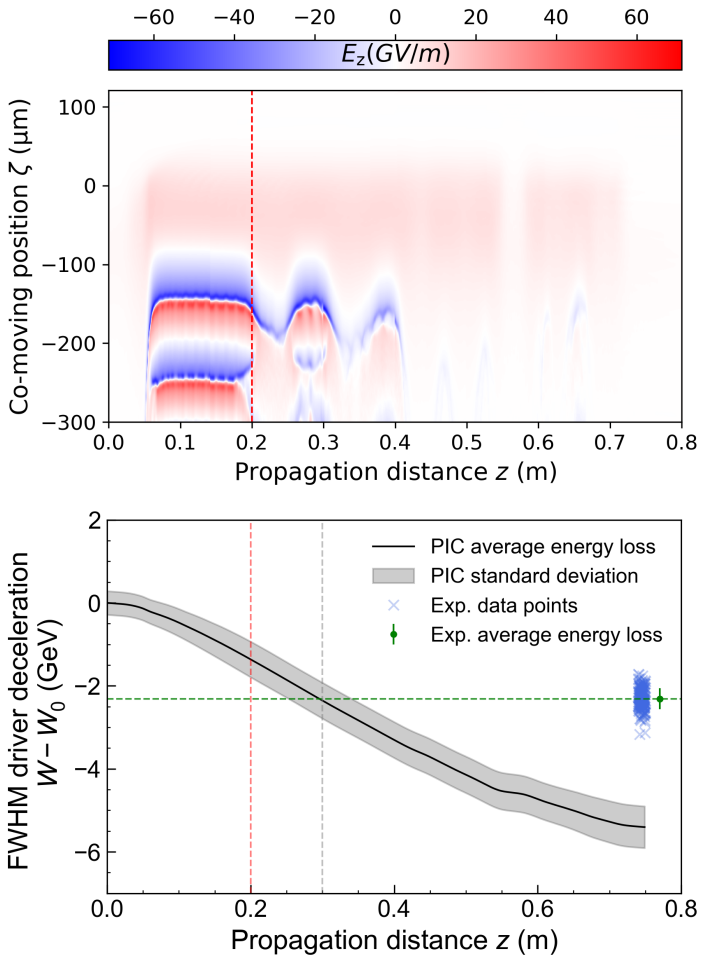

Figure 4.7: **Driver beam deceleration at the E-210.** On-axis wakefield evolution along the E-210 plasma source (top) and FACET electron driver beam (black line) deceleration (bottom) obtained from 3D PIC simulations. Additionally, experimental measurements of electron driver deceleration are presented with individual shots (blue crosses) and data set average (green dot and dashed line). The vertically dashed red line indicates the witness beam injection position, and the grey dashed line highlights the laboratory position when experimental and simulation data coincide. Produced by the author for [41] with simulation data input by T. Heinemann and experimental data input by A. Knetsch. This work is openly licensed via CC BY 4.0.

dynamic. Factors such as alignment and jitter between the electron driver beam and plasma source can also affect the stability and energy gain of the witness beam.

The figure (4.7) (bottom) shows the deceleration of the electron driver beam from the PIC simulation. Additionally, electron driver beam deceleration measurements at comparable experimental conditions are presented to support the findings. The experimentally observed driver beam deceleration of $\Delta W_{\mathrm{exp}} \approx 2.3\,\mathrm{GeV}$ (FWHM) with a range of $\Delta W_{\mathrm{min,max}} \approx 1.7\text{-}3.1\,\mathrm{GeV}$ indicates the compromised interaction of the electron driver beam with the plasma source. Although the overall trend is consistent with simulations, the deceleration values observed in the experiment are slightly lower. This may be due to suboptimal alignment and plasma source size. The simulation assumes a perfect alignment between the plasma source and electron driver beam orbit for the most optimistic plasma source scenario. However, the variation in shot-to-shot electron and preionization laser beam pointing can significantly impact the conditions required to drive a strong blowout over the tens of centimetres plasma source. The observed variation in the driver beam deceleration between shots suggests substantial shot-to-shot jitters between electron and laser beams. This conclusion is supported by the measured jitter of electron driver beam, preionization and injector laser pulses shown in figure (4.8). The pointing jitter analysis of the electron driver, preionization laser, and injector laser beam at the IP reveals that the centroid variation of the preionization laser pulse dominates the overlap of the electron driver beam and the plasma source. The electron driver beam and injector laser pulse exhibit similar statistical jitter variation, which enabled adequate precision for plasma photocathode injection in combination with the plasma afterglow alignment method discussed in section (4.1.2).

Summarizing, the plasma source topology and confined width presented significant operational constraints to the stability of the E-210 experiment. These constraints limited the potential of phase constant acceleration in PWFA, leading to high shot-to-shot variation of the accelerator regime and the injected witness beam parameters. The plasma source boundaries prevented operation at reduced plasma densities for better injection phase stability, as the blowout radius at a longer plasma wavelength would have exceeded the channel boundaries. Fortunately, the technical constraint of improving the plasma source could be resolved in future experiments. The successor experimental programme, "E-310: Trojan Horse-II" at SLAC FACET-II, aims to produce wider plasma sources for larger blowout sizes, coupled with potentially better stability

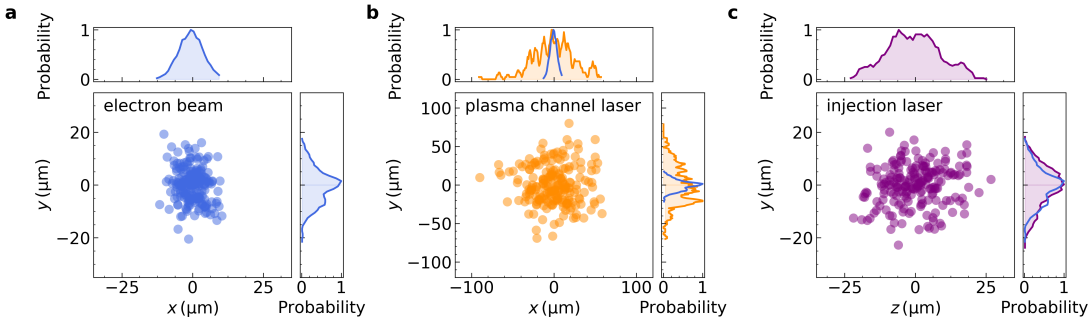

Figure 4.8: **Experimental pointing jitter analysis at the E-210.** Pointing jitter of electron driver (a), preionization (b) and injector beam (c) at the IP. Note the larger range of the x- and y-axis in the middle panel compared to the left and right panels. The blue solid line in the middle and right panel is electron beam data from the left panel. Produced by the author for [39, 41] jointly with O. Karger. This work is openly licensed via CC BY 4.0.

of incoming electron driver and laser beams [296–298]. This is expected to improve witness beam quality, tuneability, and stability [39–41]. The next section (4.2) develops strategies for removing the shortcomings of the E-210 experiment and elaborates on expected witness beam quality and stability under optimized conditions.

4.2 WITNESS BEAM PARAMETER STABILITY AND FUTURE DIRECTIONS

This section elaborates on potential pathways for future plasma photocathode implementation and improvements at SLAC FACET-II and elsewhere. A significant fraction of this section investigates the generation and acceleration of ultra-high 5D brightness witness beams in a dephasing-free PWFA stage with a supreme focus on the reproducibility and tuneability of the witness beam properties. A detailed PIC simulation-based statistical analysis is performed to identify prime sources of jitter and their impact on beam property variation, considering the lessons learned from the first plasma photocathode realization.

In general, witness beam parameter variation from shot-to-shot is primarily dictated by two primary jitter sources: the jitter of the PWFA stage (*the accelerator*) and the plasma photocathode laser pulse releasing the witness beam (*the injector*). First, the stabilisation of the PWFA stage is discussed, and then the stability of the injector laser pulse in collinear geometry is investigated. The results and considerations in this section

have direct implications for developing an ultra-high brightness PWFA stage for hard XFEL in section (6) and other applications. The author published a significant portion of the discussion in [39–41].

4.2.1 *PWFA stability considerations*

The stability of the incoming electron driver beam, the reproducibility of a wide plasma source, and the coupling of the electron driver beam into the plasma source determine the stability of the PWFA stage. Maintaining the PWFA dark current free is also highly desired for plasma photocathode injection [146].

The stability of the electron driver beam in PWFA relies on the stability of the rf-accelerator or, in the case of Hybrid LWFA→PWFA, on the stability of the LWFA stage that generates the electron driver beam. At SLAC FACET, for instance, a thermionic gun was used as the electron source for the electron driver beam. In contrast, at SLAC FACET-II, a photocathode rf-gun is employed to deliver electrons for the linac, potentially producing electron driver beams of better quality and enhanced stability at nominal 10 GeV beam energy [296–298].

In the E-210 experiment, the reproducibility and generation of wide plasma sources were largely constrained by the energy budget and stability of the high-power laser system. The upgraded high-power laser at SLAC FACET-II is expected to deliver laser pulses at higher energy (up to 500 mJ) and with improved stability. Using innovative preionization laser optics (such as axicon or axilens) along with the upgraded laser system may produce tens of centimetres plasma sources, supporting wide blowouts for multi-GeV witness beam energy gains. Fig.(4.9) shows an example of a wide plasma source. Unlike in E-210, the plasma source in Fig.(4.9) has nearly a uniform diameter of $D \approx 200\,\mu$m with a nearly flat-top plasma density profile in the central part of the channel. Once the background gas is fully field-ionized, laser pulse intensity variation may not significantly impact the plasma source topology. Excess laser energy may not significantly affect the channel topology at the femtosecond to the picosecond time scale after generation. However, the deposited laser energy will heat the plasma. Over a much longer time scale (nanoseconds), the heated plasma may exhibit hydrodynamic plasma expansion similar to HOFI channels [150]. Recent observations at SLAC FACET-II [299] support this consideration.

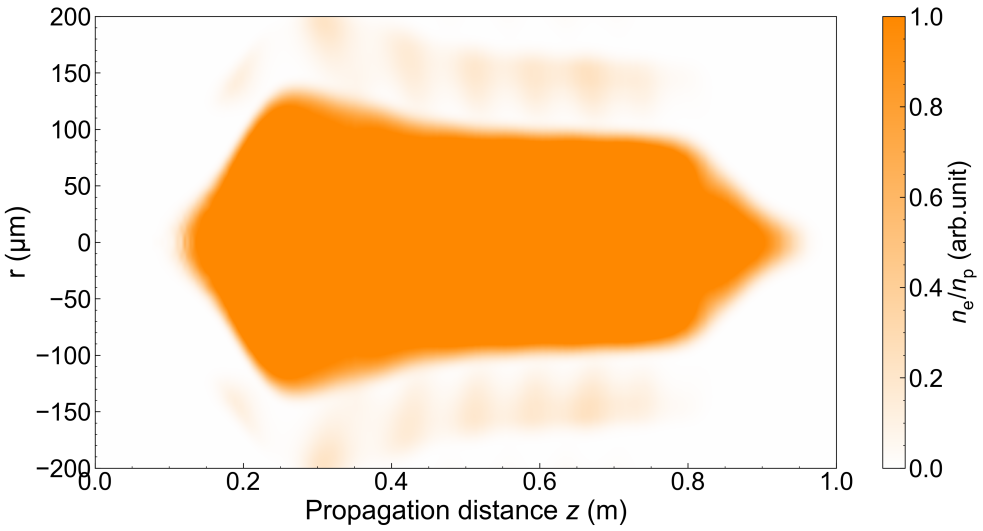

Figure 4.9: **Wide plasma source.** Potential plasma source for the next generation of plasma photocathode experiments at SLAC FACET-II. A. Hewitt provided data, and the author produced the figure.

A wide plasma source can alleviate the transverse alignment and pointing jitter requirements between the electron driver beam and the preionization laser pulse. Maintaining precise alignment and pointing jitter control between the electron driver beam and the plasma source may not be necessary as long as the blowout is fully contained inside the plasma source. In such a scenario, plasma source boundary effects may not compromise the injection and acceleration of a witness beam. Additionally, plasma sources as in Fig.(4.9) may allow operating the PWFA stage at comparably lower plasma densities ($n_p \approx 10^{16} - 10^{17}\,\mathrm{cm}^{-3}$) and produce blowouts at plasma wavelength up to $\lambda_p \approx 250\,\mu$m, which can improve the injection phase stability of the plasma photocathode and contribute to enhancing the witness beam's emittance, brightness, and parameter stability (see section (4.2.2)).

Further, operating at longer plasma wavelengths reduces the density requirements on the electron driver beam to drive a blowout, which naturally mitigates dark current production in the PWFA stage because of the decreased space charge fields of the electron driver beam and plasma wakefields [146]. Figure (4.10) presents ADK ionization calculations of helium gas (left) and helium ions (right) (potential HIT media) for a FACET-II-like electron driver beam for two plasma wavelengths ($\lambda_p \approx 100\,\mu$m (top panels), $\lambda_p \approx 250\,\mu$m (bottom panels)) as a function of electron beam radius and charge. The duration of the electron driver beams is longitudinally matched to the

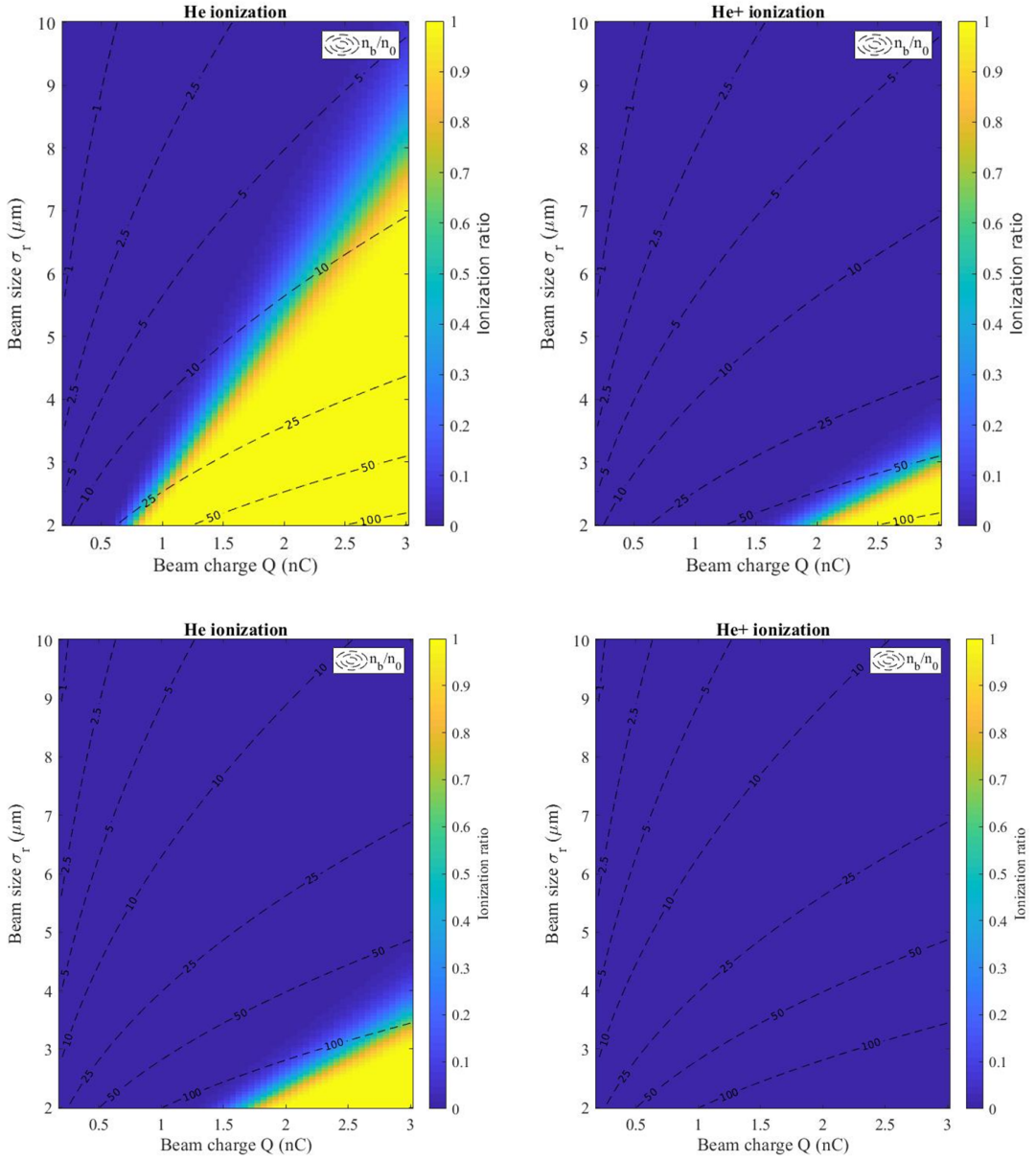

Figure 4.10: **Electron driver beam ionisation rate at FACET-II.** ADK ionization calculations of helium gas (left) and helium ions (right) for FACET-II electron beams as a function of beam radius and charge for two different plasma wavelength of $\lambda_p \approx 100\,\mu$m (top panels) and $\lambda_p \approx 250\,\mu$m (bottom panels). The electron beam duration is longitudinally matched to the plasma wavelengths for resonant wakefield excitation. The black dashed lines indicate the beam-to-plasma density ratio n_b/n_0.

corresponding plasma wavelength. At $100\,\mu$m plasma wavelength in Fig.(4.10) (top left), the electron driver beam at blowout regime relevant densities ($n_\mathrm{b}/n_0 \gg 1$) will likely field-ionize helium and populate the blowout with dark current. This will likely deplete the background helium reservoir so that no HIT medium is left for the plasma photocathode laser pulse. The situation improves when the background helium is preionized to support the blowout, as displayed in Fig.(4.10) (top right). A wide range of electron driver beam parameters can drive a blowout without running into the danger of depleting the second level of helium. Then, the second ionization level of helium can be employed as the HIT medium for the plasma photocathode laser. The situation is significantly improved at $\lambda_\mathrm{p} \approx 250\,\mu$m plasma wavelength. Because of the reduced driver beam density, the ionization of helium is reduced, and the ionization ratio of the second level of helium is nearly zero. This is a desired scenario for the plasma photocathode injection. A dark-current-free PWFA is driven in the blowout regime at a comparably long plasma wavelength.

In conclusion, in the upcoming plasma photocathode experiment (E-310), the recent SLAC FACET-II facility upgrades will be utilized to enhance the stability of the PWFA stage. The aim is to establish favourable conditions for collinear and revised 90° geometry plasma photocathode injection in PWFA. The findings of this section will contribute to the experimental preparation at E-310 and guide designing an ultra-high brightness PWFA stage for hard XFEL. In the next section (4.2.2), the PWFA stability arguments outlined in this section are considered, and the impact of the plasma photocathode jitter on the witness beam parameter variation is investigated.

4.2.2 *Plasma photocathode injector stability analysis*

The focus of this section is to investigate how the quality and stability of the witness beams are affected by variations in intensity, spatiotemporal alignment jitter, and synchronization of the plasma photocathode laser pulse concerning the blowout. An extensive 3D PIC simulation campaign studies the impact in a dedicated PWFA stage. To eliminate the jitter caused by the PWFA stage, the strategy discussed in sections (4.1.4-4.2.1) for PWFA stability is utilized. The aim is to operate at a longer plasma wavelength, with a plasma source wide enough to engulf the blowout structure ($D_\mathrm{channel} \gg R_\mathrm{b}$) and with sufficient width margin to consider electron driver and preionization laser

beam pointing jitters. Additionally, the electron driver beam will be optimized for dark-current-free operation. The operation point is discussed below.

The plasma stage comprises a uniform preionized hydrogen channel at a plasma density of $n_{\mathrm{p,H}} \approx 1.78 \times 10^{16}\,\mathrm{cm}^{-3}$, corresponding to $\lambda_{\mathrm{p}} \approx 250\,\mu\mathrm{m}$ plasma wavelength with a blowout radius of $R_{\mathrm{b}} \approx 65\,\mu\mathrm{m}$ when considering dense FACET-II type of electron driver beams. The FACET-II electron driver beam at energy of $W = 10\,\mathrm{GeV}$ and a charge of $Q_{\mathrm{d}} = 1.5\,\mathrm{nC}$ is compressed to $\sigma_{\mathrm{z,rms}} \approx 32\,\mu\mathrm{m}$, such that the PWFA stage is driven near the resonance condition $\sigma_{\mathrm{z}} = \sqrt{2}/k_{\mathrm{p}}$ at the peak current of $I_{\mathrm{peak}} \approx 5.5\,\mathrm{kA}$. Assuming a symmetric normalized emittance of $\epsilon_{\mathrm{n,x,y}} \approx 50\,\mu$m-rad in both transverse planes, the final focusing at FACET-II (Twiss beta-function of $\beta \approx 8\,\mathrm{cm}$) yields a matched beam size of $\sigma_{\mathrm{x,y}} \approx 4.5\,\mu\mathrm{m}$ according to Eq.(3.49) at the plasma stage entrance. The peak density of the electron driver beam is then $n_{\mathrm{d}} \approx 9.0 \times 10^{17}\,\mathrm{cm}^{-3}$, which is $n_{\mathrm{d}} \approx 52 \times n_{\mathrm{p}}$ enabling operation of the PWFA stage in the deep blowout regime with the trapping potential $\Delta\psi$ sufficient for plasma photocathode injection.

The hydrogen plasma is combined with neutral helium at a density of $n_{\mathrm{He}} \approx 2.3 \times 10^{17}\,\mathrm{cm}^{-3}$ to serve as a HIT medium for the plasma photocathode laser pulse. This helium-rich combination of H_2/He mixture, with $n_{\mathrm{He}} \approx 12.5 \times n_{\mathrm{H_2}}$, is necessary to drive a large blowout at a long plasma wavelength and at the same time provides sufficient HIT density for pC-level charge yield via ADK ionization. The PWFA configuration supports plasma photocathode injection in arbitrary angle geometry, but the highest beam quality is expected from collinear injection geometry, which will be employed. The collinear plasma photocathode laser pulse with a pulse duration of $\tau = 50\,\mathrm{fs}$ (FWHM) is focused down to a spot size of $w_0 = 7\,\mu\mathrm{m}$ (r.m.s) at $z \approx 1.9\,\mathrm{mm}$ from the start of the uniform plasma section. With a few μ-Joule laser energy, the dimensionsless laser amplitude can reach $a_0 = 0.018$ at the laser pulse focal point, which is just above the ionization threshold of helium. Note the laser-ionized plasma temperature study presented in figure (3.4) is based on the plasma photocathode laser parameters from this section. These parameters are optimized to ensure that beam-loading does not significantly change the trapping process and positions of the witness beams. The plasma photocathode-released electrons are largely decoupled from the wakefield generation, allowing the released electrons to be controlled with the laser pulse intensity and background HIT density. When electrons are released via plasma photocathode within the trapping potential, all released electrons will be trapped and form the witness beam. This enables accurate

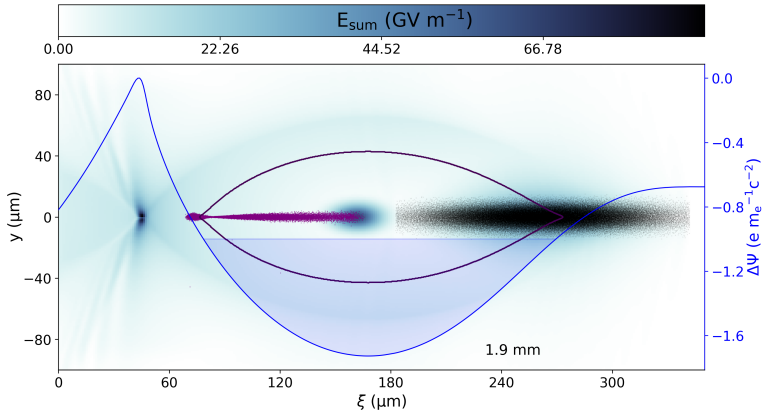

Figure 4.11: **Long plasma wavelength PWFA stage for ultra-high brightness witness beam production.** Long plasma wavelength PWFA stage for ultra-high brightness witness beam production and enhanced parameter stability via plasma photocathode. The FACET-II type driver beam (black dots) sets up a blowout in hydrogen plasma of density $n_{\mathrm{p,H}} \approx 1.78 \times 10^{16}\,\mathrm{cm}^{-3}$, corresponding to a plasma wavelength $\lambda_{\mathrm{p}} \approx 250\,\mu\mathrm{m}$. The sum of the wakefield is presented such that the plasma photocathode laser is visible, releasing helium electrons (purple dots) at the electrostatic trapping potential $\Delta\Psi$ centre (blue solid line). The shaded region indicates the trapping threshold $\Delta\Psi < -1$. Produced by the author for [41]. This work is openly licensed via CC BY 4.0.

control over final witness beam properties via the injector laser pulse parameters. Figure (4.11) displays the reference 3D PIC simulation of the outlined working point. The electron driver beam drives a strong blowout, and the snapshot is taken where a plasma photocathode laser pulse releases helium electrons at the trapping potential minimum $\Delta\Psi_{\mathrm{min}} \approx -1.7$. The helium electrons released first are already trapped at the blowout rear. Details of the numerical setup are discussed in [41].

The impact of the plasma photocathode laser pulse intensity jitter is investigated by varying the injector laser pulse amplitude a_0 up to $\pm 2\%$ around the baseline value of $a_0 = 0.018$. In principle, modern laser systems with advanced feedback loops can deliver better laser intensity stability. However, the conservative $\pm 2\%$ variation highlights the stability of the plasma photocathode injection process. The injected witness beams are accelerated to tens of MeV while tracking various electron beam properties. Figure (4.12) summarises the results of this effort.

Figure (4.12) shows that with increasing laser intensity, the amount of charge and peak current increases linearly within the range of this study (note: at much higher

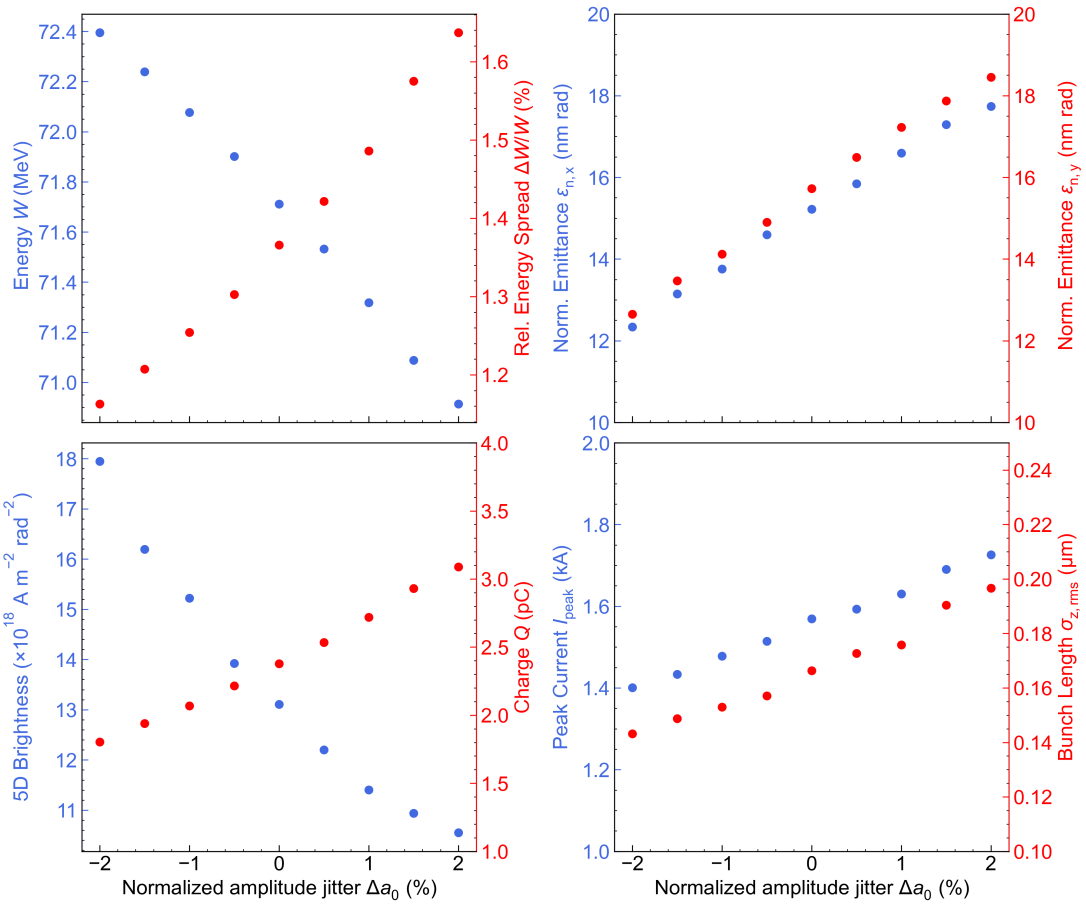

Figure 4.12: **Investigation of plasma photocathode intensity variation impact on the witness beam properties.** Witness beam parameters variation is presented as a function of the relative change of the dimensionless laser amplitude of the injector laser pulse around the baseline values of $a_0 = 0.018$. Produced by the author for [41]. This work is openly licensed via CC BY 4.0.

laser intensities, the ADK ionization rate may saturate due to complete depletion of the HIT medium), however, the 5D brightness decreases and shows an opposite trend. It may initially appear contradictory, but a closer look reveals that the normalized emittance increases linearly due to elevated space charge contributions during the initial formation phase of the witness beam. A similar counter-intuitive trend is visible for the energy and energy spread of the witness beam. The laser intensity does not impact the acceleration of the witness beam, but because of the higher peak current, beam loading starts to reduce the local acceleration gradients, and the final energy deviates by a few hundred keV from the reference energy. The projected energy spread varies in both directions on the order of $\sim 0.1\%$ from the nominal value because the witness beam length changes as a function of a_0. Interestingly, the reason for this is twofold. On the one hand, beam loading elongates the witness beam; on the other hand, variation in a_0 changes the ionization front movement of the injector laser and enlarges or reduces the spread of release position. This interpretation of witness beam length variation is supported by the laser pulse electric field evolution (Eq.(3.18) in combination with the trapping expression (Eq.(3.41)). However, overall, the witness beam parameter variations are relatively minor. For example, the statistical variation of energy on the order of hundreds of keV, relative energy spread variation of $\pm 0.15\%$, charge variation at sub-pC level, and normalized emittance jitter at the nm-rad level represent exceptional witness beam parameter stability orders of magnitude better than state-of-the-art. Table (4.1) summarises further details.

Figure (4.13) summarises the simulation results of the temporal jitter of the plasma photocathode laser pulse. The injector laser pulse position is shifted relative to the trapping potential minimum by up to $\Delta\tau = 30\,\mathrm{fs}$ towards the blowout vertex. The trapping potential is a line-symmetric function; hence, plasma photocathode laser pulse variation towards the electron driver beam would yield comparable results for $\Delta\tau = -30\,\mathrm{fs}$. The charge and normalized emittance of the witness beam are unaffected by the timing of the injector laser pulse. However, the energy and relative energy spread increases linearly with increasing timing. Moving the release position away from the trapping potential minimum results in a later trapping position at high accelerating gradients. At the same time, the pulse duration of the witness beam increases, resulting in a reduced peak current and beam loading. The decreased peak current slightly reduces the 5D brightness. Statically, the timing variation within this study's range has

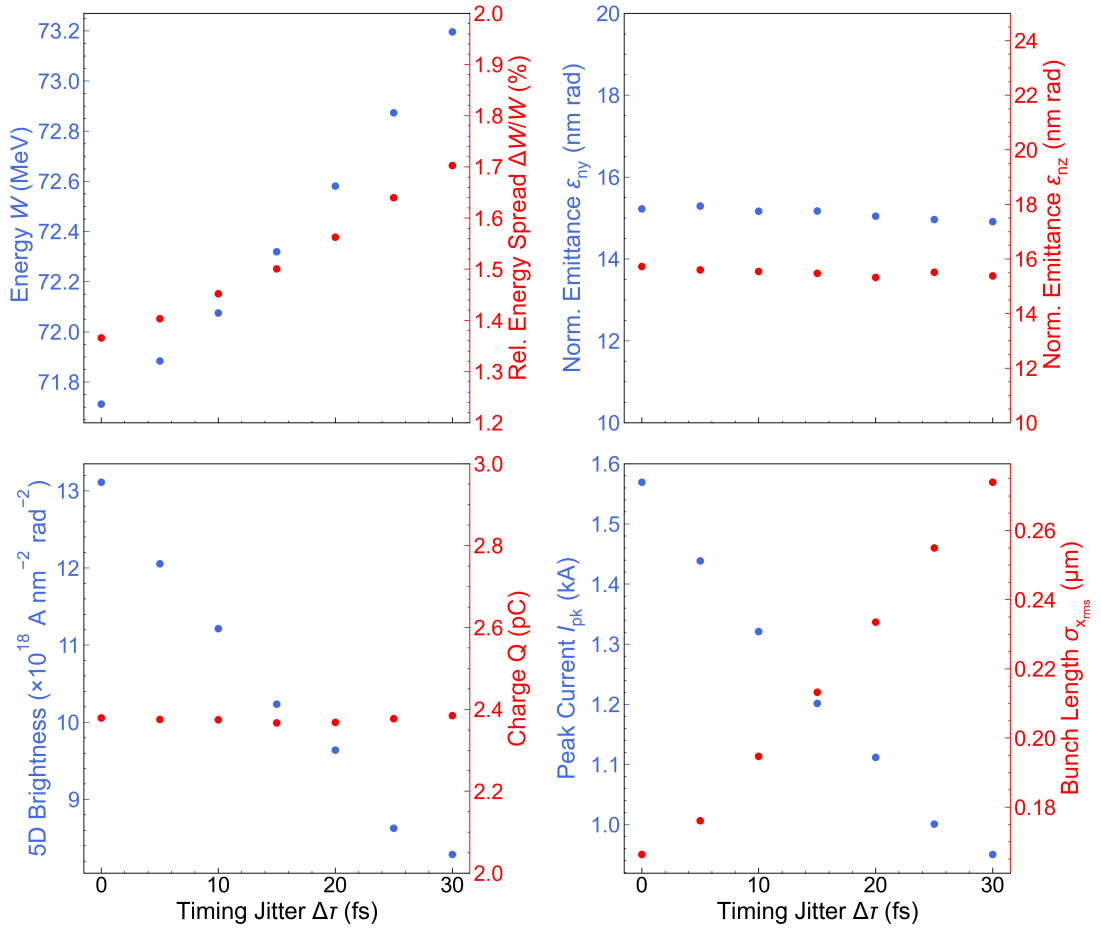

Figure 4.13: **Influence of timing variation of the plasma photocathode laser on the witness beam properties.** Witness beam parameters variation is presented as a function of plasma photocathode timing variation $\Delta\tau$ relative to the trapping potential minimum. Data generated by the author for [41]. This work is openly licensed via CC BY 4.0.

a tolerable impact on the witness beam properties and stability. The beam parameters and repeatability perform similar or even better than the injector laser pulse intensity variation study. To a large extent, this exceptional stability performance and robustness are inherent to the plasma photocathode injection method.

The reasoning behind this stability is that the parabolic shape of the trapping potential has a shallow slope near the minimum. Hence, when the laser pulse timing jitters around this potential minimum, the released electrons experience minor deviation in initial trapping potential values $\Delta\Psi(\zeta_\mathrm{i})$. Because of the quadratic dependency of the release position in the trapping position expression (Eq.(3.41)), the final trapping positions of the witness beams are very similar within the blowout. Hence, the timing variation of the injector laser on the order of tens of fs translates into much less trapping position variation within the wakefield phase. Further, because the wakefield is dephasing-free, the witness beams experience a nearly constant accelerating gradient from shot-to-shot over the propagation distance. This constitutes a *self-stabilisation mechanism* as a direct consequence of the underlying physics and provides an excellent mechanism for further improving witness beam energy stability towards applications such as XFELs, other light sources and possibly HEP applications.

Lastly, the misalignment of the plasma photocathode laser relative to the blowout axis by up to $\Delta Y = 10\,\mu$m is investigated for $\Delta\tau = 0\,$fs. Figure (4.14) displays off-axis helium electron release, and figure (4.15) shows the variation of witness beam parameters across the scan. Because these helium electrons are at rest when liberated from their parent atoms, they slip towards the blowout vertex while subject to the accelerating gradient of the wakefield. The immobile hydrogen ion background also attracts them back to the axis. The amount of released and trapped charge is not affected by the misalignment of the injector laser due to the 100% charge capture efficiency. The normalized emittance in the misalignment plane increases due to the wakefield kicks by up to $\approx$50 nm rad for the maximum misalignment of $\Delta Y = 10\,\mu$m and by $\approx$15 nm rad on average.

Nevertheless, this indicates a remarkable resilience, even considering these extreme misalignment values. If laser-to-electron beam alignment on the μm-level is achieved, for example, with the plasma afterglow method presented in section (4.1.2), then the resulting emittance growth can be indeed regarded as negligible. The other witness beam parameters are determined by reasoning similar to that used for the timing scan.

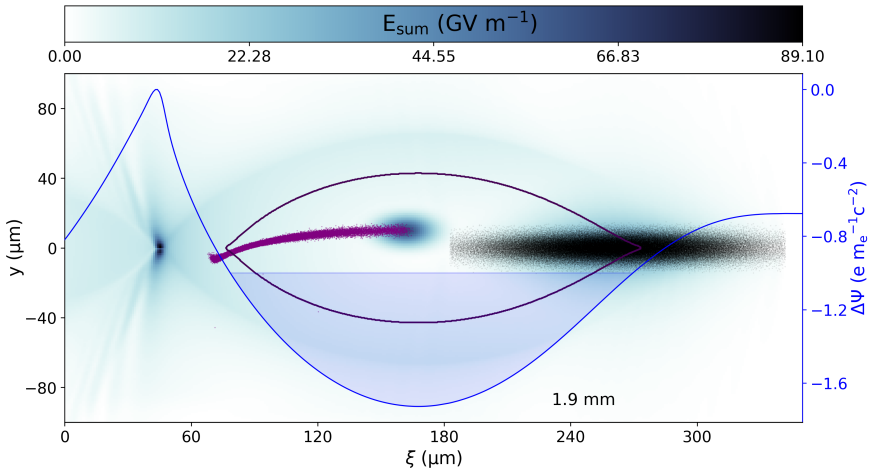

Figure 4.14: **Transversely misaligned plasma photocathode laser pulse relative to the blowout axis.** The FACET-II type driver beam (black dots) sets up a blowout in hydrogen plasma of density $n_{\mathrm{p,H}} \approx 1.78 \times 10^{16}\,\mathrm{cm}^{-3}$, corresponding to a plasma wavelength $\lambda_{\mathrm{p}} \approx 250\,\mu\mathrm{m}$. The sum of the wakefield is presented such that the misaligned plasma photocathode laser is visible, releasing helium electron (purple dots) off-axis within the electrostatic trapping potential (blue) $\Delta\Psi$. Data produced by the author for [41]. This work is openly licensed via CC BY 4.0.

Electrons released off-axis obtain a transverse kick from the wakefield and experience an effective reduced trapping potential according to Eq.(3.39).

Like the timing jitter, the witness beam's initial misalignment release position does not translate into centroid amplitude on the same scale in the blowout. When the witness beam is trapped, the centroid oscillation amplitude is adiabatically damping with increasing electron beam energy [41]. For example, at just a few tens of MeV at the end of these simulations, the centroid amplitude is below μm-level [41]; further reduction of the centroid amplitude is potentially expected when the witness beam is accelerated to higher energies and is expected to contribute to pointing stabilisation. This *self-aligning feature* of the witness beam injected with plasma photocathodes into the blowout could be highly beneficial for satisfying the tight alignment tolerances of subsequent beam transport line elements and the undulators in XFELs. This is in contrast to electron beams injected externally into the wakefield at relativistic energies, where the electron beams will maintain their initial misalignment during trapping and perform betatron oscillation with their initial centroid amplitude and potentially translate into pointing

Table 4.1: Witness beam parameter summary of plasma photocathode laser jitter analysis.

Beam parameter	Timing jitter $\Delta\tau$	Pointing jitter ΔX	Laser amplitude jitter Δa_0
Energy W (MeV)	72.38 ± 0.69	72.15 ± 0.59	71.69 ± 0.68
Energy spread (%)	1.52 ± 0.11	1.41 ± 0.05	1.38 ± 0.15
Charge (pC)	2.375 ± 0.006	2.371 ± 0.005	2.41 ± 0.42
Peak current I_p (kA)	1.23 ± 0.21	1.32 ± 0.21	1.56 ± 0.11
Bunch length (μm)	0.22 ± 0.04	0.19 ± 0.03	0.17 ± 0.02
Normalized emittance $\epsilon_{\mathrm{n,x}}$ (nm rad)	15.11 ± 0.13	29.91 ± 11.80	15.17 ± 1.77
Normalized emittance $\epsilon_{\mathrm{n,y}}$ (nm rad)	15.51 ± 0.12	15.38 ± 0.48	15.66 ± 1.90
5D brightness ($\times 10^{18}$ A m^{-2}rad^{-2})	10.45 ± 1.65	7.11 ± 3.66	13.5 ± 2.40

jitter at the plasma stage exit. For example, the recent experimental results on external injection in PWFA [300] suggests that angular misalignment between driver and witness beam of the order of $0.25\,\mathrm{mrad} < \Delta x' < 0.5\,\mathrm{mrad}$ can result in normalized emittance growth on the order of $\Delta\epsilon_\mathrm{n} \approx 1\,\mu$m-rad. A simplified geometric consideration can contrast this to the misalignment study in this section. Comparably, the misalignment of the plasma photocathode injector laser pulse relative to the driver beam by up to $\Delta Y = 10\,\mu$m corresponds to pointing angle of $\Delta Y' \approx \arctan(\Delta Y/0.5\lambda_\mathrm{p}) \approx 80\,\mathrm{mrad}$, where the plasma wavelength is $\lambda_\mathrm{p} \approx 250\,\mu$m. The resulting maximum normalised emittance growth in plasma photocathode injection is $\Delta\epsilon_\mathrm{n} \approx 0.05\,\mu$m-rad in this study. This shows that the plasma photocathode injection could potentially tolerate orders of magnitude larger angular misalignment while allowing normalized emittance preservation on the nm-rad scale.

Summarizing, the spatiotemporal alignment synchronization and intensity variation study indicate that witness beam properties are highly stable, even when considering the realistic variation of plasma photocathode laser parameters. Statistical analysis of the data in the table (4.1) reveals that witness beam parameter stability is exceptional, with variations in energy on the sub-MeV scale, relative energy spread variation of $\pm 0.15\%$, charge variation at sub-pC to fC level, peak current variation at the sub-kA level, and normalized emittance jitter at the nm-rad level. These stability values are either on the same level as state-of-the-art or exceed the stability by orders of magnitude in absolute values. For instance, in the design considerations of LCLS at SLAC [301], energy stability

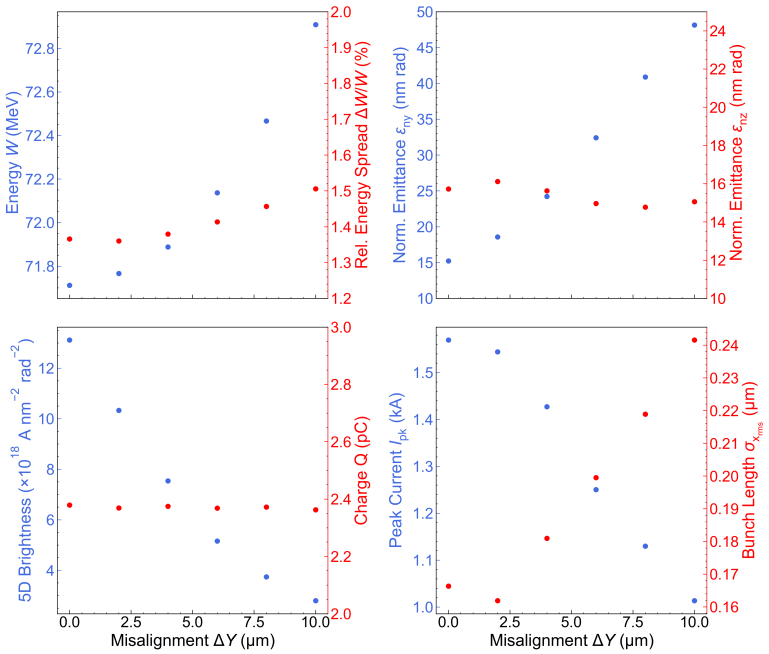

Figure 4.15: **Influence of misalignment of the plasma photocathode laser pulse relative to the blowout axis on the witness beam properties.** Witness beam parameter variation is shown as a function of plasma photocathode misalignment ΔY relative to the blowout axis. Data generated by the author for [41]. This work is openly licensed via CC BY 4.0.

$< 0.1\,\%$, charge stability $< 2\,\%$, peak current stability $< 12\,\%$, and emittance stability on the order of $0.1\,\mu$m-rad were considered acceptable for the world-first hard XFEL. From a plasma-based accelerator perspective, the stability of witness beam parameters is exceptional. It can be further improved by reducing the plasma photocathode laser pulse jitters below the values assumed for the current study. Most importantly, the 5D brightness of these beams is maintained at the $10^{18} - 10^{19}\,(\mathrm{Am}^{-2}\mathrm{rad}^{-2})$-level across the parameter variations, as evident from the table (4.15).

4.3 DISCUSSION

In summary, the FACET E-210 experiment was successful in demonstrating key milestones such as the feasibility of plasma photocathode injector [39], the realization of the first density downramp injection in PWFA [166], the development of plasma afterglow based spatiotemporal alignment diagnostics for intense particle and laser beams [38]. A more detailed summary of the E-210 achievements is provided in [40, 41]. The robustness of the plasma photocathode injection method is evident from the fact that the injection even worked under highly constrained experimental boundary conditions. A thorough review, evaluation, and interpretation of the E-210 experiment informed the next-generation plasma photocathode experiment at SLAC FACET-II and elsewhere, and it revealed general strategies for improving PWFA stage stability for plasma photocathodes. For example, reproducible electron driver beams and wide plasma sources are the primary components for a stable PWFA stage. Wide plasma sources allow operation at longer plasma wavelengths, significantly benefiting plasma photocathode-produced witness beam quality, stability, and tuneability. Indeed, an extensive jitter analysis of the plasma photocathode injection laser demonstrates exceptional witness beam parameter stability comparable to or even better than state-of-the-art. The findings are highly encouraging towards the next generation of plasma photocathode implementation and provide valuable guidelines for designing the ultra-high brightness PWFA stage for the XFEL application in this work.

5

A NOVEL ELECTRON BEAM ENERGY CHIRP COMPENSATION METHOD

This chapter provides a detailed analysis of the challenges that arise during electron beam acceleration, extraction and beam transport when considering the large longitudinal energy chirp inherent to plasma-accelerated electron beams. The impact on electron beam quality and quality preservation is evaluated, and how this may limit their suitability for high-demanding applications, such as XFELs. Further, state-of-the-art and plasma-based energy chirp compensation technologies (dechirping methods) are reviewed, concluding that none are compatible with ultra-high 5D brightness electron beams anticipated from plasma photocathode injection in PWFA. Initially, this realization triggered the invention of a new technique to compensate for the energy chirp of ultra-high 5D brightness electron beams directly within the same plasma stage, where witness beam injection and acceleration occur. The proposed approach has been validated using an advanced 3D PIC simulation, and its stability, limitations, and capabilities are discussed in detail. The conclusive results are published by the author as equally first authors in [42] and as an inventor in [302], and the follow-up explorations are partially contributed to [41, 43].

5.1 A PATH TOWARDS ULTRA-HIGH 6D BRIGHTNESS ELECTRON BEAMS

This section introduces a novel energy chirp compensation method to reduce the energy spread of ultra-high 5D brightness electron beams from plasma photocathode towards ultra-high 6D brightness electron beams required for high-gain hard XFELs. First, dechirping methods are reviewed, and the motivation for a novel energy chirp

compensation approach is outlined. Then, the basic idea and reasoning of the concept are introduced. Finally, the concept is elaborated in a fully explicit 3D PIC simulation.

5.1.1 *Review of energy chirp compensation methods*

The energy spread criterion is crucial in free-electron laser interaction, as discussed in chapter (2). The total projected energy spread consists of the uncorrelated (slice) and the correlated (energy chirp) energy spread. Both energy spread contributions must be minimized to achieve projected (slice) compact 6D phase space electron beams. In conventional accelerators, energy chirp is intentionally imposed on the electron beam longitudinal phase space to take advantage of the particle path differences in magnetic chicanes for electron beam compression, as discussed in section (2.1.4). Typically, off-crest acceleration of the electron beam in rf-cavities is utilized to obtain energy-chirped beams with projected relative energy spreads of $\Delta W/W < 0.5\,\%$ [303].

In contrast, the acceleration of electron beams in a plasma-based accelerator inherently results in the development of energy chirp due to the "sawtooth" shaped accelerating gradient with peak fields at the 10-100 GV/m scale. The witness beam trapped at the accelerating phase of the wakefield in figure (5.1) (a) shows a substantial difference in the level of acceleration between the witness beam head and the witness beam tail. As a result, the witness beam head has lower energy than the witness beam tail, leading to a significant accumulation of energy chirp over the acceleration distance in the plasma wakefield accelerator. The longitudinal phase space of a witness beam with the typical negative energy chirp is illustrated in figure (5.1) (b) at the end of the acceleration. The negative energy chirp can lead to several issues, including the one discussed in section (3.2.7). Extraction of energy-chirped electron beams from the plasma-based accelerator stage can significantly compromise electron beam normalized emittance due to non-matched transverse forces. The impact of non-matched transverse forces on the electron beam quality can be partially minimized using specialized plasma density extraction ramps [275, 276]. However, it still results in 0.1 μm-rad scale emittance growth at best, which is unacceptable for electron beams with nm-rad normalised emittances.

Additionally, chromatic aberration during electron beam capture and transport in a subsequent beam transport line can dramatically deteriorate electron beam normalized emittance and quality due to the significant energy spread/chirp [304–307]. Also, emit-

tance growth can occur during entry or reentry into a subsequent plasma accelerator stage in a multi-stage accelerator approach [308, 309]. The energy spread/chirp can compromise or even prevent the XFEL interaction (see section (2.2.3)). Preserving electron beam emittance on the nm-rad level is nearly as important and challenging as generating electron beams with nm-rad emittance. Hence, solving plasma-based accelerators' energy spread and chirp challenge is paramount for enabling ultra-compact PWFA-based XFEL while preserving the normalised emittance of electron beams on the nm-rad scale. Below, a few relevant energy spread compensation methods are reviewed.

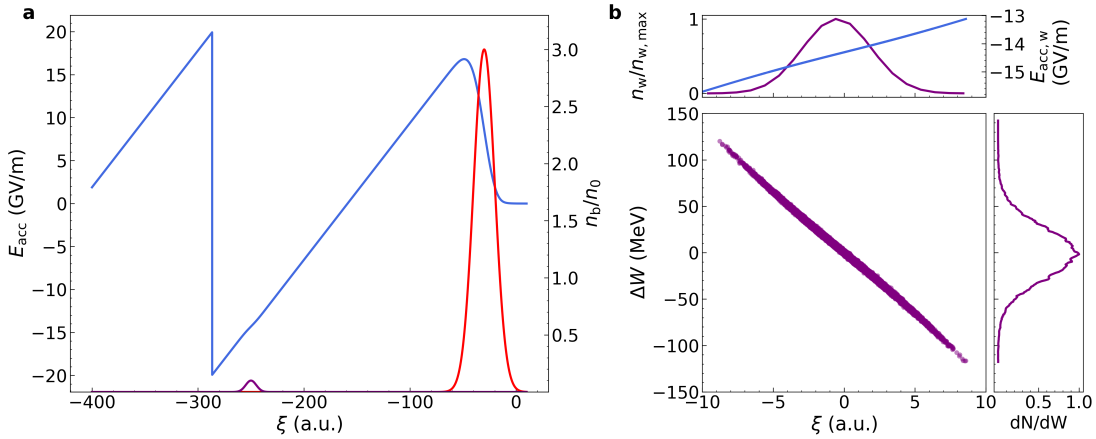

Figure 5.1: **Reduced model based on 1D cold fluid calculation of witness beam acceleration in a PWFA stage**. (a) On-axis wakefield excited by a Gaussian-shaped electron driver beam (red solid line) with a trapped witness beam (purple solid line) and (b) the final longitudinal phase space of the witness beam at the end of the acceleration with the projected longitudinal density (top panel, purple line) and energy spectrum (right panel, purple line). The witness beam developed a significant time-energy correlation due to the steep acceleration gradient (top panel, blue line) at the trapping position.

Passive corrugated metal structures [310, 311], self-induced wakefields in dielectric structures [312], and phase space rotation that uses the rf-dephasing techniques [303] are state-of-the-art technologies that can handle relative energy spreads or chirps of up to $\Delta W/W < 0.1 - 0.5\,\%$. This is because the wakefields generated by these structures for dechirping have magnitudes of approximately MV/m, which results in dechirping efficiency of the same order MeV/m. However, accelerated electron beams in a plasma-based accelerator typically exhibit projected energy spreads one order of magnitude larger, approximately $\Delta W/W \simeq 1 - 10\,\%$, compared to linac-generated electron beams.

Additionally, conventional methods can only be applied after the plasma stage. Therefore, state-of-the-art technologies are not well suited for plasma-based electron beams.

Beam loading in the plasma accelerator stage via the witness beam is proposed in early studies to create a uniform accelerating gradient at the witness beam trapping position by shaping electron beam current profile [269, 270, 313] (see also theory discussion in Sec.(3.2.6)). In this approach, optimal beam loading is obtained with carefully tailored triangular-like or uniform current profiles of witness beams at the corresponding accelerating phase within the wakefield, typically at multi-kA peak currents (see figures (3.13)-(3.14)). A Gaussian-like beam may lead to a non-uniform accelerating gradient, resulting in an electron beam with substantially non-linear longitudinal phase space curvature. The core of the electron beam may be dechirped while the head and the tail may still accumulate significant energy chirp during the acceleration. The first experimental evidence for non-linear phase spaces due to beam loading is presented in [314]. Figure (5.2) (a) shows the beam loading of a Gaussian-like electron beam, and figure (5.2) (b) presents the resulting longitudinal phase space of a witness beam. Large chirped wings in longitudinal phase space may turn into unwanted current spikes at the head and tail of the electron beam in a dispersion section of a beamline or within the undulator and generate CSE radiation [121, 315]. Additionally, recent theoretical studies suggest that maintaining the energy chirp during the acceleration can help mitigate witness beam housing instabilities due to the BNS-like damping effect (see detailed discussion in section (3.2.7)) and possibly minimize coherent density modulation along the witness beam due to the betatron oscillation.

The plasma photocathode injection method can produce a witness beam with sufficient charge for beam loading. For example, simply by tuning the HIT density, the plasma photocathode laser pulse releases different amounts of charge even if no laser parameters are tuned or by tuning the laser pulse energy, duration or spot size. As discussed in sections (3.2.5)-(3.1.3), the integrated ADK ionisation rate and the background HIT density define the total amount of charge. Typically, an injector laser pulse with a Gaussian temporal profile produces a witness beam with a Gaussian-like current profile, which would limit the reach of the projected relative energy spread as discussed above and in section (3.2.6). A witness beam with a flat-top or triangular current profile can also be produced by precisely controlling the amount of charge released as a function of time via the properties of the plasma photocathode laser pulse in combination with the

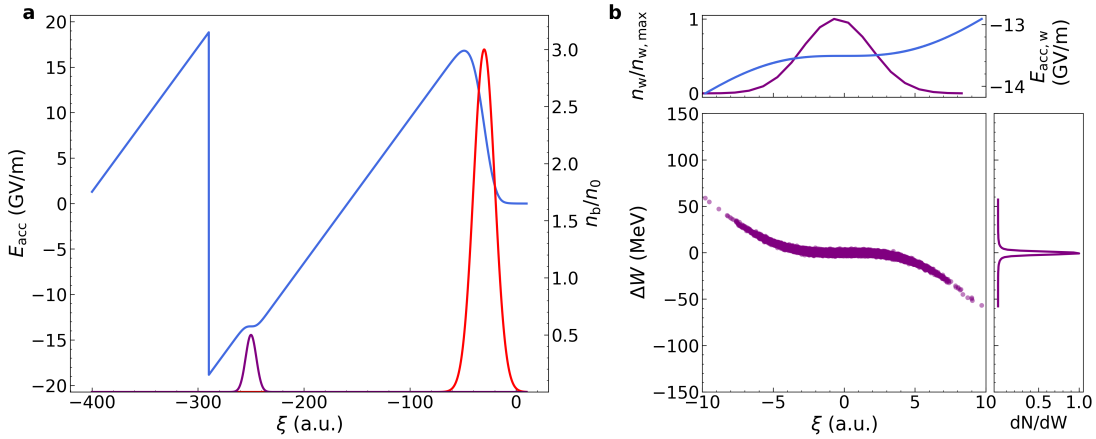

Figure 5.2: **Calculation based on a reduced model of witness beam loading of the wakefield in a similar PWFA stage as in Fig.(5.1).** (a) On-axis wakefield beam loaded by a Gaussian-shaped witness beam (purple solid line) and (b) the final longitudinal phase space of the witness beam at the end of the acceleration with the projected longitudinal density (top panel, purple line) and energy spectrum (right panel, purple line). The phase space is flat at the centre of the witness beam with non-negligible energy chirp at the wings due to the non-linear loaded accelerating gradient (top panel, blue line) at the trapping position.

density form factor of the background HIT species. However, this requires a completely different class of plasma photocathode injectors and will be explored and tested in future works.

Additionally, in the blowout regime, electron beams with tens to hundreds of pC charge are required to obtain the necessary multi-kA beam currents for beam loading of the GV/m-scale wakefields. Releasing this large amount of charge may induce a non-negligible space charge-driven emittance growth due to the rapid velocity compression of the witness beams to kA peak currents during the trapping process. Because electrons born at rest are in particular vulnerable to space charge repulsion effects [145], comparable to the space charge degradation effects observed in conventional electron guns [316, 317] (see also section (2.1.4)). Nevertheless, beam loading with standard plasma photocathodes could produce witness beams of sufficient quality for soft X-ray FELs; however, hard XFELs may require different solutions for the energy chirp compensation of ultra-high 5D brightness electron beams.

Some other plasma-based dechirping techniques propose complex plasma density modulation or accurate shaping of the plasma profile [318–320] for alternating the

witness beam between different phases of the wakefield. These methods require exact matching of the witness beam to the changing wakefields along the entire length of the plasma-based accelerator. Further, multi-stage approaches use wakefields produced in a subsequent plasma stage by the witness beam itself or via PWFA or LWFA to reverse the energy chirp of the witness beam [321–324]. But, multi-stage approaches may suffer from emittance growth on the $0.1 - 1.0\,\mu$m-rad level during the extraction and face spatiotemporal misalignment issues of the witness beam into the subsequent plasma stage and are incompatible with fs duration and ultra-high 5D brightness electron beams anticipated from plasma photocathodes.

In conclusion, it is crucial to eliminate the energy chirp of the electron beam for beam quality preservation before the beam is extracted from the plasma accelerator stage and transported through the post-plasma electron beam line. At the time of the research, none of the state-of-the-art methods were compatible with electron beams anticipated from plasma photocathodes. Even recently proposed plasma-based dechirping methods [318–324] can not cope with nm-rad emittance beams. Therefore, the shortcomings of the methods to deal with ultra-high 5D brightness and ultra-low emittance witness beams in the same plasma stage have motivated the development of a novel energy chirp compensation method described in this chapter. The following section (5.1.2) outlines the basic principles of this novel dechirping method.

5.1.2 *Basic concept of the energy chirp compensation approach*

Ironically, the idea behind the novel energy chirp compensation method is already embedded in the sawtooth-shaped accelerating gradient of the wakefield. The typical negative energy chirp originates from the linear slope of the accelerating gradient, resulting in the witness beam head-tail energy correlation shown in figure (5.3) (a). Conversely, at the blowout vertex, where the wakefield slope is reversed, a witness beam trapped in this position will accumulate a positive energy chirp during acceleration. The witness beam head experiences a higher accelerating gradient than the witness beam tail. Initially, the approach was to trap the witness beam at the blowout rear to accumulate a positive energy chirp. Then, a gentle plasma density downramp would have elongated the plasma wavelength at a later acceleration stage, placing the witness beam at a wakefield phase position with an opposite slope and initiating dechirping. However, this

implementation proved unfeasible in the blowout regime because the applicable region with accelerating and focusing fields at the blowout rear is tiny and notoriously unstable. It would require the exact timing of the witness beam concerning the wakefield phase and exact control over the plasma density profile initiating dechirping. Nevertheless, the idea of using a reversed accelerating gradient slope for dechirping persisted, albeit in a more controlled way, with beam loading of a second electron beam overlapped spatially with the witness beam.

In this novel dechirping method, first, a high-quality witness beam is injected via the plasma photocathode into the wakefield and is accelerated to relativistic energies. During the acceleration, the witness beam accumulates a negative energy chirp. With increasing beam energy, the witness beam will be more immune against space charge-induced quality degradation because of the decaying space charge force scaling $F_{\mathrm{sc}} \propto \gamma_{\mathrm{rel}}^{-2}$. Note that already at a witness beam energy of 100 MeV, the space charge forces are suppressed by $\gamma_{\mathrm{rel}}^{-2} = 200^{-2} \approx 2.5 \times 10^{-6}$. At the later stage of the acceleration, when the witness beam becomes relativistically stable, an additional tailored, high-charge electron bunch (**"escort" bunch**) is spatially overlapped with the witness beam at its trapping position (see figure (5.3) (b)). For example, figure (5.3) (b) shows that an escort bunch with density $n_b/n_0 = 0.5$ can flatten the local wakefield while c) and d) demonstrate overloading of the accelerating gradient slope [325, 326] if the escort bunch density is increased further to $n_b/n_0 = 1.0$ and $n_b/n_0 = 1.5$, respectively. In the first scenario ($n_b/n_0 = 0.5$), the energy chirp of the witness beam accumulated until then is frozen, and no further energy chirp is added due to the flat wakefield. In the latter one, active dechirping is induced. Here, the witness beam tail (high energy electrons) is subject to a lower accelerating gradient than the witness beam head (low energy electrons). This initiates a counter-clockwise rotation in the longitudinal phase space of the witness beam. While the witness beam undergoes this counter-clockwise rotation, the optimum extraction position from the plasma stage is when the energy chirp is compensated, and the projected energy spread is minimized. As such, the charge density values of the escort bunch enable an independent tuning parameter to modify the accelerating gradient at the witness beam trapping position. Figure (5.3) is based upon The reduced model derived in section (5.1.3).

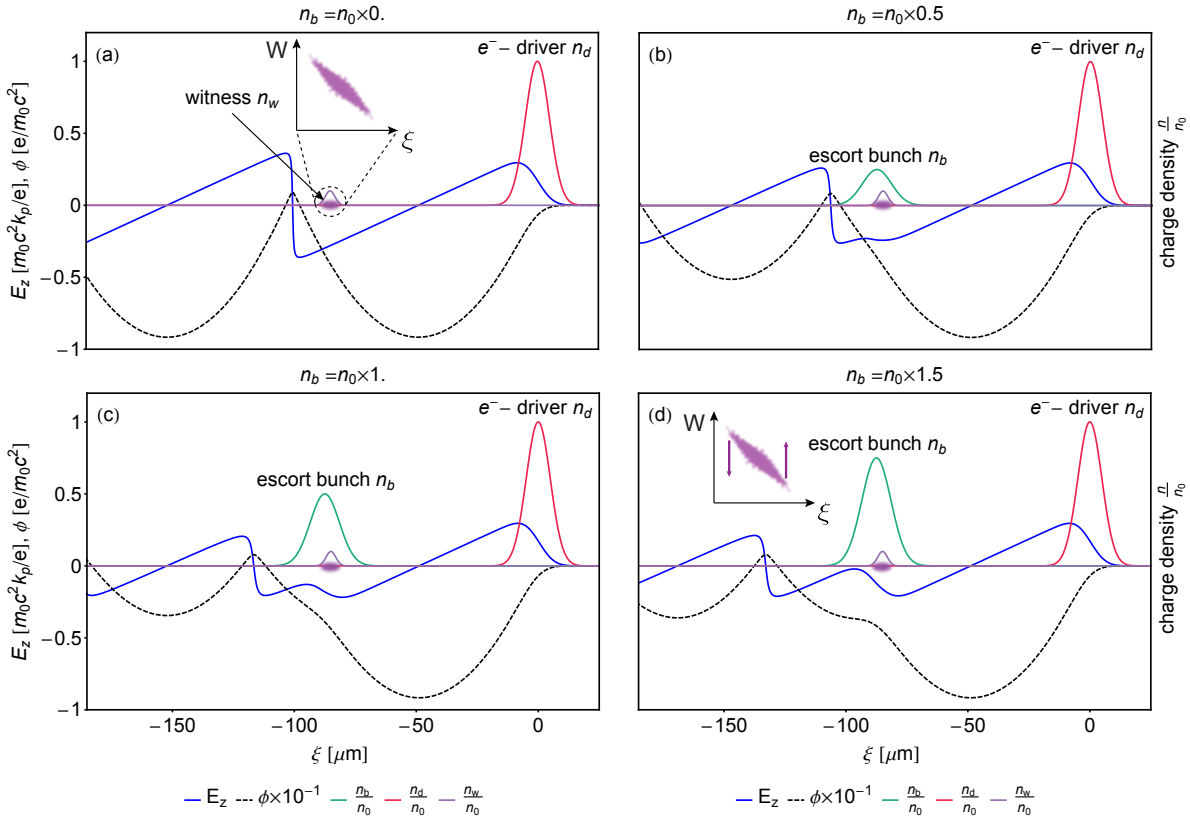

Figure 5.3: **Reduced model calculation based on the 1D fluid equations of the escort-bunch-based dechirping concept.** The plasma wave of density $n_0 = 1.1 \times 10^{17}\,\mathrm{cm}^{-3}$ is being driven by a non-evolving electron beam (red curve), propagating to the right. The on-axis longitudinal electric field E_z (blue line) and electrostatic potential ϕ (dashed black line) can be loaded by adding an escort bunch (green curve) with charge density n_b. The escort bunch can flatten or reverse the longitudinal electric field locally. Four cases to consider: (a) unloaded case ($n_b = 0$), where the position of the witness beam n_w (purple curve) and its resulting energy chirp is indicated schematically, (b) $n_b/n_0 = 0.5$, (c) $n_b/n_0 = 1.0$ and (d) $n_b/n_0 = 1.5$. The electron witness beam position and size (purple) are indicated, allowing the electric accelerating field that the witness would sample to be visualized. The insets in (a,d) are the longitudinal phase spaces of the witness beam, which indicate the phase evolution for the (a) unloaded and (d) loaded cases. Produced by the author for [42]. This work is openly licensed via CC BY 4.0.

5.1.3 *Reduced model development of the novel energy chirp compensation concept*

A one-dimensional semi-analytical model is developed to study the basic features of the escort-bunch-based dechirping method qualitatively while still providing a sufficient theoretical description of the underlying physics. The starting point of the derivation is the quasi-static 1D cold fluid model of the plasma wakefield discussed in section (3.2.2).

First, the system's total charge density $\rho_{\mathrm{tot,new}}$ is determined by considering the witness beam and escort bunch charge densities and the contributions from the electron driver beam, plasma ions and plasma electrons. Hence, the total charge density contributions in plasma read

$$\rho_{\mathrm{tot,new}} = -e(n_{\mathrm{e}} - n_0 + n_{\mathrm{d}} + n_{\mathrm{w}} + n_{\mathrm{esc}}), \tag{5.1}$$

where n_{w} and n_{esc} represent the charge distribution of the witness and escort beam, respectively. The charge distribution of electron driver beam $n_{\mathrm{d}}(\xi)$, witness beam $n_{\mathrm{w}}(\xi)$ and escort bunch $n_{\mathrm{esc}}(\xi)$ are defined as a function of the co-moving coordinate ξ. The background plasma electrons n_{e} and ion charge density profile n_0 are assumed uniform. As discussed in section (3.2.2), the wakefield is excited by a relativistic non-evolving electron driver beam n_{d} with velocity $v_{\mathrm{d}} \sim v_{\mathrm{ph}} \sim c_0$ in the quasi-static approximation. The Poisson equation of the system is obtained by following the algebra introduced in section (3.2.2). This allows the formulation of a differential equation of the electrostatic potential as

$$k_{\mathrm{p}}^{-2}\frac{\partial^2\phi_0}{\partial\xi^2} = \frac{n_{\mathrm{d}}(\xi) + n_{\mathrm{esc}}(\xi) + n_{\mathrm{w}}(\xi)}{n_0} + \frac{1}{2(1+\phi_0)^2} - \frac{1}{2}. \tag{5.2}$$

The co-moving coordinate ξ is independent, and the electrostatic wake potential ϕ_0 is a dependent variable. Solving this Inhomogeneous Second Order Differential Equation analytically is challenging for arbitrary configurations of $n_{\mathrm{d}}(\xi)$, $n_{\mathrm{w}}(\xi)$, and $n_{\mathrm{esc}}(\xi)$; however, numerical methods can provide an approximated solution to Eq.(5.2). The axial electric wakefield is computed with $E_{\mathrm{z}}(\xi) = -E_{\mathrm{wb}}d_\xi\phi_0(\xi)$ as a function of ξ, where ϕ_0 is a solution to Eq.(5.2).

Once the axial wakefield $E_{\mathrm{z}}(\xi)$ expression is obtained, it allows deriving a simple term for the witness beam energy gain. The dephasing-free acceleration in PWFA ($v_{\mathrm{d}} \sim v_{\mathrm{ph}} \sim c_0$) allows a non-evolving accelerating gradient to be assumed at the witness

beam trapping position, meaning $\partial_t E_{\mathrm{z,w}} = \mathrm{const}$. Then, the change of the relativistic Lorentz factor $d\gamma_{\mathrm{rel}}$ per unit length element dz is

$$d\gamma_{\mathrm{rel}} = \frac{e}{m_{\mathrm{e}} c_0^2} E_{\mathrm{z,w}} dz. \tag{5.3}$$

Here $E_{\mathrm{z,w}}$ is in units of eV/m. Integrating the above expression over the acceleration distance z_{acc} yields

$$W = E_{\mathrm{z,w}} z + W_0, \tag{5.4}$$

where $W \approx \gamma_{\mathrm{rel}} m_{\mathrm{e}} c_0^2 / e$ is the final energy of an electron beam, and the integration constant $W_0 = \gamma_0 m_{\mathrm{e}} c_0^2 / e$ is the initial energy. Equations (5.2-5.4) build the semi-analytical framework for the escort-based dechirping approach.

The initial exploration of the dechirping method with the reduced model is approached by solving the problem in two parts. First, the wakefield is calculated with a trapped witness beam at the accelerating phase. This wakefield calculation is then used to determine the acceleration of the witness beam and its longitudinal phase space evolution. Second, at the release position of an escort bunch, the wakefield is recalculated to account for the beam loading of the escort bunch at the witness beam trapping position, and the evolution of the witness beam longitudinal phase space is advanced.

Figure (5.4) (a) shows the on-axis wakefield E_{acc} excited by the relativistic electron beam (red line) with Gaussian-shaped charge density at a maximum value of $n_{\mathrm{d}}/n_0 = 3$. The Gaussian-shaped witness beam (purple line) is placed at the accelerating phase of the wakefield. The peak charge density of the witness beam $n_{\mathrm{w}}/n_0 = 0.1$ is chosen such that beam loading effects become negligible at the corresponding acceleration phase of the wakefield. The initial longitudinal phase space density of the witness beam is represented by a random multi-variable distribution with Gaussian distribution in all directions. The initial witness beam of 1 MeV mean energy is loaded into the wakefield without an initial energy chirp. Then, the witness beam is accelerated for $z_{\mathrm{acc}} = 0.1\,\mathrm{m}$ (see figure (5.5) (a)). The longitudinal phase space of the witness beam is advanced according to Eq.(5.4). The typical negative energy chip is apparent due to the local acceleration gradient $E_{\mathrm{acc,w}}$ indicated by the blue line in the top panel. Now, a Gaussian-shaped escort bunch with $n_{\mathrm{esc}}/n_0 \approx 1.1$ is loaded into the wakefield, which reverses the accelerating gradient at the witness beam trapping position (see figure (5.4) (b)). The witness beam phase space from the first section interacts with the

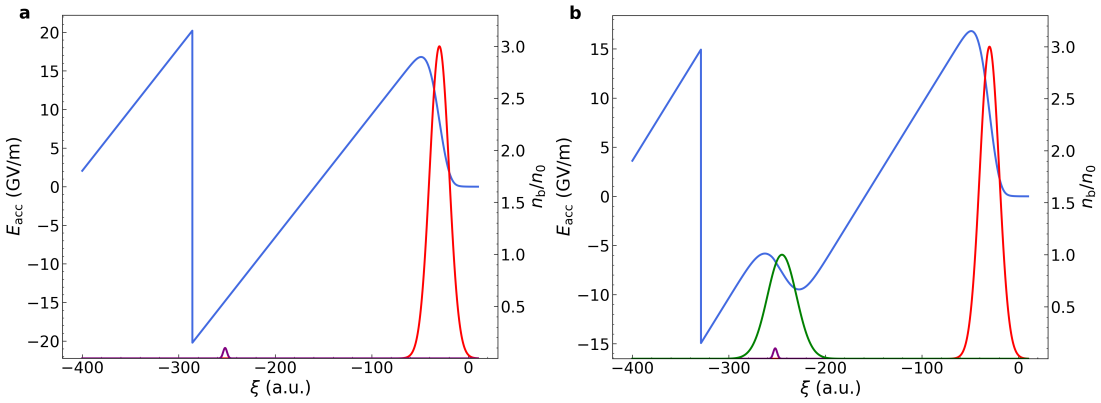

Figure 5.4: **Reduced model calculation based on the 1D cold fluid equations.** Reduced model calculation of the on-axis wakefield based on the 1D cold fluid equations at the acceleration phase (a) and dechirping section (b). The on-axis wakefield E_{acc} as a function of the co-moving coordinate is represented by the blue line, the electron driver beam normalized charge density n_{b}/n_0 (red line) excites the wakefield. The purple line represents the accelerated witness beam charge density. In panel (b), additionally, the charge density of the escort bunch is shown (green line), which overloads the wakefield at the witness beam trapping position.

overloaded wakefield. It rotates counter-clockwise until the energy chirp is compensated, as presented in figure (5.5) (b). Further acceleration leads to over-rotation of the phase space (see in Fig.(5.5) (c)), and the witness beam develops a positive energy chirp. A witness beam with a positive energy chirp might have exciting applications in its own right; however, for minimized energy spread/chirp for FEL applications, the optimum extraction position from the plasma stage is at the position shown in figure (5.5) (b). Here, the linear energy chirp of the witness beam is nearly cancelled.

Figure (5.6) displays the evolution of the witness beam average energy W and projected absolute energy spread ΔW during the acceleration and dechirping. The energy gain and absolute energy spread increase linearly until the escort bunch is loaded into the wakefield at $z_{\mathrm{acc}} = 0.1\,\mathrm{m}$. Then, the witness beam continues gaining energy linearly. However, at a slightly reduced rate due to beam loading, the absolute energy spread drops in a parabolic-like manner from its peak value of $\Delta W_{\mathrm{s}} \approx 25\,\mathrm{MeV}$ to its minimum value of $\Delta W_{\mathrm{f}} \approx 2.5\,\mathrm{MeV}$ at $z_{\mathrm{acc}} = 0.21\,\mathrm{m}$. The total absolute energy spread reduction amounts to $\Delta W_{\mathrm{diff}} = \Delta W_{\mathrm{s}} - \Delta W_{\mathrm{f}} \approx 22.5\,\mathrm{MeV}$ on a dechirping distance of $z_{\mathrm{dechirp}} = 11\,\mathrm{cm}$. This suggests a dechirping efficiency of $\eta_{\mathrm{dechirp}} = \Delta W_{\mathrm{diff}}/\Delta z_{\mathrm{dechirp}} \approx 2\,\mathrm{GeV/m}$. Note, the dechirping efficiency is one order of magnitude better than state-of-the-art methods.

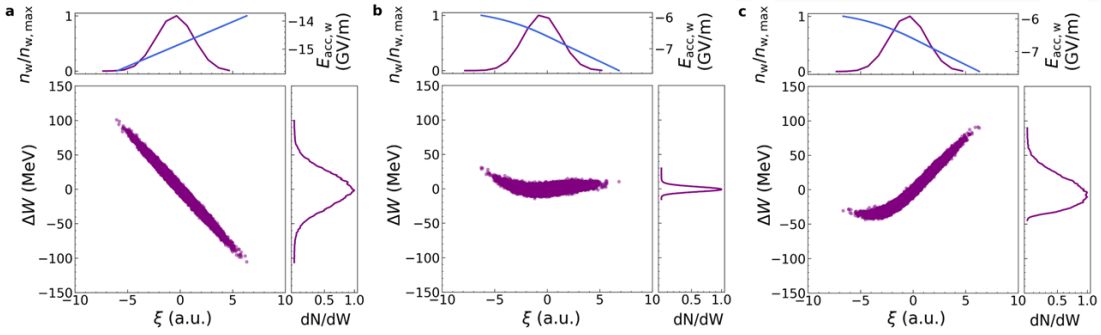

Figure 5.5: **Reduced model calculation of a witness beam's longitudinal phase space evolution during acceleration and dechirping.** Reduced model calculation of a witness beam's longitudinal phase space evolution during acceleration and dechirping in a single PWFA stage. Witness beam longitudinal phase space is presented just before escort bunch release (a), at the optimum dechirping (b) and overcompensation (c). The top and right panels show the charge projection (purple lines) to the corresponding axis, and the local longitudinal wakefield (blue line) experienced by the witness beam is overlaid in the top panels.

Beyond that optimum dechirping point, the energy spread increases again because of the overcompensation.

In principle, this dechirping method applies to any configuration of injection methods in PWFA or LWFA. However, the highest benefit is gained for witness beams with cutting-edge emittance and ultra-high 5D brightness. The plasma photocathode injection technique is a prime candidate for promising electron beams with ultra-high 5D brightness compared with state-of-the-art and existing plasma-based accelerators, respectively. Therefore, sufficiently dechirping an ultra-high 5D brightness electron beam has the potential to produce electron beams with unprecedented 6D brightness. The versatile capabilities of the plasma photocathode injectors in PWFA enable the generation of multi-bunches [120]. This makes the plasma photocathode method a natural fit for this dechirping scheme. The following section (5.1.4) scrutinises the dechirping concept developed in this section with a proof-of-concept 3D PIC simulation. The configuration in figure (5.7) schematically shows a potential setup for such a multi-bunch injector configuration, which is approximated in the 3D PIC simulation.

In figure (5.7), a pre-ionization laser pulse generates a sufficiently wide plasma source, counter-propagating from the bottom right, ionizing a background LIT medium. A relativistic electron driver beam (red) from the top left sets up the blowout. A beam

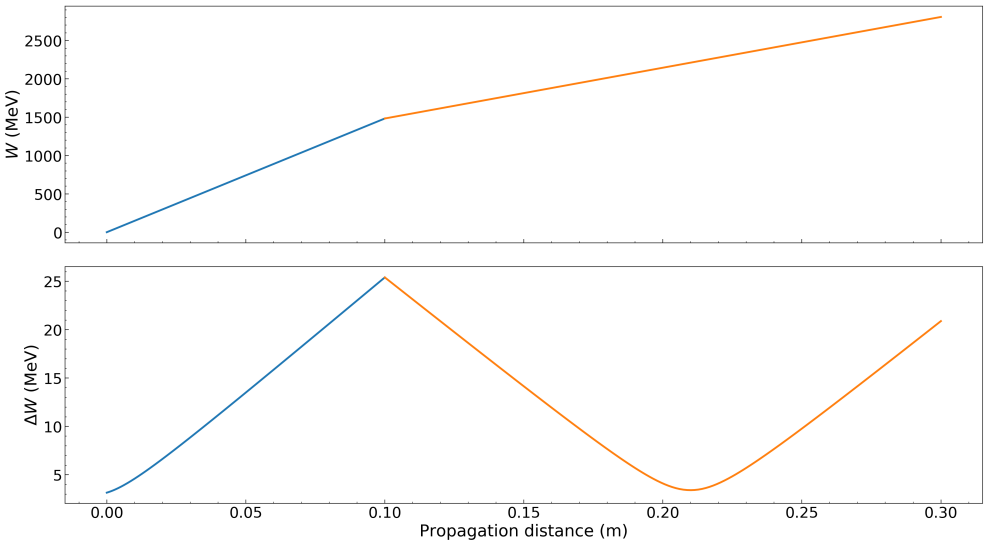

Figure 5.6: **Cold fluid reduced model-based witness beam parameter evolution calculations during acceleration and dechirping.** Witness beam parameter evolution during acceleration and dechirping. The evolution of energy (top) and absolute energy spread (bottom) before (blue solid line) and after (orange solid line) escort bunch release is displayed. At the optimum dechirping point, the accumulated energy chirp is nearly cancelled.

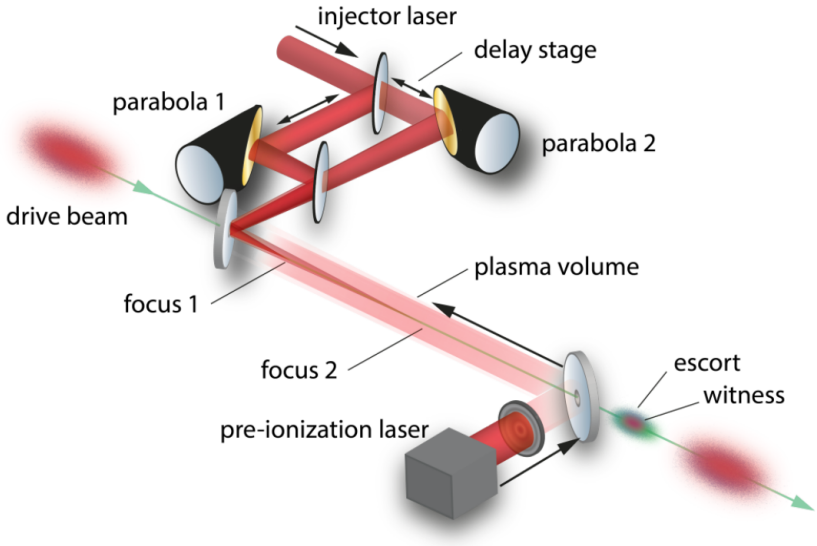

Figure 5.7: **Escort-based dechirper setup.** A potential experimental configuration for the escort-bunch-based energy chirp compensation approach. Produced by the author for [42] jointly with P. Scherkl. This work is openly licensed via CC BY 4.0.

splitter divides the main injector laser pulse into two laser arms, which can be individually focused by their parabolas with corresponding f-numbers. In this configuration, the *injector laser pulse 1* is tightly focused by *parabola 1* and reaches its focal point (*focus 1*) at the start of the PWFA stage. This low-intensity laser pulse ionizes a background HIT medium and liberates ultra-cold electrons directly inside the wakefield, resulting in an ultra-high 5D brightness witness beam. At the later position in the plasma stage, the *second injector laser pulse* with slightly higher intensity reaches its focal position (*focus 2*) and releases a high-charge escort bunch. The release phase of the escort bunch within the wakefields is set such that the trapped escort bunch position overlaps with the witness beam. The dechirping of the high-quality witness beam commences when the charge density of the escort bunch is sufficiently high, such that the local wakefield is overloaded. A significant advantage of this all-optical configuration is that all laser pulses originate from the same laser system. Hence, they intrinsically exhibit temporal synchronization. Once the plasma photocathode injector is realized in the collinear geometry, an additional laser pulse for the escort bunch does not impose significant additional conceptual complexity.

5.1.4 *Proof-of-principle 3D Particle-In-Cell simulation*

This section presents a proof-of-concept 3D PIC simulation of the escort-bunch-based dechirping in a single plasma photocathode PWFA stage. The 3D PIC simulation enables studying the full extent of this configuration while considering various dynamics and interaction effects, for example, resolving the electron driver beam and wakefield interaction or the trapping dynamics of a witness and escort beam, respectively. The main goal of this modelling effort is to showcase the feasibility of this dechirping method while maintaining the computational costs and complexity at a manageable level. Therefore, for this study, a plasma wavelength of $\lambda_p \approx 100\,\mu$m has been chosen. This keeps the simulation box size small enough to enable simulation over multi-cm while allowing sufficiently small grid resolution to resolve relevant physics (see appendix (8.2.2) for simulation box details).

The short plasma wavelength prohibits using the typically hydrogen/helium mixtures for the LIT/HIT combination because of the electron driver beam ionization hot spots resulting in dark current in PWFA as discussed in section (4.2). Therefore, the

plasma medium here comprises a preionized lithium vapour of density $n_\mathrm{p} = n_\mathrm{LIT} \approx 1.1 \times 10^{17}\,\mathrm{cm}^{-3}$ (similar configuration as in early PWFA experiments at FACET [37] and seminal plasma photocathode paper [144]) corresponding to a plasma wavelength of $\lambda_\mathrm{p} \approx 100\,\mu\mathrm{m}$. The HIT medium for the plasma photocathode lasers is simply the next ionization level of lithium ions Li^+ with the ionization energy of $I_{\mathrm{pot,Li^+}} = 75.64\,\mathrm{eV}$. Hence, the density of the HIT medium is the same as the plasma density $n_\mathrm{HIT} = n_\mathrm{p}$. This relatively high ionization threshold of Li^+ compared to helium $I_\mathrm{He} = 24.58\,\mathrm{eV}$ mitigates driver beam ionization for a broader range of electron driver beam parameters.

An ultra-relativistic bi-Gaussian electron beam of $Q_\mathrm{d} = 2\,\mathrm{nC}$ charge at a mean energy of $W_\mathrm{d} \approx 10\,\mathrm{GeV}$ with $\Delta W/W_\mathrm{d} = 1\,\%$ relative energy spread excites the plasma wakefield. The driver beam is compressed to a r.m.s length of $\sigma_\mathrm{z,d} \approx 20\,\mu\mathrm{m}$ for resonant wake excitation and is focused down to $\sigma_\mathrm{y,x,d} \approx 7.5\,\mu\mathrm{m}$ in both transverse dimensions with a normalized emittance of $\epsilon_\mathrm{y,x,n} = 5\,\mathrm{mm\text{-}mrad}$. This results in a "pencil"-like driver beam with peak density $n_\mathrm{d} \approx 6.4 \times n_p$, which exceeds the blowout condition by a margin and drives a strong wakefield. A strong wakefield ensures that the electrostatic trapping potential is $\Delta\Psi \leq -1$, allowing plasma photocathode injection in the PWFA stage. At the same time, the wakefield and electron driver beam are tuned for a dark-current-free operation of the accelerator. The electron driver beam parameters are well within the specification of the SLAC FACET-II [296, 298] facility. Key results of this study are discussed in figures (5.8)-(5.11).

Figure (5.8) shows snapshots of the wakefield at different positions in the laboratory frame along the PIC simulation. In (a), the wakefield (colour-coded) is established by the relativistic driver beam (red dots) moving to the right. The blue solid line shows the longitudinal on-axis wakefield with peak accelerating gradient field of the order of $E_\mathrm{z,peak} \approx 80\,\mathrm{GV/m}$ at the rear of the blowout. Here, the first plasma photocathode laser pulse of FWHM pulse duration of $\tau_\mathrm{0,w} = 25\,\mathrm{fs}$ with a normalized intensity of $a_\mathrm{0,w} = 0.1$ and r.m.s spot size of $w_\mathrm{0,w} = 7\,\mu\mathrm{m}$ is at its focal point and is in the process of releasing Li^+-electrons (purple dots) at a co-moving distance of $\Delta\xi_\mathrm{w,rel} \approx 50\,\mu\mathrm{m}$ from the electron driver beam centre of mass position. Because the intensity of the laser pulse is just above the tunnel ionization threshold of Li^+, the released electrons are cold [144, 145] (see also discussion on laser ionization in section (3.1.4)). Combined with the confined ionization volume, the occupied transverse phase space is compact, resulting in ultra-low normalized emittance values of a few tens of $\epsilon_\mathrm{n} \sim$ nm-rad. Normalized emittance

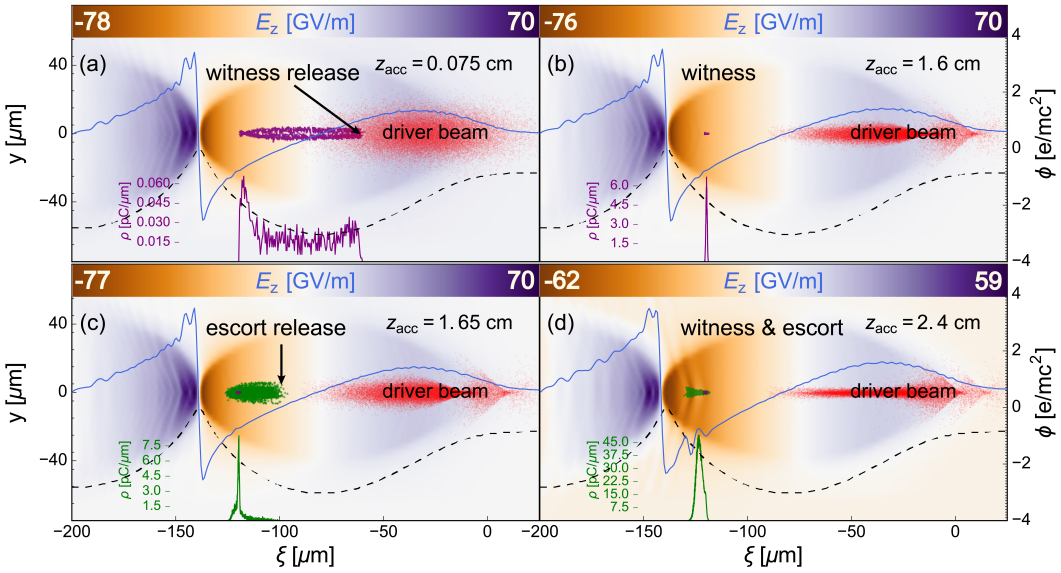

Figure 5.8: **Snapshots of a 3D PIC simulation of the novel dechirping concept.** It shows the FACET-II-like electron driver beam (red dots) drives a PWFA stage in the blowout regime, evidenced by the on-axis longitudinal electric field E_z (blue solid line). The electrostatic on-axis potential ϕ is shown as a black dashed line and reveals the ability of the blowout to trap electrons from rest. The witness beam longitudinal charge profiles are presented as a purple solid line, and the escort bunch is shown as a green solid line. The plasma photocathode ionization front is not shown in (a), which releases the witness beam electrons (purple dots) by ionizing the lithium ions. In (b), the witness beam is fully formed and accelerated to an energy of $W \approx 500\,\mathrm{MeV}$. In (c), the escort bunch is released, beginning to overload the wakefield, and in (d), the escort bunch is entirely trapped, overlaps with the witness beam spatially, and reverses the local accelerating field slope, causing the witness beam to dechirp. Produced by the author for [42]. This work is openly licensed via CC BY 4.0.

degradation due to space charge repulsive effects is minimized thanks to the rapid acceleration of the witness beam to relativistic energies, which allows the initial thermal emittance to be maintained. The total charge released by the laser pulse amounts to 5 pC and is quickly velocity compressed to a maximum length of $\sigma_{z,max} \approx 2\,\mu$m resulting in a peak current of $I_{peak} \approx 2.0\,$kA. After the witness beam is fully formed, it is further accelerated to high energies in the dephasing-free wakefield. After an acceleration distance of $\Delta z_{acc} \approx 1.525\,$cm the witness beam gained $W_w \approx 500\,$MeV energy (see figure (5.8) (b)). This makes the witness beam relativistically immune to space charge effects thanks to the $\mathbf{F_{sc}} \propto \gamma_{rel}^{-2}$ scaling. In figure (5.8) (c) the much longer $\tau_{0,esc} = 80\,$fs escort bunch laser pulse with a higher normalized intensity of $a_{0,esc} = 0.11$ and a r.m.s spot size of $w_{0,esc} = 10\,\mu$m reaches its focal point at $z_{acc} = 1.65\,$cm. It releases Li^+ electrons (green dots) at a distance of $\Delta\xi_{esc,rel} \approx 80\,\mu$m from the driver beam centre. The total charge of $Q_{esc} \approx 184\,$pC is trapped and is compressed to a maximum bunch length of $\sigma_{z,max} \approx 11\,\mu$m at the witness beam trapping position. Figure (5.8) (d) displays spatially overlapped escort bunch (green dots) and witness beam (purple dots). The longitudinal on-axis wakefield shows that the escort bunch peak current of $I_{esc,peak} \approx 14\,$kA suffices to overload the wakefield at the witness beam trapping position. The witness beam is fully engulfed within the dechirping region produced by the escort bunch. This is possible because the injector laser pulse is specifically designed to produce a long enough escort bunch, as the length of the escort bunch defines the overall dechirping region. The production of witness and escort beams with significantly different properties is only possible because both injector laser pulses can be independently adjusted and tuned for their respective purposes. The versatile nature of the plasma photocathode injection method is highly advantageous in this scenario.

Two factors are leveraged to produce a long escort bunch. Increased ionization volume in the trapping potential, in combination with beam loading and space charge effects, is exploited during the trapping process to produce a long escort bunch. The longer injector laser for the escort bunch exhibits an increased spread of the ionization front compared to the witness beam laser pulse. Therefore, the release volume maps a larger region of the trapping potential, resulting in an overall longer escort bunch. Then, during the trapping process, beam loading and space charge fields of already trapped electrons prevent trapping at similar co-moving positions and result in the elongation of the escort bunch. Overall, this naturally helps to enlarge the dechirping region and

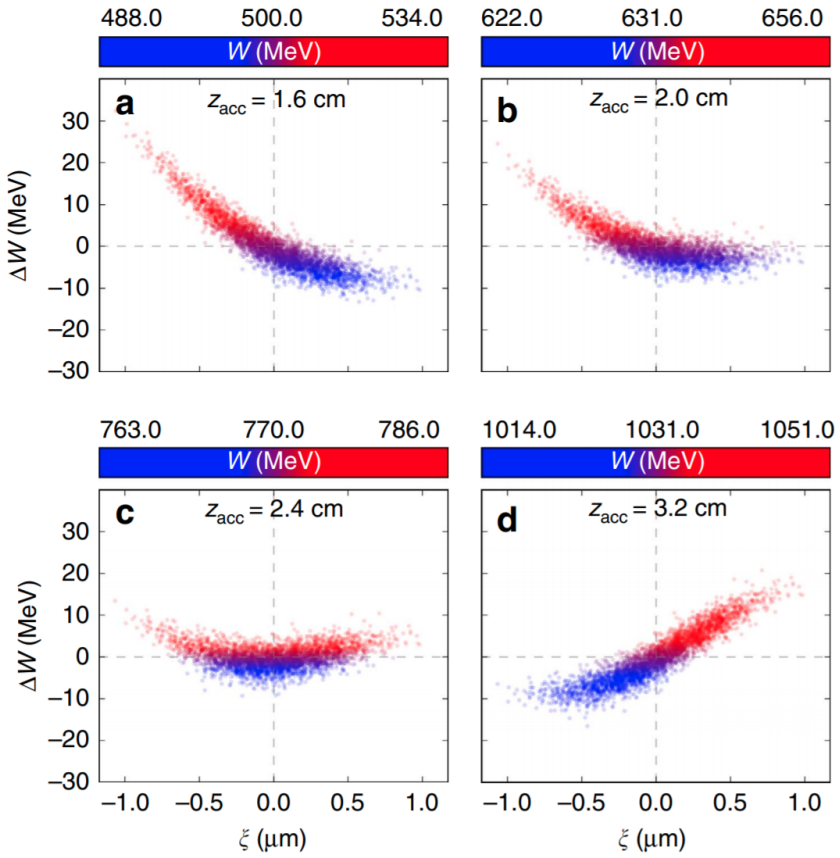

Figure 5.9: **3D PIC-simulation results of the longitudinal phase space evolution.** 3D PIC-simulation results are depicted, showing the longitudinal phase space evolution of the negative chirped witness beam just before escort bunch release (a), after dechirping distance of $\Delta z_{acc} = 0.35\,\text{cm}$ (b) and at $z_{acc} = 2.4\,\text{cm}$ at optimum dechirping (c). Continued propagation results in further counter-clockwise phase-space rotation and drives the witness beam to accumulate positive energy chirp. Produced by the author for [42]. This work is openly licensed via CC BY 4.0.

may provide an intrinsic remedy against potential laser pulse timing jitters. Overall, the overloading region is formed as predicted by the considerations in section (5.1.2) and dechirping of the witness beam is observed, as discussed below.

Figure (5.9) displays the evolution of the longitudinal phase space of the witness beam during the dechirping process. In (a), the witness beam longitudinal phase space is shown at the laboratory frame position $z_{acc} \approx 1.6\,\text{cm}$ just before the escort bunch release. Here, the witness beam is accelerated for approximately $\Delta z_{acc} \approx 1.525\,\text{cm}$ and exhibits a typical negative energy chirp inherent to plasma-based accelerators. When the escort bunch is released at $z_{acc} \approx 1.65\,\text{cm}$ (see figure (5.8) (c)) and is entirely trapped at the witness beam position the dechirping process sets in. In (b), the longitudinal phase

space of the witness beam is already rotated counter-clockwise while the overloaded local wakefield further accelerates the witness beam to higher energies. This observation aligns with the predictions from the semi-analytical model introduced in section (5.1.2). In (c), the energy chirp of the witness beam is compensated. The absolute energy spread is reduced down to a minimum value of $\Delta W_{\mathrm{rms}} \approx 2.56\,\mathrm{MeV}$ at a mean energy of $W_{\mathrm{mean}} \approx 770\,\mathrm{MeV}$. This optimum dechirping position is considered for extraction from the plasma stage, for example, for FEL or other applications demanding low-energy spread beams. In (d), the acceleration and dechirping process is continued. As a result, the witness beam phase space rotates further counter-clockwise. Eventually, it accumulates a positive energy chirp such that the head of the witness beam has higher energy than the tail.

The plasma photocathode injection method can potentially produce witness beams with unprecedented 5D brightness. A minimized energy spread will transform an initially ultra-high brightness beam into a witness beam with unprecedented 6D brightness, a key milestone towards an ultra-high gain FEL interaction. Therefore, witness beam quality preservation during the dechirping process is a mandatory requirement. Figure (5.10) summarises the evolution of crucial witness beam properties during the acceleration and dechirping process. In (a), the witness beam gains energy (black solid line) linearly from the injection position at $z_{\mathrm{i}} \approx 0.075\,\mathrm{cm}$ over the entire simulation distance. The absolute energy spread growth as a result of negative energy chirp accumulation to a maximum value of $\Delta W \approx 6.36\,\mathrm{MeV}$ at $z_{\mathrm{acc}} = 1.6\,\mathrm{cm}$. The escort bunch injector laser starts to release electrons at $z_{\mathrm{acc}} > 1.6\,\mathrm{cm}$. This is approximately one Rayleigh length $Z_{\mathrm{R,esc}} \approx 392\,\mu\mathrm{m}$ before it reaches its focal point at $z_{\mathrm{acc}} = 1.65\,\mathrm{cm}$ where the laser ionization is peaking and decreases beyond that point when the laser pulse starts diffracting. The trapped escort bunch starts to overload the wakefield locally and induces the dechirping of the witness beam. After escort bunch release, the absolute energy spread decreases in a parabolic-like shape to a minimum value of $\Delta W_{\mathrm{rms,min}} \approx 2.56\,\mathrm{MeV}$ at the optimum dechirping position $z_{\mathrm{opt}} = 2.4\,\mathrm{cm}$ (see figure (5.9) (c)). The relative energy spread at this position is reduced by approximately one order of magnitude from $\Delta W_{\mathrm{rms,max}}/W_{\mathrm{mean}} \approx 1.3\,\%$ to $\Delta W_{\mathrm{rms,min}}/W_{\mathrm{mean}} \approx 0.3\,\%$ at the optimum dechirping position at the mean witness beam energy of $W_{\mathrm{mean}} \approx 770\,\mathrm{MeV}$ (see figure (5.10) (b)). This corresponds to a dechirping efficiency of $\eta_{\mathrm{dechirp}} \approx 500\,\mathrm{MeV/m}$. The dechirping efficiency is by a factor of four smaller than in the theoretical scenario in section (5.1.3)

because the overloaded region slope in the PIC simulation is shallow compared to the theoretical case. In (b), the relative energy spread (dashed blue line) follows a similar trend as the absolute energy spread with an equivalent minimum position.

In figure (5.10) (b), during the initial trapping and then acceleration phase, the normalized emittance (black solid line) in both planes decreases to a minimum value $\epsilon_{\mathrm{n}} \approx 26\,\mathrm{nm\text{-}rad}$ at $z_{\mathrm{acc}} = 0.6\,\mathrm{cm}$ and increases beyond this point likely because of phase-mixing and decoherence of the phase space due to the accumulation of negative energy chirp. Chromatic emittance growth nearly stops when dechirping is initiated, such that the normalized emittance saturates at $\epsilon_{\mathrm{n}} \approx 32\,\mathrm{nm\text{-}rad}$. In section (5.2.3), results from a comparable scenario reveal that without dechirping, the normalized emittance at the plasma stage exit may increase by a factor of two. Emittance preservation is important because of its strong dependency in 5D (6D) brightness $B_{\mathrm{5D,6D}} \propto \epsilon_{\mathrm{n}}^{-2}$. Hence, the emittance strongly dominates the evolution and the reach of the 5D (6D) brightness of the witness beam, as evident from the figure (5.10) (c). The 6D brightness additionally considers the relative energy spread of the witness beam. The 5D brightness (black solid line) at the optimum dechirping point is at an unprecedented level of $B_{\mathrm{5D}} \approx 2.0{\times}10^{18}\,\mathrm{A/m^2rad^2}$ and thanks to the minimized relative energy spread the 6D brightness of the witness beam is peaking at record values of $B_{\mathrm{6D}} \approx 5.5 \times 10^{17}\,\mathrm{A/m^2rad^2/0.1\%bw}$ as well. Beyond the optimum dechirping point, the 5D brightness remains unchanged. However, the 6D brightness declines because the witness beam starts accumulating a positive energy chirp, and the relative energy spread increases, as shown in figure (5.10) (b). Therefore, for beams with the highest 6D brightness, the optimum dechirping position is an ideal extraction point from the plasma stage.

In any PWFA, separation of the energy-depleted electron driver beam and the high-quality witness beam is desirable or even required for clean utilisation of these high-quality witness beams for applications. Foremost, a well-defined and isolated witness beam at the entrance of an undulator will enable clean XFEL photon production, as suggested in chapter (6). Therefore, the high-quality witness should be isolated from the energy-depleted driver beam without quality loss in a dedicated electron beam line downstream of the plasma stage. The energy difference between the electron driver and the witness beam can be leveraged to separate these charge populations by introducing a dispersion section in a beam transport line. A standard chicane can achieve such a dispersion section (see section (2.1.4) on chicane), which will enforce path differences

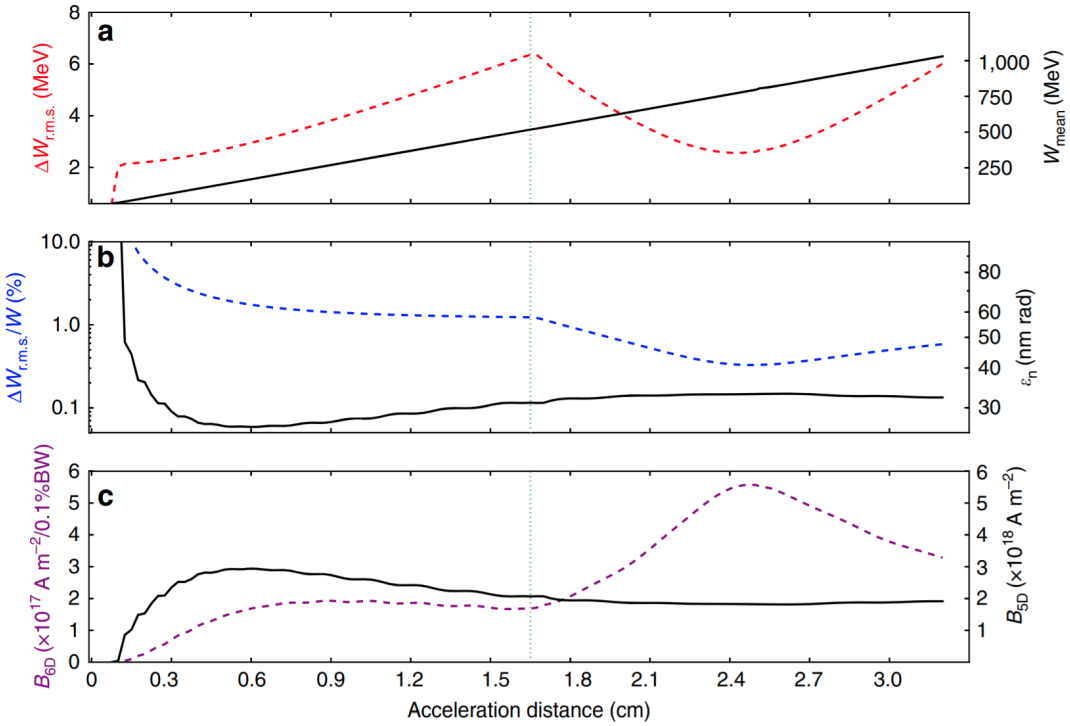

Figure 5.10: **Witness beam parameter evolution along the acceleration and dechirping in the PWFA stage.** Data shows the evolution of witness beam parameters from the point of witness release up to the overdechirping stage. In (a), average energy W_{mean} (black solid line) and r.m.s energy spread ΔW_{rms} (red dashed line) are plotted. In (b), relative energy spread $\Delta W_{\mathrm{rms}}/W$ (blue dashed line) and normalized transverse emittance ϵ_{n} (black solid line), and in (c), 6D (purple dashed line) and 5D (black solid line) brightness are presented. The escort bunch is released at the laboratory position of $z_{\mathrm{acc}} = 1.65\,\mathrm{cm}$ (indicated by a green dotted line), leading to the onset of witness beam dechirping. At the optimum point of $z_{\mathrm{acc}} = 2.4\,\mathrm{cm}$ in the laboratory frame, the minimum value of ΔW_{rms} is reached, leading to the maximum 6D brightness. Produced by the author for [42]. This work is openly licensed via CC BY 4.0.

for the two charge populations due to the energy-dependent bending angle in dipoles. In this case, the chicane also has the additional function of separating the escort bunch from the witness beam. This does not introduce additional complexity because of the sufficient energy separation between the escort bunch and witness beam, as highlighted in figure (5.11). In chapter (6), a beam transport line, including a dedicated separation line, is designed for the plasma-based XFEL. Additionally, controlled separation of the beams may allow exploiting the driver and escort beams to be integrated into an energy recovery scheme for high wall-plug efficiency of a PWFA stage [327]. While the escort bunch has significantly lower brightness than the witness beam from a plasma photocathode perspective, it is still exceptional compared to state-of-the-art beams and, therefore, may be employed for less demanding applications [40, 41].

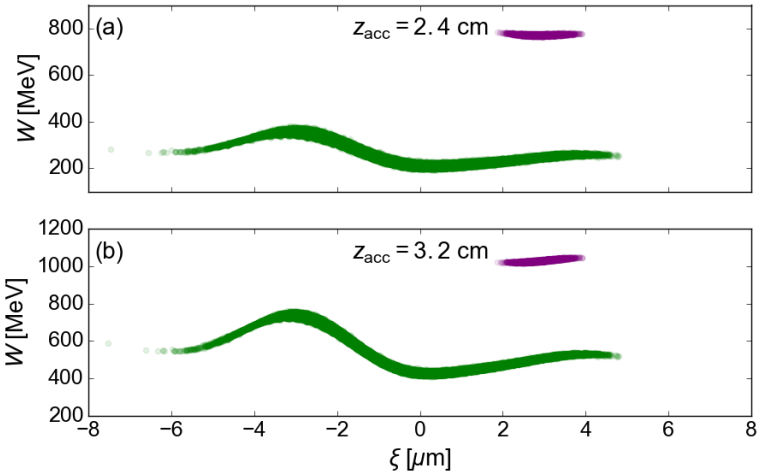

Figure 5.11: **Longitudinal phase space of escort and witness beam at the end of the PWFA stage**. The longitudinal phase space of the witness beam (purple) and escort bunch (green) is shown at the end of the plasma stage. The witness beam has a flat phase space and has significantly higher energy than the escort bunch. Produced by the author for [42]. This work is openly licensed via CC BY 4.0.

Summarizing, the proof-of-concept 3D PIC simulation demonstrates that the escort bunch dechirping method is feasible and enables reduction of the relative energy spread of an ultra-high 5D brightness beam by one order of magnitude down to 0.3 % level in a single PWFA stage while preserving witness beam normalized emittance ϵ_n at the tens of nm-rad level during the dechirping process. The minimum absolute energy spread is minimized to $\Delta W_{\mathrm{rms,min}} \approx 2.56\,\mathrm{MeV}$, which corresponds to the initial residual absolute energy spread ΔW_{res}. Assuming that this residual energy spread is a constant quantity,

then simple considerations suggest that dechirping at higher energies may allow achieving lower relative energy spread values because of the adiabatic damping of the relative energy spread with increasing witness beam energies $\propto \Delta W_{\mathrm{res}}/W_{\mathrm{mean}}$. The reduced relative energy spread, in combination with the already ultra-high 5D brightness witness beam, opens up the path towards witness beams with unprecedented 6D brightness, peaking at record values of $B_{\mathrm{6D}} \approx 5.5 \times 10^{17}\,\mathrm{A/m^2rad^2/0.1\%bw}$ in this study. For comparison the 6D brightness reach of existing and upcoming state-of-the-art facilities is $B_{\mathrm{6D}} \approx 7.0 \times 10^{15}\,\mathrm{A/m^2rad^2/0.1\%bw}$ (EuXFEL), $B_{\mathrm{6D}} \approx 5.0 \times 10^{15}\,\mathrm{A/m^2rad^2/0.1\%bw}$ (SACLA), and $B_{\mathrm{6D}} \approx 1.4 \times 10^{16}\,\mathrm{A/m^2rad^2/0.1\%bw}$ (LCLS-II) [328]. The 6D brightness values of the witness beam exceed state-of-the-art rf-based accelerators by orders of magnitude, even at considerably lower witness beam energy. Reducing the residual energy spread and dechirping at higher energies may produce much higher 6D brightness witness beams. Section (5.2) investigates pathways to increase the 6D brightness reach of this new class of witness beams by understanding the origin of the residual energy spread and determining the limitations and the stability of this approach.

5.2 CAPABILITIES AND LIMITATIONS OF THE ENERGY CHIRP COMPENSATION APPROACH

This section explores the origin of the residual energy spread and the theoretical reach of energy spread of witness beams produced via the plasma photocathode. Then, the impact of spatiotemporal jitters of the injector lasers is discussed, and the effects on the minimum obtainable energy spread are investigated. Finally, extracting the witness beam from the plasma stage is explored through various extraction downramps while applying witness beam dechirping. The findings from these sections are an integral part of the conceptual design of the plasma-based XFEL in chapter (6).

5.2.1 *Witness beam energy spread reach*

The witness beam's projected (slice) energy spread is an elementary parameter for the XFEL performance. Therefore, this section investigates the origin of the residual energy spread ΔW_{res}, which remains after dechirping and determines the minimum achievable relative projected and slice energy spread of the witness beam.

In the PIC simulation presented in section (5.1.4), electrons liberated from the parent atoms with the plasma photocathode laser are labelled with unique tags of increasing float numbers corresponding to their "birth time". Particles released first have a lower tag number than particles released later, and the evolution of individual macroparticles of the witness beam is observed during the release, trapping and acceleration process. This procedure allows for monitoring the formation of the longitudinal phase space of the witness beam and enables a deeper investigation of the process.

Figure (5.12) shows the longitudinal phase space of the witness beam at the optimum dechirping position, colour-coded with the particle tags. It shows that particles released first (blue) have higher energy than particles released last (red). This leads to an energy deviation from the mean energy and defines the width of the energy deviation, representing the maximum residual energy spread of the witness beam. This observation suggests that the plasma photocathode laser pulse and the plasma wakefield accelerator may largely determine the residual energy spread. A similar observation in related schemes in LWFA is also reported [329], but quantification has not yet been provided. Therefore, a scaling law for the residual energy spread of the witness beam is derived based on the observation made in the PIC simulation.

A few assumptions are needed to simplify the algebra. The blowout is assumed to be strong enough to support plasma photocathode injection. The charge density of the witness beam is sufficiently low compared with the plasma density $n_\mathrm{w} \ll n_\mathrm{p}$; therefore, beam loading effects are negligible during the trapping process. Further, the injector laser pulse duration is significantly smaller than the inverse of the plasma frequency $\tau_0 \ll \omega_\mathrm{p}^{-1}$. Hence, the ionization front movement of the laser pulse is negligible compared with the blowout length, such that electrons are released at the same wakefield phase. As a direct consequence, particles are released at the same trapping potential value and, therefore, are trapped at approximately the same position in the rear of the wakefield. Finally, the laser pulse waist is much smaller than the blowout radius $w_0 \ll R_\mathrm{b}$, constraining the betatron amplitude of the particles during the release process.

Consider a plasma photocathode laser pulse reaching its focal point at $z_\mathrm{w,focus}$ with an a_0 just above the tunnel ionization threshold of a HIT medium. The laser pulse starts exceeding the ionization threshold approximately at one Rayleigh length Z_R before the focal point (see section (3.1.4) for laser ionization), meaning that the first electron e_1^- is released at $z_\mathrm{ioniz,i} = z_\mathrm{w,focus} - Z_\mathrm{R}$. The ionization increases at the focal

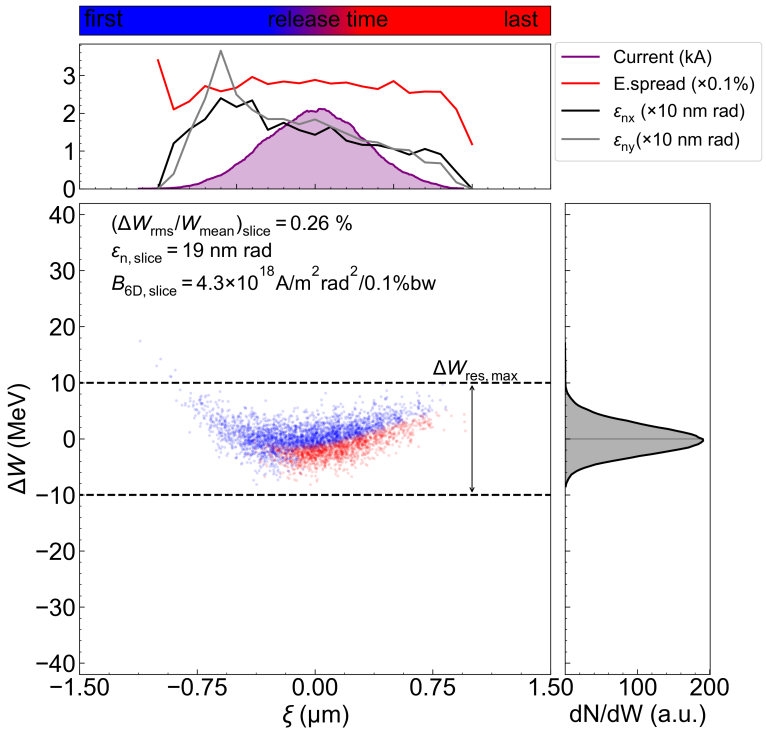

Figure 5.12: **Witness beam longitudinal phase space at the optimum dechirping.** Witness beam longitudinal phase space at the optimum dechirping point colour-coded with birth time during the release process. Electrons released first in the wakefield are blue, and electrons released last are red. Slice witness properties are presented in the top panel. The energy spread projection is in the right panel. Produced by the author for [40, 42]. This work is openly licensed via CC BY 4.0.

point and decreases beyond that point because of laser pulse diffraction. The release of electrons stops one Rayleigh length after the focal point, meaning that the last electron e_2^- is released at $z_{\text{ioniz,f}} = z_{\text{w,focus}} + Z_{\text{R}}$. The total ionization length is then $\Delta z_{\text{ioniz}} = z_{\text{ioniz,f}} - z_{\text{ioniz,i}} = 2Z_{\text{R}}$. Therefore, the release time difference between the first and the last electron is $t_{\text{ioniz}} = 2Z_{\text{R}}/c$. This means when the last electron is released at rest by the time t_{ioniz}, the first electron has already been accelerated by a distance of $2Z_{\text{R}}$ in the laboratory frame at its trapping position in the co-moving frame and corresponding electric field $E_{\xi,\text{trap}}$. This difference in energy gain determines the residual energy deviation. With these considerations in mind, the maximum energy deviation or residual energy spread reads

$$\Delta W_{\text{res,max}} = W_1 - W_2, \tag{5.5}$$

where W_1 and W_2 are the energies of the first and last released electron, respectively. The first term in the expression is obtained by considering the acceleration of the first electron over a distance of $2Z_{\text{R}}$ at the trapping position by the corresponding electric field $E_{\xi,\text{trap}}$. Mathematically it reads

$$\Delta W_{\text{res,max}} = E_{\xi,\text{trap}} \times 2Z_{\text{R}}. \tag{5.6}$$

The second term in equation (5.5) vanishes because the last electron is born at rest, implying $W_2 = 0$.

Equation (5.6) computes the maximum absolute energy spread as a function of the accelerating electric field and injector laser *Rayleigh length*. However, a more common measure is given by the r.m.s value of the absolute energy spread. The spectral density of the witness beam has a Gaussian-like distribution, as depicted in figure (5.12) (left panel). The $5\sigma_{\text{rms}}$ range of this distribution takes approximately 99% of the witness beam particles into account, indicated by the horizontal black dashed lines. Therefore, the maximum energy deviation can be expressed as $\Delta W_{\text{res,max}} = 5 \times \Delta W_{\text{res,rms}}$. Rearranging this expression and plugging in the known quantities, yields for the r.m.s absolute energy spread in units of eV

$$\begin{aligned} \Delta W_{\text{res,rms}} &= \frac{\Delta W_{\text{res,max}}}{5} \\ &= \frac{2}{5} \times E_{\xi,\text{trap}} \times z_{\text{R}} \\ &= \frac{2\pi}{5} \times \frac{E_{\xi,\text{trap}} \times w_0^2}{\lambda_l}. \end{aligned} \tag{5.7}$$

The residual energy spread depends linearly on the accelerating gradient and is inversely proportional to the laser wavelength while strongly dependent on the laser spot size. Equation (5.7) has been presented in [42] and later confirmed and extended by [330]. The extension considers the ionization spread σ_Ψ in the injection phase as an additional factor in Eq.(5.6). However, as the following calculations show, this contribution is small due to the negligible ionization front movement. Eq.(5.7) predicts $\Delta W^{\mathrm{theo}}_{\mathrm{res,rms}} \approx 2.55\,\mathrm{MeV}$ for the r.m.s residual energy spread when considering $\lambda_\mathrm{l} = 800\,\mathrm{nm}$ wavelength laser pulse at a spot size of $w_0 = 7.0\,\mu\mathrm{m}$ and the electric field value of $|E_{\xi,\mathrm{trap}}| \approx 33.19\,\mathrm{GV/m}$ at the trapping position of the witness beam. This prediction is in excellent agreement with the 3D PIC simulation result of $\Delta W^{\mathrm{sim}}_{\mathrm{res,rms}} \approx 2.56\,\mathrm{MeV}$. The theoretical prediction and simulation deviate only by 0.4 % from the value provided by the scaling law. This substantial agreement between the PIC simulation and the simplified analysis indicates that the residual energy spread is predominantly determined by the release duration of electrons and the wakefield itself.

Further, one can approximate the electric field $E_{\mathrm{z,trap}}$ at the trapping position to generalize the model. For example, one may use the cold wave-breaking field in Eq.(3.24) or use more advanced wakefield models from section (3.2.2). However, the central objective of this exercise is to gain physical insight into the relation between residual energy spread and the plasma wavelength without introducing mathematical complexity. Therefore, the cold wave breaking field is considered here, which suffices for the purpose. Hence, the electric field at the trapping position is approximated by the cold wave breaking electric field $E_{\xi,\mathrm{trap}} \equiv E_0 = cm_\mathrm{e}\omega_\mathrm{p}/e = 2\pi c^2 m_\mathrm{e}/e\lambda_\mathrm{p}$, where the plasma frequency is substituted with $\omega_\mathrm{p} = 2\pi c/\lambda_\mathrm{p}$. Combining these considerations in Eq.(5.7) yields

$$\Delta W_{\mathrm{res,rms}} = \frac{4\pi^2 m_\mathrm{e} c^2}{5e} \times \frac{w_0^2}{\lambda_\mathrm{p}\lambda_\mathrm{l}}. \tag{5.8}$$

The residual energy spread is inversely proportional to the plasma wavelength. Further, equation (5.8) suggests that operation at a longer plasma wavelength will lead to a smaller residual energy spread. This finding aligns well with the general beam parameter stability strategy discussed in section (4.2). A larger blowout will result in higher beam parameter stability, simultaneously allowing for a smaller residual energy spread and reduced initial emittance due to minimized wakefield kicks, as discussed in section (4.2.2). Overall, operation at longer plasma wavelengths with a tightly focused injector laser pulse is a powerful strategy for minimizing the residual energy spread and enabling even

higher 6D brightness beams. This trend is reflected in figure (5.13) where the relative energy spread is plotted as a function of mean beam energy and plasma wavelength based on Eq.(5.8). In figure (5.13) (a) the injector laser spot size is $w_0 = 5\,\mu$m, while in (b) it is slightly larger with $w_0 = 7\,\mu$m. This shows that combining larger blowouts and smaller injector laser spot size can yield projected and slice relative energy spread values at the 0.1-0.01 %-level relevant for hard XFEL operation at a few GeV beam energies.

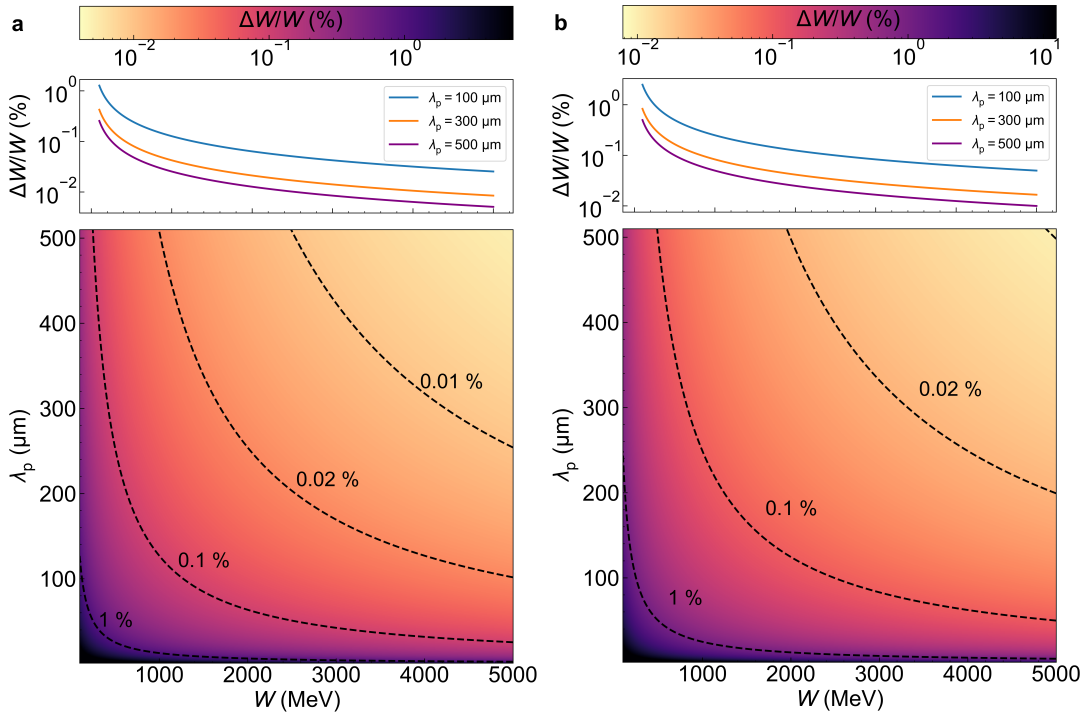

Figure 5.13: **The reach of relative energy spread.** Evaluation of Eq.(5.7)-(5.8) in terms of relative energy spread as a function of witness beam energy and plasma wavelength for two different injection laser waist sizes (5 μm (a) and 7 μm (b)). The top panel highlights the adiabatic decrease of the relative energy spread as a function of beam energy for a few selected plasma wavelengths.

In conclusion, a simple analytical model for the residual energy spread of the witness beam produced via plasma photocathode is developed and extended. Based on this model, plasma photocathode and PWFA stage parameters can be found to improve the quality of witness beams further. Key findings are that the projected and slice energy spread could be significantly enhanced by reducing ionisation volumes of the injector laser in the co-moving frame, operating the PWFA stage at longer plasma wavelengths, or decreasing wakefield amplitudes at the witness beam trapping position. Fortunately, these measures for improving the energy spread will also contribute to the reduction of

witness beam emittance and significantly increase the 6D brightness of witness beams. The prospects of harnessing these ultra-high 6D brightness witness beams for hard XFELs are highly promising. However, a crucial question remains: whether these witness beams can be dechirped at high stability and, more importantly if they survive the extraction from the plasma stage. These questions are addressed in the next section.

5.2.2 *Energy spread stability*

This section investigates the influences of spatiotemporal misalignment of the plasma photocathodes producing the witness and escort beam. This will reveal whether the minimum energy spread at the optimum dechirping can be produced reliably from shot-to-shot when plasma photocathode laser offsets concerning the wakefield are considered. As established in section (4.2.2), the temporal synchronization precision of the plasma photocathode has a minor impact on the final witness beam trapping position when operating near or at the trapping potential minimum. Additionally, the injector laser pulses for the witness and escort beams are inherently synchronized because escort and witness beam lasers originate from the same laser system, and, therefore, timing variation between both laser pulses is regarded as a secondary factor. A potential transverse offset of the injector laser pulse(s) concerning the wakefield axis and/or between both pulses is considered. It may impact the final relative energy spread and dechirping efficiency. The transverse offset of the escort bunch laser may not change the dechirping of the witness beam significantly due to the self-aligning feature of electrons released at rest via the plasma photocathode, as revealed in section (4.2.2). Therefore, the study in this section focuses on the impact of witness beam laser misalignment while escort-bunch-based dechirping is applied.

The 3D PIC simulation set-up in section (5.1.4) is a baseline case. Then, the witness beam injector laser pulse is misaligned by up to $8\,\mu$m in the transverse direction. Figure (5.14) shows the evolution of witness beam energy (a), absolute (relative) energy spread and energy chirp (b) after the escort bunch is released and trapped. The solid lines indicate the baseline case, and the shaded region indicates the standard deviation bands resulting from potential misalignment or shot-to-shot jitter of the plasma photocathode laser pulse. In figure (5.14), the standard deviation bands reveal that just before dechirping, the witness beams arrive at the escort bunch release position

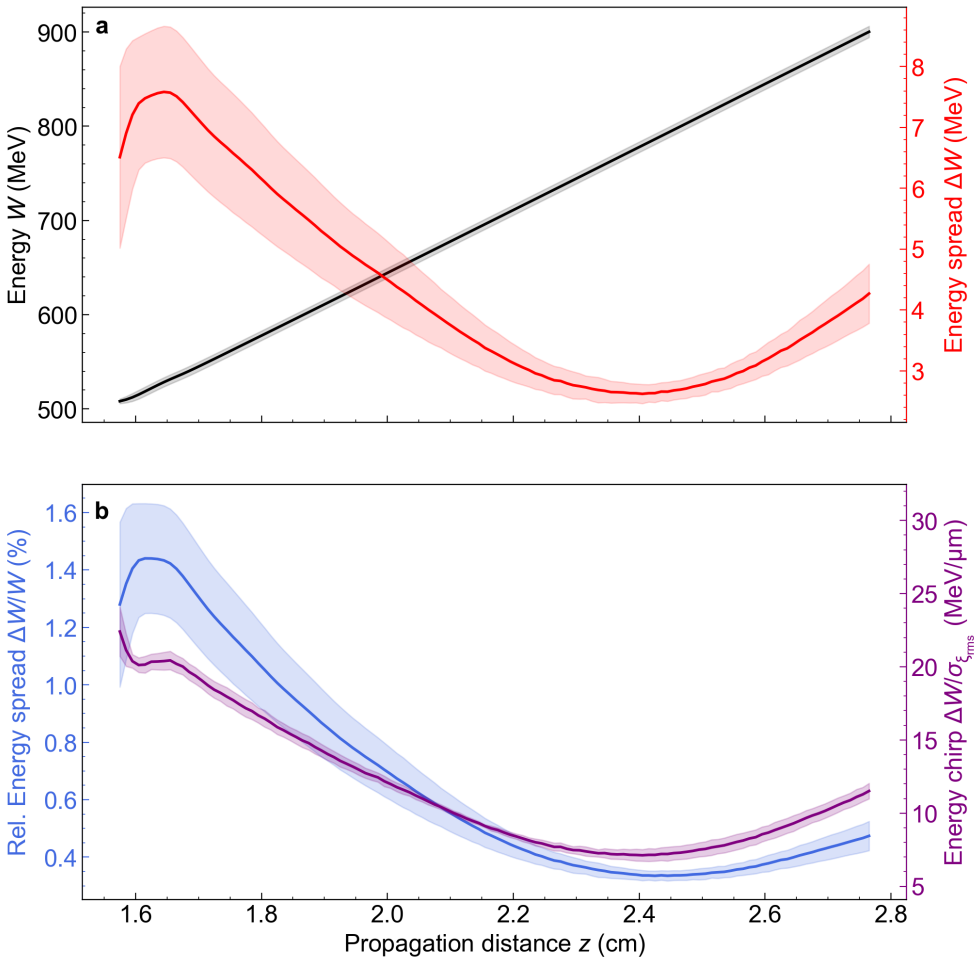

Figure 5.14: **Impact of witness beam injector laser misalignment on the stability and efficiency of the novel energy chirp compensation concept.** In (a), witness beam energy and absolute energy spread are presented. In (b), relative energy spread and energy chirp evolution are depicted during dechirping. The shaded regions indicate the confidence bands resulting from five transverse misalignment cases up to 8 μm. Produced by the author for [41]. This work is openly licensed via CC BY 4.0.

with different energy spreads. This can be attributed to slightly longer witness beams with trapping positions further towards the blowout vertex. However, at the minimum dechirping point, all beams approach similar minimum energy spread values at similar laboratory frame positions. This behaviour may contradict a linear translation of a jitter-to-beam parameter assumption. A closer look at the data in figure (5.15) reveals a *self-compensation effect*, which is discussed below.

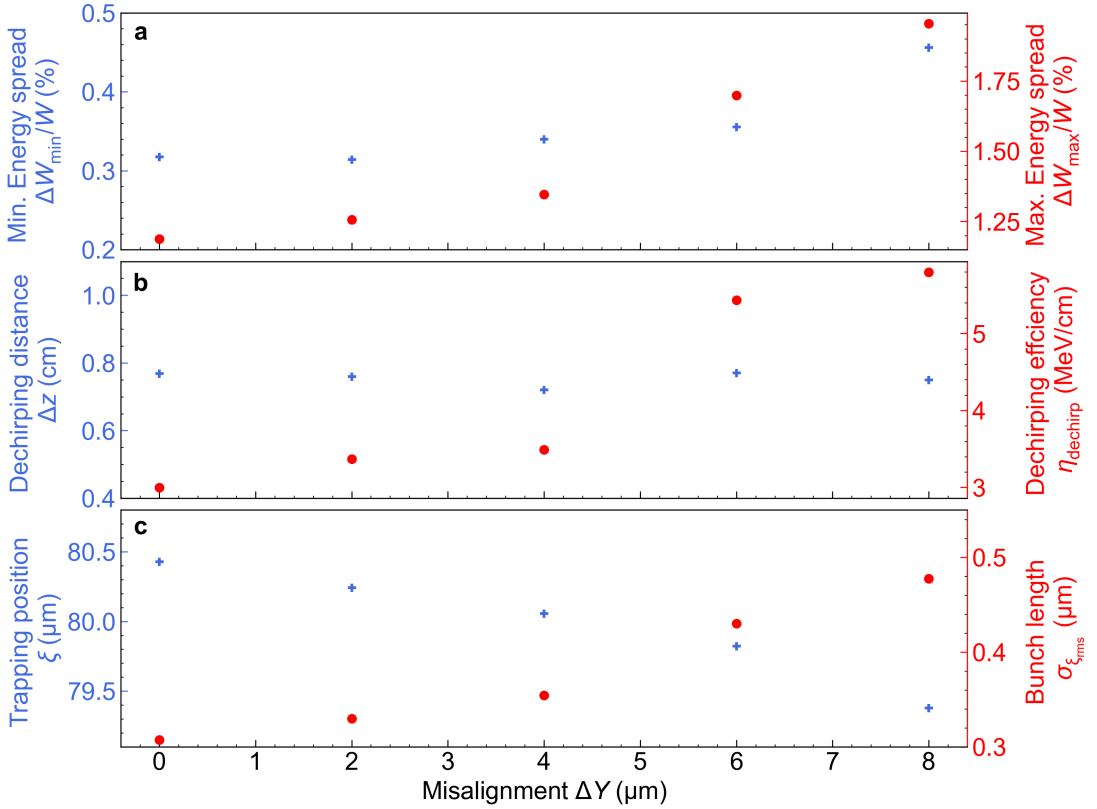

Figure 5.15: **Correlation of various parameters with the witness beam injector laser misalignment at the optimum dechirping point.** In (a), the minimum (at the optimum dechirping position) and maximum (just before escort release) relative energy spread are presented. In (b), dechirping distances and efficiency are displayed, and in (b), witness beam trapping position and witness beam length are plotted. Decreasing trapping positions correspond to wakefield phases closer to the blowout rear. Data published by the author in [43].

Indeed, figure (5.15) (a-b) supports the initial observation in Fig.(5.14) that the minimum energy spread and dechirping distances do not change significantly, even though the maximum relative energy spread increases with off-axis injection. Electrons released off-axis are trapped slightly more downstream in the wakefield because the

effective trapping potential is slightly lower, and the formed witness beam has a slightly longer duration (see figure (5.14) (c)). These longer witness beams sample a wider phase range of the wakefield, hence a larger range of accelerating electric field amplitudes, and as a result, will accumulate a larger energy spread from head to tail. However, during dechirping, the longer witness beam also covers a larger fraction of the dechirping area; hence, the dechirping efficiency increases and counteracts the larger energy chirp of the witness beams. This self-compensation is very interesting in its own right, and future work will investigate it. However, here, it ensures that the relative energy spread of the witness beams minimizes at a similar value and position at the plasma stage exit.

Summarising, misalignment of the injector laser pulse does not significantly impact the dechirping during the acceleration. Even transverse misalignment of the injector laser up to 8.0 μm in the transverse direction in a $\lambda_p \approx 100\,\mu$m does not impact the minimum achievable energy spread and dechirping point within the PWFA stage. This is enabled by a self-compensation effect counteracting the effects of injector laser misalignment on the witness beam by a self-adapting dechirping efficiency mechanism. These results are promising for exploiting ultra-high 6D brightness witness beams for applications such as hard XFELs in chapter (6).

5.2.3 *Extraction from the plasma stage*

Extracting the witness beam from the plasma stage is highly delicate because of the non-matched beam size and chromatic aberration; significant beam quality degradation may occur, as discussed in section (3.2.7). A density downramp at the desired position at the end of the plasma stage allows increasing the witness beam size gradually to a level manageable by conventional particle beam optics at the exit of the plasma stage (see detailed discussion in the results chapter (6)). Therefore, the extraction of witness beams from the plasma stage and beam quality preservation obtained significant attention in the scientific community (see section (3.2.7)). Additionally, the energy spread/chirp can degrade the beam quality dramatically during the extraction, characterised by rapid normalized emittance growth, compromising the brightness of the witness beam. To understand the impact of extraction from the plasma stage in the present scenario, the effects of extraction density downramps are investigated. The shape of these density ramps, $n \propto \exp(-z/L)$ and $n \propto \cos^2(z/L)$, where L is the length of the ramp, is largely

motivated by laser-produced plasma source in section (3.1.4) and chapter (4) but also other types of gas sources, such as plasma cells or gas jets may exhibit similar density shapes. The aim of this section is not to investigate the best possible extraction density ramp shape but rather to understand whatever the low energy spread and emittance survives the extraction from the plasma stage. Hence, the performance of the novel dechirping method in 3D PIC simulations and the impact on witness beam quality are evaluated.

A similar 3D PIC simulation setup as in section (5.1.4) is considered a baseline case. The witness beam is accelerated and is dechirped at the same position as in the previous simulations. However, now at the propagation distance of $z = 2\,\mathrm{cm}$ plasma density downramps of the form $n(z) \propto \cos^2(z/L)$ in Fig.(5.16) and $n(z) \propto \exp(-z/L)$ in Fig.(5.17) are implemented releasing the witness beam into the vacuum. The length of the ramps is scanned between $L_{\mathrm{ramp}} = 7 - 9\,\mathrm{mm}$ to understand the sensitivity of witness beam parameters to variations in downramp lengths. A reference case without dechirping and extraction is included for comparison (grey lines).

The primary purpose of these extraction ramps is a gentle reduction of the accelerating and focusing fields of the blowout, such that the witness beam may exit the plasma stage in an adiabatic fashion. Both types of ramps studied in this thesis achieve this at different rates along the propagation distance. However, the energy gain terminates quickly when the plasma density approaches approximately $n/n_{\mathrm{p}} \approx 0.5$. This happens much quicker for the exponential $n \propto e^{-z/L}$ ramp than for the $n \propto \cos^2(z/L)$ ramp. Therefore, ramp length variation has much less of an impact on the energy jitter with the $n \propto e^{-z/L}$ ramp, as evident from the relative energy jitter on the 0.1 %-scale. Overall, independent of the extraction ramp form factor and length, the minimum dechirping point and energy spread remain nearly invariant, as evident from the figure (5.16)-(5.17) and the absolute energy spread at the optimum dechirping point varies on the keV-scale for both cases. The dechirping action of the escort bunch is not affected by the extraction ramps because the slope of the dechirping region is already overloaded. Therefore, decreasing wakefield strength along the extraction ramps can not impact the dechirping region.

In figures (5.16)-(5.17) (c), the normalized emittance exhibits significant growth without dechirping and extraction due to phase mixing in the witness beam (grey solid lines). The dechirping is initiated at $z \approx 1.65\,\mathrm{cm}$ and the extraction density downramps are released at $z \approx 2\,\mathrm{cm}$. When dechirping is initiated, the emittance growth

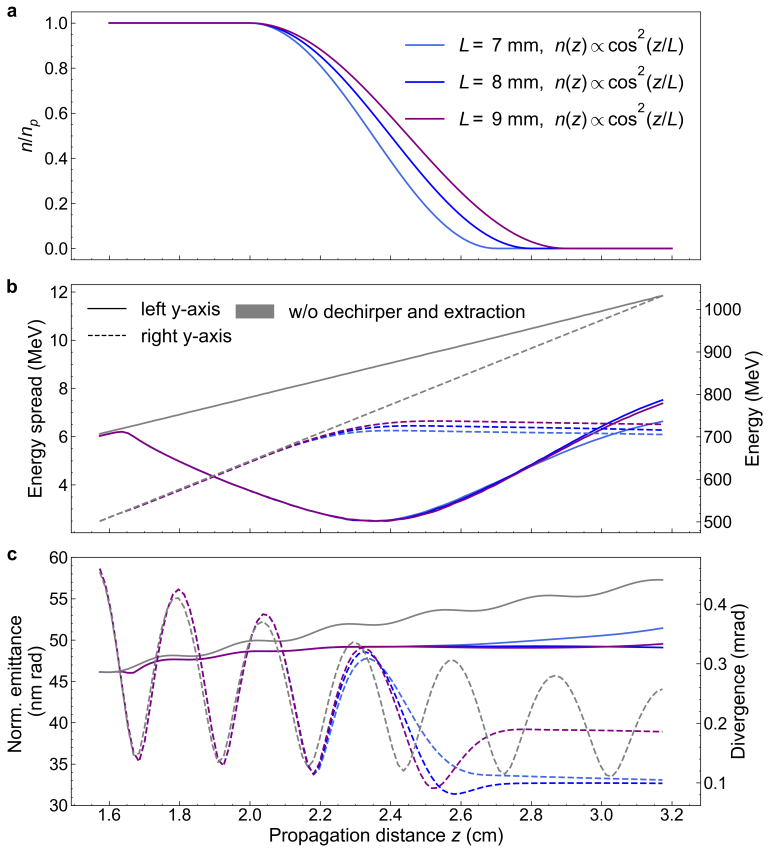

Figure 5.16: **Witness beam dechirping and extraction investigation based on 3D PIC simulation for a $n(z) \propto \cos^2(z/L)$ density extraction ramp.** Extraction of the witness beam with a $n(z) \propto \cos^2(z/L)$ shaped density downramp with different ramp lengths L from the plasma stage and evolution of witness beam parameters during dechirping and extraction are presented. The extraction density donwramp profiles are normalised to the nominal plasma density n_p (a). The witness beam parameters during dechirping and extraction are presented in (b) for the absolute energy spread (solid lines) and energy evolution (dashed lines) and in (c) for normalized emittance (solid lines) and divergence (dashed lines). The grey solid and dashed lines are overlaid for comparison, where no dechirping and extraction are applied.

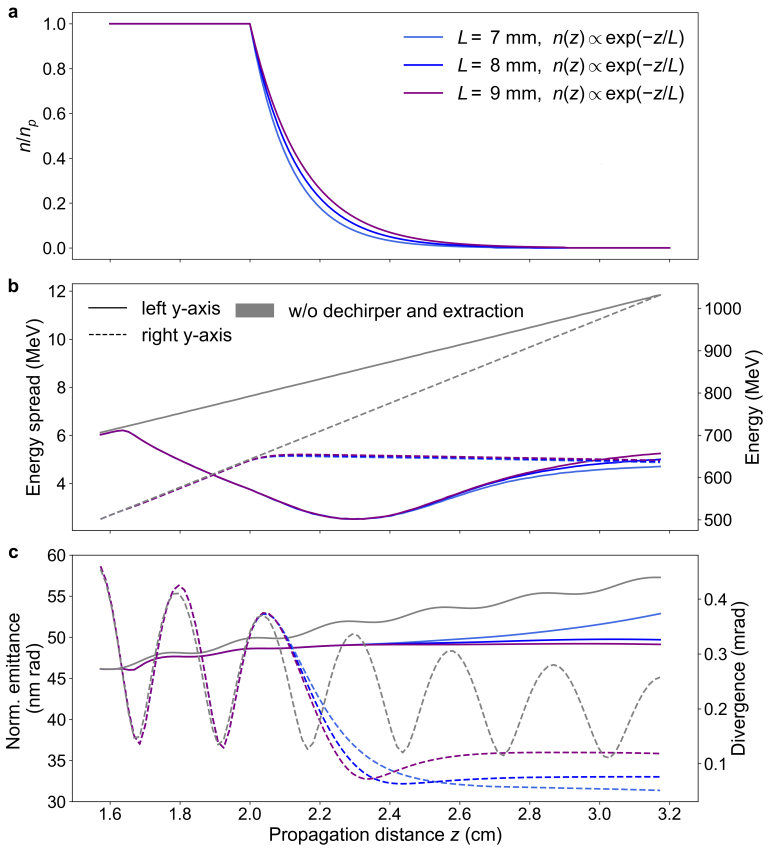

Figure 5.17: **Witness beam dechirping and extraction investigation based on 3D PIC simulation for a $n(z) \propto \exp(-z/L)$ density extraction ramp.** Extraction of the witness beam with a $n(z) \propto \exp(-z/L)$ shaped density downramp with different ramp lengths L from the plasma stage and evolution of witness beam parameters during dechirping and extraction are displayed. The extraction density downramp profiles are normalised to the nominal plasma density n_p (a). The witness beam parameters during dechirping and extraction are presented in (b) for the absolute energy spread (solid lines) and energy evolution (dashed lines) and in (c) for normalized emittance (solid lines) and divergence (dashed lines). The grey solid and dashed lines are overlaid for comparison, where no dechirping and extraction are applied.

levels off and remains nearly constant until the optimum dechirping point, thanks to the decreasing relative energy spread down to $\Delta W/W < 1\%$. The low energy spread minimizes contributions of the chromatic amplitude $\mathcal{W}$ in Eq.(3.54) to the emittance growth (see Sec.(3.2.7)). Beyond the optimum dechirping point, the witness beam accumulates a positive energy chirp, increasing the relative energy spread. The larger relative energy spread increases the chromatic amplitude, leading to emittance growth by just a few nm-rad. Remember from section (3.2.7) in the literature, emittance growth of the order of 0.1 μm-rad is reported during extraction; it is regarded as acceptable for beams with μm-rad initial emittance. The escort bunch dechirper and extraction combined effect suggests that this approach may allow limiting emittance growth to the nm-rad scale and enable the preservation of nm-rad scale normalized emittance witness beams. The overall divergences are reduced after both extraction ramps below the reference case minima, corresponding to $\sigma_{\theta,\mathrm{ref}} \approx 0.15\,\mathrm{mrad}$. The divergence average value and variation at the exit of the plasma stage is slightly better for the $n(z) \propto \exp(-z/L)$ ramp with $\sigma_\theta \approx 0.089\,\mathrm{mrad} \pm 0.02\,\mathrm{mrad}$ compared to the $n(z) \propto \cos^2(z/L)$ ramp with $\sigma_\theta \approx 0.13\,\mathrm{mrad} \pm 0.04\,\mathrm{mrad}$.

In conclusion, the novel dechirping approach works during extraction, and the performance of the dechirper is unaffected by the extraction ramp shape or length. Witness beams converge to the same absolute energy spread values at the optimum dechirping position. The normalized emittance of the witness beam is preserved during dechirping. The low energy spread also facilitates witness beam normalized emittance preservation during extraction from the plasma stage at an exceptional nm-rad level. The divergences of the witness beam are reduced, and the beam sizes are increased. Overall, the performance of the $n(z) \propto \exp(-z/L)$ shaped extraction ramp is much better regarding final beam parameters and stability. The preservation of normalized emittance on the nm-rad scale is in stark contrast to the commonly reported μm-rad emittance growth during extraction from the plasma stage. The observations and findings are integral for preserving beam quality during electron beam transport in a post-plasma beam line. The possibility of energy, energy spread, and emittance stability is highly encouraging for the feasibility of the dechirping approach for the PWFA XFEL application.

5.3 DISCUSSION

Generating ultra-high 5D brightness witness beams via the plasma photocathode in PWFA is highly attractive. In particular, it combines an injector, compressor and accelerator in a single plasma stage. However, having the capability of energy chirp compensation in the same plasma stage was the missing piece towards generating ultra-high 6D brightness electron beams and preserving them inside the plasma stage, during extraction and in the post-plasma electron beam line. The lack of dechirping methods capable of dealing with ultra-high 5D brightness electron beams and preservation of beam emittances on the nm-rad-level inspired the development of a novel energy chirp compensation approach.

This novel scheme for energy chirp compensation in PWFA is highly flexible because the dechirping of the ultra-high 5D-brightness witness beam is decoupled from the witness beam production. The central trick is to reverse the local wakefield at the witness beam trapping position at a later acceleration stage via beam loading of a second charge population (escort bunch). This ensures that the witness beam reaches relativistic energies and becomes immune to space charge emittance degradation. With this preservation of witness beam emittance on the nm-rad level can be facilitated during dechirping. The proof-of-principle 3D PIC simulation suggests that the projected relative energy spread of the witness beam can be decreased by at least one order of magnitude to sub-1% level with prospects towards sub-0.1% level relative energy spreads at higher witness beam energies. In principle, this method is fully scalable to the energy levels required for HEP. In this thesis, attention is only devoted to GeV-level energies necessary for the hard XFEL applications. The dechirping method is also applicable to other plasma-based acceleration and injection methods. However, by far, the highest impact is anticipated from applying the scheme to witness beams with already ultra-high 5D brightness, as promised by the plasma photocathode injection in a dephasing-free PWFA. Reduced relative energy spreads in conjunction with ultra-high 5D-brightness opens the path to unprecedented 6D-brightness electron beams. An in-depth investigation of witness beam release and trapping dynamics revealed the origin of the residual energy spread to be the release time and the wakefield at the witness beam trapping position. A simple scaling law of the residual energy spread captures these findings. It outlines a pathway towards further minimising projected (slice) relative energy spreads at the

optimum dechirping point by controlling release time via the plasma photocathode laser pulse and/or operating at longer plasma wavelength or reduced wakefield gradients. Based on this analysis, projected relative energy spreads at the sub-0.1% level can already be obtained at a few GeV witness beam energies with sub-MeV residual energy spreads.

An initial analysis of spatiotemporal jitters of the injector lasers and investigation of their impact on the performance of the dechirper conclude that the optimum dechirping point and the energy spread are largely insensitive to misalignment or pointing jitters. This is enabled by a self-adapting mechanism of the dechirping efficiency discovered in this work. Further, the extraction of the witness beam from the plasma stage does not impact the performance of the dechirper and preservation of witness beam emittance on the nm-rad level is observed thanks to the sub-1% level relative energy spreads. These results are highly encouraging towards witness beam transport and the PWFA XFEL application.

Beyond the study in this chapter, potentially dechirping of two or more witness beams generated with plasma photocathode injector [120] is possible for multi-colour light sources. Accurate control of the longitudinal phase space of the witness beam without changing its other properties is accessible, for example, negative or positive chirps in a wide range or even more advanced production of non-linear chirps by controlling the local wakefield shape with the escort bunch current profile. Further, this approach may inherently mitigate beam quality degradation due to hose instabilities (see section (3.2.7)) inside the plasma stage because the energy chirp is only compensated at the end of the plasma stage. The escort-bunch may be integrated into an energy recovery scheme for high wall-plug efficiency of a PWFA stage [327] or used for less demanding light source applications [40].

Fundamentally, on the way towards PWFA XFELs, these ultra-high 6D brightness beams with ultralow normalized emittance, low energy spread and high peak current may enable the possibility to fulfil the **Emittance criterion** (Eq.(2.72)) and the **Energy spread criterion** (Eq.(2.65)) at the same time and therefore result in high gain XFEL. Such high-quality witness beams may push the boundaries of today's available light sources to an unprecedented level [40], which may lead, in turn, to new scientific frontiers.

6

NEXT-GENERATION FREE-ELECTRON LASER NEAR THE COLD BEAM LIMIT

This chapter presents the findings of the research effort developing an ultra-compact hard X-ray free-electron laser powered by ultra-high 6D brightness electron beams from a single PWFA stage. The results were obtained through a high-fidelity start-to-end simulation project. The chapter starts with a brief review of the current status and recent progress in the field. Then, the PWFA stage producing the ultra-high 6D brightness beams is investigated in a fully explicit 3D PIC simulation. A beam transport line is designed and optimized to capture, isolate, and refocus these ultra-high quality witness beams into an undulator section without degrading the quality. The undulator section is designed to leverage these unprecedented witness beams for ultra-high gain in the Ångstrom to sub-Ångstorm wavelength FEL near the cold beam limit. These three building blocks simultaneously solve many challenges discussed in previous chapters and enable the PWFA XFEL concept developed in this chapter. Figure (6.1) shows the setup of the PWFA XFEL with the three building blocks. The author published a significant portion of this chapter in [40, 41, 44].

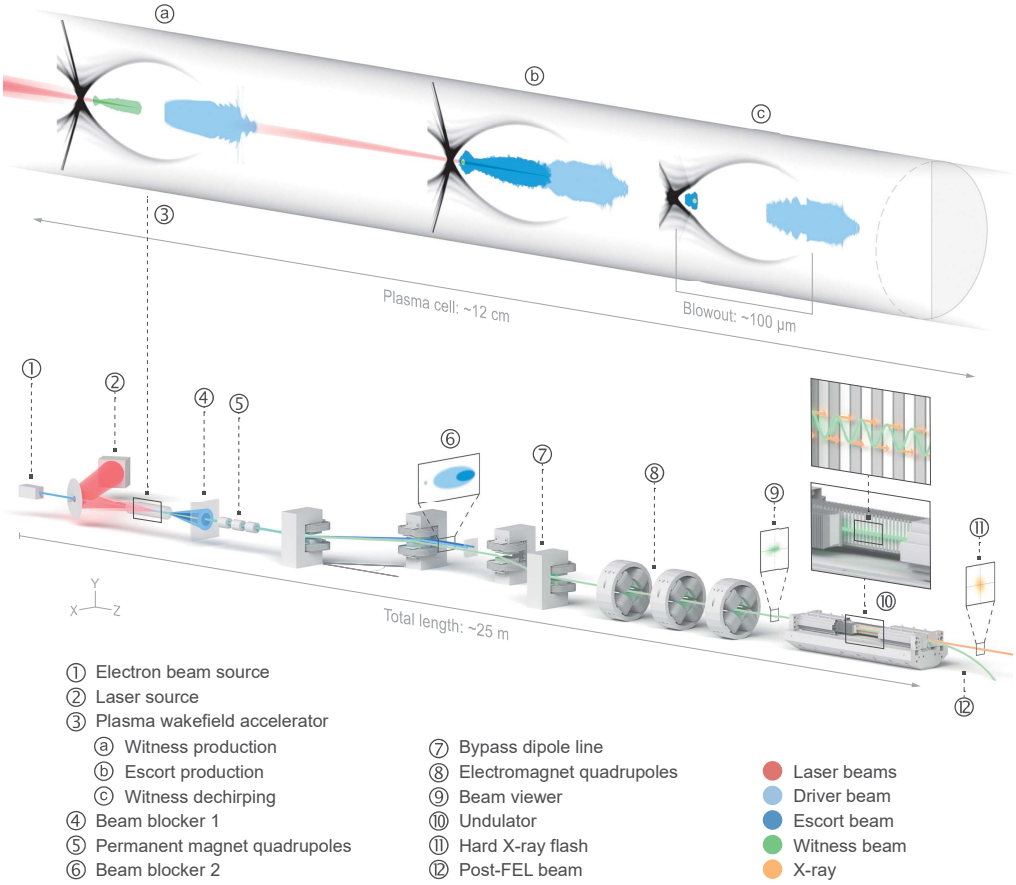

Figure 6.1: **Setup of an ultra-compact X-ray free-electron laser.** Configuration of the PWFA-powered ultra-compact XFEL highlighting the components of the three building blocks. The setup begins with the electron driver beam from a linac or an LWFA stage (1), exciting the PWFA in perionized plasma (3). Next, a collinear plasma photocathode laser (2) produces the ultrabright witness electron beam (a), followed by a second plasma photocathode (b) that produces a high-charge escort bunch for dechirping. This escort bunch dechirps the witness beam via beam loading (c). Three electron populations leave the plasma stage with different properties. A high divergence escort and electron driver beams are partially dumped into a beam blocker (4). The ultra-high quality witness beam passes the beam blocker and is then captured by a strong permanent magnet quadrupole triplet (5). The remaining driver and escort charge is dumped by a dipole-based bypass line (chicane) (7), and the isolated witness bunch (9) is matched by an electromagnet quadrupole triplet and refocused (8) into the undulator (10). Attosecond duration X-ray laser pulses (11) are produced from the witness beam in the undulator. Finally, the beam is removed from the axis (12). Produced for [44]. This work is openly licensed via CC BY 4.0.

6.1 REVIEW OF PLASMA-BASED FREE-ELECTRON LASERS

The scientific community has long hoped to be able to create a free-electron laser powered by compact plasma-based accelerators. The goal is to make this versatile research tool more widely accessible, even in small university laboratories, and have a transformative impact on the entire research landscape.

Some early suggestions of plasma-based FELs required advanced configuration of plasma, accelerator and lasers [331]. However, before the experimental observation of quasi-monoenergetic beams in the early 2000s (see section (3.2.1)), there was little hope for the electron beams with Maxwellian-like spectral distribution to drive an FEL, as the electron beam quality was by far not close to the FEL requirements. The breakthrough in beam quality with the quasi-monoenergetic electron beams significantly nourished the plasma-based FEL R&D in the following years [332, 333].

Even though the electron beam quality regarding the energy spread, emittance, and peak current was still insufficient for FEL lasing even at the visible or *extreme ultraviolet* (EUV) FEL wavelength range, the production of incoherent undulator radiation in the visible to soft X-ray spectral range [334, 335] was a crucial milestone and is routinely achieved today [336, 337]. This motivated further research to compensate for beam quality limitations [338, 339].

The enormous energy spread threatens beam quality inside the plasma stage. It can significantly degrade beam quality during the extraction from the plasma stage and in the beam transport line towards the FEL [275, 304, 308, 336] (see sections (2.1)-(3.2.7)). Various post-plasma compensation approaches have been developed to overcome certain beam quality limitations. These approaches compensate for energy spread constraints or increase peak current after beam generation and various other schemes [121, 243, 318, 321, 323, 324, 338, 340–342], and many focus on demonstrating soft X-ray FELs [171, 343]. Some progress is made with the recent experimental breakthroughs reporting on SASE FEL gain in the EUV (27 nm) [344] and IR (800 nm) [345] wavelength range, and externally seeded FELs at 270 nm [346] and at 800 nm [347] wavelengths. These first experimental results certainly nourish hope and have raised attention for "The race for wakefield-driven FELs" [348]. However, simultaneously tackling energy spread, emittance, peak current, and beam quality preservation challenges at GeV beam energies are necessary to meet the energy spread and emittance condition at the hard XFEL

regimes [40, 42] and improved 5D (6D) brightness electron beams are needed to reach the sub-meter scale gain length regime.

In this context, an interesting parallel can be drawn between plasma-based and rf-based accelerators where in rf-accelerators, novel electron beam sources from photocathode injectors opened the door towards the 4^{th} generation light source [9, 82] due to improved electron beam brightness. Similarly, the electron beams from plasma-based accelerators must take the next leap in beam quality improvement to enable ultra-compact XFELs. Innovative solutions are needed to simultaneously fulfil the energy spread and emittance conditions at the hard X-ray wavelength. Therefore, the following sections present a blueprint and proposal for a PWFA-powered ultra-compact hard X-ray FEL backed by a high-fidelity start-to-end simulations framework. These results simultaneously solve the beam quality and beam quality preservation challenge in a self-consistent way along the three building blocks of the PWFA hard XFEL, namely the plasma wakefield acceleration stage, electron beam transport line and the undulator section.

6.2 DEVELOPMENT OF ULTRA-HIGH 6D BRIGHTNESS PWFA STAGE

This section presents the results of the PWFA stage producing the multi-GeV and ultra-high 6D brightness witness beams via the escort-bunch-based dechirping approach developed in chapter (5), required to power a hard XFEL. First, the design considerations of the PWFA stage are discussed, and then, the fully explicit 3D PIC simulation results are presented. The reasoning behind the specific configuration of the PWFA stage is informed by the electron beam quality requirements for hard XFEL interaction and the lessons learned from the results in chapters (4) and (5).

6.2.1 *Design consideration of the PWFA stage*

The plasma density predominantly determines the PWFA stage regarding the plasma wavelength, needed plasma source width, the choice of LIT and HIT species combination, and the electron driver beam and the plasma photocathode laser pulses, as discussed in section (4.2).

In principle, operation at longer plasma wavelength, for example, $250\,\mu$m is desired due to the advantages of obtainable beam quality and stability; however, from the

experimental and simulation point of view, it will require a wide plasma source to engulf the long and wide blowout, which also puts limits on the simulation necessitating a large simulation box. The computational costs associated with this are manageable for short propagation distances in fully explicit 3D PIC codes, as presented in section (4.2.2). However, multi-cm acceleration distances must be modelled at high resolution to obtain witness beam energies on the multi-GeV scale. This exceeds computational resources, even those provided by large computation time awards with multi-millions of core hours, such as at the National Energy Research Scientific Computing Center. To reduce computational costs, the PWFA stage is operated in a preionized helium plasma of density $n_\mathrm{p} \approx 1.1 \times 10^{17}\,\mathrm{cm}^{-3}$, corresponding to a plasma wavelength of $\lambda_\mathrm{p} \approx 100\,\mu\mathrm{m}$. The plasma source has a cylindrical geometry for simplicity and is motivated by the consideration in section (4.2.1). Future studies will address the generation of the plasma source in more detail. More importantly, the plasma source is wide enough with a diameter of $D = 1.5 \times \lambda_\mathrm{p}$ to engulf the $100\,\mu\mathrm{m}$ plasma wavelength blowout, suppressing channel boundary effects encountered at the E-210 experiment (see section (4.1.4)). This configuration is a trade-off between witness beam quality, high fidelity of the 3D PIC simulation and available HPC resources.

In this configuration, the first level of helium serves as the LIT medium to support the blowout, and the second ionization level of helium is used as the HIT medium for the plasma photocathode lasers. Using the second ionization level of helium as HIT medium at the selected plasma wavelength enables the use of a wide range of electron driver beam parameters for dark-current free operation of the PWFA stage, according to the field ionization calculations presented in figure (4.10) in section (4.2.1).

Reduced models introduced in section (3.3.2), (3.2.6) and (5.1.2) are utilized to inform the initial design of the PWFA stage, but also to investigate suitable electron driver, witness beam and escort bunch parameters. The findings of this initial study inform the working points described below and serve as a low-cost guide for the fully explicit, high-fidelity 3D PIC simulations using the PIC code VSim.

The electron driver beam charge is optimized to $Q = 600\,\mathrm{pC}$ and compressed to a length of $\sigma_\mathrm{z,rms} \approx 12.7\,\mu\mathrm{m}$, resulting in a peak current of $I_\mathrm{p} \approx 5.5\,\mathrm{kA}$, allowing excitation of a blowout near the longitudinal resonance condition. To enter the blowout regime, the electron driver beam is focused to $\sigma_\mathrm{x,y,rms} \approx 4.0\,\mu\mathrm{m}$ at projected normalized emittance of $\epsilon_\mathrm{n,(x,y)} \approx 2\,\mu\mathrm{m\text{-}rad}$ in both transverse planes at the entrance of the plasma

source. Transverse matching of the electron driver beam is not attempted to reduce the complexity of the configuration, but instead, an *acclimatization phase* is introduced, allowing to stabilise the wakefield for plasma photocathode injection. The acclimatization phase is discussed later in detail. This, combined with the energy of $W = 2.5\,\mathrm{GeV}$ and relative energy spread of $\Delta W/W = 2.0\,\%$, enables driving a stable PWFA stage for sufficiently long propagation distance to obtain transformer ratio $T > 1$ (Eq.(3.35)), which ensures that the final witness beam energy is higher than the initial electron driver beam energy. These electron driver beam parameters are easily obtainable in rf-based linacs but may also be produced within the Hybrid LWFA→PWFA platform in the near future. Note the rf-linac or the LWFA stage are not modeled for driver beam production as this would exceed the scope of this work, however, future work will address this when it comes to experimental implementation of the concept.

The normalised emittance and residual energy spread of the witness beam fundamentally depend on the ionisation volume of the plasma photocathode laser pulse. Both quantities benefit from spatiotemporal confined release volumes inside the blowout according to the findings and scaling described in section (3.2.5)-(5.2.1). Therefore, a tightly focused Gaussian laser pulse with reduced Rayleigh length can release electrons from helium ions spatiotemporally confined inside the wakefield and simultaneously minimize longitudinal and transverse witness beam thermal properties, reducing the 6D phase space volume $\det(\Sigma_{6\mathrm{D,r}})$ of the witness beam. More advanced plasma photocathodes, such as SSTF or AMBER (see section (3.2.5)), may realize more compact ionisation volumes in PWFA but have to be experimentally explored and are not considered in this work.

The high-quality witness beam is generated by a first plasma photocathode tri-Gaussian laser pulse, which is focused to a spot size of $w_{0,1,\mathrm{rms}} \approx 5\,\mu\mathrm{m}$ with a pulse duration of $\tau_{1,\mathrm{FWHM}} = 15\,\mathrm{fs}$. The short pulse duration produces a quasi-static co-moving ionization front in the trapping potential of the wakefield. The quasi-static ionization front enables electrons to be released within a confined region of the trapping potential, and the electrons are predestined to form an ultra-short trapped witness beam. The normalized intensity $a_{0,1} \approx 0.0595$ at the focal point of the laser is just above the tunnel-ionization threshold of He^+. At the given laser parameters, the averaged ADK model (see section (3.1.3)) predicts 1.4 pC charge for the witness beam.

The requirements on the escort bunch are quite different compared to the witness beam. Here, the aim is to produce a rather long and high peak current electron beam to overload the wakefield locally at the witness beam trapping position. Therefore, the second plasma photocathode laser pulse has been designed with this in mind. But thanks to the plasma photocathodes' versatility, the properties of the laser pulses can be independently adjusted to produce the desired escort bunch. Because the background HIT density is uniform, the escort bunch injector laser pulse can be tuned to release a sufficient amount of charge. This is achieved by a larger spot size of $w_{0,2,\mathrm{rms}} \approx 9\,\mu\mathrm{m}$ and a normalized intensity of $a_{0,2} \approx 0.062$, increasing the ionization volume and the release rate of HIT electrons. The longer pulse duration of $\tau_{2,\mathrm{FWHM}} = 80\,\mathrm{fs}$ additionally enlarges the electron release region within the trapping potential and results in an elongated escort bunch for a large dechirping region. With these parameters, ADK calculations predict a charge of $Q_{\mathrm{esc}} \approx 136\,\mathrm{pC}$ for the escort bunch. Both plasma photocathode lasers are implemented as Ti:sapphire laser pulses with a central wavelength of 800 nm and polarization in the x-direction as envelope pulses in the paraxial approximation.

The findings of chapters (4) and (5) not only advanced the understanding of plasma photocathode injection mechanism and PWFA but initiated the development of sophisticated numerical methods enabling the modelling and post-processing of these highly demanding simulation scenarios at high-fidelity. Various novel techniques are deployed for high-resolution simulations at multi-cm propagation distances, resolving accurately relevant physics while keeping the computing time reasonable. Here, a co-moving window with a Cartesian simulation grid is employed, where the cell sizes in the longitudinal and the transverse directions are $0.1\,\mu\mathrm{m}$ and $1\,\mu\mathrm{m}$, respectively. The integration time step is optimized to a temporal resolution of $\Delta\tau_{\mathrm{CFD}} \approx 333\,\mathrm{as}$ for reduced numerical instabilities [349, 350]. More details on the simulation box are summarized in the appendix (8.2.3). Digital smoothing of the currents in the system is used, and the VSim perfect dispersion approach is harnessed to minimise numerical Cherenkov radiation [292]. A split field approach is developed for general noise and stray field reduction, where plasma, electron beams and laser pulse EM-fields are independently initialized, cleaned of instabilities, and self-consistently recombined into the PIC cycle for accurate modelling. Electromagnetic field reflections are minimised with absorption boundaries. The electron driver beam is modelled with variable-weight macroparticles to reduce numerical hose instability seed, while the background helium plasma (LIT) is modelled with one *macroparticle-per-cell*

(PPC). At the same time, the HIT medium for the witness beam release is implemented as a cold fluid, which allows the PPC to be adjusted independently for the witness and escort beam, respectively. The total number of macroparticles for the individual electron beams can be adjusted to satisfy corresponding numerical needs. The final trapped witness and escort beam consists of $\sim 200\,\mathrm{k}$ and $\sim 1.2\,\mathrm{million}$ macroparticles, respectively. It ensures modelling of the dechirping area with much higher accuracy and fidelity than in chapter (5). The following section (6.2.2) presents the fully explicit 3D PIC simulation results of the PWFA equipped with the plasma photocathode-based injector, accelerator, compressor and dechirper in the same plasma stage.

6.2.2 *Generation and acceleration of ultra-high 6D brightness beams*

The PWFA stage configuration discussed in the previous stage is implemented into a high-fidelity 3D PIC simulation with the fully explicit Cartesian PIC code VSim [287]. The combination of spatial and temporal resolution of the simulation, long propagation distance for multi-GeV witness energies, and handling of ultra-high brightness witness beams significantly increased the complexity of the simulation and the demand for HPC resources. Therefore, a sophisticated management approach is necessary to solve individual system problems in specialised simulation campaigns. The results of these specialised simulation campaigns are then combined into a final master-optimized input deck. This master input deck is then harnessed to study the PWFA stage for the hard XFEL.

The PWFA stage consists of several phases: acclimatization (i), injector (ii), accelerator (iii), dechirper (iv), and extractor (iv) section. These different phases are discussed in the following 3D PIC simulation, and a representative 3D PIC simulation is summarized in the figure (6.3). Panel (a) of the figure shows the plasma density profile with focal positions of the injector and dechirper plasma photocathode laser pulses in the laboratory frame. In (b), the evolution of the on-axis wakefield is shown along the different phases of the PWFA stage. Panel (c) displays the evolution of projected and slice properties of the witness beam along the propagation distance. Finally, panel (d) shows the longitudinal phase spaces of the electron driver beam, escort bunch and witness beam at the end of the plasma stage, and (e) is a zoom-in of the witness beam longitudinal phase space.

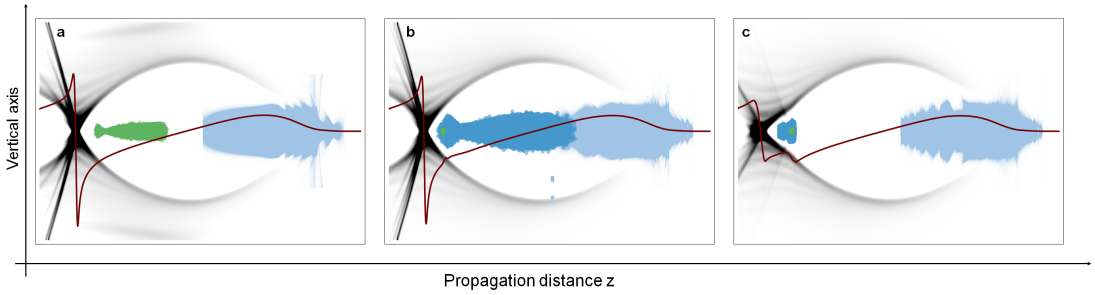

Figure 6.2: **Snapshots of the 3D PIC simulation of witness production and dechirping for the XFEL.** The electron driver beam (light blue) sets up the blowout in helium plasma (grey) with the on-axis longitudinal wakefields (dark red). In (a), the first plasma photocathode laser pulse liberates electrons from He^+ (green), forming the ultra-high brightness witness beam; in (b), at the later stage of the acceleration, the escort bunch is released by a second plasma photocathode laser pulse and in (c), the escort bunch (dark blue) is trapped. It overloads the wakefield at the witness beam trapping position and dechirps the witness beam. These snapshots are the same as presented in Fig. (6.1).

Selected snapshots of the simulation are presented in figure (6.2). A detailed discussion is delivered below.

In principle, the electron driver beam transverse size can be exactly matched to the plasma density. However, this will introduce additional complexity to the setup, necessitating a high gradient focusing optics based on plasma lenses for driver beam in-coupling, such as considered in [324]. Further, shot-to-shot variation of driver beam properties may contribute to the variation of the wake formation. Here, chromatic decoherence is leveraged to stabilise the wakefield and produce an experimentally robust PWFA stage at the expense of 2.5 cm longer plasma stage. An acclimatization distance of 2.5 cm ensures that the electron driver beam is well-matched to the plasma density and produces a stable and consistent wakefield at the witness beam injection position in the laboratory frame. It is achieved by balancing space charge, plasma focusing, and magnetic pinch forces. The results can be seen in figure (6.3) (b,i). After the acclimatization phase, the PWFA stage offers ideal conditions for the plasma photocathode injection and subsequent stable acceleration in the dephasing-free PWFA stage. This is evident from the wakefield evolution in figure (6.3) (b) at the witness beam trapping position (grey solid line).

The injection of the witness beam is realized by a sub-mJ-scale plasma photocathode laser which reaches its focal point with a spot size of $w_{0,1,\mathrm{rms}} \approx 5\,\mu\mathrm{m}$ at $z_{\mathrm{acc}} \approx 2.5\,\mathrm{cm}$. The laser pulse liberates cold electrons via tunnelling ionization of the helium ion He^+ inside the plasma wave for approximately two Rayleigh lengths $2Z_{\mathrm{R}} \approx 196\,\mu\mathrm{m}$. The release position of the electrons is just outside the electrostatic potential minimum of the wake in the co-moving frame (see figure 6.2 (a)). The electron charge released inside the plasma wave amounts to 1.4 pC and is in excellent agreement with the theoretically predicted ADK calculations of release charge. The small size of the injector spot helps to minimize the thermal normalized emittance and the slice energy spread of the beam, according to Eq.(3.42) and Eq.(5.8), respectively. The ultracold electrons are quickly captured with 100% charge capture efficiency and compressed longitudinally while being matched transversely in the plasma wave. They form the ultrabright witness beam, which has a duration of 520 as (r.m.s) and an ultralow projected (average slice) emittance of $\epsilon_{\mathrm{n,(x,y)}} \approx 23(17)\,\mathrm{nm\text{-}rad}$. Due to its sub-fs duration, the witness beam exhibits a peak current of $I_{\mathrm{p}} \approx 1.2\,\mathrm{kA}$. It is phase-locked in the accelerating phase of the PWFA and gains energy at a rate of $\approx 30\,\mathrm{GV/m}$, as shown in figure (6.3) (b,ii). After propagating for about 8 cm, it reaches 1.75 GeV energy. The average slice emittance is preserved on the nm-rad level, and the projected emittance rises by less than ten nm-rad, thanks to the minimized betatron phase mixing. The projected (average slice) emittance of the witness beam is $\epsilon_{\mathrm{n,(x,y)}} \approx 32(20)\,\mathrm{nm\text{-}rad}$ just before the escort-bunch release via the second plasma photocathode laser pulse.

The second, more intense, longer and softer focused plasma photocathode laser releases the escort bunch after the witness beam is accelerated over $z_{\mathrm{acc}} \approx 8\,\mathrm{cm}$ in the plasma stage. The nominal centre of the second plasma photocathode laser is shifted by $15\,\mu\mathrm{m}$ relative to the potential minimum towards the electron driver beam to ensure trapping of the escort bunch at the witness beam position, as displayed in figure (6.2) (b). The released escort bunch charge amounts to $Q_{\mathrm{esc}} \approx 136\,\mathrm{pC}$ and is compressed to a multi-kA peak current electron beam at the witness beam trapping location. It overloads the wake locally, as seen in figure (6.3) (b,iii) and figure (6.2) (c). Even at these elevated charge levels, the normalized emittance of the escort bunch is $\epsilon_{\mathrm{n,(x,y)}} \approx 350\,\mathrm{nm\text{-}rad}$. These emittance values are comparable to the most advanced conventional injectors at the SwissFEL [351]. The escort bunch initiates the dechirping, and the accumulated positive energy chirp of the witness beam is reversed, as seen in figure (6.3) (c). At this

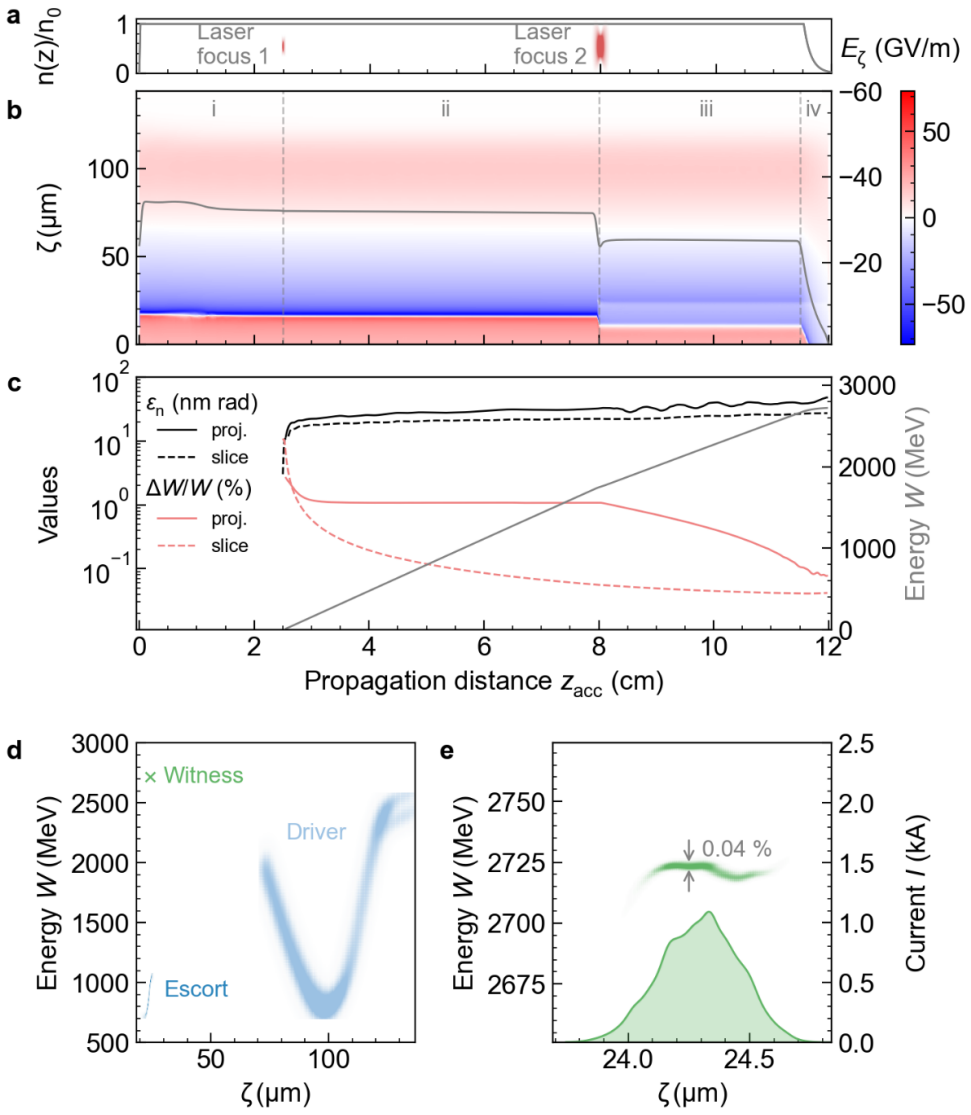

Figure 6.3: **3D Particle-in-cell simulation of PWFA stage for the hard XFEL.** In panel (a), the plasma density profile (grey line) $n(z)/n_0$ rapidly increases and remains constant until the extraction downramp with the density profile $n_{\text{exit}}(z) \simeq \exp(-z/L)$. The intensity evolution (red colour) of the plasma photocathode laser foci that create witness (1) and escort (2) electrons are also displayed. In panel (b), the colour-coded on-axis longitudinal wakefield evolution E_ζ vs co-moving coordinate ζ is depicted, along with the electric field evolution at the witness beam position (solid grey line, right y-axis). The dashed lines indicate the various phases, including acclimatization (i), witness acceleration (ii), witness dechirping and acceleration (iii), and extraction phases (iv). In panel (c), the projected and average slice emittance and energy spread (left y-axis) and energy (right y-axis) are presented. In panel (d), an overview of the longitudinal phase spaces of the driver, escort, and witness beam, and in panel (e), the longitudinal phase space of the witness beam with the current profile (green line) is given at the end of the PWFA stage. Produced by the author for [44]. This work is openly licensed via CC BY 4.0.

point, the witness beam has an energy of $W \sim 1.75\,\mathrm{GeV}$ and is immune to the space charge forces of the escort charge. It continues to be accelerated without significant emittance growth (see figure (6.3) (c)).

As the energy chirp of the witness beam decreases, the relative slice energy spread also decreases adiabatically. Energy chirp minimization is reflected by the convergence of projected and slice energy spread. This near-convergence is an extraordinary indication of the high beam quality in the plasma and an essential requirement to extract the witness beam robustly from the plasma stage while preserving its quality at these levels of emittance and brightness. Further, this feature of a small energy spread and emittance across the beam can also be utilized for the FEL process by allowing global beam matching to the undulator instead of slice-by-slice conditioning.

In figure 6.3 (e), the flat longitudinal phase space of the witness beam is illustrated, which is crucial for preserving emittance at the nm-rad-level. The projected (slice) relative energy spread amounts to $\Delta W/W \approx 0.08\ (0.04)\,\%$. The plasma density profile is reduced (Fig.(6.3) (a)) with an extraction downramp of the form $\mathrm{n_{exit}}(z) \simeq \exp(-z/L)$. The form factor of the extraction ramp is informed by the studies in section (5.2.3), and the length is optimized to $L_{\mathrm{exit}} \approx 5\,\mathrm{mm}$ to position the optimum dechirping point into the vacuum. At this stage, the witness beam has higher energy than the driver and escort beam (figure 6.3 (d)). Now expanding transversely, the escort bunch is overlapped spatially with the witness beam to ensure a smooth transition into the vacuum. The witness beam is released at a beam energy of $W \approx 2.725\,\mathrm{GeV}$ into the vacuum.

During the extraction, the loss of transverse focusing leads to an increase in the size of the witness beam, but the negligible chromaticity secures it to be emitted into the vacuum with a projected (average slice) of $\epsilon_{\mathrm{n,(x,y)}} \approx 45\ (20)\,\mathrm{nm\text{-}rad}$. It ensures that the slice emittance is preserved at the nm-rad level, and the projected emittance grows by only around $\sim 10\,\mathrm{nm\text{-}rad}$ during dechirping and expansion. At the end of the plasma stage, the witness beam produced by the amalgamated plasma photocathode injector, PWFA compressor, accelerator, and dechirper reaches a projected (slice) 6D brightness of $B_{\mathrm{6D}} \approx 1.3 \times 10^{18} (7.5 \times 10^{18})\,\mathrm{Am^{-2}rad^{-2}/0.1\%bw}$. Thanks to the various innovations, the 6D brightness values of the witness beam are an order of magnitude brighter than in chapter (5) and many orders of magnitude brighter than the state-of-the-art initial electron drive beam.

To summarize, an ultra-high quality witness beam is generated, accelerated, dechirped, and extracted from the plasma stage without significantly compromising beam quality, with 6D brightness values that are orders of magnitude larger than state-of-the-art. This may have a transformative impact on high-gain PWFA XFELs. However, beam transport is known to degrade witness beam quality potentially; hence, in the following, the 6D phase spaces of the three populations of beams are converted into the format of the particle tracking code ELEGANT for a seamless transition to an optimized beam transport line. The beam transport line is designed and evaluated in the following section (6.3).

6.3 ELECTRON BEAM TRANSPORT LINE

In this section, a dedicated beam transport line is designed for the witness beam capture, isolation, and refocusing into an undulator section. First, the design's reasoning is briefly discussed, and then the 6D phase spaces of all three charge populations are obtained from the 3D PIC simulation and tracked through the beam transport line.

6.3.1 *Design of witness beam transport line*

The beam transport line, which is approximately 10 m long, is optimized using the particle tracking code ELEGANT (see also section (2.3.1)). The results obtained from ELEGANT are cross-checked with the particle tracking code GPT [352]. The latter considered an advanced CSR model and 3D space charge modelling, and both codes produced comparable results for the witness beam evolution. A seamless "handshake" from the PWFA stage to the transport line is necessary for a high-fidelity simulation, such that the complete 6D phase space distributions of the three electron beams are converted to ELEGANT. The built-in simplex algorithm optimizes the beam transport line for the witness beam energy of $W \approx 2.7\,\mathrm{GeV}$. The tracking of particles is carried out with the accuracy of the third-order transfer matrix. All three electron beam populations' 6D phase space distributions and projected and slice beam properties are individually monitored and analyzed along the beam transport line.

As discussed in chapter (5), the generation and acceleration of ultra-high 6D brightness electron beams are paramount for the XFEL application and preservation of the

witness beam normalized emittance is crucial during transport to the application at the nm-rad-level. As such, beam quality degradation cannot be tolerated, even if it is only a hundred nm-rad at average projected (slice) normalized emittance levels of $\epsilon_{n,(x,y)} \approx 46.6(20)$ nm-rad in the capturing, isolation and refocusing section of a transport line.

Fortunately, the sub-0.1% relative energy spread of the witness beam at the plasma stage exit can alleviate many of the beam quality degradation dangers, as elaborated in section (3.2.7) and chapter (5). This is why energy spread/chirp reduction must be secured within the plasma accelerator stage. The low energy spread of the witness beam at the plasma stage exit renders inconsequential beamline chromaticities and preserves projected (slice) normalized emittance and energy spread. Further, although the extraction density ramp increases, the r.m.s witness beam size to $\sigma_{x,y} \approx 0.19\,\mu$m and reduces the r.m.s divergences to $\sigma_{\theta,x,y} \approx 0.045$ mrad at the exit, the witness beam still exhibits comparatively small beam size and divergences to be handled by conventional *electromagnet quadrupoles* (EMQs). Therefore, a combination of high-gradient *permanent magnet quadrupoles* (PMQs) is considered for the capturing line just after the plasma stage. Before the PMQ triplet, a collimator filters out the particularly divergent fraction of the electron driver and escort beams. The collimator is modelled as a black absorber in ELEGANT to reduce computational load. Simple radiation transport calculations of the collimators suggest the feasibility of the filtering approach because of the comparatively low electron driver beam and escort electron energies at the exit of the plasma stage. Future studies will explore the technical realization in more detail and consider secondary particle productions and other relevant mechanisms.

The PMQ triplet is arranged in an F-D-F configuration in the X-direction (F: focusing, D: defocusing) and opposite in the Y-direction. The first two quadrupoles are 10 cm long, and the last is half that length for controlling the phase advance of the phase space. The PMQ triplet is optimized such that the witness beam is achromatically collimated (Twiss $\alpha \approx 0$) downstream at the entrance of the EMQ triplet, located 7.5 m downstream in the beam transport line from the exit of the PMQ triplet. A focusing gradient of 700 T/m is required to capture and collimate the witness beam. This type of PMQ is routinely produced [353, 354]. The C-chicane comprises four rectangular bending magnets (B) to isolate the witness beam. Numerically, the built-in CSR model in ELEGANT [355, 356] considers potential quality degradation due to CSR in the

chicane. The first two dipoles $B_1 - B_2$ deflect the witness beam, and the last two dipoles $B_3 - B_4$ bring back the witness beam to the beamline axis. Each dipole is $L = 0.4\,\mathrm{m}$ long, with a bend angle of $\theta \approx 2\,\mathrm{mrad}$ in the horizontal direction. The drift distance between $B_1 - B_2$ and $B_3 - B_4$ is $D = 1.5\,\mathrm{m}$, while the distance between $B_2 - B_3$ is $0.2\,\mathrm{m}$. As a result, the $|R_{56}| \approx 0.0014\,\mathrm{mm}$ element is relatively small, CSR does not degrade the witness beam quality, but the bending of charges is sufficient to deflect the remaining charge of the electron driver beam and escort bunch without affecting the high-quality witness beam. The witness beam enters the matching section after drifting for a distance of $1.7\,\mathrm{m}$ from the exit of the chicane, such that the witness beam is fully collimated (Twiss $\alpha \approx 0$) at the entrance of the first EMQ. Finally, this section comprises an F-D-F configured standard EMQ triplet. Each quadrupole in the triplet is $0.3\,\mathrm{m}$ long, and it has a focusing gradient of $45\,\mathrm{T/m}$. The EMQ triplet is tuned to focus the witness beam into the undulator mid-point, where the exponential amplification regime of the radiation is expected. Further, the focus is optimized to minimize radiation diffraction contribution to the gain length inside the undulator.

The ELEGANT simulation results of witness beam capturing, collimation, isolation and matching are presented in the following section. The transport line parameters are summarized in the appendix (8.2.4).

6.3.2 *Capture, separation and matching of the witness beam*

This section presents the results of the driver, escort and witness beam particle tracking with ELEGANT through the optimized beamline. Figure (6.5) summarises the particle tracking along the beamline, presenting relevant FEL witness beam properties. In (a), slice normalized emittance and relative energy spread are presented. In (b), the evolution of the Twiss β-function is displayed alongside the centroid x-position of the three electron beams, and finally, (c) depicts the longitudinal phase space of the witness beam with overlaid slice properties at the undulator entrance.

Driver, escort and witness differ in energy, emittance and divergence, which allows separation of escort and driver to isolate the witness beam. The beam transport line commences with a $10\,\mathrm{cm}$ drift distance. All three electron populations diverge significantly in the drift without focusing plasma forces, but the degree of divergence is quantitatively different, depending on individual beam quality and energy. The electron

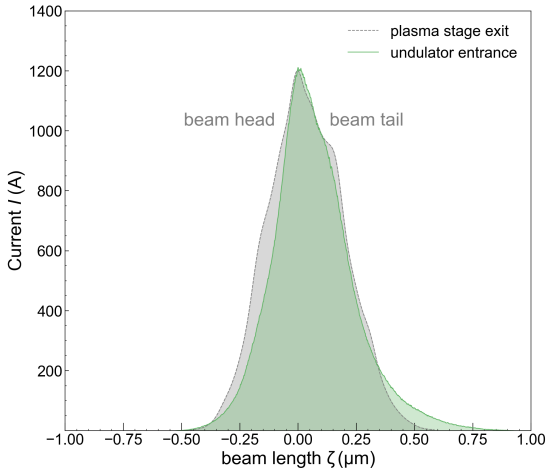

Figure 6.4: **Witness beam current profile before and after the beam transport line.** Witness beam current profile at the plasma stage exit (grey) and the undulator entrance (green) is presented. Witness beam tail is slightly decompressed in the chicane due to the remaining energy chirp. Produced by the author for [44]. This work is openly licensed via CC BY 4.0.

driver beam diverges the fastest, followed by the moderate-quality escort bunch, while the high-quality witness beam diverges the least. A collimator with a 0.5 mm aperture, placed just before the first PMQ, filters 40 % of the driver and a small fraction of the escort bunch charge. The collimator protects the subsequent PMQ triplet from direct charge impact from intense electron beams and reduces the risk of demagnetization of the magnets. The PMQ triplet captures the witness beam, which leaves the plasma with increased β-Twiss of $\beta_{\mathrm{x,y}} \approx 0.5\,\mathrm{cm}$ and α-Twiss parameter close to zero corresponding to nearly collimated witness beam. The witness beam's Twiss β function rapidly increases in the drift section and inside the PMQ-triplet (figure (6.5) (b)). Nevertheless, the witness beam size stays sufficiently small thanks to the nm-rad normalised emittance and sub-0.1 mrad divergence. The relative energy spread and normalized emittance of the witness beam are preserved, and the witness beam leaves the PMQ-triplet nearly collimated, propagating to the chicane.

Here, the different electron energies allow the separation of the remaining driver and escort electrons from the witness beam in the chicane line. After travelling a distance of 1 m, the remaining electron driver beam, escort bunch, and the high-quality witness beam with different chromatic properties enter a symmetric C-chicane. The first dipole B_1 deflects all three electron beams in the transverse x-direction. However, the three

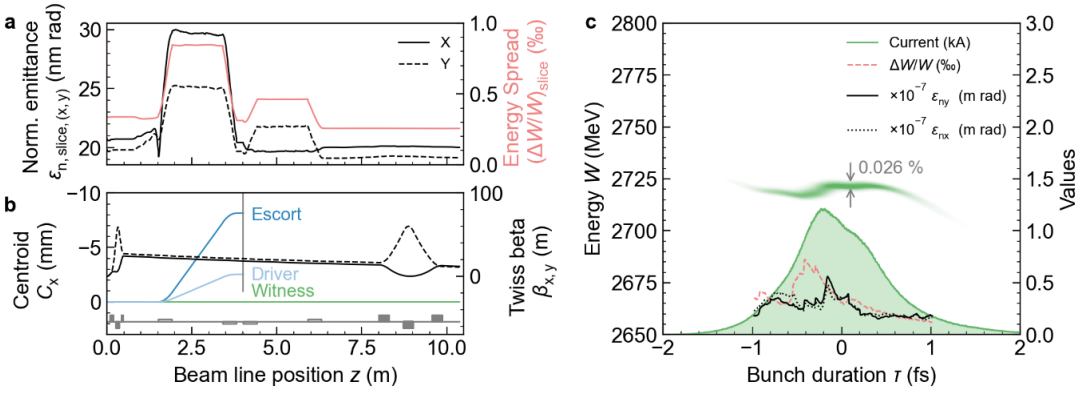

Figure 6.5: **Witness beam transport.** In panel (a), the evolution of the average transverse slice emittance $\epsilon_{\mathrm{n,slice}}$ and the average slice energy spread $(\Delta W/W)_{\mathrm{s}}$ while being transported through the permanent magnet triplet, the four chicane line dipoles and the electromagnet triplet is shown. In panel (b), the deflection of the centroid C_{x} of the electron driver beam, escort, and witness (left y-axis) and the evolution of the witness Twiss-parameter β (x: solid, y: dashed) are displayed. In panel (c), the longitudinal phase space (left y-axis) and the slice current I, energy spread $(\Delta W/W)_{\mathrm{s}}$, and emittances $\epsilon_{\mathrm{n,s}}$ (right y-axis) of the witness beam are shown just before entering the undulator. Produced by the author for [44]. This work is openly licensed via CC BY 4.0.

charge populations are dispersed by different amounts due to their mean energy, energy spread and quality differences, as shown in figure (6.5) (b). The second dipole B_2 bends the three populations back parallel to the propagation axis, and the dispersion function of all three populations reaches its maximum. The witness beam deviates a few μm from the central axis. On the other hand, driver and escort electrons are kicked out several millimetres. This enables easy isolation of the witness beam by inserting a second collimator of 0.4 mm aperture, which blocks the driver and escort beams but lets the witness beam pass through. Alternatively, the driver and escort beams could be directed towards diagnostics, potentially used as energy recovery beams, or exploited for other applications. However, an exact beamline configuration of such a sustainable utilisation of beams is beyond the scope of the present thesis and may be investigated in future works.

The isolated witness beam passes in its entirety through the energy collimator, and the last two dipoles bring the witness beam back on-axis while compensating for the dispersion. The small bend angle of $\theta \approx 2$ mrad of the chicane changes the orbit of the

high-energy witness beam negligibly, thus avoiding witness beam quality degradation by CSR (figure (6.5) (a)-(b)). Because the witness beam exhibits minor correlated energy spread at its tail, slight decompression and reorganisation of the charge occurs (see figure (6.4)). This decompression does not change the peak current of the witness beam because the longitudinal phase space in the central part is nearly flat. However, averaging over the entire witness beam results in a slightly longer r.m.s beam duration, positively affecting the witness beam slice energy spread.

The witness beam is focused by the subsequent EMQ triplet, narrowing its size to around $3\,\mu$m at the centre of the undulator section. In the undulating plane, the average beam size across the entire undulator length is $4\,\mu$m. Combined with the ultrahigh brightness and associated gain, this eliminates the need for external focusing structures to achieve optimal coupling with the emerging photon field. The absence of external focusing is made possible by the short saturation length of the PWFA-powered XFEL, which enables ultra-high gain in the undulator section. In contrast, km-scale hard XFEL machines rely on FODO-focusing to keep the electron beam focused over hundreds of meters within the undulator section. Then, an intricate phase shifter arrangement between the FODO modules is necessary to maintain the resonance condition along the long undulator section in conventional XFELs, but all of this is not needed here, thanks to the unique characteristics of the PWFA XFEL.

Summarising, the witness beam has a duration of 570 as with peak current of $I_{\mathrm{p}} \approx 1.2\,\mathrm{kA}$, projected (average slice) relative energy spread of $\Delta W/W \approx 0.08(0.026)\,\%$ and projected (average slice) normalized emittance of $\epsilon_{\mathrm{n,(x,y)}} \approx 46.6(20)\,\mathrm{nm\text{-}rad}$ (figure (6.5) (c)), and a 6D projected (average slice) brightness of $B_{\mathrm{6D}} \approx 1.3 \times 10^{18}(1.1 \times 10^{19})\,\mathrm{Am^{-2}rad^{-2}/0.1\%bw}$ at the entrance of the undulator. The 6D brightness values of this new class of electron beams are far beyond the reach of conventional rf-cavity-based or plasma-based accelerators. These record 6D brightness values at the entrance of the undulator are mutually enabled by simultaneously preserving projected (slice) normalized emittance on the few nm-rad level and projected (slice) relative energy spread at the sub-0.1% level from within the plasma stage through the beamline into the undulator. The next section (6.4) leverages this ultra-high 6D brightness beam for hard X-ray production in a dedicated undulator section.

6.4 ATTOSECOND-ANGSTROM CLASS ULTRA-COMPACT FREE-ELECTRON LASER

This section presents hard XFEL simulation results based on the ultra-high quality witness beam transported from the PWFA stage. The simulation is performed with the unaveraged FEL code Puffin introduced in section (2.3.2). First, a suitable undulator configuration is investigated, then the simulation settings are briefly discussed, and eventually, the results of the XFEL simulations are presented and discussed.

6.4.1 *Undulator configuration and performance estimates*

In this section, a suitable undulator configuration is investigated for the emission of 8.3 keV (Case I: C1) and 15.7 keV (Case II: C2) coherent photons, corresponding to resonance wavelength of $\lambda_r \approx 0.149$ nm and $\lambda_r \approx 0.079$ nm in the undulator section of the PWFA XFEL. These two showcases leverage the potential of ultra-high 6D brightness beams and push the plasma-based accessible resonant wavelengths by order of magnitude even compared to the advanced and elaborated efforts in the community [171]. Further, the $\lambda_r \approx 0.15$ nm is comparable with the conventional km-scale XFELs [301] and is highly demanded by the user community for the light-matter type of experiments [2] and the $\lambda_r \approx 0.08$ nm shows the straightforward scalability towards sub-Å wavelength regime by simply changing the undulator configuration towards higher photon energies, thanks to the witness beam's copious quality budget.

The Ming Xie formalism introduced in section (2.2.4) alongside the emittance and energy spread conditions are utilised to explore potential undulator configuration and evaluate the corresponding FEL performances in terms of the degradation parameter Λ. Figure (6.6) summarises the results, wherein (a) the slice normalized emittance is divided by the photon emittance $4\pi\epsilon_n/\gamma_{rel}\lambda_r \leq 1$ and in (b), the slice relative energy spread is normalized by the FEL parameter $(\Delta W/W)_s/\rho_{FEL} \leq 1$. Values smaller than one show the parameter regions where the conditions are fulfilled. In (c), the 3D gain length degradation parameter $(1 + \Lambda)$ is shown, and figure (6.6) (d) shows the corresponding resonance photon energies.

Figure (6.6) (a) and (b) suggest that both conditions are satisfied for a wide range of undulator parameters and corresponding photon energies by a large margin, thanks to the

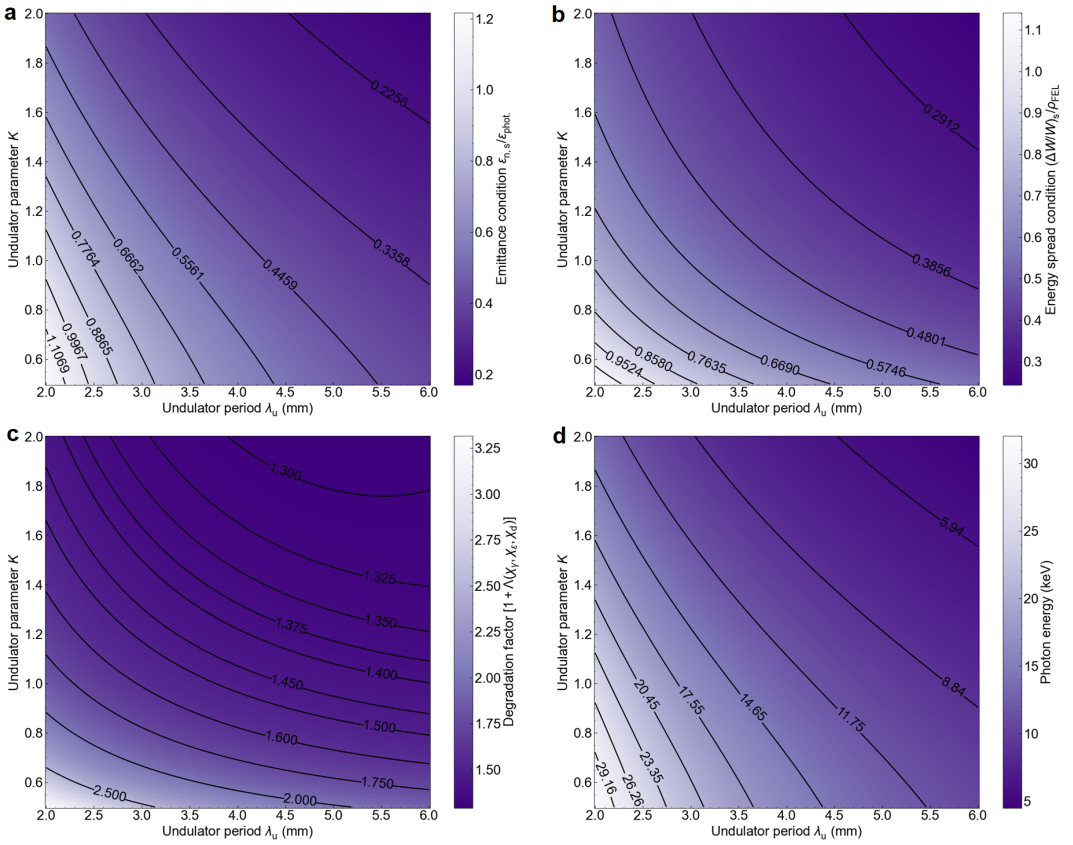

Figure 6.6: **Evaluation of XFEL performance and accessible photon energies as a function of undulator parameter.** Emittance (a) and energy spread (b) criterion, FEL degradation (c) and resonance condition (d) are evaluated as the function of undulator parameters considering Eq.(2.74) (Ming Xie formalism) for the witness beam produced in the PWFA stage. The emittance and energy spread condition is satisfied for a wide range of undulator parameters. When approaching very high photon energies $> 25\,\mathrm{keV}$, the conditions start to reach unity, reflected by the increase of the degradation parameter.

ultra-low normalized emittance and relative energy spread of the witness beam. According to Eq.(2.73) and (2.69), this will manifest in a high degree of transverse coherence and long coherence time radiation pulse at saturation. However, when increasingly approaching harder photons ($> 25\,\mathrm{keV}$), both parameters become larger than one, and gain length degradation significantly increases, as evident from the figure (6.6) (c). Nevertheless, the degradation parameter stays largely < 2 for the displayed undulator parameter range, again the result of the ultra-high beam quality of the witness beam.

Resonance emission at the target photon energies of 8.3 keV and 15.7 keV can be accessed with a wide range of undulator parameters, but the working point of this study is informed by exploiting the full potential of beams enabled by the plasma photocathode and dechirper approach. This pushes the XFEL to the near cold beam limit regime where the degradation factor $(1 + \Lambda)$ is approaching near unity. Additional restriction ensures that the realisation of the XFEL approach is possible with existing or upcoming advanced undulator technologies [97–99], discussed in section (2.2.2).

The two XFEL showcases are based on SASE in planar undulators of periods $\lambda_\mathrm{u} = 5\,\mathrm{mm}$ and $\lambda_\mathrm{u} = 3\,\mathrm{mm}$ with undulator parameters $K = 1.18$ and $K = 1$, respectively. These undulators produce radiation at the resonance wavelength of $\lambda_\mathrm{r} \approx 0.149\,\mathrm{nm}$ and $\lambda_\mathrm{r} \approx 0.079\,\mathrm{nm}$ with the $W \approx 2.725\,\mathrm{GeV}$ witness beam and corresponding Lorentz factor $\gamma_\mathrm{rel} \approx 5332$. The FEL parameter ρ_FEL for these two cases is $\rho_\mathrm{FEL,C1} \approx 0.075 \times 10^{-2}$ and $\rho_\mathrm{FEL,C2} \approx 0.055 \times 10^{-2}$. This shows that the witness beam with projected (average slice) relative energy spread $\Delta W/W \approx 0.08(0.026)\,\%$ easily satisfies the energy spread condition for both undulator scenarios. Similarly, the emittance condition is fulfilled for both cases due to the projected (average slice) normalized emittance of $\epsilon_{\mathrm{n,(x,y)}} \approx 46.6(20)\,\mathrm{nm\text{-}rad}$. The analysis suggests that FEL lasing is possible and the 1D power gain lengths for both cases, $L_\mathrm{1d,C1} \approx 30\,\mathrm{cm}$ and $L_\mathrm{1d,C2} \approx 25\,\mathrm{cm}$, are on the sub-metre scale.

The EMQ-triplet focuses the witness beam to an average beam size of $\sigma_\mathrm{y} \approx 4\,\mu\mathrm{m}$ insider the undulator and ensures optimal overlap of the radiation field and the electron beam for high coupling over an extended distance along the undulator. The electron beam size dictates the widths of the emerging radiation field such that the corresponding Rayleigh lengths of the radiation pulses are $Z_\mathrm{R,FEL,C1} \approx 1.39\,\mathrm{m}$ and $Z_\mathrm{R,FEL,C2} \approx 2.55\,\mathrm{m}$ for the two cases. The short 1D gain length allows for managing diffraction-induced

gain length degradation by stratifying the condition $Z_{\mathrm{R,FEL}} > 2L_{\mathrm{1d}}$, without further external focusing along the undulator.

Nevertheless, the actual gain length in 3D will be longer due to energy spread, non-zero emittance, and diffraction contributions. Using the Ming Xie formalism introduced in section (2.2.4), it is possible to estimate the 3D gain length with $L_{\mathrm{g,th}} = L_{\mathrm{1d}}(1 + \Lambda(\chi_{\gamma_{\mathrm{rel}}}, \chi_\epsilon, \chi_{\mathrm{d}}))$ (Eq.(2.74)). The energy spread, emittance and radiation diffraction contributions are expressed with the scaled parameters $\chi_{\gamma_{\mathrm{rel}}}$, χ_ϵ and χ_{d}, respectively, and all three contributions are encapsulated in the degradation parameter Λ. The contributions from the respective scaled parameters are negligible when $\chi_{\gamma_{\mathrm{rel}}} < 1/\sqrt{3},\ \chi_\epsilon < 1,$ and $\chi_{\mathrm{d}} < 1/2$.

The following evaluates contributions from the individual scaled parameters to the gain length degradation Λ for the two cases. The calculated values of the three scaled parameters are $\chi_{\gamma_{\mathrm{rel}},\mathrm{C1}} \approx 0.198$, $\chi_{\epsilon,\mathrm{C1}} \approx 0.048$, and $\chi_{\mathrm{d,C1}} \approx 0.479$ for Case I, and $\chi_{\gamma_{\mathrm{rel}},\mathrm{C2}} \approx 0.276$, $\chi_{\epsilon,\mathrm{C2}} \approx 0.075$, and $\chi_{\mathrm{d,C2}} \approx 0.212$ for Case II. For both XFEL cases the contributions from the scaled parameters are negligible and the above conditions are satisfied by a margin. This is a strong signature of a stable XFEL working point and is far way from a *cliff-edge regime* where minor variations in electron beam properties terminate the XFEL process. The stability of the XFEL working points is verified in section (6.5). A low emittance results in a short 1D power gain length but also manifests advantageously in 3D gain length through minimized pure emittance and shared terms. The 3D power gain length is estimated to be $L_{\mathrm{g,C1}} \approx 49\,\mathrm{cm}$ and $L_{\mathrm{g,C2}} \approx 42\,\mathrm{cm}$ for the two respective cases. Note the similar 3D gain length between the two cases, which only deviates by a few centimetres. At shorter radiation wavelengths, the degradation contributions from energy spread and emittance terms are increased when considering the same electron beam. Still, they are somewhat compensated by the reduced diffraction term due to the longer Rayleigh lengths at shorter radiation wavelengths such that the 3D gain lengths of C1 and C2 are very similar.

Summarizing, the ultra-high 6D brightness witness beam allows access to FEL regimes near the cold beam regime, where 3D effects are nearly suppressed, and the 3D gain length approaches the 1D gain length. This study's small difference between the 1D and 3D gain lengths indicates an increasingly clean FEL process. In contrast, in current state-of-the-art XFELs, the difference between 1D and 3D gain lengths can be on the order of meters, dramatically increasing the facility's footprint. The 1D and 3D gain lengths

are on the sub-meter scale, indicating that the XFEL may saturate after a few meters. The selected working point for the aimed photon energies confirms this. The undulator parameters are a balanced decision to achieve the target photon energies, leveraging the ultra-low emittance of the witness beam and maximizing FEL performance. The undulator configuration is challenging and future-looking, yet it is expected to become within reach, given the trend and R&D focus of undulator technologies [97–99]. To achieve maximum performance and capability, combining low electron energy, ultra-high 6D brightness beams, and short-period undulators is exclusively accessible by ultralow emittance beams.

6.4.2 *Preparation of XFEL simulation*

The three-dimensional, unaveraged FEL simulation code Puffin (see section (2.3.2)) is used to model the FEL interaction in a time-dependent mode. The unaveraged FEL equations allow for consideration of the collective interaction of electrons with broad bandwidth radiation, such as electron beam shot-noise, CSE effects, and radiation diffraction, as detailed in [357]. Before the FEL simulation, the six-dimensional phase space of the witness beam is extracted from the beam transport line simulation and translated into the Puffin format. The number of macroparticles in 3D is upsampled with a Joint Cumulative Distribution Function from initially $\approx$ 200k to 3.9 million macroparticles to ensure an accurate FEL interaction modelling with sufficient macroparticles per radiation wavelength. It produces a smooth current profile on the length scale of the cooperation length and avoids unphysical CSE emission. Note that the FEL simulation uses approximately half the number of real electrons for the 1.4 pC witness beam, and a Poisson noise generator [118] is applied to the electron witness beam for realistic shot-noise representation (see also section (2.3.2)).

The magnetic field of the planar undulator with horizontal orientation is modelled with entrance and exit tapering poles to avoid electron beam steering within the undulator. Unlike other undulator period averaging FEL codes, Puffin integrates the FEL equations in discrete steps within a single pole, for example, with 30 steps per undulator period. The simulation box is large enough to accommodate witness beam evolution and diffraction of the radiation pulse over the entire undulator length.

The electromagnetic field is sampled in the longitudinal direction with ten cells per resonance wavelength, allowing self-consistent modelling of higher harmonics up to $\lambda_5 = 2\lambda_s = \lambda_r/5$. However, the wavelength cut-off is set at the 4^{th} harmonics due to increasing computing demand for shorter wavelengths at higher harmonics. This highly accurate FEL process modelling provides additional insights into the physics of the FEL interaction.

Ten simulations for each XFEL case with initially different shot noises are performed to reflect the SASE radiation power statistics. In particular, it is crucial for SASE FEL as it starts from noise in the electron beam (see section (2.2.3)). The results of these simulations are statically evaluated for average power gain curves, radiation profile and spectrum and corresponding standard deviations. Puffin models the radiation spectrum with a defined wavelength cut-off set by the user. All wavelengths up to the cut-off are contained within the electromagnetic field of the radiation pulse. Thus, a spectral filter is applied to the electromagnetic field to obtain the power gain curve, pulse profile, and spectrum at the the fundamental mode.

6.4.3 *Ultra-compact hard X-ray free-electron laser*

The XFEL performance estimates obtained in section (6.4.1) suggest that lasing is possible at the Å and sub-Å wavelength with the representative witness beam of this study and predicts saturation of the XFEL after few meters of undulator section thanks to the ultra-high 6D brightness of the witness beam. The hard XFEL regime is at the cold beam limit. This regime is beyond the reach of most advanced FEL facilities today due to the lack of electron beams with the required beam quality. While these predictions are very promising, they are based on the average properties of the witness beams and are limited by the uncertainties of the model employed. In figure (6.5) in section (6.3.2), the slice properties of the witness beam exhibit non-uniformity on the scale of the cooperation length. This can change the local gain length along the witness beam and, combined with the slippage effects of radiation, may impact the FEL performance and is of particular concern if FEL does not saturate before the radiation pulse outruns the electron beam temporally.

Further, CSE and CSR effects and sideband amplification outside the resonance wavelength can lead to efficiency degradation of the FEL process and many other

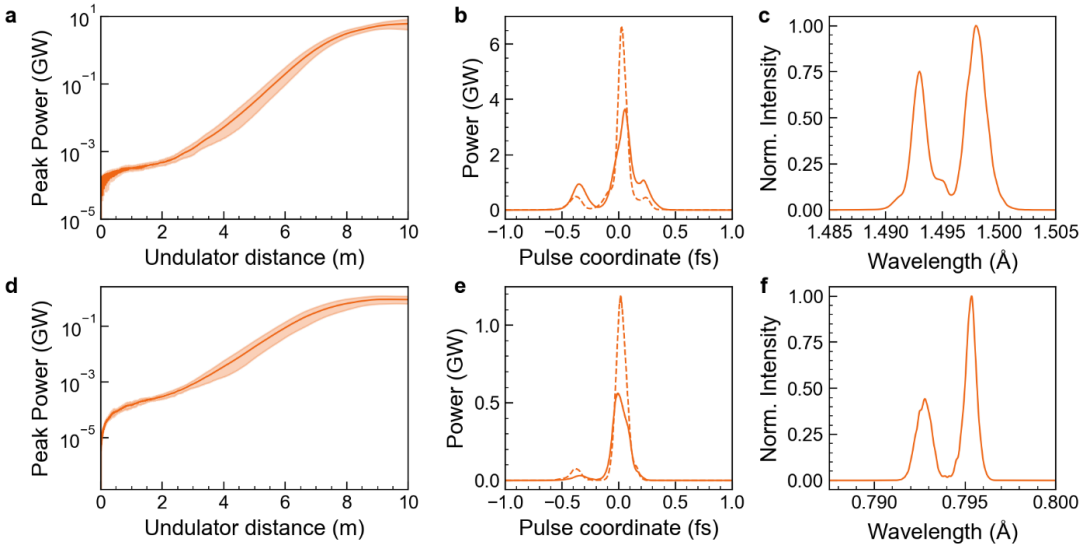

Figure 6.7: **X-ray FEL pulse generation simulated with Puffin.** Panels a)-c) and d)-f) present the coherent power gain curve of the hard X-ray photon pulse over the undulator distance, duration, and spectrum. The undulator has $\lambda_u = 5\,\text{mm}$ (a-c) and $\lambda_u = 3\,\text{mm}$ (d-f). The shaded plot indicates the power gain variation for ten simulated shots with different initial shot noises, and the dark orange solid line represents the average power gain across shots. The gain lengths are estimated with an exponential fit to be $L_{g,sim,C1} \approx 0.54\,\text{m}$ and $L_{g,sim,C2} \approx 0.62\,\text{m}$, respectively. In b) and e), the solid line represents the average across ten shots, while the dashed line is a single-shot representation. In c) and f), the radiation spectra are averaged over ten shots. Figure (6.1) (inset 11) depicts a representative radiation profile at the undulator exit. Produced by the author for [44]. This work is openly licensed via CC BY 4.0.

secondary effects, which are not incorporated into the Ming Xie model. The XFEL performance has to be investigated in a time-dependent 3D FEL simulation, including most of the relevant effects at high fidelity with the 3D FEL code Puffin.

The central results of these efforts are reported in figure (6.7), and supportive material is provided in figure (6.8). The power gain curve along the undulator for the two cases is plotted in figure (6.7) (a) and (d). The SASE process starts rapidly due to the witness beam's ultrahigh brightness and high charge density. The lethargy regime, where mode selection occurs, ends just after $\sim 2-3\,\text{m}$, exponential gain kicks in, and the XFEL reaches saturation quickly. Saturation is reached after approximately $\sim 10\,\text{m}$, consistent with typical estimates of the saturation power length $L_{sat} \sim 18-20L_g$. The best fit at the linear regime of the power gain curve estimates the 3D gain length for the two

cases to be $L_{\mathrm{g,sim,C1}} \approx 0.54\,\mathrm{cm}$ and $L_{\mathrm{g,sim,C2}} \approx 0.62\,\mathrm{cm}$. These gain length estimates align with the 3D predictions, and the observed gain length differs from the theoretical 1D gain length by only a few 10s of cm. The sub-Ångstrom case has a slightly longer gain length, likely due to energy and energy spread diffusion, coherent spontaneous emission (CSE), and CSR losses. The standard deviation bands of the power gain curve are widespread at the linear regime but converge towards the average value at the saturation.

The average (peak) powers in the GW range align with theoretical XFEL extraction efficiency estimates. Remember, the average power is calculated from ten XFEL simulations of electron beams with different initial shot-noises. At a total witness beam energy of 0.378 J and power of $P_{\mathrm{beam}}[\mathrm{TW}] = W_0[\mathrm{GeV}]I_{\mathrm{p}}[\mathrm{kA}] \approx 3.27\,\mathrm{TW}$, it is possible to estimate the maximum total radiation power at saturation using $P_{\mathrm{sat}} \approx 1.6\rho_{\mathrm{FEL}}P_{\mathrm{beam}}[\mathrm{TW}]$ for the two cases presented. The radiation power predictions yield $P_{\mathrm{sat,C1}} \approx 4\,\mathrm{GW}$ and $P_{\mathrm{sat,C2}} \approx 2.8\,\mathrm{GW}$ and in Puffin, the average radiation powers observed are $P_{\mathrm{sat,sim,C1}} \approx 4\,\mathrm{GW}$ and $P_{\mathrm{sat,sim,C2}} \approx 0.5\,\mathrm{GW}$, respectively, and, individual shots come close to the theoretical value and produce $\mathcal{O}(10^9 - 10^{10})$ number of photons per pulse tightly packed into a sub-fs duration within the 0.1 % spectral bandwidth (see below). Overall, the simulated and predicted characteristics of the XFEL are in agreement, suggesting that the XFEL is operated near the cold beam limit.

The witness beam that powers the XFEL is ultra-short with r.m.s duration of 570 attoseconds, corresponding to a length of $\sigma_{\mathrm{z,rms}} \approx 171\,\mathrm{nm}$. While this is advantageous for generating radiation pulses with similar duration, it can pose difficulties in ensuring that they overlap temporally with the ultra-short witness beams during the entire interaction. Due to inherent slippage, the radiation pulse may outpace the electron beam before the XFEL reaches saturation. This can result in an incoherent prepulse preceding the fully coherent main pulse. The XFEL must be saturated before slippage effects compromise the radiation pulse's temporary structure and mode content.

The total slippage time is $S = L_{\mathrm{sat}}\lambda_{\mathrm{r}}/(\lambda_{\mathrm{u}}c_0)$, for the two showcases this results in $S_{\mathrm{C1}} \approx 1.1\,\mathrm{fs}$ and $S_{\mathrm{C2}} \approx 0.9\,\mathrm{fs}$. This is well within the central (FWHM) electron beam current region, and the ultrashort gain length ensures that saturation occurs before the radiation pulse surpasses the electron beam. Further, the cooperation lengths are $L_{\mathrm{c,C1}} \approx 16.2\,\mathrm{nm}$ and $L_{\mathrm{c,C2}} \approx 16.5\,\mathrm{nm}$ based on Eq.(2.66), respectively. At a beam length of $\sigma_{\mathrm{z,rms}} \approx 171\,\mathrm{nm}$, the anticipated number of radiation spikes for the Ångstrom and

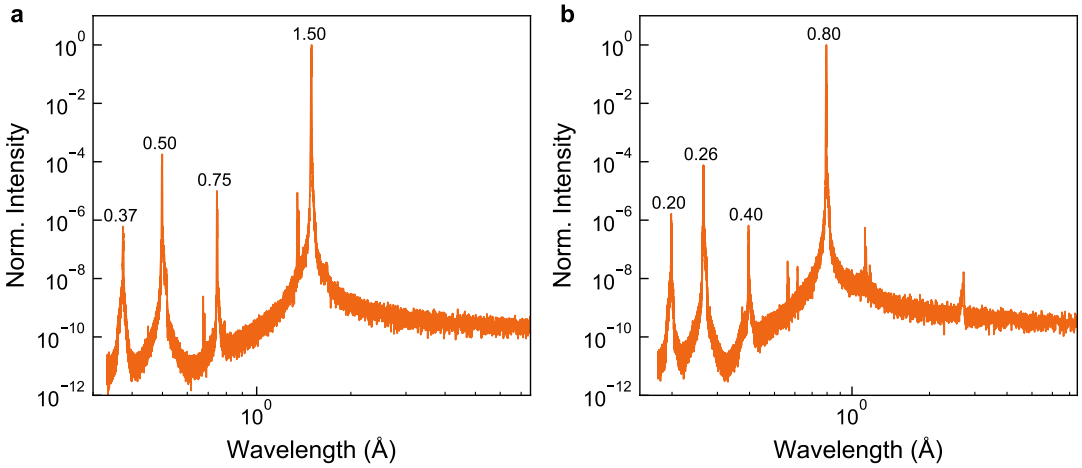

Figure 6.8: **Full radiation spectra for the two XFEL cases at saturation.** The full spectra of the $\lambda_r \approx 1.5\,\text{Å}$ and $\lambda_r \approx 0.8\,\text{Å}$ cases are presented in panel (a) and (b), respectively. Further, even and odd harmonics are highlighted following the λ_r/n scaling up to $n = 4$ of the fundamental modes. The shortest radiation wavelengths observable are $\lambda_r/4 \approx 0.37\,\text{Å}$ and $\lambda_r/4 \approx 0.2\,\text{Å}$ for the two respective cases and consistent with the Nyquist frequency cut-off. Produced by the author for [44]. This work is openly licensed via CC BY 4.0.

sub-Ångstrom case is $M_{C1} \approx 1.7$ and $M_{C2} \approx 1.6$ based on Eq.(2.70), respectively. Consequently, almost isolated, coherent near single-spike radiation pulses are automatically produced. This is verified by the Puffin simulations depicted in Figure (6.7) (b) and (e). All simulations generate an almost completely isolated, coherent near single-spike pulse, with FWHM average radiation pulse durations for the prominent spike of around $\Delta\tau \approx 100\,\text{attosecond}$. A notable feature is the clarity of these isolated pulses in the temporal domain. The variation in radiation power shown in Figure (6.7) (a) and (d) follows the expected statistical properties of the near single-spike regime and agrees with the theoretical expectations.

Figures (6.7) (c) and (f) depict lasing at the fundamental wavelength in both cases, as evidenced by the radiation spectrum. Two wavelength modes are present, which denote strong longitudinal coherence (see discussion on temporal coherence Eq.(2.69) and (2.70)), with an average FWHM bandwidth of approximately $\Delta\lambda \approx 0.6\,\text{picometre}$ around the fundamental wavelength. The corresponding average time-bandwidth product is around $\text{TBP} \approx 1.8$, suggesting that additional enhancements could potentially result in Fourier transform limited XFEL pulses, pushing the XFEL to its ultimate limits.

The clean XFEL process is also evident from the complete radiation spectrum for the two cases at saturation (see figure (6.8)) up to 4^{th} harmonics—the radiation spectrum peaks at the fundamentals and higher harmonics, while sideband amplification is strongly minimized. Signature of pronounced radiation spikes in the spectrum down to $\lambda_{\text{r,C2}}/4 \approx 0.2\,\text{Å}$ wavelength is visible, which is a potential indication that even shorter radiation wavelengths may be possible. Here, the electromagnetic recoil effects and quantized nature of the radiation are negligible even for the shortest wavelength in this study because the "quantum FEL parameter" $\rho_{\text{QFEL}} = \rho_{\text{FEL}} m_{\text{e}} c \gamma_{\text{r}} / \hbar k_{\text{FEL}}$ [358] is much larger than one for both cases even for the 4^{th} harmonics, $\rho_{\text{QFEL,C1}} \approx 53.4$ and $\rho_{\text{QFEL,C2}} \approx 24.1$. Future work will elaborate on the possibility of even harder XFEL photon energies ($> 25 - 50\,\text{keV}$). However, pushing the photon energies towards the rest mass energy of electrons ($\sim 511\,\text{keV}$) or, in other words, when the resonance wavelength approaches the electron Compton wavelength ($\lambda_{\text{c,r}} \approx 0.0243\,\text{Å}$), the XFEL will increasingly enter the quantum regime, where $\rho_{\text{QFEL}} < 1$ becomes smaller than one, and quantum treatment of the interaction will be required.

Table 6.1: **Summary of the attosecond-Ångstrom class FEL performance.** Key PWFA XFEL performance parameters from the Ming Xie theory and 3D Puffin simulations are presented.

Symb.	λ_{u}	K	λ_{r}	E_{ph}	ρ_{1D}	L_{1D}
Units	(mm)		[nm]	(keV)	$\times 10^{-4}$	(m)
C_1	5	1.18	0.149	8.3	7.6	0.3
C_2	3	1.0	0.079	15.7	5.5	0.25
	$L_{\text{G,th}}$	$L_{\text{G,sim}}$	$P_{\text{r,th}}$	$P_{\text{r,sim}}$	$\Delta\tau$	β^*
	(m)	(m)	(GW)	(GW)	(attosec)	(m)
C_1	0.49	0.54	4.0	4.0	$\simeq$100	$\simeq$2.4
C_2	0.42	0.62	2.8	0.5	$\simeq$100	$\simeq$2.4

In conclusion, advanced 3D Puffin simulations confirm that the ultra-high 6D brightness witness beam generated in the PWFA stage and transported to the undulator section can drive an ultra-compact hard XFEL. The XFEL is operated near the cold

beam limit as predicted by the theoretical estimates in section (6.4.1). Further, the characteristics of the radiation pulse with attoseconds pulse duration without requiring delicate beam manipulation techniques at Ångstrom and sub-Ångstrom wavelength are produced just in a 10-meter undulator section. The performance of the PWFA XFEL is summarized in the table (6.1). The prospects towards even harder photons are evident from the theoretical estimates and directly from the 3D FEL results through the observation of higher harmonics and may be explored in the future. These results encourage the experimental realization of ultra-compact hard XFELs powered by plasma photocathode PWFA.

6.5 SUPPLEMENTARY CONSIDERATIONS AND EXPERIMENTAL PATHWAYS

The attainment of attosecond duration hard XFEL pulses is a crucial objective. But the true impetus behind these endeavours lies in their potential to facilitate groundbreaking scientific experiments. Therefore, this section delves into the practicality, examining XFEL tunability, reproducibility, and experimental feasibility.

The inherent radiation power fluctuation in SASA FEL can be minimised by utilizing innovative approaches from the conventional FEL community, such as various seeding or self-seeding mechanisms. It will improve the temporal and spectral properties of the radiation pulse and enable fully coherent attosecond pulses. However, it is important to note that the performance stability of the FEL is significantly determined by variations in the electron beam parameters driving the XFEL. In-depth investigations into the tunability and stability of witness beams generated, dechirped, and extracted from PWFA-equipped with plasma photocathodes in sections (4.2.1) and (5.2) have concluded that within a reasonable variation range the impact of laser intensity and spatiotemporal jitter of the injector laser pulse on witness beam parameter variations is minor. Nonetheless, it is crucial to understand how such variations in electron beam parameters may impact the PWFA XFEL performance, particularly in identifying if the working point of the XFEL is on a cliff-edge. A cliff-edge working point would be susceptible to minor electron beam parameter variation and could practically prevent reliable experimental operation of the machine.

The STAFF tool (System Trade Analysis for an FEL Facility) [359] is utilized to examine the PWFA XFEL working points' sensitivity by varying crucial witness beam

slice parameters (normalized emittance, relative energy spread, peak current) and focusing (Twiss beta function) by up to ±5 % at the undulator entrance. These witness beam parameter variations are well within the reach of plasma photocathodes according to the results summarised in the table (4.1) in section (4.2.2). The results of this sensitivity analysis for the two cases of the study are summarized in figure (6.9), which displays the relative variation of the FEL performances normalized to the nominal cases. Across both cases (C1, C2), the deviation from the nominal values is less than ±2.5 %, and the XFEL performance remains highly stable. Although a slightly higher variation in the photon count is observed for the sub-Ångstrom case when changing the energy spread, though the 3D gain length remains stable. The exceptional stability of the PWFA XFEL is due to its operation near the cold beam limit, where the FEL requirements and Ming Xie scaled parameter conditions ($\chi_{\gamma_{\mathrm{rel}}} < 1/\sqrt{3},\ \chi_{\epsilon} < 1,$ and $\chi_{\mathrm{d}} < 1/2$) are satisfied by a significant margin. Witness beam parameter variations do not significantly impact the gain and FEL performances, as shown in Fig.(6.6). A comparable case is presented in Fig.(2.10), where calculations at the cold beam limit display sub-cm variation of the 3D gain length. This XFEL stability plateau is likely uniquely accessible with ultra-cold beams and is expected to improve even further at higher witness energies with beneficial effects on the emittance and energy spread conditions and scaled Ming Xie parameters.

By operating at longer plasma wavelengths in the PWFA stage and synchronizing lasers and electron beams to 10 fs at linac facilities, witness beam quality and parameter stability can be significantly improved, as discussed in section (4.2.2). Further, the Hybrid LWFA→PWFA configuration may offer small footprint systems with even better timing synchronization than linac-powered PWFA. This intrinsic temporal synchronization in Hybrid LWFA→PWFA systems raises hope for exact temporal injection precision (see Sec.(3.2.8)). These two directions provide potential pathways for the experimental realization of this concept. Whether the electron driver beam for PWFA originates from a linac or an LWFA stage, the plasma photocathode injection combined with the escort bunch dechirping technique can pave the way to the ultra-compact attosecond-Ångstrom class XFEL developed in this thesis.

The distance from the plasma photocathode PWFA stage to the end of the undulator in the showcased demonstrations is approximately 25 meters. In the case of linac-driven PWFA, the total system length would primarily be determined by the linac length.

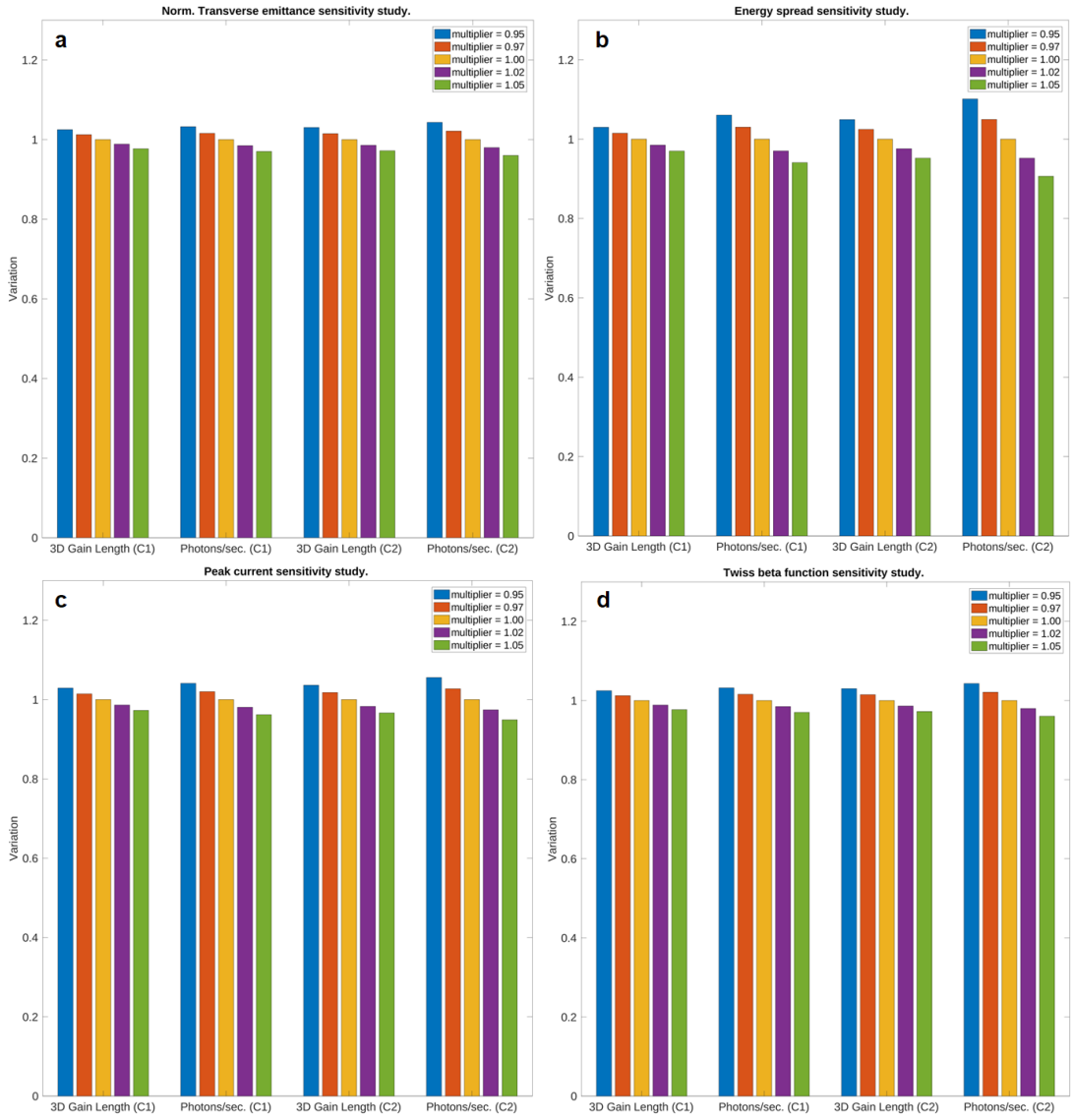

Figure 6.9: **Ultra-compact PWFA XFEL sensitivity study for the 0.15 nm (C1) and 0.08 nm (C2) cases.** Crucial witness beam slice properties are varied near the nominal values by up to ±5 % and the XFEL performance for the two cases (C1, C2) is evaluated with the STAFF tool [359] based on the Ming Xie formalism. In (a), normalized slice emittance, in (b) slice relative energy spread, in (c) peak current and in (d), twiss beta function variation impact on the two XFEL cases are presented. The study shows that the working points are highly robust against significant variation of the witness beam parameters and show less than ±2.5 % variation of the XFEL across the parameters and working points.

However, the quality requirements for a driver beam in a plasma photocathode PWFA system are significantly lower in emittance and energy spread compared to driving a traditional FEL. This creates more opportunities for mixed-mode installations, such as using linac-generated electron beams that have powered an undulator in a traditional FEL setup to also serve as an **energy** and **brightness booster** stage for a plasma photocathode PWFA arm. Such an extension, referred to as an afterburner plasma-XFEL, would enhance the overall capabilities and efficiency of the facility, including existing and future FELs.

When implementing a Hybrid LWFA→PWFA setup, the experimental section utilizing X-ray pulses post-plasma may have the most significant spatial footprint. By realizing the PWFA XFEL concept through this method, a standalone miniaturized FEL system can be produced and pave the way for exploring new capabilities and modalities in photon science. This includes a Hybrid LWFA→PWFA-based XFEL arm at current or future linac-based FEL facilities, or even multiple XFEL-arms at any geometry and energy level, coexisting with other laser and particle beams, as illustrated in figure (7.2). The possibilities for configurations and applications of miniaturized XFEL systems remain largely untapped, with potential use cases beyond what the current user community can foresee.

Both PWFA [204, 360] and LWFA [361] can operate at kHz or potentially MHz repetition rates, which could lead to the realization of the PWFA XFEL presented here at high repetition rates. This would result in high average power XFEL radiation and the ability to deploy various adaptive stabilization mechanisms and data-driven optimization methods [199]. Currently, most LWFA and PWFA experiments are performed at a repetition rate of 1-10 Hz. However, there are efforts to develop 100 Hz LWFA systems based on high peak power Ti:sapphire laser systems [362] and potential prospects for kHz and MHz repetition rates with thin-disk lasers [363] and optical fibre lasers [364, 365]. These advancements in laser technology provide encouraging prospects for realizing plasma photocathodes at linacs with up to kHz and MHz repetition rates. They may also allow high average power Hybrid LWFA→PWFA systems, ultimately enabling high average power miniaturized XFEL systems proposed in this work.

Enhancing capacity over the long term is undoubtedly important, but the quality of the electron beams produced and the resulting photon pulses are even more critical than quantity. This is why just 1-5 pC of witness charge compressed into kA peak currents,

with ultra-low emittance and low energy spread, is sufficient to power hard XFEL. A much larger charge fraction of the electron beam contributes to the FEL process. This, in turn, leads to an increased number of "useful" photons at the desired photon energy within a specified bandwidth that can be harnessed in precision experiments. In this regard, a clean photon pulse from a well-defined electron beam with ultrahigh quality is an asset, as it may generate clean and conclusive data for evaluation and potentially result in a significant reduction in experimental time. The increased repetition rate and elevated number of "useful" photons can dramatically improve the quality of future experiments compared to current state-of-the-art XFELs.

When considering the economic aspects of an XFEL machine, the 1D gain length plays a significant role in determining civil engineering expenses and environmental impact. Hence, the gain length elongation in 3D will have a proportionally larger economic impact when dealing with a few meter-scale 1D gain lengths than the proposed sub-meter gain length regime. Therefore, minimising 1D and 3D gain lengths is crucial for the machine's efficiency and overall impact. While wall-plug energy efficiency is important for facility design, capabilities like attosecond pulse duration and sub-Ångstrom wavelengths this approach promises have far-reaching implications for science and experiments. At the heart of it is the **brightness-transforming** component of the present concept, which is necessary for plasma-accelerated electron beams to reach the quality threshold for the hard XFEL regime; without it, the efficiency of coherent hard X-ray photon production would be zero.

6.6 DISCUSSION

The findings reported in this chapter will have direct ramifications for the advancement of next-generation, plasma-based free-electron lasers and the exploration of attosecond pulses at Ångstrom and sub-Ångstrom wavelength.

The concept invented here can generate electron and photon beams that surpass even the most advanced state-of-the-art km-scale hard X-ray facilities in terms of bright, distinct, and ultrashort photon pulse production. High-fidelity start-to-end simulations for the three building blocks (plasma accelerator stage, transport line, and undulator) revealed three significant breakthroughs.

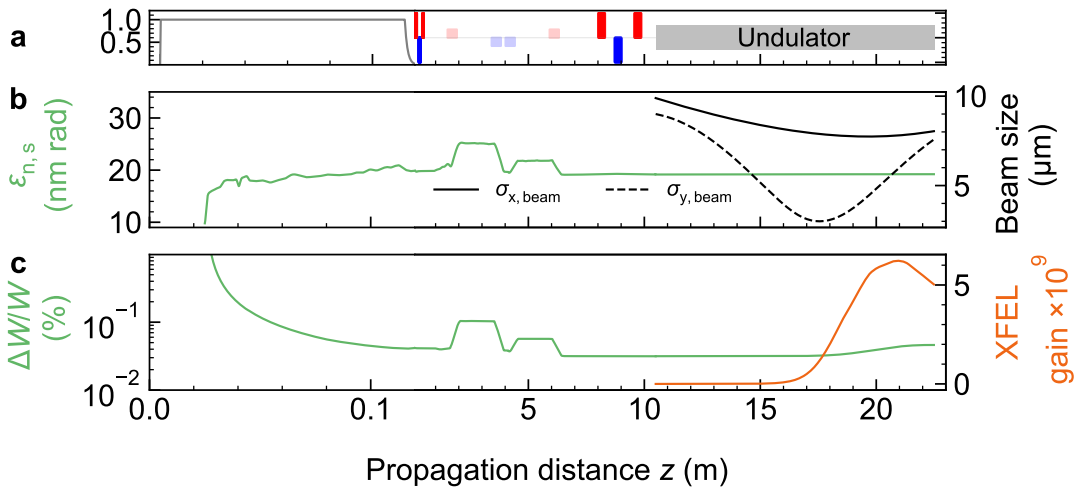

Figure 6.10: **Witness beam key parameter preservation and evolution along the PWFA XFEL.** In (a), starting from the left, the plasma density profile (grey) is plotted, followed by the transport line elements for the witness beam (red and blue) and the undulator section (grey solid line). In (b), normalized average slice emittance evolution over the 23-meter propagation distance (green solid line) and the witness beam focusing inside the undulator (black dashed line for the vertical plane and solid line for the horizontal plane) is depicted. The green line represents the slice energy spread evolution across the three building blocks, while the orange line shows a selected XFEL gain curve in the undulator. Produced by the author for [44]. This work is openly licensed via CC BY 4.0.

Firstly, the plasma photocathode injector and dechirper techniques work synergistically to produce fully dechirped attosecond electron beams with a slice energy spread of only 0.04 % at multi-GeV energies and a normalized projected emittance of $\epsilon_{n,(x,y)} \approx$ 23(17) nm-rad. Secondly, these beams can be transported without significant quality loss in practical settings. Although transporting beams with substantially higher energy spread and μm-rad level emittance from today's plasma accelerators poses challenges, the much better initial beam quality achieved directly within the plasma accelerator stage reduces beam quality preservation challenges during transport. The final projected normalized emittance at the entrance of the undulator has increased by only sub-2 nm-rad compared to the plasma stage exit, and the final projected slice energy spread remains nearly identical to the initial values. Thirdly, when focused on undulators, these cold beams are ideal for ultrahigh gain and enable coherent, high-contrast XFELs near the cold beam limit regime. Figure (6.10) summarizes the evolution of witness beam parameters from the start-to-end of the plasma-XFEL and highlights beam quality preservation along the 25 m of the system and table (6.2) presents witness beam parameters at selected positions across the three building blocks of the PWFA XFEL. These witness beams produce distinct, coherent, hard X-ray pulses with sub-Å, attosecond-scale characteristics without needing electron beam manipulation or photon pulse cleaning. The analysis in section (6.5) suggests that such a plasma-XFEL may be within technical reach, considering stability, repetition rate, efficiency, and practical considerations. The ultra-high quality electron beam allows the XFEL to operate near the cold beam limit, achieving exceptional stability.

Further improvements in electron beam quality could push the XFEL to its Fourier transform limits, resulting in attosecond duration hard X-ray pulses with advanced capabilities. These capabilities include obtaining clean diffraction images, imaging electronic motion at the natural time and length scale, and many other applications. The implications of this work suggest the possibility of harder photon energies, multi-colour pulses, and photon pulses with improved modalities. The LWFA-driven PWFA, equipped with a plasma photocathode, could pave the way towards miniaturization of the technology, enabling the ubiquitous use of hard XFELs as diagnostics for probing plasma, nuclear, or high-energy physics and other applications. For example, a previously unfeasible configuration of a multi-FEL facility with inherently synchronised X-ray,

laser and electron beams at arbitrary geometry at IP. These prospects may completely change the way XFELs are used in the future.

Table 6.2: **PWFA XFEL witness beam parameters summary**. A summary of the witness beam parameters at the different locations $W_1 - W_5$ with the initial electron driver beam properties is presented. The z-positions along the three building blocks correspond to the scale in figure (6.10). Witness beam parameters are displayed just after plasma photocathode injection and trapping (W_1), before escort bunch release (W_2), at the optimum dechirping and plasma stage exit (W_3), at the undulator entrance (W_4) and post XFEL interaction (W_5).

	Incoming Driver	W_1	W_2	W_3	W_4	W_5
z-position (m)	0	0.032	0.08	0.12	10.5	23
Energy (GeV)	2.5	0.230	1.750	2.725	2.725	2.725
Duration (fs)	42	0.52	0.52	0.52	0.57	0.57
Peak Current (kA)	$\simeq 5.5$	$\simeq 1.2$	$\simeq 1.2$	$\simeq 1.2$	$\simeq 1.2$	$\simeq 1.2$
Proj. and (slice) norm. emittance (nm-rad)	2×10^3	23(17)	32 ($\simeq 20$)	45 ($\simeq 20$)	46.6 ($\simeq 20$)	46.6 ($\simeq 20$)
Proj. and (slice) energy spread (%)	2.0 (2.0)	1.1 (0.4)	1.1 (0.05)	0.08 (0.04)	0.08 (0.026)	0.08 (0.05)
Proj. 6D brightness ($Am^{-2}rad^{-2}/0.1\%bw$)	7.0×10^{13}	4.0×10^{17}	2.0×10^{17}	1.3×10^{18}	1.3×10^{18}	1.3×10^{18}
Slice 6D brightness ($Am^{-2}rad^{-2}/0.1\%bw$)	7.0×10^{13}	1.0×10^{18}	6.6×10^{18}	7.5×10^{18}	1.1×10^{19}	6.0×10^{18}

7

CONCLUSIONS AND OUTLOOK

This chapter summarises the results of the current thesis, concludes and outlines the future directions of the R&D and discusses potential photon and fundamental science modalities accessible in the near future with ultra-bright electron and photon beams.

7.1 SUMMARY

This thesis presents a blueprint for an ultra-compact, plasma-based hard XFEL near the cold beam limit with unprecedented electron and photon beam quality based on three distinct breakthroughs [39, 42, 44]. The results simultaneously solve the obstacles that have hindered the realisation of ultra-compact, plasma-based hard XFEL and open the path towards an innovative and viable hard XFEL concept.

The first successful experimental implementation of the plasma photocathode in a 90° geometry has demonstrated the feasibility of the injection concept and confirmed its accordance with theoretical predictions and simulations. The plasma afterglow spatiotemporal alignment method was integral to successfully implementing plasma photocathode injection in the PWFA, even under compromised experimental boundary conditions. Experimental and simulation data analysis revealed straightforward pathways to improve witness beam stability and quality in future experiments. For example, if the plasma source diameter is much larger than the blowout radius $D_{\mathrm{channel}} \gg R_{\mathrm{b}}$, then the variation of the diameter, shape and alignment of the plasma source from shot-to-shot may not play a significant role in energy gain, quality and stability of the witness beam. Such a PWFA configuration provides the optimal environment for a stable collinear plasma photocathode injection. A thorough study of realistic spatiotemporal and intensity jitter of the plasma photocathode laser pulse uncovered

that the witness beam quality could exceed even the best rf-based accelerators, with exceptional witness beam parameter stability. This is highly promising for the next generation of plasma photocathode injection experiments and ultra-compact hard XFELs powered by these ultra-high 5D brightness witness beams. Combining an injector, compressor, and accelerator in a single plasma stage using a plasma photocathode PWFA is highly attractive. However, the ability to compensate for energy chirp in the same plasma stage is missing in the all-plasma capability to generate ultra-high 6D brightness electron beams.

The second main achievement of this thesis tackles the challenge of large energy spread and energy chirp of the ultra-high 5D brightness witness beams in plasma-based accelerators by developing a novel energy chirp compensation approach. This unique approach leverages beam loading via a second electron beam (escort bunch) released during the later acceleration stage of the ultra-high 5D brightness witness beam. This trick ensures that the witness beam is immune to the space charge forces of the escort bunch and facilitates the preservation of witness beam quality during dechirping. The escort bunch can be created by any method capable of producing high-charge and high-peak current beams, but in this case, a second plasma photocathode laser pulse is utilized to take advantage of the inherent temporal synchronisation and stabilisation features of plasma photocathodes. This innovative method elegantly solves several problems, including dealing with electron beams of unprecedented ultra-high 5D brightness in the same plasma stage, decoupling the dechirping of the witness beams from the acceleration and generation process, witness beam quality preservation during dechirping and extraction from the plasma stage, and robustness of the dechirping process against spatiotemporal jitter of the witness beam injector laser. Thanks to the intrinsic stabilization properties of the plasma photocathodes in PWFA, this method generates reliably ultra-high 6D-brightness electron beams with ultralow normalized emittance, low energy spread, and high peak current at exceptional stability. Furthermore, it may help preserve the witness beam quality during transport towards the XFEL application. It can have a transformative impact on light and particle sources and may lead to new scientific frontiers. This approach is applicable at higher beam energies relevant to HEP, may enable the generation of multi-energy electron beams for multi-chromatic light sources, and allows accurate control of the longitudinal phase space of the witness beam.

The third main achievement of this thesis reaches a significant breakthrough: A plasma-based attosecond-Ångstrom class free-electron laser concept has been developed through a high-fidelity start-to-end simulations framework. Building on the findings of previous achievements of this thesis, a dedicated PWFA acceleration stage has been designed to create electron beams with unparalleled 6D brightness values with record characteristics. The witness beam properties in terms of projected (slice) normalized emittance are preserved on the nm-rad level with sub-0.1 %-level projected (slice) relative energy spread values at multi-GeV energies during acceleration, dechirping and extraction from the plasma-stage. A beam transport line has been designed and optimized to preserve the witness beam's quality during capture from the plasma stage, transport, isolation, and refocusing into an undulator section for hard X-ray coherent photon production. The undulator configuration is designed to harness the full potential of this new class of electron beams for high photon gain. In the undulator section, the hard XFEL saturates after 10 meters with a sub-meter scale 3D gain length close to the idealised 1D gain length at the cold beam regime. The sub-fs duration witness beam produces near-isolated single spikes at 100 as duration at GW-level peak power. The radiation wavelength is tuned down to 0.8 Å with prospects for even short wavelength. The hard X-ray photon pulse characteristics suggest that the radiation pulses are close to the transformer limit, and future investigation may enable fully coherent single-spike radiation pulses. A forward-looking analysis of the PWFA hard XFEL concept concludes with the system's experimental feasibility and prospective exceptional stability.

7.2 CONCLUSIONS AND OUTLOOK

The radiation characteristics of the PWFA XFEL presented in this thesis are pushing the boundaries of scientific exploration and enter the "novel frontier of science" region in figure (1.1) in chapter (1). These coherent radiation pulses, operating in the attosecond-Ångstrom range, have the potential to revolutionize attosecond pump and probe experiments, enabling observation of electron motion and ultra-fast charge transfer at their natural time and length scales in atoms, molecules, and solids. Additionally, actual diffraction before distraction experiments for determining the structure of single molecules may become a reality, ultimately advancing fields such as chemistry, biochemistry, and medicine. These developments may have a catalytic effect on the

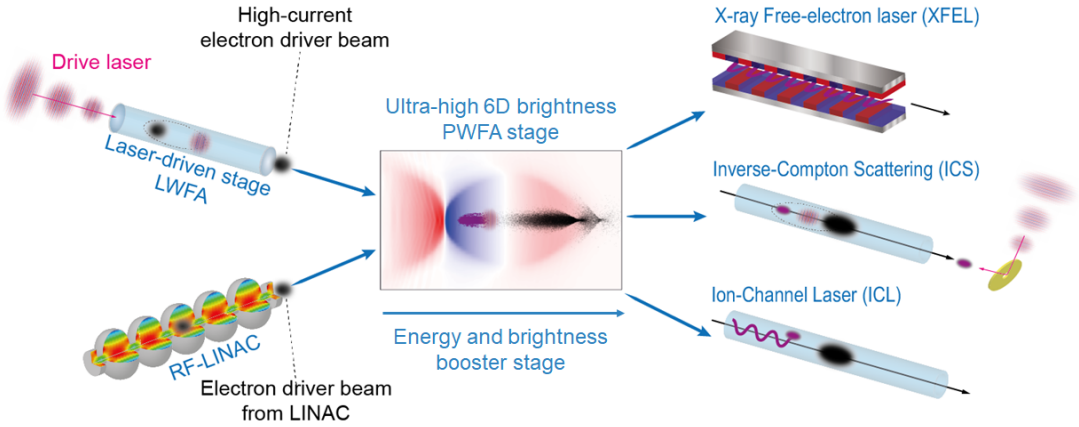

Figure 7.1: **Energy and brightness booster PWFA stage.** Experimental pathway of realising plasma photocathode PWFA stage and potential light source applications of ultra-high 6D brightness. Produced by the author for [40] and adapted for the thesis.

R&D landscape and revolutionize science, technology, and society in ways limited by our imagination. A few selected future avenues and experimental pathways towards realizing the PWFA XFEL concept are outlined below.

The experimental demonstrations of 90° plasma photocathode at SLAC FACET [39] and at Hybrid LWFA→ PWFA [263] mark vital experimental milestones. However, realising plasma photocathode in collinear geometry and increasingly approaching and measuring the ultra-high quality electron beams is the next challenge aimed at the E-310 experiment at SLAC FACET-II and with the Hybrid LWFA→ PWFA platform. The demonstration of the escort bunch-based dechirping approach is aimed at the E-313 experiment at SLAC FACET-II, where the author is one of the principal investigators. An experimental realisation of the PWFA XFEL developed in this thesis would be a breakthrough. Even a subset of the capabilities is regarded as a milestone (see review protocol of [44]), for this vision to succeed a programmatic R&D program will be required at dedicated linacs or Hybrid LWFA→ PWFA facilities. First attempts to establish such an R&D program were made [366, 367], and other efforts are underway. A reasonable strategy would be to start with single electron bunch beam loading of the wakefield and systematically attain the ultra-high 6D brightness electron beams presented in this thesis.

The ultra-high 6D brightness PWFA stage can unfold its potential as a standalone system. It can also enhance the capabilities and modalities of existing and future linac-based FELs and compact LWFA facilities via Hybrid LWFA→ PWFA. For example, an

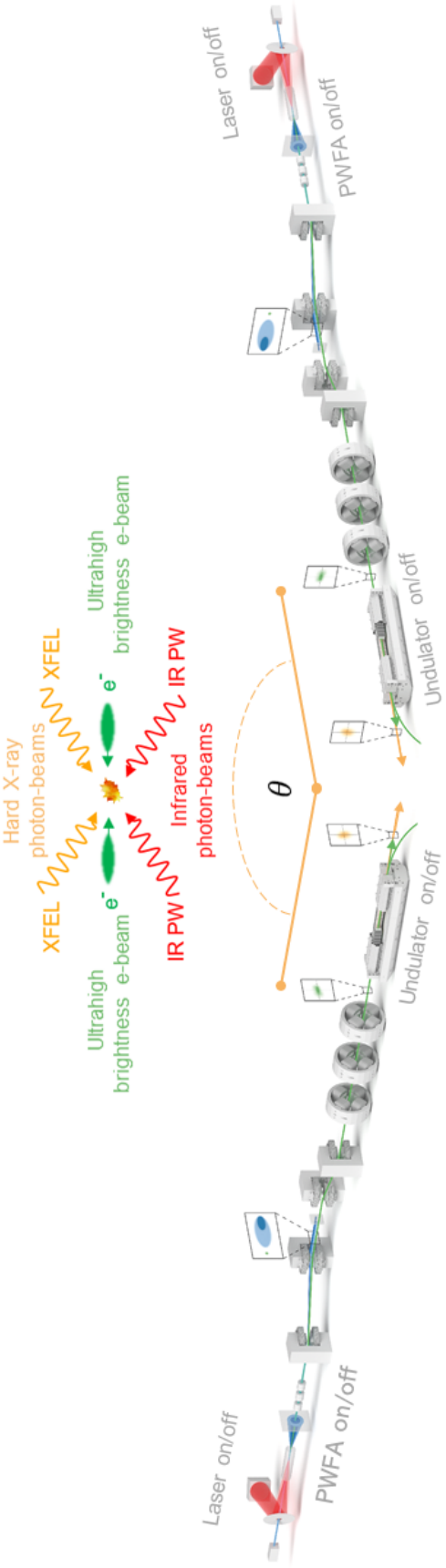

Figure 7.2: **Future vision of a multi-PWFA XFEL concept.** Future vision of a multi-PWFA XFEL concept in collider configurations with various permutations for utterly novel photon science, particle and fundamental physics exploration.

ultra-high 6D brightness PWFA stage can serve as an energy and brightness booster stage in conventional linacs and post-LWFA stages, as illustrated in figure (7.1). This plasma stage can be placed before the undulator section at existing and future FEL facilities to enhance the FEL capabilities or post-FEL interaction to utilize the FEL beam for an afterburner PWFA stage. As a result, the ultra-high 6D brightness PWFA stage can act as a gateway towards a wide range of light sources, including the present PWFA hard XFEL concept, Inverse Compton Scattering and Ion Channel Laser, and other applications discussed in [40, 41]. Due to its compact nature, the ultra-high 6D brightness PWFA stage and its resulting applications, such as light sources, can be ubiquitously deployed as diagnostic tools for probing or driving plasma, nuclear processes and nuclear fusion, high-energy physics, quantum electrodynamics, fundamental physics, and many other applications discussed in [41].

A completely novel modality for exploring fundamental physics and science could be achieved through the implementation of multiple Hybrid LWFA→ PWFA-powered ultra-compact XFELs in collider geometry at a single site or in combination with linac-powered PWFA, as illustrated in figure (7.2). The potential scientific inquiries enabled by this technology would encompass multi-directional and multi-coloured probing of matter and vacuum and investigating topics such as quantum electrodynamics and direct photon-photon processes. The direct photon-photon process is a key prediction of the standard model but is experimentally not verified in a direct observation. Further, utilizing XFEL photons as plasma and target diagnostics in nuclear fusion reactors may become feasible [41, 44], and/or XFEL photons may be leveraged to assist nuclear fusion [368]. There is also the possibility of tomographic imaging and probing of single molecules and matter with multi-directional and multi-coloured photon pulses from these ultra-compact hard XFELs in collider geometry. Such a PWFA XFEL-collider system could also be installed at conventional existing or forthcoming XFEL facilities to enhance the facility's capabilities. An especially appealing configuration would involve the integration of all-optical Hybrid LWFA→ PWFA systems in collider geometry, with beams of TW- to PW-call lasers, ultrabright electron beams, and hard XFEL pulses or γ-ray pulses generated by these ultra-bright electron beams, all intrinsically synchronized at the interaction point [41, 44, 369, 370]. Here, only a handful of aspirations for such a machine are discussed. However, there are likely more use cases for such a machine that are not captured in this thesis. Although the current hard XFELs based on linacs are

exclusively km-scale machines and make such a configuration unimaginable, the results of this thesis and the significant advancements in the Hybrid LWFA→ PWFA concept inspire reasonable optimism for the realization of this vision.

8

APPENDIX I

Here, supplementary material is provided for this thesis.

8.1 APPENDIX CHAPTER 2

This section provides supplementary content for the chapters (2).

8.1.1 *Appendix Transfer Matrix*

This section introduces transfer matrices relevant to this thesis. The matrix for the drift section is

$$\mathbf{R}_{\mathrm{Drift}} = \begin{pmatrix} 1 & l & 0 & 0 & 0 & 0 \\ 0 & 1 & 0 & 0 & 0 & 0 \\ 0 & 0 & 1 & l & 0 & 0 \\ 0 & 0 & 0 & 1 & 0 & 0 \\ 0 & 0 & 0 & 0 & 1 & 0 \\ 0 & 0 & 0 & 0 & 0 & 1 \end{pmatrix}. \tag{8.1}$$

The transfer matrix of a quadrupole reads

$$\mathbf{R}_{\mathrm{QD}} = \begin{pmatrix} \cos\kappa & \frac{1}{\sqrt{|k_1|}}\sin\kappa & 0 & 0 & 0 & 0 \\ -\sqrt{|k_1|}\sin\kappa & \cos\kappa & 0 & 0 & 0 & 0 \\ 0 & 0 & \cosh\kappa & \frac{1}{\sqrt{|k_1|}}\sinh\kappa & 0 & 0 \\ 0 & 0 & \sqrt{|k_1|}\sinh\kappa & \cosh\kappa & 0 & 0 \\ 0 & 0 & 0 & 0 & 1 & 0 \\ 0 & 0 & 0 & 0 & 0 & 1 \end{pmatrix}. \tag{8.2}$$

The dipoles employed in the chicane for the electron beams separation section are rectangular dipole magnets with parallel entrance and exit faces. The transfer matrix for a rectangular dipole can be constructed from the transfer matrix of a sector dipole magnet $\mathbf{R}_{\text{Sector}}$ (entrance and exit face are perpendicular to the design orbit) with an additional edge-focusing matrix $\mathbf{R}_{\text{edge}}$. The transfer matrix of a rectangular dipole is then

$$\mathbf{R}_{\text{Rectangular}} = \mathbf{R}_{\text{edge}} \cdot \mathbf{R}_{\text{Sector}} \cdot \mathbf{R}_{\text{edge}}, \tag{8.3}$$

where the transfer matrix of a sector dipole magnet is

$$\mathbf{R}_{\text{Sector}} = \begin{pmatrix} \cos\theta & \rho\sin\theta & 0 & 0 & 0 & \rho(1-\cos\theta) \\ -\frac{1}{\rho}\sin\theta & \cos\theta & 0 & 0 & 0 & \sin\theta \\ 0 & 0 & 1 & \rho\theta & 0 & 0 \\ 0 & 0 & 0 & 1 & 0 & 0 \\ -\sin\theta & \rho(\cos\theta-1) & 0 & 0 & 1 & -\rho(\theta-\sin\theta) \\ 0 & 0 & 0 & 0 & 0 & 1 \end{pmatrix} \tag{8.4}$$

and the transfer matrix of edge-focusing reads

$$\mathbf{R}_{\text{edge}} = \begin{pmatrix} 1 & 0 & 0 & 0 & 0 & 0 \\ \frac{\tan\theta/2}{\rho} & 1 & 0 & 0 & 0 & 0 \\ 0 & 0 & 1 & 0 & 0 & 0 \\ 0 & 0 & -\frac{\tan\theta/2}{\rho} & 1 & 0 & 0 \\ 0 & 0 & 0 & 0 & 1 & 0 \\ 0 & 0 & 0 & 0 & 0 & 1 \end{pmatrix}. \tag{8.5}$$

8.1.2 *Appendix Ming Xie coefficients*

The table (8.1) contains the fitting coefficients of the Ming Xie fitting function presented in Eq.(2.75).

Table 8.1: Xie fitting parameters for Λ Eq.(2.75) according to [111].

$a_1 = 0.45$	$a_2 = 0.57$	$a_3 = 0.55$	$a_4 = 1.6$
$a_5 = 3$	$a_6 = 2$	$a_7 = 0.35$	$a_8 = 2.9$
$a_9 = 2.4$	$a_{10} = 51$	$a_{11} = 0.95$	$a_{12} = 3$
$a_{13} = 5.4$	$a_{14} = 0.7$	$a_{15} = 1.9$	$a_{16} = 1140$
$a_{17} = 2.2$	$a_{18} = 2.9$	$a_{19} = 3.2$	

8.2 APPENDIX CHAPTERS 4 AND 5

This section provides supportive material for the chapters (4) and (5).

8.2.1 *Data access*

The data set for the publication [39] is available from the corresponding authors upon reasonable request. Data associated with the publication [42] is publicly accessible under the doi: `https://doi.org/10.15129/3563d476-7a65-497c-9c7e-5a1f7a57591f`. The complete data set produced for the publication [44] is publicly accessible under the doi: `https://doi.org/10.15129/176712e5-7677-461e-9d78-bb9af35cff76`.

8.2.2 *Appendix proof-of-concept simulation parameters in chapter 5*

The novel dechirper concept in section (5.1.4) was modelled with the 3D PIC code VSim. The input file consists of more than 3400 lines of instructions for the PIC engine; however, below, a subset of the parameters is provided for reference.

```
##############################################
```

```
###
### Input file : res4wedding80fsV3.pre
### Output file: res4wedding80fsV3.in
###
################################################

DX = 8e-07 # longitudinal resolution (meters)
DY = 3.2e-06 # transverse resolution (meters)
DZ = 3.2e-06 # transverse resolution (meters)
DT = 1.3342563807926082e-15 # integration time step (seconds)
NX = 288  # numbers of grid cells in the longitudinal direction
NY = 48   # numbers of grid cells in the transverse direction
NZ = 48   # numbers of grid cells in the transverse direction
LX = 0.0002304 # LX, LY, LZ are the corresponding  simulation box sizes (meters)
LY = 0.0001536
LZ = 0.0001536
PTCL_ORDER = 3 # macro-particle order
PTCL_INTERPOLATION = "esirk3rdOrder" # interpolation method
NDIM = 3 # Simulation dimension here 3D
SIMTIME = 8.339102379953802e-11 # Total simulation time (seconds)
NDUMPS = 625 # Number of data checkpoints
NSTEP_TMP = 62500 # Total number of computed time steps
```

8.2.3 *Appendix PWFA stage simulation parameters in chapter 6*

The input file for the advanced PWFA stage for the XFEL application in section (6.2.2) is highly optimized for numerical efficiency, enabling the modelling of multi-cm long plasma stages at high-fidelity. The input file contains many important innovations in ≈ 2000 lines of instructions for the PIC engine. Below are only the essential simulation box parameters.

```
################################################
###
### Input file : thpwfaxfel_v8b.pre
### Output file: thpwfaxfel_v8b.in
###
################################################
```

```
DX = 1e-07 # longitudinal resolution (meters)
DY = 1e-06 # transverse resolution (meters)
DZ = 1e-06 # transverse resolution (meters)
DT = 3.3356409519815204e-16 # integration time step (seconds)
NX = 1440  # numbers of grid cells in the longitudinal direction
NY = 145   # numbers of grid cells in the transverse direction
NZ = 145   # numbers of grid cells in the transverse direction
LX = 0.000144 # LX, LY, LZ are the corresponding  simulation box sizes (meters)
LY = 0.000144
LZ = 0.000144
PTCL_ORDER = 3 # Macro-particle order
PTCL_INTERPOLATION = "esirk3rdOrder" # interpolation method
NDIM = 3 # Simulation dimension here 3D
SIMTIME = 5.003461427972281e-10 # total simulation time (seconds)
NDUMPS = 1499 # Number of data checkpoints
NSTEP_TMP = 1500000 # total number of computed time steps
```

8.2.4 *Appendix beam transport line*

The optimized particle tracking simulation in section (6.3) is based on the below example beam line lattice.

```
! Below, quadrupole elements are defined
! L: length of the element in meters and K1: strength of the quadrupole
QM1: QUAD,L=0.1,K1=79.99
QM2: QUAD,L=0.1,K1=-79.48
QM3: QUAD,L=0.05,K1=79.70
QM4: QUAD,L=0.3,K1=4.60
QM5: QUAD,L=0.3,K1=-5.00
QM6: QUAD,L=0.3,K1=4.72

! Below drift elements are defined L: length of the element in meters
DQM: DRIF,L=0.1
DQM1: DRIF,L=0.064
DQM2: DRIF,L=0.071
DQM3A: DRIF,L=1.030
```

```
DQM4: DRIF,L=0.409
DQM5: DRIF,L=0.551
DQM6: DRIF,L=0.5
! Below drift elements in the chicane are defined
! L: length of the element in meters, DZ: integration step size in meters
BDCSR1: CSRDRIFT,L=1.5,DZ=0.001,USE_STUPAKOV=1
BDCSR2: CSRDRIFT,L=0.2,DZ=0.001,USE_STUPAKOV=1
BDCSR3: CSRDRIFT,L=1.70,DZ=0.001,USE_STUPAKOV=1

! Below, collimator elements are defined as black body
RCOLDM: ECOL,L=0.0001,X_MAX=0.25e-3,Y_MAX=0.25e-3
RCOLB2: ECOL,L=0.0001,X_MAX=0.2e-3,Y_MAX=0.2e-3

! Below, dipole magnets are defined considering CSR
! L: length of the element, ANGLE: bend angle in (rad)
B1: CSRCSBEND,L=0.4,ANGLE=0.002,CSR=1,N_KICKS=400,BINS=1000,SG_HALFWIDTH=1, USE_STUPAKOV=1
B2: CSRCSBEND,L=0.4,ANGLE=-0.002,CSR=1,N_KICKS=400,BINS=1000,SG_HALFWIDTH=1, USE_STUPAKOV=1
B3: CSRCSBEND,L=0.4,ANGLE=-0.002,CSR=1,N_KICKS=400,BINS=1000,SG_HALFWIDTH=1, USE_STUPAKOV=1
B4: CSRCSBEND,L=0.4,ANGLE=0.002,CSR=1,N_KICKS=400,BINS=1000,SG_HALFWIDTH=1, USE_STUPAKOV=1

! Below, the three building blocks of the example beam transport line are defined
PMQ_TRIPLET: LINE=(QM1,DQM1,QM2,DQM2,QM3)
EMQ_TRIPLET: LINE=(QM4,DQM4,QM5,DQM5,QM6)
CHICANE: LINE=(B1,BDCSR1,B2,BDCSR2,RCOLB2,B3,BDCSR1,B4)

! Below, the complete beam transport line is defined
PWFA_XFEL_BEAMLINE: LINE=(DQM,RCOLDM,PMQ_TRIPLET,DQM3A,CHICANE,BDCSR3,EMQ_TRIPLET,DQM6)
```

BIBLIOGRAPHY

1. Eberhardt, W., Himpsel, F. & Hemminger, J. Next Generation Photon Sources for Grand Challenges in Science and Energy. *Department of Energy's Office of Science (https://science.osti.gov/-/media/bes/pdf/reports/files/Next-Generation_Photon_Sources_rpt.pdf)* (2009).

2. Marangos, J. *et al.* UK-XFEL Science Case. https://www.clf.stfc.ac.uk/Pages/UK-XFEL-science-case.aspx (2020).

3. Akhoundova, D. & Rubin, M. A. The grand challenge of moving cancer whole-genome sequencing into the clinic. *Nature medicine* **30,** 39–40 (2024).

4. Sosinsky, A., Ambrose, J., Cross, W., Turnbull, C., Henderson, S., Jones, L., Hamblin, A., Arumugam, P., Chan, G., Chubb, D., *et al.* Insights for precision oncology from the integration of genomic and clinical data of 13,880 tumors from the 100,000 Genomes Cancer Programme. *Nature Medicine* **30,** 279–289 (2024).

5. Nenner, I. in *Applications of High Field and Short Wavelength Sources* ThD1 (1997).

6. Hwang, C., Jan, J., Chang, C., Chen, S., Chang, C. & Uen, T. Development trends for insertion devices of future synchrotron light sources. *Physical Review Special Topics-Accelerators and Beams* **14,** 044801 (2011).

7. Robinson, A. L. History of Synchrotron Radiation. *Synchrotron Radiation News* **28,** 4–9 (2015).

8. Pellegrini, C. Design considerations for a SASE X-ray FEL. *Nuclear Instruments and Methods in Physics Research Section A: Accelerators, Spectrometers, Detectors and Associated Equipment* **475.** FEL2000: Proc. 22nd Int. Free Electron Laser Conference and 7th FEL Users Workshop, 1 –12 (2001).

9. Pellegrini, C. The history of X-ray free-electron lasers. *The European Physical Journal H* **37,** 659–708 (2012).

10. Chapman, H. N., Barty, A., Bogan, M. J., Boutet, S., Frank, M., Hau-Riege, S. P., Marchesini, S., Woods, B. W., Bajt, S., Benner, W. H., *et al.* Femtosecond diffractive imaging with a soft-X-ray free-electron laser. *Nature Physics* **2,** 839–843 (2006).

11. Chapman, H. N., Fromme, P., Barty, A., White, T. A., Kirian, R. A., Aquila, A., Hunter, M. S., Schulz, J., DePonte, D. P., Weierstall, U., *et al.* Femtosecond X-ray protein nanocrystallography. *Nature* **470,** 73–77 (2011).

12. Strickland, D. & Mourou, G. Compression of amplified chirped optical pulses. *Optics Communications* **56,** 219 –221 (1985).

13. Krause, J. L., Schafer, K. J. & Kulander, K. C. High-order harmonic generation from atoms and ions in the high intensity regime. *Physical Review Letters* **68,** 3535 (1992).

14. L'Huillier, A. & Balcou, P. High-order harmonic generation in rare gases with a 1-ps 1053-nm laser. *Physical Review Letters* **70,** 774 (1993).

15. Paul, P.-M., Toma, E. S., Breger, P., Mullot, G., Augé, F., Balcou, P., Muller, H. G. & Agostini, P. Observation of a train of attosecond pulses from high harmonic generation. *Science* **292,** 1689–1692 (2001).

16. *The Nobel Prize in Physics 2018* NobelPrize.org. `https://www.nobelprize.org/prizes/physics/2018/press-release/`. (2018).

17. *The Nobel Prize in Physics 2023* NobelPrize.org. `https://www.nobelprize.org/prizes/physics/2023/press-release/`. (2023).

18. Agostini, P. & DiMauro, L. F. The physics of attosecond light pulses. *Reports on progress in physics* **67,** 813 (2004).

19. Krausz, F. & Ivanov, M. Attosecond physics. *Reviews of modern physics* **81,** 163 (2009).

20. Zewail, A. H. Laser femtochemistry. *Science* **242,** 1645–1653 (1988).

21. Nisoli, M., Decleva, P., Calegari, F., Palacios, A. & Martín, F. Attosecond electron dynamics in molecules. *Chemical reviews* **117,** 10760–10825 (2017).

22. Hentschel, M., Kienberger, R., Spielmann, C., Reider, G. A., Milosevic, N., Brabec, T., Corkum, P., Heinzmann, U., Drescher, M. & Krausz, F. Attosecond metrology. *Nature* **414,** 509–513 (2001).

23. Lindroth, E., Calegari, F., Young, L., Harmand, M., Dudovich, N., Berrah, N. & Smirnova, O. Challenges and opportunities in attosecond and XFEL science. *Nature Reviews Physics* **1,** 107–111 (2019).

24. Mak, A., Shamuilov, G., Salén, P., Dunning, D., Hebling, J., Kida, Y., Kinjo, R., McNeil, B. W., Tanaka, T., Thompson, N., *et al.* Attosecond single-cycle undulator light: a review. *Reports on Progress in Physics* **82,** 025901 (2019).

25. Remacle, F. & Levine, R. D. An electronic time scale in chemistry. *Proceedings of the National Academy of Sciences* **103,** 6793–6798 (2006).

26. Rudenko, A, Inhester, L, Hanasaki, K, Li, X, Robatjazi, S., Erk, B, Boll, R., Toyota, K, Hao, Y, Vendrell, O, *et al.* Femtosecond response of polyatomic molecules to ultra-intense hard X-rays. *Nature* **546,** 129–132 (2017).

27. Neutze, R., Wouts, R., van der Spoel, D., Weckert, E. & Hajdu, J. Potential for biomolecular imaging with femtosecond X-ray pulses. *Nature* **406,** 752–757 (2000).

28. Ekeberg, T., Assalauova, D., Bielecki, J., Boll, R., Daurer, B. J., Eichacker, L. A., Franken, L. E., Galli, D. E., Gelisio, L., Gumprecht, L., *et al.* Observation of a single protein by ultrafast X-ray diffraction. *Light: Science & Applications* **13,** 15 (2024).

29. *Nobel Prize lecture* NobelPrize.org. `https://www.nobelprize.org/prizes/physics/2023/agostini/lecture/`. (2023).

30. Tanaka, T. Proposal for a pulse-compression scheme in x-ray free-electron lasers to generate a multiterawatt, attosecond x-ray pulse. *Physical review letters* **110,** 084801 (2013).

31. Marinelli, A, MacArthur, J, Emma, P, Guetg, M, Field, C, Kharakh, D, Lutman, A., Ding, Y & Huang, Z. Experimental demonstration of a single-spike hard-X-ray free-electron laser starting from noise. *Applied Physics Letters* **111,** 15 (2017).

32. Huang, S, Ding, Y, Feng, Y, Hemsing, E, Huang, Z, Krzywinski, J, Lutman, A., Marinelli, A, Maxwell, T. & Zhu, D. Generating single-spike hard X-ray pulses with nonlinear bunch compression in free-electron lasers. *Physical review letters* **119,** 154801 (2017).

33. Rebernik Ribič, P., Abrami, A., Badano, L., Bossi, M., Braun, H.-H., Bruchon, N., Capotondi, F., Castronovo, D., Cautero, M., Cinquegrana, P., *et al.* Coherent soft X-ray pulses from an echo-enabled harmonic generation free-electron laser. *Nature Photonics* **13,** 555–561 (2019).

34. Duris, J., Li, S., Driver, T., Champenois, E. G., MacArthur, J. P., Lutman, A. A., Zhang, Z., Rosenberger, P., Aldrich, J. W., Coffee, R., *et al.* Tunable isolated attosecond X-ray pulses with gigawatt peak power from a free-electron laser. *Nature Photonics* **14,** 30–36 (2020).

35. Kang, H.-S. & Ko, I. S. Attosecond XFEL for pump–probe experiments. *Nature Photonics* **14,** 7–8 (2020).

36. Aicheler, M., Burrows, P, Draper, M, Garvey, T., Lebrun, P, Peach, K, Phinney, N, Schmickler, H, Schulte, D. & Toge, N. *A Multi-TeV linear collider based on CLIC technology: CLIC Conceptual Design Report* tech. rep. (SLAC National Accelerator Lab., Menlo Park, CA (United States), 2014).

37. Litos, M. *et al.* High-efficiency acceleration of an electron beam in a plasma wakefield accelerator. *Nature* **515,** 92–95 (2014).

38. Scherkl, P. *et al.* Plasma photonic spatiotemporal synchronization of relativistic electron and laser beams. *Phys. Rev. Accel. Beams* **25,** 052803 (2022).

39. Deng, A., Karger, O., Heinemann, T., Knetsch, A., Scherkl, P., Manahan, G. G., Beaton, A., Ullmann, D., Wittig, G., Habib, A. F., *et al.* Generation and acceleration of electron bunches from a plasma photocathode. *Nature Physics* **15,** 1156–1160 (2019).

40. Habib, A. F., Scherkl, P., Manahan, G. G., Heinemann, T., Ullmann, D., Sutherland, A., Knetsch, A., Litos, M., Hogan, M., Rosenzweig, J., *et al. Plasma accelerator-based ultrabright x-ray beams from ultrabright electron beams* in *Advances in Laboratory-based X-Ray Sources, Optics, and Applications VII* **11110** (2019).

41. Habib, A. F., Heinemann, T., Manahan, G. G., Ullmann, D., Scherkl, P., Knetsch, A., Sutherland, A., Beaton, A., Campbell, D., Rutherford, L., *et al.* Plasma photocathodes. *Annalen der Physik* **535,** 2200655 (2023).

42. Manahan, G. G. and Habib, A. F. *et al.* Single-stage plasma-based correlated energy spread compensation for ultrahigh 6D brightness electron beams. *Nature communications* **8,** 15705 (2017).

43. Manahan, G. G., Habib, A., Scherkl, P, Ullmann, D, Beaton, A, Sutherland, A, Kirwan, G, Delinikolas, P, Heinemann, T, Altuijri, R, *et al.* Advanced schemes for underdense plasma photocathode wakefield accelerators: pathways towards ultrahigh brightness electron beams. *Philosophical Transactions of the Royal Society A* **377,** 20180182 (2019).

44. Habib, A. F. *et al.* Attosecond-Angstrom free-electron-laser towards the cold beam limit. *Nature communications* **14,** 1054 (2023).

45. Geiger, H. On the Scattering of the α-Particles by Matter. *Proceedings of the Royal Society of London. Series A, Containing Papers of a Mathematical and Physical Character* **81,** 174–177 (1908).

46. Rutherford, E. LXXIX. The scattering of α and β particles by matter and the structure of the atom. *The London, Edinburgh, and Dublin Philosophical Magazine and Journal of Science* **21,** 669–688 (1911).

47. *SLAC homepage* Stanford Linear Accelerator Center. `https://www6.slac.stanford.edu/` (2023).

48. Lawrence, E. O. & Livingston, M. S. A method for producing high speed hydrogen ions without the use of high voltages. *Phys. Rev* **37,** 178 (1931).

49. Courant, E. D., Livingston, M. S., Snyder, H. S. & Blewett, J. P. Origin of the "Strong-Focusing" Principle. *Phys. Rev.* **91,** 202–203 (1953).

50. Courant, E. D. & Snyder, H. S. Theory of the alternating-gradient synchrotron. *Annals of physics* **3,** 1–48 (1958).

51. *CERN homepage* CERN. `https://home.cern/science/accelerators/future-circular-collider` (2023).

52. Wiedemann, H. *Particle Accelerator Physics* (Springer-Verlag Berlin Heidelberg, 2007).

53. Stanley Humphries, J. *Charged Particle Beams* (2002).

54. Reiser, M. *Theory and design of charged particle beams* (John Wiley & Sons, 2008).

55. Wille, K. *The Physics of Particle Accelerators* (Oxford University Press, 2000).

56. Di Mitri, S. On the Importance of Electron Beam Brightness in High Gain Free Electron Lasers. *Photonics* **2,** 317 (2015).

57. Schaber, J., Xiang, R. & Gaponik, N. Review of photocathodes for electron beam sources in particle accelerators. *Journal of Materials Chemistry C* **11,** 3162–3179 (2023).

58. Einstein, A. Über einen die Erzeugung und Verwandlung des Lichtes betreffenden heuristischen Gesichtspunkt. *Annalen der Physik* **322,** 132–148 (1905).

59. Prat, E., Aiba, M., Bettoni, S., Beutner, B., Reiche, S. & Schietinger, T. Emittance measurements and minimization at the SwissFEL Injector Test Facility. *Phys. Rev. ST Accel. Beams* **17,** 104401 (2014).

60. Rosenzweig, J. B., Cahill, A., Carlsten, B, Castorina, G, Croia, M, Emma, C., Fukusawa, A, Spataro, B, Alesini, D, Dolgashev, V., *et al.* Ultra-high brightness electron beams from very-high field cryogenic radiofrequency photocathode sources. *Nuclear Instruments and Methods in Physics Research Section A: Accelerators, Spectrometers, Detectors and Associated Equipment* **909,** 224–228 (2018).

61. Di Mitri, S. Bunch length compressors. *CERN Yellow Reports: School Proceedings* **1,** 363–363 (2018).

62. Charles, T. K., Paganin, D. M., Latina, A., Boland, M. J. & Dowd, R. T. Current-horn suppression for reduced coherent-synchrotron-radiation-induced emittance growth in strong bunch compression. *Phys. Rev. Accel. Beams* **20,** 030705 (2017).

63. Castro, P. *Beam trajectory calculations in bunch compressors of TTF2* (Dt. Elektronen-Synchrotron DESY, 2003).

64. Stulle, F. *A bunch compressor for small emittances and high peak currents at the VUV Free-Electron Laser* PhD thesis (Deutsches Elektronen-Synchrotron (DESY), 2004).

65. Huang, Z. & Kim, K.-J. Formulas for coherent synchrotron radiation microbunching in a bunch compressor chicane. *Phys. Rev. ST Accel. Beams* **5,** 074401 (2002).

66. Heifets, S., Stupakov, G. & Krinsky, S. Coherent synchrotron radiation instability in a bunch compressor. *Phys. Rev. ST Accel. Beams* **5,** 064401 (2002).

67. McNeil, B. W. J. X-ray free-electron lasers. *Nature Photonics* **4,** 814–821 (2010).

68. Gorn, E. J. *Traveling-wave electron reaction device* US2591350A. 1947.

69. Motz, H. Applications of the radiation from fast electron beams. *Journal of Applied Physics* **22,** 527–535 (1951).

70. Kulipanov, G. N. Ginzburg's invention of undulators and their role in modern synchrotron radiation sources and free electron lasers. *Physics-Uspekhi* **50,** 368 (2007).

71. Phillips, R. The ubitron, a high-power traveling-wave tube based on a periodic beam interaction in unloaded waveguide. *IRE Transactions on Electron Devices* **7,** 231–241 (1960).

72. Madey, J. M. Stimulated emission of bremsstrahlung in a periodic magnetic field. *Journal of Applied Physics* **42,** 1906–1913 (1971).

73. Elias, L. R., Fairbank, W. M., Madey, J. M., Schwettman, H. A. & Smith, T. I. Observation of stimulated emission of radiation by relativistic electrons in a spatially periodic transverse magnetic field. *Physical Review Letters* **36,** 717 (1976).

74. Deacon, D. A. G., Elias, L. R., Madey, J. M. J., Ramian, G. J., Schwettman, H. A. & Smith, T. I. First Operation of a Free-Electron Laser. *Phys. Rev. Lett.* **38,** 892–894 (1977).

75. Hogan, M, Pellegrini, C, Rosenzweig, J, Travish, G, Varfolomeev, A, Anderson, S, Bishofberger, K, Frigola, P, Murokh, A, Osmanov, N, *et al.* Measurements of high gain and intensity fluctuations in a self-amplified, spontaneous-emission free-electron laser. *Physical review letters* **80,** 289 (1998).

76. Pile, G, Bailey, J., Barsz, T, Berg, W, Collins, J., Den Hartog, P., Friedsam, H., Jaski, M., Lee, S., Lill, R., *et al.* Design and Construction of the Linac Coherent Light Source (LCLS) Undulator System. *Proceedings of FEL08,* 460–466 (2009).

77. Colson, W. One-body electron dynamics in a free electron laser. *Physics Letters A* **64,** 190–192 (1977).

78. Hopf, F., Meystre, P, Scully, M. & Louisell, W. Classical theory of a free-electron laser. *Physical Review Letters* **37,** 1215 (1976).

79. Orzechowski, T. J., Anderson, B., Fawley, W. M., Prosnitz, D., Scharlemann, E. T., Yarema, S., Hopkins, D., Paul, A. C., Sessler, A. M. & Wurtele, J. Microwave radiation from a high-gain free-electron laser amplifier. *Phys. Rev. Lett.* **54,** 889–892 (1985).

80. Group, L. D. S. *et al. LCLS Design Study Report* tech. rep. (SLAC, 1998).

81. Arthur, J *et al.* {Linac Coherent Light Source (LCLS)} Conceptual Design Report. *SLAC-R-593* (2002).

82. Emma, P, Akre, R, Arthur, J, Bionta, R, Bostedt, C, Bozek, J, Brachmann, A, Bucksbaum, P, Coffee, R, Decker, F.-J., *et al.* First lasing and operation of an ångstrom-wavelength free-electron laser. *Nature photonics* **4,** 641–647 (2010).

83. Pile, D. X-rays: First light from SACLA. *Nature Photonics* **5,** 456 (2011).

84. Prat, E., Abela, R., Aiba, M., Alarcon, A., Alex, J., Arbelo, Y., Arrell, C., Arsov, V., Bacellar, C., Beard, C., *et al.* A compact and cost-effective hard X-ray free-electron laser driven by a high-brightness and low-energy electron beam. *Nature Photonics* **14,** 748–754 (2020).

85. Weise, H., Decking, W., *et al.* Commissioning and first lasing of the European XFEL. *Proc. FEL'17,* 9–13 (2017).

86. Georgescu, I. The first decade of XFELs. *Nature Reviews Physics* **2,** 345–345 (2020).

87. The next decade of XFELs. *Nature Reviews Physics* **2,** 329 (2020).

88. Pellegrini, C. The development of XFELs. *Nature Reviews Physics* **2,** 330–331 (2020).

89. Fawley, W. *Ginger FEL simulation code* tech. rep. (LBNL technical report, 2001).

90. Reiche, S. GENESIS 1.3: a fully 3D time-dependent FEL simulation code. *Nuclear Instruments and Methods in Physics Research Section A: Accelerators, Spectrometers, Detectors and Associated Equipment* **429,** 243–248 (1999).

91. Campbell, L. & McNeil, B. Puffin: A three dimensional, unaveraged free electron laser simulation code. *Physics of Plasmas* **19,** 9 (2012).

92. Clarke, J. E. *The Science and Technology of Undulators and Wigglers* (Oxford University Press, 2004).

93. Schmüser, P., Dohlus, M., Rossbach, J. & Behrens, C. *Free-Electron Lasers in the Ultraviolet and X-Ray Regime* (Societ'a Italiana di Fisica, 2012).

94. Clarke, J. A. *The science and technology of undulators and wigglers* **4** (Oxford University Press on Demand, 2004).

95. Elleaume, P, Chavanne, J & Faatz, B. Design considerations for a 1 Å {SASE} undulator. *Nuclear Instruments and Methods in Physics Research Section A: Accelerators, Spectrometers, Detectors and Associated Equipment* **455,** 503 –523 (2000).

96. O'Shea, F. H., Marcus, G., Rosenzweig, J. B., Scheer, M., Bahrdt, J., Weingartner, R., Gaupp, A. & Grüner, F. Short period, high field cryogenic undulator for extreme performance x-ray free electron lasers. *Phys. Rev. ST Accel. Beams* **13,** 070702 (2010).

97. Harrison, J., Joshi, A., Lake, J., Candler, R. & Musumeci, P. Surface-micromachined magnetic undulator with period length between 10 μ m and 1 mm for advanced light sources. *Physical Review Special Topics-Accelerators and Beams* **15,** 070703 (2012).

98. Rosenzweig, J., Majernik, N, Robles, R., Andonian, G, Camacho, O, Fukasawa, A, Kogar, A, Lawler, G, Miao, J., Musumeci, P, *et al.* An ultra-compact x-ray free-electron laser. *New Journal of Physics* **22,** 093067 (2020).

99. Schmid, S. A. & Niedermayer, U. Design study of a dielectric laser undulator. *Physical Review Accelerators and Beams* **25,** 091301 (2022).

100. Huang, Z. & Kim, K.-J. Review of x-ray free-electron laser theory. *Physical Review Special Topics-Accelerators and Beams* **10,** 034801 (2007).

101. Press, W., Teukolsky, S. & Flannery, W. V. B. *Numerical recipes in C* (Cambridge University Press Cambridge, London, UK, 1988).

102. Emma, C., Wu, J., Fang, K., Chen, S., Serkez, S. & Pellegrini, C. Terawatt x-ray free-electron-laser optimization by transverse electron distribution shaping. *Phys. Rev. ST Accel. Beams* **17,** 110701 (2014).

103. Saldin, E., Schneidmiller, E., Yurkov, M., *et al.* Influence of an energy chirp on SASE FEL operation. *Proceedings of FEL2005, Stanford, CA, USA,* 258–261 (2005).

104. Saldin, E. L., Schneidmiller, E. A. & Yurkov, M. V. Self-amplified spontaneous emission FEL with energy-chirped electron beam and its application for generation of attosecond x-ray pulses. *Physical Review Special Topics-Accelerators and Beams* **9,** 050702 (2006).

105. Pierce, J. Transverse Fields in Traveling-Wave Tubes. *Bell System Technical Journal* **27,** 732–746 (1948).

106. Bonifacio, R., Pellegrini, C. & Narducci, L. M. Collective instabilities and high-gain regime in a free electron laser. *Optics Communications* **50,** 373–378 (1984).

107. Bonifacio, R. & Casagrande, F. The superradiant regime of a free electron laser. *Nuclear Instruments and Methods in Physics Research Section A: Accelerators, Spectrometers, Detectors and Associated Equipment* **239,** 36 –42 (1985).

108. Saldin, E., Schneidmiller, E. & Yurkov, M. Coherence properties of the radiation from SASE FEL. *Nuclear Instruments and Methods in Physics Research Section A: Accelerators, Spectrometers, Detectors and Associated Equipment* **507,** 106–109 (2003).

109. Rosenzweig, J., Alesini, D, Andonian, G, Boscolo, M, Dunning, M, Faillace, L, Ferrario, M, Fukusawa, A, Giannessi, L, Hemsing, E, *et al.* Generation of ultra-short, high brightness electron beams for single-spike SASE FEL operation. *Nuclear Instruments and Methods in Physics Research Section A: Accelerators, Spectrometers, Detectors and Associated Equipment* **593,** 39–44 (2008).

110. Kim, K.-J. Brightness, coherence and propagation characteristics of synchrotron radiation. *Nuclear Instruments and Methods in Physics Research Section A: Accelerators, Spectrometers, Detectors and Associated Equipment* **246,** 71–76 (1986).

111. M.Xie. Design Optimization for an X-Ray Free Electron Laser Driven by SLAC Linac. *Proc. Of 1995 Part. Accel. Conf.* **183** (1996).

112. Flottmann, K, Lidia, S. & Piot, P. Recent improvements to the astra particle trackingcode. *Proceedings of the 2003 Particle Accelerator Conference* **5,** 3500–3502 (2003).

113. De Loos, M., Van der Geer, S., *et al. General Particle Tracer: A new 3D code for accelerator and beamline design* in *5th European Particle Accelerator Conference* **1241** (1996), e96.

114. Borland, M. *Elegant: A flexible SDDS-compliant code for accelerator simulation* tech. rep. (Argonne National Lab., IL (US), 2000).

115. Campbell, L., MNeil, B., Smith, J., Traczykowski, P., *et al.* An Updated Description of the FEL Simulation Code Puffin. *9th Int. Particle Accelerator Conf.(IPAC'18),* 4579–4582 (2018).

116. Campbell, L. *GitHub repository: Puffin* `https://github.com/UKFELs/Puffin`, commit:master:7927560. 2020-2023.

117. Allan, R., Campbell, L., Colin, A., Dunning, D, McNeil, B., Muratori, B, Smith, J., Thompson, N., Traczykowski, P & Williams, P. HPC simulation suite for future FELs, e69 (2015).

118. McNeil, B., Poole, M. & Robb, G. Unified model of electron beam shot noise and coherent spontaneous emission in the helical wiggler free electron laser. *Physical Review Special Topics-Accelerators and Beams* **6,** 070701 (2003).

119. Traczykowski, P, Campbell, L. & McNeil, B. Up-sampling of electron beam simulation particles with addition of shot-noise. *Computer Physics Communications* **286,** 108661 (2023).

120. Hidding, B., Karger, O, Wittig, G, Aniculaesei, C, Jaroszynski, D, McNeil, B., Campbell, L., Islam, M., Ersfeld, B, Sheng, Z.-M., *et al.* Tunable electron multibunch production in plasma wakefield accelerators. *arXiv:1403.1109* (2014).

121. Alotaibi, B. M., Altuijri, R., Habib, A., Hala, A., Hidding, B., Khalil, S. M., McNeil, B. & Traczykowski, P. Plasma wakefield accelerator driven coherent spontaneous emission from an energy chirped electron pulse. *New Journal of Physics* **22,** 013037 (2020).

122. Garcia, B. W., Marcus, G., Campbell, L. T., McNeil, B. W. & Reiche, S. Comparing FEL Codes for Advanced Configurations. **2017,** SLAC–PUB–17138 (2018).

123. Bellan, P. M. *Fundamentals of plasma physics* (Cambridge university press, 2008).

124. Chen, F. F. & von Goeler, S. E. Introduction to plasma physics and controlled fusion volume 1: Plasma physics. *Physics Today* **38,** 87 (1985).

125. Chen, F. English. in *Introduction to Plasma Physics* 1–16 (Springer US, 1974).

126. Tajima, T., Yan, X. & Ebisuzaki, T. Wakefield acceleration. *Reviews of Modern Plasma Physics* **4,** 1–72 (2020).

127. Gibbon, P. Physics of high-intensity laser-plasma interactions. *La Rivista del Nuovo Cimento* **35,** 607–644 (2012).

128. Hershberger, W. Reflections from a plasma sphere and relationship between plasma frequency and the classical electron radius. *Journal of Applied Physics* **43,** 5204–5205 (1972).

129. Hooker, S. & Webb, C. *Laser physics* (Oxford University Press, 2010).

130. Keldysh, L. Ionization in the field of a strong electromagnetic wave. *Zh. Eksperim. i Teor. Fiz.* **47** (1964).

131. Bauer, D. Plasma formation through field ionization in intense laser–matter interaction. *Laser and Particle Beams* **21,** 489–495 (2003).

132. Ammosov, M. V., Delone, N. B. & Krainov, V. P. *Tunnel ionization of complex atoms and atomic ions in electromagnetic field* in *1986 Quebec Symposium* (1986), 138–141.

133. Bruhwiler, D. L., Dimitrov, D. A., Cary, J. R., Esarey, E., Leemans, W. & Giacone, R. E. Particle-in-cell simulations of tunneling ionization effects in plasma-based accelerators. *Physics of Plasmas (1994-present)* **10,** 2022–2030 (2003).

134. Krainov, V. P. Ionization rates and energy and angular distributions at the barrier-suppression ionization of complex atoms and atomic ions. *J. Opt.Soc. Am. B* **14,** 425 (1997).

135. Svelto, O., Hanna, D. C., *et al. Principles of lasers* (Springer, 2010).

136. Weiner, A. M. *Ultrafast optics* (John Wiley & Sons, 2011).

137. Corner, L. *Introduction to Laser Physics* 2020.

138. Dawson, J. M. Nonlinear Electron Oscillations in a Cold Plasma. *Phys. Rev.* **113,** 383–387 (1959).

139. Burnett, N. & Corkum, P. B. Cold-plasma production for recombination extreme-ultraviolet lasers by optical-field-induced ionization. *JOSA B* **6,** 1195–1199 (1989).

140. Rae, S. & Burnett, K. Possible production of cold plasmas through optical-field-induced ionization. *Physical Review A* **46,** 2077 (1992).

141. Chen, M, Esarey, E, Schroeder, C., Geddes, C. & Leemans, W. Theory of ionization-induced trapping in laser-plasma accelerators. *Physics of Plasmas* **19,** 033101 (2012).

142. Lehe, R., Kirchen, M., Andriyash, I. A., Godfrey, B. B. & Vay, J.-L. A spectral, quasi-cylindrical and dispersion-free Particle-In-Cell algorithm. *Computer Physics Communications* **203,** 66–82 (2016).

143. Schroeder, C. B., Vay, J.-L., Esarey, E., Bulanov, S. S., Benedetti, C., Yu, L.-L., Chen, M., Geddes, C. G. R. & Leemans, W. P. Thermal emittance from ionization-induced trapping in plasma accelerators. *Phys. Rev. ST Accel. Beams* **17,** 101301 (2014).

144. Hidding, B., Pretzler, G., Rosenzweig, J. B., Koenigstein, T., Schiller, D. & Bruhwiler, D. L. Ultracold Electron Bunch Generation via Plasma Photocathode Emission and Acceleration in a Beam-Driven Plasma Blowout. *Phys. Rev. Lett.* **108,** 035001– (2012).

145. Xi, Y., Hidding, B., Bruhwiler, D., Pretzler, G. & Rosenzweig, J. B. Hybrid modeling of relativistic underdense plasma photocathode injectors. *Phys. Rev. ST Accel. Beams* **16,** 031303 (2013).

146. Manahan, G., Deng, A, Karger, O, Xi, Y, Knetsch, A, Litos, M, Wittig, G, Heinemann, T, Smith, J, Sheng, Z., *et al.* Hot spots and dark current in advanced plasma wakefield accelerators. *Physical Review Accelerators and Beams* **19,** 011303 (2016).

147. Vafaei-Najafabadi, N, Shaw, J., Marsh, K., Joshi, C & Hogan, M. *Meter scale plasma source for plasma wakefield experiments* in *AIP Conference Proceedings* **1507** (2012), 650–655.

148. Green, S., Adli, E, Clarke, C., Corde, S., Edstrom, S., Fisher, A., Frederico, J, Frisch, J., Gessner, S, Gilevich, S, *et al.* Laser ionized preformed plasma at FACET. *Plasma Physics and Controlled Fusion* **56,** 084011 (2014).

149. Shalloo, R. J., Arran, C., Corner, L., Holloway, J., Jonnerby, J., Walczak, R., Milchberg, H. M. & Hooker, S. M. Hydrodynamic optical-field-ionized plasma channels. *Phys. Rev. E* **97,** 053203 (2018).

150. Mewes, S. M., Boyle, G. J., Pousa, A. F., Shalloo, R. J., Osterhoff, J., Arran, C., Corner, L., Walczak, R., Hooker, S. M. & Thévenet, M. Demonstration of tunability of HOFI waveguides via start-to-end simulations. *Phys. Rev. Res.* **5,** 033112 (2023).

151. Alfvén, H. & Wernholm, O. A new type of accelerator. *Arkiv for Fysik* **5,** 175–176 (1952).

152. Budker, G. Relativistic stabilized electron beam. *Soviet J. Atomic Energy* **1,** 673—686 (1956).

153. Veksler, V. I. Coherent principle of acceleration of charged particles. *CERN Symposium on High Energy Accelerators and Pion Physics,* 80–83 (1956).

154. Fainberg, Y. B. The use of plasma waveguides as accelerating structures in linear accelerators (1956).

155. Ruth, R. D., Chao, A., Wilson, P. B. & Morton, P. A plasma wake field accelerator. *Part. Accel.* **17,** 171 (1985).

156. Chen, P. The plasma wake field accelerator. *AIP Conference Proceedings* **130,** 201–212 (1985).

157. Katsouleas, T. Physical mechanisms in the plasma wake-field accelerator. *Phys. Rev. A* **33,** 2056–2064 (1986).

158. Rosenzweig, J. Nonlinear plasma dynanics in the plasma wakefield accelerator. *IEEE transactions on plasma science* **15,** 186–191 (1987).

159. Rosenzweig, J. B., Cline, D. B., Cole, B., Figueroa, H., Gai, W., Konecny, R., Norem, J., Schoessow, P. & Simpson, J. Experimental Observation of Plasma Wake-Field Acceleration. *Phys. Rev. Lett.* **61,** 98–101 (1988).

160. Rosenzweig, J. B., Breizman, B., Katsouleas, T. & Su, J. J. Acceleration and focusing of electrons in two-dimensional nonlinear plasma wake fields. *Phys. Rev. A* **44,** R6189–R6192 (1991).

161. Barov, N., Rosenzweig, J. B., Conde, M. E., Gai, W. & Power, J. G. Observation of plasma wakefield acceleration in the underdense regime. *Phys. Rev. ST Accel. Beams* **3,** 011301 (2000).

162. Suk, H., Barov, N., Rosenzweig, J. B. & Esarey, E. Plasma Electron Trapping and Acceleration in a Plasma Wake Field Using a Density Transition. *Phys. Rev. Lett.* **86,** 1011–1014 (2001).

163. Lu, W., Huang, C., Zhou, M., Mori, W. B. & Katsouleas, T. Nonlinear theory for relativistic plasma wakefields in the blowout regime. *Physical review letters* **96,** 165002 (2006).

164. Blumenfeld, I. *et al.* Energy doubling of 42[thinsp]GeV electrons in a metre-scale plasma wakefield accelerator. *Nature* **445,** 741–744 (2007).

165. Hidding, B., Manahan, G., Heinemann, T, Scherkl, P, Habib, F, Ullmann, D, Beaton, A, Sutherland, A, Knetsch, A, Karger, O, *et al.* First measurements of Trojan Horse injection in a plasma wakefield accelerator. *8th International Particle Accelerator Conference, Copenhagen, pp.TUYB1* (2017).

166. Ullmann, D, Scherkl, P, Knetsch, A, Heinemann, T, Sutherland, A, Habib, A., Karger, O., Beaton, A, Manahan, G., Deng, A, *et al.* All-optical density downramp injection in electron-driven plasma wakefield accelerators. *Physical Review Research* **3,** 043163 (2021).

167. Caldwell, A., Lotov, K., Pukhov, A. & Simon, F. Proton-driven plasma-wakefield acceleration. *Nature Physics* **5,** 363–367 (2009).

168. Adli, E., Ahuja, A., Apsimon, O, Apsimon, R., Bachmann, A.-M., Barrientos, D, Batsch, F., Bauche, J., Berglyd Olsen, V., Bernardini, M, *et al.* Acceleration of electrons in the plasma wakefield of a proton bunch. *Nature* **561,** 363–367 (2018).

169. Hidding, B, Foster, B, Hogan, M., Muggli, P & Rosenzweig, J. Directions in plasma wakefield acceleration. *Philosophical Transactions of the Royal Society A* **377,** 20190215 (2019).

170. Hidding, B., Hooker, S., Jamison, S., Muratori, B., Murphy, C., Najmudin, Z., Pattathil, R., Sarri, G., Streeter, M., Welsch, C., *et al.* Plasma Wakefield Accelerator Research 2019-2040: A community-driven UK roadmap compiled by

the Plasma Wakefield Accelerator Steering Committee (PWASC). *arXiv preprint arXiv:1904.09205* (2019).

171. Assmann, R., Weikum, M., Akhter, T, Alesini, D, Alexandrova, A., Anania, M., Andreev, N., Andriyash, I, Artioli, M, Aschikhin, A, *et al.* EuPRAXIA conceptual design report. *The European Physical Journal Special Topics* **229,** 3675–4284 (2020).

172. Geddes, C., Assmann, R, Hogan, M. & Musumeci, P. Report of the Accelerator Frontier Topical Group 6 on Advanced Accelerator Concepts for Snowmass 2021. *arXiv preprint arXiv:2208.13279* (2022).

173. Colby, E. R. & Len, L. Roadmap to the future. *Reviews of Accelerator Science and Technology* **9,** 1–18 (2016).

174. Adolphsen, C, Angal-Kalinin, D, Arndt, T, Arnold, M, Assmann, R, Auchmann, B, Aulenbacher, K, Ballarino, A, Baudouy, B, Baudrenghien, P, *et al.* European Strategy for Particle Physics–Accelerator R&D Roadmap. *arXiv preprint arXiv:2201.07895* (2022).

175. Tajima, T. & Dawson, J. M. Laser Electron Accelerator. *Phys. Rev. Lett.* **43,** 267–270 (1979).

176. Esarey, E., Sprangle, P., Krall, J. & Ting, A. Overview of plasma-based accelerator concepts. *Plasma Science, IEEE Transactions on* **24,** 252–288 (1996).

177. Akhiezer, A. I. & Polovin, R. Theory of wave motion of an electron plasma. *Soviet Phys. JETP* **3** (1956).

178. Modena, A, Najmudin, Z, Dangor, A., Clayton, C., *et al.* Electron acceleration from the breaking of relativistic plasma waves. *Nature* **377,** 606 (1995).

179. Clayton, C., Tzeng, K.-C., Gordon, D, Muggli, P, Mori, W., Joshi, C, Malka, V., Najmudin, Z, Modena, A, Neely, D, *et al.* Plasma wave generation in a self-focused channel of a relativistically intense laser pulse. *Physical review letters* **81,** 100 (1998).

180. Malka, V., Faure, J., Marques, J., Amiranoff, F., Rousseau, J.-P., Ranc, S, Chambaret, J., Najmudin, Z, Walton, B, Mora, P, *et al.* Characterization of electron beams produced by ultrashort (30 fs) laser pulses. *Physics of Plasmas* **8,** 2605–2608 (2001).

181. Jakobsson, O, Hooker, S. & Walczak, R. GeV-scale accelerators driven by plasma-modulated pulses from kilohertz lasers. *Physical Review Letters* **127,** 184801 (2021).

182. Van de Wetering, J. J., Hooker, S. M. & Walczak, R. Stability of the modulator in a plasma-modulated plasma accelerator. *Phys. Rev. E* **108,** 015204 (2023).

183. Ross, A. J., Chappell, J., van de Wetering, J. J., Cowley, J., Archer, E., Bourgeois, N., Corner, L., Emerson, D. R., Feder, L., Gu, X. J., *et al.* Resonant excitation of plasma waves in a plasma channel. *Physical Review Research* **6,** L022001 (2024).

184. Pukhov, A. & Meyer-ter Vehn, J. Laser wakefield acceleration: the highly non-linear broken-wave regime. *Applied Physics B* **74,** 355–361 (2002).

185. Mangles, S. P. D. *et al.* Monoenergetic beams of relativistic electrons from intense laser-plasma interactions. *Nature* **431,** 535–538 (2004).

186. Geddes, C. G. R., Toth, C., Tilborg, J. v., Esarey, E., Schroeder, C. B., Bruhwilder, D., Nieter, C., Cary, J. & Leemans, W. P. High-quality electron beams from a laser wakefield accelerator using plasma-channel guiding. *Nature* **431,** 538–541 (2004).

187. Faure, J., Glinec, Y., Pukhov, A., Kiselev, S., Gordienko, S., Lefebvre, E., Rousseau, J. P., Burgy, F. & Malka, V. A laser-plasma accelerator producing monoenergetic electron beams. *Nature* **431,** 541–544 (2004).

188. Hidding, B. *et al.* Generation of Quasimonoenergetic Electron Bunches with 80-fs Laser Pulses. *Phys. Rev. Lett.* **96,** 105004 (2006).

189. Osterhoff, J. *et al.* Generation of Stable, Low-Divergence Electron Beams by Laser-Wakefield Acceleration in a Steady-State-Flow Gas Cell. *Phys. Rev. Lett.* **101,** 085002 (2008).

190. Faure, J., Rechatin, C., Norlin, A., Lifschitz, A., Glinec, Y. & Malka, V. Controlled injection and acceleration of electrons in plasma wakefields by colliding laser pulses. *Nature* **444,** 737–739 (2006).

191. Leemans, W. P., Nagler, B., Gonsalves, A. J., Toth, C., Nakamura, K., Geddes, C. G. R., Esarey, E., Schroeder, C. B. & Hooker, S. M. GeV electron beams from a centimetre-scale accelerator. *Nature Physics* **2,** 696–699 (2006).

192. Oz, E. *et al.* Ionization-Induced Electron Trapping in Ultrarelativistic Plasma Wakes. *Phys. Rev. Lett.* **98,** 084801 (2007).

193. Faure, J., Rechatin, C., Lundh, O., Ammoura, L. & Malka, V. Injection and acceleration of quasimonoenergetic relativistic electron beams using density gradients at the edges of a plasma channel. *Physics of Plasmas (1994-present)* **17,** – (2010).

194. Gonsalves, A., Nakamura, K., Lin, C., Panasenko, D., Shiraishi, S., Sokollik, T., Benedetti, C., Schroeder, C., Geddes, C., Van Tilborg, J., *et al.* Tunable laser plasma accelerator based on longitudinal density tailoring. *Nature Physics* **7,** 862–866 (2011).

195. Lundh, O., Lim, J, Rechatin, C., Ammoura, L, Ben-Ismaïl, A., Davoine, X, Gallot, G., Goddet, J.-P., Lefebvre, E, Malka, V., *et al.* Few femtosecond, few kiloampere electron bunch produced by a laser–plasma accelerator. *Nature Physics* **7,** 219–222 (2011).

196. Gonsalves, A., Nakamura, K, Daniels, J, Benedetti, C, Pieronek, C, De Raadt, T., Steinke, S, Bin, J., Bulanov, S., Van Tilborg, J, *et al.* Petawatt laser guiding and electron beam acceleration to 8 GeV in a laser-heated capillary discharge waveguide. *Physical review letters* **122,** 084801 (2019).

197. Couperus, J., Pausch, R, Köhler, A, Zarini, O, Krämer, J., Garten, M, Huebl, A, Gebhardt, R, Helbig, U, Bock, S, *et al.* Demonstration of a beam loaded nanocoulomb-class laser wakefield accelerator. *Nature communications* **8,** 487 (2017).

198. Wenz, J., Döpp, A., Khrennikov, K., Schindler, S., Gilljohann, M., Ding, H., Götzfried, J, Buck, A., Xu, J., Heigoldt, M., *et al.* Dual-energy electron beams from a compact laser-driven accelerator. *Nature Photonics* **13,** 263–269 (2019).

199. Maier, A. R., Delbos, N. M., Eichner, T., Hübner, L., Jalas, S., Jeppe, L., Jolly, S. W., Kirchen, M., Leroux, V., Messner, P., *et al.* Decoding sources of energy variability in a laser-plasma accelerator. *Physical Review X* **10,** 031039 (2020).

200. Hidding, B., Beaton, A., Boulton, L., Corde, S., Doepp, A., Habib, F. A., Heinemann, T., Irman, A., Karsch, S., Kirwan, G., *et al.* Fundamentals and applications of hybrid lwfa-pwfa. *Applied Sciences* **9,** 2626 (2019).

201. Hidding, B, Königstein, T, Osterholz, J, Karsch, S., Willi, O & Pretzler, G. Monoenergetic energy doubling in a hybrid laser-plasma wakefield accelerator. *Physical review letters* **104,** 195002 (2010).

202. Chou, S., Xu, J., Khrennikov, K., Cardenas, D. E., Wenz, J., Heigoldt, M., Hofmann, L., Veisz, L. & Karsch, S. Collective Deceleration of Laser-Driven Electron Bunches. *Phys. Rev. Lett.* **117,** 144801 (2016).

203. Kurz, T. *et al.* Demonstration of a compact plasma accelerator powered by laser-accelerated electron beams. *Nature Communications* **12,** 2895 (2021).

204. Gilljohann, M., Ding, H., Döpp, A, Götzfried, J, Schindler, S, Schilling, G, Corde, S, Debus, A, Heinemann, T, Hidding, B, *et al.* Direct observation of plasma waves and dynamics induced by laser-accelerated electron beams. *Physical Review X* **9,** 011046 (2019).

205. Couperus Cabadağ, J., Pausch, R, Schöbel, S, Bussmann, M, Chang, Y.-Y., Corde, S, Debus, A, Ding, H., Döpp, A, Foerster, F., *et al.* Gas-dynamic density downramp injection in a beam-driven plasma wakefield accelerator. *Physical Review Research* **3,** L042005 (2021).

206. Foerster, F. M. *et al.* Stable and High-Quality Electron Beams from Staged Laser and Plasma Wakefield Accelerators. *Phys. Rev. X* **12,** 041016 (2022).

207. Esarey, E., Schroeder, C. B. & Leemans, W. P. Physics of laser-driven plasma-based electron accelerators. *Rev. Mod. Phys.* **81,** 1229–1285 (2009).

208. Wenz, J. & Karsch, S. Physics of laser-wakefield accelerators (LWFA). *arXiv:2007.04622* (2020).

209. Krushelnick, K. & Malka, V. Laser wakefield plasma accelerators. *Laser & Photonics Reviews* **4,** 42–52 (2010).

210. Joshi, C. *et al.* High energy density plasma science with an ultrarelativistic electron beam. *Physics of Plasmas* **9,** 1845–1855 (2002).

211. Nicholson, D. R. & Nicholson, D. R. *Introduction to plasma theory* (Cambridge Univ Press, 1983).

212. Tidman, D. A. & Krall, N. A. *Shock waves in collisionless plasmas* (Wiley-Interscience New York, 1971).

213. Bulanov, S., Kirsanov, V. & Sakharov, A. Excitation of ultrarelativistic plasma waves by pulse of electromagnetic radiation. *JETP Lett* **50,** 4–25 (1989).

214. Sprangle, P, Esarey, E. & Ting, A. Nonlinear theory of intense laser-plasma interactions. *Physical review letters* **64,** 2011 (1990).

215. Esarey, E. & Pilloff, M. Trapping and acceleration in nonlinear plasma waves. *Physics of Plasmas* **2,** 1432–1436 (1995).

216. Esarey, E., Schroeder, C. B. & Leemans, W. P. Physics of laser-driven plasma-based electron accelerators. *Rev. Mod. Phys.* **81,** 1229–1285 (2009).

217. Barov, N., Rosenzweig, J., Thompson, M. & Yoder, R. Energy loss of a high-charge bunched electron beam in plasma: Analysis. *Physical Review Special Topics-Accelerators and Beams* **7,** 061301 (2004).

218. Lotov, K. V. Blowout regimes of plasma wakefield acceleration. *Phys. Rev. E* **69,** 046405 (2004).

219. Kostyukov, I, Pukhov, A & Kiselev, S. Phenomenological theory of laser-plasma interaction in "bubble" regime. *Physics of Plasmas (1994-present)* **11,** 5256–5264 (2004).

220. Golovanov, A., Kostyukov, I., Pukhov, A. & Thomas, J. Generalised model of a sheath of a plasma bubble excited by a short laser pulse or by a relativistic electron bunch in transversely inhomogeneous plasma. *Quantum Electronics* **46,** 295 (2016).

221. Thomas, J., Kostyukov, I. Y., Pronold, J., Golovanov, A. & Pukhov, A. Non-linear theory of a cavitated plasma wake in a plasma channel for special applications and control. *Physics of Plasmas* **23,** 053108 (2016).

222. Golovanov, A. A., Kostyukov, I. Y., Reichwein, L, Thomas, J & Pukhov, A. Excitation of strongly nonlinear plasma wakefield by electron bunches. *Plasma Physics and Controlled Fusion* **63,** 085004 (2021).

223. Reichwein, L, Thomas, J, Golovanov, A, Kostyukov, I & Pukhov, A. Fixing E-field divergence in strongly non-linear wakefields in homogeneous plasma. *Plasma Physics and Controlled Fusion* **62,** 115017 (2020).

224. Baxevanis, P. & Stupakov, G. Novel fast simulation technique for axisymmetric plasma wakefield acceleration configurations in the blowout regime. *Phys. Rev. Accel. Beams* **21,** 071301 (2018).

225. Pousa, A. F., Assmann, R. & de la Ossa, A. M. *Wake-T: a fast particle tracking code for plasma-based accelerators* in *Journal of Physics: Conference Series* **1350** (2019), 012056.

226. Rosenzweig, J. B. Nonlinear plasma dynamics in the plasma wake-field accelerator. *Phys. Rev. Lett.* **58.** PWFA, 555–558 (1987).

227. Blumenfeld, I. *et al.* Scaling of the longitudinal electric field and transformer ratio in a nonlinear plasma wakefield accelerator. *Phys. Rev. ST Accel. Beams* **13,** 111301 (2010).

228. Loisch, G. *et al.* Observation of High Transformer Ratio Plasma Wakefield Acceleration. *Phys. Rev. Lett.* **121,** 064801 (2018).

229. Stark, R., Uhm, H. & Lampe, M. *Beam head erosion* in *The 1987 IEEE international conference on plasma science (Abstracts)* (1987).

230. Zhou, M., Clayton, C., Huang, C., Joshi, C., Lu, W., Marsh, K., Mori, W., Katsouleas, T., Muggli, P., Oz, E., *et al. Beam head erosion in self-ionized plasma wakefield accelerators* in *Particle Accelerator Conference, 2007. PAC. IEEE* (2007), 3064–3066.

231. Kelliher, M. & Beadle, R. Pulse-shortening in electron linear accelerators. *Nature* **187,** 1099–1099 (1960).

232. Altenmueller, O., Koontz, R., Kruse, C., Loew, G. & Miller, R. BEAM BREAK-UP EXPERIMENTS AT SLAC (1966).

233. Panofsky, W. & Bander, M. Asymptotic Theory of Beam Break-Up in Linear Accelerators. *Review of Scientific Instruments* **39,** 206–212 (1968).

234. Chao, A. W., Richter, B. & Yao, C.-Y. Beam emittance growth caused by transverse deflecting fields in a linear accelerator. *Nuclear Instruments and Methods* **178,** 1–8 (1980).

235. Lau, Y. Y. Classification of beam breakup instabilities in linear accelerators. *Phys. Rev. Lett.* **63,** 1141–1144 (1989).

236. Novokhatski, A. *BNS damping* in *CERN Yellow Reports: Conference Proceedings* **9** (2020), 68–68.

237. Balakin, V., Novokhatsky, A. & Smirnov, V. *VLEPP: transverse beam dynamics* in *Proc. of the 12th Int. Conf. on High Energy Accelerators, Fermilab* (1983).

238. Whittum, D. H., Sharp, W. M., Yu, S. S., Lampe, M. & Joyce, G. Electron-hose instability in the ion-focused regime. *Phys. Rev. Lett.* **67,** 991–994 (1991).

239. Mehrling, T. J., Fonseca, R. A., Martinez de la Ossa, A. & Vieira, J. Mitigation of the Hose Instability in Plasma-Wakefield Accelerators. *Phys. Rev. Lett.* **118,** 174801 (2017).

240. Mehrling, T. J., Benedetti, C., Schroeder, C. B., Esarey, E. & Leemans, W. P. Suppression of Beam Hosing in Plasma Accelerators with Ion Motion. *Phys. Rev. Lett.* **121,** 264802 (2018).

241. Mehrling, T., Fonseca, R., de la Ossa, A. M. & Vieira, J. Mechanisms for the mitigation of the hose instability in plasma-wakefield accelerators. *Physical Review Accelerators and Beams* **22,** 031302 (2019).

242. Martinez de la Ossa, A., Mehrling, T. J. & Osterhoff, J. Intrinsic Stabilization of the Drive Beam in Plasma-Wakefield Accelerators. *Phys. Rev. Lett.* **121,** 064803 (2018).

243. Pompili, R., Alesini, D, Anania, M., Behtouei, M, Bellaveglia, M, Biagioni, A, Bisesto, F., Cesarini, M, Chiadroni, E, Cianchi, A, *et al.* Energy spread minimization in a beam-driven plasma wakefield accelerator. *Nature Physics* **17,** 499–503 (2021).

244. Kallos, E., Katsouleas, T., Kimura, W. D., Kusche, K., Muggli, P., Pavlishin, I., Pogorelsky, I., Stolyarov, D. & Yakimenko, V. High-gradient plasma-wakefield acceleration with two subpicosecond electron bunches. *Physical review letters* **100,** 074802 (2008).

245. Schröder, S., Ludwig, K., Aschikhin, A., D'Arcy, R., Dinter, M, Gonzalez, P, Karstensen, S., Knetsch, A., Libov, V., Lindstrøm, C. A., *et al. Tunable and precise two-bunch generation at FLASHForward* in *Journal of Physics: Conference Series* **1596** (2020), 012002.

246. Clayton, C. E., Adli, E., Allen, J, An, W, Clarke, C., Corde, S., Frederico, J, Gessner, S, Green, S., Hogan, M. J., *et al.* Self-mapping the longitudinal field structure of a nonlinear plasma accelerator cavity. *Nature communications* **7,** 12483 (2016).

247. Schröder, S., Lindstrøm, C. A., Bohlen, S., Boyle, G, D'Arcy, R., Diederichs, S., Garland, M. J., Gonzalez, P, Knetsch, A., Libov, V., *et al.* High-resolution sampling of beam-driven plasma wakefields. *Nature Communications* **11,** 5984 (2020).

248. Lindstrøm, C. A. *et al.* Energy-Spread Preservation and High Efficiency in a Plasma-Wakefield Accelerator. *Phys. Rev. Lett.* **126,** 014801 (2021).

249. Faure, J. *Plasma Injection Schemes for Laser-Plasma Accelerators* tech. rep. (CERN, 2017).

250. Corde, S., Thaury, C., Lifschitz, A., Lambert, G., Ta Phuoc, K, Davoine, X, Lehe, R, Douillet, D, Rousse, A. & Malka, V. Observation of longitudinal and transverse self-injections in laser-plasma accelerators. *Nature communications* **4,** 1501 (2013).

251. Brantov, A., Esirkepov, T. Z., Kando, M, Kotaki, H, Bychenkov, V. Y. & Bulanov, S. Controlled electron injection into the wake wave using plasma density inhomogeneity. *Physics of Plasmas* **15,** 073111 (2008).

252. Suk, H., Barov, N., Rosenzweig, J. B. & Esarey, E. Plasma Electron Trapping and Acceleration in a Plasma Wake Field Using a Density Transition. *Phys. Rev. Lett.* **86,** 1011–1014 (2001).

253. Wittig, G. *et al.* Optical plasma torch electron bunch generation in plasma wakefield accelerators. *Phys. Rev. ST Accel. Beams* **18,** 081304 (2015).

254. Knetsch, A. *et al.* Stable witness-beam formation in a beam-driven plasma cathode. *Phys. Rev. Accel. Beams* **24,** 101302 (2021).

255. Zhang, C, Huang, C.-K., Marsh, K., Xu, X., Li, F, Hogan, M, Yakimenko, V, Corde, S, Mori, W. & Joshi, C. Effect of fluctuations in the down ramp plasma source profile on the emittance and current profile of the self-injected beam in a plasma wakefield accelerator. *Physical Review Accelerators and Beams* **22,** 111301 (2019).

256. Pak, A., Marsh, K. A., Martins, S. F., Lu, W., Mori, W. B. & Joshi, C. Injection and Trapping of Tunnel-Ionized Electrons into Laser-Produced Wakes. *Phys. Rev. Lett.* **104,** 025003 (2010).

257. Mora, P. & Antonsen Jr, T. M. Kinetic modeling of intense, short laser pulses propagating in tenuous plasmas. *Physics of Plasmas* **4,** 217–229 (1997).

258. Vafaei-Najafabadi, N., Marsh, K. A., Clayton, C. E., An, W., Mori, W. B., Joshi, C., Lu, W, Adli, E., Corde, S., Litos, M, *et al.* Beam loading by distributed injection of electrons in a plasma wakefield accelerator. *Physical Review Letters* **112,** 025001 (2014).

259. Martinez de la Ossa, A., Grebenyuk, J., Mehrling, T., Schaper, L. & Osterhoff, J. High-Quality Electron Beams from Beam-Driven Plasma Accelerators by Wakefield-Induced Ionization Injection. *Phys. Rev. Lett.* **111,** 245003 (2013).

260. Martinez de la Ossa, A., Mehrling, T., Schaper, L, Streeter, M. & Osterhoff, J. Wakefield-induced ionization injection in beam-driven plasma accelerators. *Physics of plasmas* **22,** 093107 (2015).

261. Vafaei-Najafabadi, N., Amorim, L., Adli, E, An, W, Clarke, C., Clayton, C., Corde, S, Gessner, S, Green, S., Hogan, M., *et al.* Producing multi-coloured bunches through beam-induced ionization injection in plasma wakefield accelerator. *Philosophical Transactions of the Royal Society A* **377,** 20180184 (2019).

262. Hidding, B. *et al.* Progress in Hybrid Plasma Wakefield Acceleration. *Photonics* **10,** 99 (2023).

263. Alastair Nutter and Patrick Ufer *et al. All-optical, ultracompact and ultrafast plasma photocathode wakefield acceleration* In perparation.

264. Kostyukov, I., Pukhov, A. & Kiselev, S. Phenomenological theory of laser-plasma interaction in "bubble" regime. *Physics of Plasmas* **11,** 5256–5264 (2004).

265. Knetsch, A. *Acceleration of laser-injected electron beams in an electron-beam driven plasma wakefield accelerator* PhD thesis (University of Hamburg, 2018).

266. Scherkl, P. *High-brightness plasma-based Compton backscattering source for high energy physics* PhD thesis (University of Strathclyde, 2020).

267. Bourgeois, N., Cowley, J. & Hooker, S. M. Two-Pulse Ionization Injection into Quasilinear Laser Wakefields. *Phys. Rev. Lett.* **111,** 155004 (2013).

268. Stumpf, M, Melchger, M, Montag, S & Pretzler, G. Multiparameter-controlled laser ionization within a plasma wave for wakefield acceleration. *Journal of Physics B: Atomic, Molecular and Optical Physics* **55,** 015401 (2022).

269. Katsouleas, S. W. T. & Su, J. D. J. Beam loading efficiency in plasma accelerators. *Part. Accel* **22,** 81–99 (1987).

270. Tzoufras, M., Lu, W., Tsung, F. S., Huang, C., Mori, W. B., Katsouleas, T., Vieira, J., Fonseca, R. A. & Silva, L. O. Beam Loading in the Nonlinear Regime of Plasma-Based Acceleration. *Phys. Rev. Lett.* **101,** 145002 (2008).

271. Bret, A., Gremillet, L. & Dieckmann, M. E. Multidimensional electron beam-plasma instabilities in the relativistic regime. *Physics of Plasmas* **17,** 120501 (2010).

272. Sands, M. *A beta mismatch parameter* tech. rep. (SLAC National Accelerator Lab., Menlo Park, CA (United States), 1991).

273. Lindstrøm, C. A. Staging of plasma-wakefield accelerators. *Physical Review Accelerators and Beams* **24,** 014801 (2021).

274. Lindstrøm, C. A. & Thévenet, M. Emittance preservation in advanced accelerators. *Journal of Instrumentation* **17,** P05016 (2022).

275. Mehrling, T., Grebenyuk, J., Tsung, F. S., Floettmann, K. & Osterhoff, J. Transverse emittance growth in staged laser-wakefield acceleration. *Phys. Rev. ST Accel. Beams* **15,** 111303– (2012).

276. Dornmair, I., Floettmann, K. & Maier, A. R. Emittance conservation by tailored focusing profiles in a plasma accelerator. *Phys. Rev. ST Accel. Beams* **18,** 041302 (2015).

277. Ariniello, R., Doss, C. E., Hunt-Stone, K., Cary, J. R. & Litos, M. D. Transverse beam dynamics in a plasma density ramp. *Phys. Rev. Accel. Beams* **22,** 041304 (2019).

278. Montague, B. W. S. L. *Linear optics for improved chromaticity correction* tech. rep. (SCAN-0009131, 1979).

279. Guillaume, E. *et al.* Physics of fully-loaded laser-plasma accelerators. *Phys. Rev. ST Accel. Beams* **18,** 061301 (2015).

280. Pae, K. H., Choi, I. W. & Lee, J. Self-mode-transition from laser wakefield accelerator to plasma wakefield accelerator of laser-driven plasma-based electron acceleration. *Physics of Plasmas* **17,** 123104 (2010).

281. Corde, S. *et al.* Mapping the X-Ray Emission Region in a Laser-Plasma Accelerator. *Phys. Rev. Lett.* **107,** 215004 (2011).

282. Masson-Laborde, P., Mo, M., Ali, A, Fourmaux, S, Lassonde, P, Kieffer, J., Rozmus, W, Teychenné, D & Fedosejevs, R. Giga-electronvolt electrons due to a transition from laser wakefield acceleration to plasma wakefield acceleration. *Physics of Plasmas* **21,** 123113 (2014).

283. Götzfried, J, Döpp, A, Gilljohann, M., Foerster, F., Ding, H, Schindler, S, Schilling, G, Buck, A, Veisz, L. & Karsch, S. Physics of high-charge electron beams in laser-plasma wakefields. *Physical Review X* **10,** 041015 (2020).

284. Zgadzaj, R., Silva, T, Khudyakov, V., Sosedkin, A, Allen, J, Gessner, S, Li, Z., Litos, M, Vieira, J, Lotov, K., *et al.* Dissipation of electron-beam-driven plasma wakes. *Nature Communications* **11,** 4753 (2020).

285. Rosenzweig, J. B., Cook, A., Scott, A, Thompson, M. & Yoder, R. Effects of ion motion in intense beam-driven plasma wakefield accelerators. *Physical review letters* **95,** 195002 (2005).

286. Schöbel, S., Pausch, R., Chang, Y.-Y., Corde, S., Cabadağ, J. C., Debus, A., Ding, H., Döpp, A., Foerster, F. M., Gilljohann, M., *et al.* Effect of driver charge on wakefield characteristics in a plasma accelerator probed by femtosecond shadowgraphy. *New Journal of Physics* **24,** 083034 (2022).

287. Nieter, C. & Cary, J. R. VORPAL: a versatile plasma simulation code. *Journal of Computational Physics* **196,** 448–473 (2004).

288. Lehe, R. *FBPIC* GitHub repository: `https://github.com/fbpic/fbpic`. 2020-2023.

289. Courant, R., Friedrichs, K. & Lewy, H. Über die partiellen Differenzengleichungen der mathematischen Physik. *Mathematische Annalen* **100,** 32–74 (1928).

290. Greenwood, A. D., Cartwright, K. L., Luginsland, J. W. & Baca, E. A. On the elimination of numerical Cerenkov radiation in PIC simulations. *Journal of Computational Physics* **201,** 665 –684 (2004).

291. Lehe, R., Lifschitz, A., Thaury, C., Malka, V. & Davoine, X. Numerical growth of emittance in simulations of laser-wakefield acceleration. *Phys. Rev. ST Accel. Beams* **16,** 021301– (2013).

292. Cowan, B. M., Bruhwiler, D. L., Cary, J. R., Cormier-Michel, E. & Geddes, C. G. Generalized algorithm for control of numerical dispersion in explicit time-domain electromagnetic simulations. *Physical Review Special Topics-Accelerators and Beams* **16,** 041303 (2013).

293. Karger, O. S. *Pathways towards Ultra-high brightness electron beams* PhD thesis (University of Hamburg, 2020).

294. Davidson, N., Friesem, A. & Hasman, E. Holographic axilens: high resolution and long focal depth. *Optics letters* **16,** 523–525 (1991).

295. Ullmann, D. *Laser generated plasma torch injectors for beam-driven plasma wakefield accelerators* PhD thesis (University of Strathclyde, 2021).

296. Hogan, M. *Preliminary Conceptual Design Report for the FACET-II Project at SLAC National Accelerator Laboratory* tech. rep. (SLAC National Accelerator Lab., 2016).

297. Yakimenko, V., Lipkowitz, N., Clarke, C., Hogan, M., Yocky, G., Hast, C., Green, S., Cai, Y., Phinney, N. & White, G. FACET-II accelerator research with beams of extreme intensities. *Proceedings of IPAC2016* **TUOBB02,** 1067–1670 (2016).

298. Yakimenko, V. *et al.* FACET-II facility for advanced accelerator experimental tests. *Phys. Rev. Accel. Beams* **22,** 101301 (2019).

299. Lee, V., Ariniello, R., Doss, C., Wolfinger, K., Stoltz, P., Hansel, C., Gessner, S., Cary, J. & Litos, M. Temporal evolution of the light emitted by a thin, laser-ionized plasma source. *Physics of Plasmas* **31,** 013104 (2024).

300. Lindstrøm, C., Beinortaitė, J, Björklund Svensson, J, Boulton, L, Chappell, J, Diederichs, S, Foster, B, Garland, J., González Caminal, P, Loisch, G, *et al.* Emittance preservation in a plasma-wakefield accelerator. *Nature Communications* **15,** 6097 (2024).

301. Emma, P. & Team, L. C. First lasing of the LCLS X-ray FEL at 1.5 Å. *Proceedings of PAC09, Vancouver, to be published in http://accelconf. web. cern. ch/AccelConf* (2009).

302. Hidding, B., Manahan, G., Habib, A. F., *et al. Plasma accelerator* US patent app. 11013100 and EP patent app. 3510843. 2021.

303. Emma, P. *Chirping the LCLS electron beam* tech. rep. (SLAC National Accelerator Lab., Menlo Park, CA (United States), 2018).

304. Floettmann, K. Some basic features of the beam emittance. *Phys. Rev. ST Accel. Beams* **6,** 034202 (2003).

305. Assmann, R. & Yokoya, K. Transverse beam dynamics in plasma-based linacs. *Nuclear Instruments and Methods in Physics Research Section A: Accelerators, Spectrometers, Detectors and Associated Equipment* **410,** 544 –548 (1998).

306. Antici, P. *et al.* Laser-driven electron beamlines generated by coupling laser-plasma sources with conventional transport systems. *Journal of Applied Physics* **112,** 044902 (2012).

307. Sciscio, M., Lancia, L., Migliorati, M., Mostacci, A., Palumbo, L., Papaphilippou, Y. & Antici, P. Parametric study of transport beam lines for electron beams accelerated by laser-plasma interaction. *Journal of Applied Physics* **119,** 094905 (2016).

308. Gholizadeh, R, Katsouleas, T, Muggli, P, Huang, C & Mori, W. Preservation of beam emittance in the presence of ion motion in future high-energy plasma-wakefield-based colliders. *Physical review letters* **104,** 155001 (2010).

309. Lindstrøm, C. A. & Adli, E. Design of general apochromatic drift-quadrupole beam lines. *Phys. Rev. Accel. Beams* **19,** 071002 (2016).

310. Zhang, Z., Bane, K., Ding, Y., Huang, Z., Iverson, R., Maxwell, T., Stupakov, G. & Wang, L. Electron beam energy chirp control with a rectangular corrugated structure at the Linac Coherent Light Source. *Phys. Rev. ST Accel. Beams* **18,** 010702 (2015).

311. Fu, F. *et al.* Demonstration of Nonlinear-Energy-Spread Compensation in Relativistic Electron Bunches with Corrugated Structures. *Phys. Rev. Lett.* **114,** 114801 (2015).

312. Antipov, S., Baturin, S., Jing, C., Fedurin, M., Kanareykin, A., Swinson, C., Schoessow, P., Gai, W. & Zholents, A. Experimental Demonstration of Energy-

Chirp Compensation by a Tunable Dielectric-Based Structure. *Phys. Rev. Lett.* **112,** 114801 (2014).

313. Van der Meer, S. *Improving the power efficiency of the plasma wakefield accelerator* tech. rep. (CM-P00058040, 1985).

314. Caminal, P. G. *Time-resolved Phase-space Characterisation of Plasma-wakefield-accelerated Electrons at FLASHForward* PhD thesis (Deutsches Elektronen-Synchrotron DESY, 2022).

315. Emma, C., Xu, X., Fisher, A., Robles, R, MacArthur, J., Cryan, J, Hogan, M., Musumeci, P, White, G & Marinelli, A. Terawatt attosecond x-ray source driven by a plasma accelerator. *APL Photonics* **6,** 076107 (2021).

316. Lapostolle, P. M. Possible emittance increase through filamentation due to space charge in continuous beams. *IEEE Transactions on Nuclear Science* **18,** 1101–1104 (1971).

317. Sacherer, F. J. RMS envelope equations with space charge. *IEEE Transactions on Nuclear Science* **18,** 1105–1107 (1971).

318. Brinkmann, R. *et al.* Chirp Mitigation of Plasma-Accelerated Beams by a Modulated Plasma Density. *Phys. Rev. Lett.* **118,** 214801 (2017).

319. Döpp, A., Thaury, C., Guillaume, E., Massimo, F., Lifschitz, A., Andriyash, I., Goddet, J.-P., Tazfi, A., Ta Phuoc, K. & Malka, V. Energy-Chirp Compensation in a Laser Wakefield Accelerator. *Phys. Rev. Lett.* **121,** 074802 (2018).

320. Kirchen, M., Jalas, S., Messner, P., Winkler, P., Eichner, T., Hübner, L., Hülsenbusch, T., Jeppe, L., Parikh, T., Schnepp, M., *et al.* Optimal beam loading in a laser-plasma accelerator. *Physical review letters* **126,** 174801 (2021).

321. Shpakov, V. *et al.* Longitudinal Phase-Space Manipulation with Beam-Driven Plasma Wakefields. *Phys. Rev. Lett.* **122,** 114801 (2019).

322. Wu, Y. P. *et al.* Phase Space Dynamics of a Plasma Wakefield Dechirper for Energy Spread Reduction. *Phys. Rev. Lett.* **122,** 204804 (2019).

323. D'Arcy, R. *et al.* Tunable Plasma-Based Energy Dechirper. *Phys. Rev. Lett.* **122,** 034801 (2019).

324. Ferran Pousa, A., Martinez de la Ossa, A., Brinkmann, R. & Assmann, R. W. Compact Multistage Plasma-Based Accelerator Design for Correlated Energy Spread Compensation. *Phys. Rev. Lett.* **123,** 054801 (2019).

325. Xu, J., Shen, B., Zhang, X., Wen, M., Ji, L., Wang, W., Yu, Y. & Li, Y. Overloading effect of energetic electrons in the bubble regime of laser wakefield acceleration. *Physics of Plasmas (1994-present)* **17,** 103108 (2010).

326. Rechatin, C., Faure, J., Davoine, X., Lundh, O., Lim, J, Ben-Ismaïl, A., Burgy, F., Tafzi, A., Lifschitz, A., Lefebvre, E., *et al.* Characterization of the beam loading effects in a laser plasma accelerator. *New Journal of Physics* **12,** 045023 (2010).

327. Varverakis, M., Holtzapple, R., Diederichs, S., Schroeder, C. & Gessner, S. Energy recovery in filament-regime plasma wakefield acceleration of positron beams. *arXiv:2311.07087* (2023).

328. Di Mitri, S & Cornacchia, M. Electron beam brightness in linac drivers for free-electron-lasers. *Physics Reports* **539,** 1–48 (2014).

329. Zeng, M., Chen, M., Yu, L.-L., Mori, W. B., Sheng, Z.-M., Hidding, B., Jaroszynski, D. & Zhang, J. Multichromatic narrow-energy-spread electron bunches from laser-wakefield acceleration with dual-color lasers. *Physical review letters* **114,** 084801 (2015).

330. Moon, K., Kumar, S., Hur, M. & Chung, M. Longitudinal phase space dynamics of witness bunch during the Trojan Horse injection for plasma-based particle accelerators. *Physics of Plasmas* **26,** 073103 (2019).

331. Nakajima, K, Kando, M, Kawakubo, T, Nakanishi, T & Ogata, A. A table-top X-ray FEL based on the laser wakefield accelerator-undulator system. *Nuclear Instruments and Methods in Physics Research Section A: Accelerators, Spectrometers, Detectors and Associated Equipment* **375,** 593–596 (1996).

332. Jaroszynski, D. & Vieux, G. *Coherent radiation sources based on laser plasma accelerators* in *AIP Conference Proceedings* **647** (2002), 902–914.

333. Nakajima, K. Compact X-ray sources: Towards a table-top free-electron laser. *Nature physics* **4,** 92–93 (2008).

334. Schlenvoigt, H.-P. *et al.* A compact synchrotron radiation source driven by a laser-plasma wakefield accelerator. *Nature physics* **4,** 130–133 (2008).

335. Fuchs, M., Weingartner, R., Popp, A., Major, Z., Becker, S., Osterhoff, J., Cortrie, I., Zeitler, B., Hörlein, R., Tsakiris, G. D., *et al.* Laser-driven soft-X-ray undulator source. *Nature physics* **5,** 826–829 (2009).

336. André, T, Andriyash, I., Loulergue, A, Labat, M, Roussel, E, Ghaith, A, Khojoyan, M, Thaury, C, Valléau, M, Briquez, F, *et al.* Control of laser plasma accelerated electrons for light sources. *Nature communications* **9,** 1334 (2018).

337. Maier, A. R., Kajumba, N., Guggenmos, A., Werle, C, Wenz, J., Delbos, N, Zeitler, B, Dornmair, I, Schmidt, J, Gullikson, E., *et al.* Water-window X-ray pulses from a laser-plasma driven undulator. *Scientific reports* **10,** 5634 (2020).

338. Maier, A. R., Meseck, A., Reiche, S., Schroeder, C. B., Seggebrock, T. & Grüner, F. Demonstration Scheme for a Laser-Plasma-Driven Free-Electron Laser. *Phys. Rev. X* **2,** 031019.

339. Grüner, F., Becker, S., Schramm, U, Eichner, T, Fuchs, M, Weingartner, R, Habs, D., Meyer-ter Vehn, J., Geissler, M., Ferrario, M, *et al.* Design considerations for table-top, laser-based VUV and X-ray free electron lasers. *Applied Physics B* **86,** 431–435 (2007).

340. Huang, Z., Ding, Y. & Schroeder, C. B. Compact X-ray free-electron laser from a laser-plasma accelerator using a transverse-gradient undulator. *Physical review letters* **109,** 204801 (2012).

341. Wu, Y., Hua, J., Zhou, Z, Zhang, J, Liu, S, Peng, B, Fang, Y, Nie, Z, Ning, X., Pai, C.-H., *et al.* Phase space dynamics of a plasma wakefield dechirper for energy spread reduction. *Physical review letters* **122,** 204804 (2019).

342. Hidding, B. *et al.* Tunable Electron Multibunch Production in Plasma Wakefield Accelerators. *arXiv,* 1403.1109 (2014).

343. Emma, C. *et al.* Free electron lasers driven by plasma accelerators: status and near-term prospects. *High Power Laser Science and Engineering* **9,** e57 (2021).

344. Wang, W., Feng, K., Ke, L., Yu, C., Xu, Y., Qi, R., Chen, Y., Qin, Z., Zhang, Z., Fang, M., *et al.* Free-electron lasing at 27 nanometres based on a laser wakefield accelerator. *Nature* **595,** 516–520 (2021).

345. Pompili, R, Alesini, D, Anania, M., Arjmand, S, Behtouei, M, Bellaveglia, M, Biagioni, A, Buonomo, B, Cardelli, F, Carpanese, M, *et al.* Free-electron lasing with compact beam-driven plasma wakefield accelerator. *Nature* **605,** 659–662 (2022).

346. Labat, M., Cabadağ, J. C., Ghaith, A., Irman, A., Berlioux, A., Berteaud, P., Blache, F., Bock, S., Bouvet, F., Briquez, F., *et al.* Seeded free-electron laser driven by a compact laser plasma accelerator. *Nature Photonics* **17,** 150–156 (2023).

347. Galletti, M. *et al.* Stable Operation of a Free-Electron Laser Driven by a Plasma Accelerator. *Phys. Rev. Lett.* **129,** 234801 (2022).

348. Graydon, O. The race for wakefield-driven FELs. *Nature Photonics* **16,** 750–751 (2022).

349. Vay, J.-L., Geddes, C. G., Cormier-Michel, E. & Grote, D. P. Numerical methods for instability mitigation in the modeling of laser wakefield accelerators in a Lorentz-boosted frame. *Journal of Computational Physics* **230,** 5908–5929 (2011).

350. Godfrey, B. B. & Vay, J.-L. Numerical stability of relativistic beam multidimensional PIC simulations employing the Esirkepov algorithm. *Journal of Computational Physics* **248,** 33–46 (2013).

351. Prat, E., Dijkstal, P., Aiba, M., Bettoni, S., Craievich, P., Ferrari, E., Ischebeck, R., Löhl, F., Malyzhenkov, A, Orlandi, G., *et al.* Generation and characterization of intense ultralow-emittance electron beams for compact x-ray free-electron lasers. *Physical review letters* **123,** 234801 (2019).

352. Van Der Geer, S., Luiten, O., De Loos, M., Pöplau, G & Van Rienen, U. *3D space-charge model for GPT simulations of high brightness electron bunches* in *Institute of Physics Conference Series* **175** (2005), 101.

353. Lim, J. K., Frigola, P., Travish, G., Rosenzweig, J. B., Anderson, S. G., Brown, W. J., Jacob, J. S., Robbins, C. L. & Tremaine, A. M. Adjustable, short focal length permanent-magnet quadrupole based electron beam final focus system. *Phys. Rev. ST Accel. Beams* **8,** 072401 (2005).

354. OShea, F, Andonian, G & UCLA, J. R. *PERMANENT MAGNET QUADRUPOLE FINAL FOCUS SYSTEM FOR THE MUON COLLIDER* Proceeding. IPAC 10. 2010.

355. Cheshkov, S, Tajima, T, Horton, W & Yokoya, K. Particle dynamics in multistage wakefield collider. *Physical review special topics-accelerators and beams* **3,** 071301 (2000).

356. Borland, M. Simple method for particle tracking with coherent synchrotron radiation. *Physical Review Special Topics-Accelerators and Beams* **4,** 070701 (2001).

357. Campbell, L., McNeil, B. & Reiche, S. Two-colour free electron laser with wide frequency separation using a single monoenergetic electron beam. *New Journal of Physics* **16,** 103019 (2014).

358. Bonifacio, R, Piovella, N, Robb, G. & Schiavi, A. Quantum regime of free electron lasers starting from noise. *Physical Review Special Topics-Accelerators and Beams* **9,** 090701 (2006).

359. Reinsch, M., Austin, B, Corlett, J., Doolittle, L., Penn, G, Prosnitz, D, Qiang, J, Sessler, A, Venturini, M, Wurtele, J., *et al.* SYSTEM TRADE ANALYSIS FOR AN FELFACILITY (2011).

360. D'Arcy, R., Chappell, J., Beinortaite, J., Diederichs, S., Boyle, G, Foster, B., Garland, M. J., Caminal, P. G., Lindstrøm, C. A., Loisch, G., *et al.* Recovery time of a plasma-wakefield accelerator. *Nature* **603,** 58–62 (2022).

361. Rovige, L., Huijts, J., Andriyash, I, Vernier, A, Tomkus, V, Girdauskas, V., Raciukaitis, G, Dudutis, J, Stankevic, V, Gecys, P, *et al.* Demonstration of stable long-term operation of a kilohertz laser-plasma accelerator. *Physical Review Accelerators and Beams* **23,** 093401 (2020).

362. Danson, C. N., Haefner, C., Bromage, J., Butcher, T., Chanteloup, J.-C. F., Chowdhury, E. A., Galvanauskas, A., Gizzi, L. A., Hein, J., Hillier, D. I., *et al.* Petawatt and exawatt class lasers worldwide. *High Power Laser Science and Engineering* **7,** e54 (2019).

363. Giesen, A., Hügel, H, Voss, A, Wittig, K, Brauch, U & Opower, H. Scalable concept for diode-pumped high-power solid-state lasers. *Applied Physics B* **58,** 365–372 (1994).

364. Zervas, M. N. & Codemard, C. A. High power fiber lasers: a review. *IEEE Journal of selected topics in Quantum Electronics* **20,** 219–241 (2014).

365. Corner, L. Fibre lasers for gamma colliders. *The European Physical Journal Special Topics* **223,** 1207–1211 (2014).

366. Hidding, B. & Habib, A. F. *Plasma-based hard X-Ray FEL with ultrahigh gain and sub-fs capability* SLAC FACET-II Program Advisory Committee chaired by Edda Gschwendtner. `https://facet-ii.slac.stanford.edu/proposals/pac/pac2018` (2024).

367. Hidding, B. & Habib, A. F. *Plasma-based hard X-Ray FEL with ultrahigh gain and sub-fs capability* SLAC FACET-II Program Advisory Committee chaired by Edda Gschwendtner. `https://facet-ii.slac.stanford.edu/proposals/pac/pac2022` (2024).

368. Ryndyk, D., Kohlfürst, C., Queisser, F. & Schützhold, R. Dynamically assisted tunneling in the Floquet picture. *Physical Review Research* **6,** 023056 (2024).

369. Habib, A. F. *Towards PWFA-X-FEL* Physics and Applications of High Brightness Beams. `https://indico.classe.cornell.edu/event/2170/contributions/2504/` (2023).

370. Habib, A. F. *Ultra-compact X-ray free-electron laser near the cold beam limit* IOP Particle Accelerators and Beams Conference. `https://indico.cern.ch/event/1248024/contributions/5243785/` (2023).